

NORTHWESTERN UNIVERSITY

Nanoscale Mechanics of Ductile Interphases in Solid Solution
Directionally Solidified Eutectic Composites

A DISSERTATION

SUBMITTED TO THE GRADUATE SCHOOL
IN PARTIAL FULFILLMENT OF THE REQUIREMENTS

for the degree

DOCTOR OF PHILOSOPHY

Field of Materials Science and Engineering

By

Nasim Alem

EVANSTON, ILLINOIS

June 2007

© Copyright by Nasim Alem 2007

All Rights Reserved

ABSTRACT

Nanoscale Mechanics of Ductile Interphases in Solid Solution

Directionally Solidified Eutectic Composites

Nasim Alem

Ceramic matrix composites are known for their low density, high strength and high stiffness, but lower fracture toughness compared to metal matrix composites. The addition of a reinforcing agent within the matrix can increase the toughness of the composite via many strain energy absorption mechanisms such as plastic deformation. This dissertation attempts to shed light on the competing deformation and fracture mechanisms in ductile/brittle nanoscale lamellar systems where the conventional deformation mechanisms may not apply. $\text{Ni}_x\text{Co}_{1-x}\text{O}/\text{ZrO}_2$ Directionally Solidified Eutectic (DSE) composite series has been chosen as a model system for this study.

In the first part of this dissertation, it is demonstrated that formation of a novel metal-ceramic multi-layered structure is feasible via reduction of $\text{Ni}_x\text{Co}_{1-x}\text{O}/\text{ZrO}_2$ composite as a result of the interfaces forming an electrochemical cell in a reducing atmosphere at high temperatures.

The second part of the thesis is dedicated in understanding the correlative deformation and fracture mechanisms in the reduced $\text{Ni}_x\text{Co}_{1-x}\text{O}/\text{ZrO}_2$ model system with a nanoscale Ni(Co) confined interphase. These investigations were inspired by a novel observation that there is striking dissimilarity in the interfacial fracture behavior of the reduced $\text{Ni}_x\text{Co}_{1-x}\text{O}/\text{ZrO}_2$ composite compared to that of the fully oxidized $\text{Ni}_x\text{Co}_{1-x}\text{O}/\text{ZrO}_2$ system.

A multitude of conventional and analytical electron microscopy techniques are utilized to investigate the role of the size scale, chemistry of this model system on the strain energy absorption upon deformation. FIB TEM lift-off technique is further employed to investigate the crack tip interactions with the nanoscale confined interphases in this model system. To study the role of size scale, the nanoscale deformation mechanism within the metallic interphase is investigated across 50-300 nm thickness range for the confined Ni(Co) interphase. The role of chemistry on the small scale deformation mechanisms in this model system is investigated by choosing two different compositions in the $\text{Ni}_x\text{Co}_{1-x}\text{O}/\text{ZrO}_2$ composite series: CoO/ZrO_2 with $x=0$ and $\text{Ni}_{0.5}\text{Co}_{0.5}\text{O}/\text{ZrO}_2$ with $x=0.5$. These investigations confirm that the metallic interphase, with the thickness of above 100 nm, contributes to strain energy absorption through plastic deformation. With decreasing the interphase size scale to values below 100 nm, the extent of plasticity is reduced within the metallic interphase.

Vinayak P Dravid
Ph.D. Dissertation Advisor
Materials Science and Engineering
Northwestern University
Evanston, IL

Acknowledgments

My stay at Northwestern has been not only an academic experience but also a personal journey as it taught me many lessons and made me a different person. I would like to thank many people for teaching me, believing in me and guiding me to the right direction during this period of my life.

First I would like to thank my parents, without whom I could not have made it this far. I can never repay their support and belief they had in me. I am also thankful to my brother for his support during all these years. I would like to thank my husband, Jay, for his love and patience during my academic pursuit and for growing with me throughout my education.

I would like to thank my advisor, Prof. Vinayak P. Dravid for providing me with every possible resource, despite all the difficulties, for doing excellent science. I would like to thank him for teaching me to “think out of the box”, and for introducing me to the larger scientific community.

I would like to thank Dr. Alex Revcolevschi and Dr. Luke Brewer for the original growth of the crystals used in this work. I would like to acknowledge the *NUANCE* center at Northwestern University for the use of the various instruments in the course of this study. I would like to thank all the *NUANCE* personnel particularly Dr. Jian-Guo Zheng and Dr. Shuyou Li for teaching me about the instruments in the facility and for being so patient with me. I would like to thank Dr. Masa Kawasaki from JEOL for teaching me the subtleties of getting good data from the ASTAR and for being so helpful and supportive. I would also like to acknowledge CMM at the University of Illinois at Urbana Champaign for the use of the FIB dual beam and EBSD and the help of the staff, particularly Mike Marshall.

I would like to thank Dr. Edwin Fuller and Dr. Douglas Smith among other team members at the Ceramics Division at National Institute of Standards and Technology for working so hard to host me at NIST and for their support for the miniature mechanical testing work. I would like to thank Prof. Julia Weertman and Dr. Donald Kramer for our effective discussions on my research topic. They have been very helpful in developing my research scheme. I also would like to thank my committee members, Prof. Faber, Prof. Dunand and Prof. Espinosa, for their help and guidance whenever I needed.

I would like to thank my group members for being there for me and for making my day-to-day life so enjoyable and fun. I like to thank Dr. Pradyumna Prabhumirashi and Dr. Shuyou Li for teaching me the basics of microscopy and for helping me out during the difficult times. I want to thank Dr. Luke Brewer and Dr. Tom Isabell for their support and guidance during these last five years. I like to thank Dr. Hao Hu for being a wonderful friend and for his support during the last few months of my thesis work. I also like to thank Zixiao, Mike, Suresh, Sooh-Yun, Feng, Tao, Aslam, Ethan and Ann for making my day-to-day life so terrific and for being there for me whenever I needed them. It has been great sharing the morning and afternoon coffee breaks with you.

My stay at northwestern has been really special because of many wonderful friends and colleagues. I am thankful to Mark Sinew for being such a wonderful and supportive friend for me during these years. I am also thankful to Dr. Susan Farjami for her support during the last months of my work. I would like to finally thank all the staff in the department office, particularly Joanna Gwinn and Peggy Adamson.

I like to acknowledge my funding agency for this work. The funding for this research is partially provided by the National Science Foundation (NSF) and the Department of Energy-Basic Energy Sciences (DOE-BES).

TABLE OF CONTENTS

| | |
|--|-----------|
| ABSTRACT..... | 3 |
| ACKNOWLEDGMENTS..... | 5 |
| TABLE OF CONTENTS..... | 8 |
| LIST OF ABBREVIATIONS..... | 12 |
| TABLE OF FIGURES..... | 13 |
| TABLE OF TABLES..... | 19 |
| 1 INTRODUCTION..... | 21 |
| 2 DEFORMATION AND FRACTURE PHENOMENA IN MULTI-LAYERED SYSTEMS..... | 24 |
| 2.1 Literature Review..... | 24 |
| 2.1.1 <i>Toughening Mechanisms in Ceramic Composites.....</i> | 24 |
| 2.1.2 <i>Toughening Mechanisms in Metal-Ceramic Composites.....</i> | 29 |
| 2.1.3 <i>Effect of Size Scale on the Mechanical Properties of Multi-Layered Composites.....</i> | 33 |
| 2.2 Scope of This Thesis..... | 39 |
| 2.2.1 <i>Importance of the Effect of Size Scale on the Deformation Behavior of Multi-Layered Composite Systems.....</i> | 39 |
| 2.2.2 <i>Ni_xCo_{1-x}O/ZrO₂: A Ductile-Brittle Multi-Layered Model System.....</i> | 40 |
| 2.2.3 <i>Objectives.....</i> | 48 |
| 3 DEVELOPMENT AND STRUCTURAL CHARACTERIZATION OF Ni_xCo_{1-x}O/ZrO₂(CaO) MODEL SYSTEM WITH A DUCTILE INTERPHASE..... | 53 |

| | |
|--|------------|
| | 9 |
| 3.1 Experimental Techniques..... | 53 |
| 3.1.1 Reduction Technique..... | 53 |
| 3.1.2 Transmission Electron Microscopy..... | 55 |
| 3.1.3 Principles of Scanning Transmission Electron Microscopy..... | 57 |
| 3.1.4 Electron Energy Loss Spectroscopy (EELS)..... | 58 |
| 3.2 Characterization of the $Ni_xCo_{1-x}O/ZrO_2(CaO)$ Model System Upon Reduction..... | 60 |
| 3.2.1 Microstructural Evolution of the Reduced $Ni_xCo_{1-x}O/ZrO_2(CaO)$ Model System..... | 60 |
| 3.2.2 Chemical Nature of the Reduced $Ni_xCo_{1-x}O/ZrO_2(CaO)$ System..... | 69 |
| 3.2.3 Crystallography of the Reduced $Ni_xCo_{1-x}O/ZrO_2(CaO)$ System..... | 76 |
| 3.2.4 Interfacial Structure of the Reduced $Ni_xCo_{1-x}O/ZrO_2(CaO)$ Model System..... | 85 |
| 3.2.5 Evolution of Residual Stresses in the Reduced $Ni_xCo_{1-x}O/ZrO_2(CaO)$ Model System..... | 88 |
| 3.2.6 Summary and Conclusions..... | 95 |
| 4 CRACK PROPAGATION BEHAVIOR OF $Ni_xCo_{1-x}O/ZrO_2(CaO)$ COMPOSITE WITH A NANOSCALE METALLIC INTERPHASE..... | 97 |
| 4.1 Experimental Procedures..... | 98 |
| 4.1.1 Vickers Indentation Test..... | 98 |
| 4.1.2 Nano-Indentation Test..... | 99 |
| 4.2 Interfacial Fracture Phenomena in the Pristine and Reduced $Ni_xCo_{1-x}O/ZrO_2(CaO)$ DSEs | 101 |
| 4.3 Evaluation of the Small Scale Plasticity Across the Reduced $Ni_xCO_{1-x}O/ZrO_2(CaO)$ DSEs Through Nano-Indentation Technique | 113 |
| 4.4 Summary and Conclusions | 121 |
| 5 SMALL SCALE DEFORMATION AND FRACTURE BEHAVIOR: $Ni_xCo_{1-x}O/ZrO_2(CaO)$ MODEL SYSTEM WITH A DUCTILE INTERPHASE..... | 122 |

| | |
|---|------------|
| | 10 |
| 5.1 Sample Preparation Methods | 122 |
| 5.1.1 Conventional TEM Sample Preparation Technique..... | 124 |
| 5.1.2 FIB Lift-off TEM Sample Preparation Technique..... | 125 |
| 5.2 Observations of the Small Scale Deformation Behavior in the Reduced Ni_xCo_{1-x}O/ZrO₂(CaO) Model System..... | 131 |
| 5.2.1 Observation of the Small Scale Deformation Behavior in the Metallic Interphases with the Thickness of 100 nm or Higher..... | 132 |
| 5.2.2 Observations of the Small Scale Deformation Behavior in the Metallic Interphases with the Thickness of Less Than 100 nm..... | 140 |
| 5.2.3 Mechanics of Crack Tip Interactions with the Metallic Interphase at Small Scales..... | 148 |
| 5.2.4 Differences in the Deformation Mechanisms Observed in the Metallic Interphase across the Size Scale Studied Here | 155 |
| 5.3 Operative Deformation Mechanisms in the Reduced Ni_xCo_{1-x}O/ZrO₂(CaO) Composite..... | 156 |
| 5.3.1 Dislocation Nucleation in the Metallic Interphase..... | 157 |
| 5.3.2 Deformation Twinning in the Metallic Interphase..... | 162 |
| 5.4 Summary and Conclusions | 172 |
| 6 EVALUATION OF THE MECHANICAL PROPERTIES IN THE Ni_xCo_{1-x}O/ZrO₂(CaO) MODEL SYSTEM VIA A MINIATURE MECHANICAL TESTING METHOD | 174 |
| 6.1 Design of the Theta Specimen..... | 174 |
| 6.2 Experimental Procedures..... | 178 |
| 6.3 Mechanical Testing of Ni_xCo_{1-x}O/ZrO₂(CaO) Theta Structures..... | 182 |
| 6.4 Summary and Conclusions | 185 |

| | | |
|----------|---|------------|
| | | 11 |
| 7 | SUMMARY AND CONCLUSIONS..... | 186 |
| 8 | SUGGESTIONS FOR FUTURE WORK..... | 192 |
| | REFERENCES | 194 |

LIST OF ABBREVIATIONS

| | |
|------|---|
| DSE | Directionally Solidified Eutectic |
| TEM | Transmission Electron Microscopy |
| SEM | Scanning Electron Microscopy |
| FIB | Focused Ion Beam |
| IBT | Ion Beam Thinning |
| AEM | Analytical Electron Microscopy |
| CTEM | Conventional Transmission Electron Microscopy |
| EDXS | Energy Dispersive X-ray Spectroscopy |
| EELS | Electron Energy Loss Spectroscopy |
| ADF | Annular Dark Field |
| ZLP | Zero Loss Peak |
| HCP | Hexagonal Closed Pack |
| FCC | Face Centered Cubic |
| BCC | Body Centered Cubic |
| SAD | Selected Area Diffraction |
| CTE | Coefficient of Thermal Expansion |

TABLE OF FIGURES

| | |
|---|----|
| Figure 2.1 Competition between two fracture mechanisms: Crack penetration (a) versus crack delamination along the interface (b) in a multi-layered composite. | 26 |
| Figure 2.2 Ratio of the energy release rate of a deflected crack to the maximum energy release rate of a penetrating crack as a function of α for a wedge loaded crack. ³² | 28 |
| Figure 2.3 Fracture mechanisms in both ductile and brittle manner in metal-ceramic composites. ²⁵ | 31 |
| Figure 2.4 Schematic illustration of the strengthening mechanisms: (a) Hall-Petch model indicating the yield stress of the system to be inversely proportional to the layer thickness of the film and (b) Orowan model indicating dislocation bowing along the interfaces within the film in multi-layered systems. ⁷³ | 37 |
| Figure 2.5 Yield stress of FCC thin film bound to rigid substrates as a function of film thickness with a constant grain size. In this figure τ_T is considered to be the applied stress and τ_Y to be the yield stress and l_Y to be the thickness of the film, below which the film does not yield. ⁶⁴ | 38 |
| Figure 2.6 Variation of the lattice parameter in (a) $\text{Co}_{1-x}\text{Ni}_x\text{O}$ and (b) $\text{ZrO}_2(\text{CaO})$ as a function of the composition in the $\text{Co}_{1-x}\text{Ni}_x\text{O}/\text{ZrO}_2(\text{CaO})$ composite. ^{10, 16, 17} | 42 |
| Figure 2.7 Variation of nano-hardness across the solid solution $\text{Ni}_x\text{Co}_{1-x}\text{O}$ in the single crystal and the DSE samples. ^{10, 17} | 44 |
| Figure 2.8 Schematic view of the composite showing the reduction front and formation of the metallic interphases in the $\text{Ni}_x\text{Co}_{1-x}\text{O}/\text{ZrO}_2(\text{CaO})$ system. | 46 |
| Figure 2.9 The ongoing research scheme for development of a predictive model system in deformation and fracture behavior of interface-controlled materials | 49 |
| Figure 2.10 Correlation between the extent of plasticity and the size of the ductile interphase in ductile-brittle multi-layered systems..... | 50 |
| Figure 2.11 Schematic diagram of the research scheme in the present thesis work..... | 52 |
| Figure 3.1 Heating/cooling diagram during the reduction process in this system. | 54 |
| Figure 3.2 A schematic representation indicating formation of a bright/dark field STEM image in the STEM mode. | 58 |
| Figure 3.3 Formation of shrinkage cracks at the top surface of the composite after reduction (shown with arrows on the Figure) | 62 |
| Figure 3.4 SEM micrographs of the top view (a) and cross-sectional view (b) of reduced $\text{Ni}_x\text{Co}_{1-x}\text{O}/\text{ZrO}_2(\text{CaO})$. (a) The porous matrix indicates the porous metallic Ni(Co) phase | |

surrounding the ZrO_2 fingers. (b) The bright area shown with arrows at the top portion of the sample indicates the fully reduced region in the $Ni_kCo_{1-x}O$ phase. 63

Figure 3.5 Cross-sectional microstructure of the reduced CoO/ZrO_2 sample indicating full reduction of CoO phase adjacent to the primary ZrO_2 phase. 64

Figure 3.6 SEM micrograph showing the microstructure of $Ni_kCo_{1-x}O/ZrO_2(CaO)$ system (a) before reduction and (b) after reduction (different region). Note the formation of bright metallic layers along the interfaces after reduction. 65

Figure 3.7 (a) SEM micrograph of the reduced DSEs indicating porosity formation along the metal- ZrO_2 interphase. (b) Binarized image of the SEM micrograph indicating the pores as white areas in the black matrix. 67

Figure 3.8 Porosity distribution at the (a) cross-section and (b) along the depth in the partially reduced regions of the $Ni_kCo_{1-x}O/ZrO_2(CaO)$ sample with $x=0.5$. (c) The distribution profile for the area of the porosity after reduction of the sample. 68

Figure 3.9 EDXS spectrum showing the chemistry of ZrO_2 in the $Ni_{0.5}Co_{0.5}O/ZrO_2$ and presence of small amount of Ni and Co in ZrO_2 71

Figure 3.10 (a) DF STEM image of the reduced CoO/ZrO_2 composite along with electron energy loss spectra across the interface showing (b) Zr $M_{4,5}$ and Ca $L_{2,3}$ edge, (c) O K edge and (d) Co $L_{2,3}$ edge moving from Co interphase to ZrO_2 . (The black line on the STEM image shows the region of analysis) Step size=0.65nm 74

Figure 3.11 Electron energy loss spectra across the CoO-Co interface showing (a) the rise of O K edge and (b) Co $L_{2,3}$ edge moving from Co interphase to CoO. (The area of analysis is shown in figure 3.10 (a)) Step size=0.65nm 75

Figure 3.12 (a) Typical microstructure of the reduced composite with the metallic interphase maintaining single crystal structure (60 nm in this area) and (b) Small size twins are infrequently observed within the metallic interphase at such size scale (shown with arrows on the image). ... 77

Figure 3.13 Bright field image of Co interphase with its SAD pattern in the reduced $CoO/ZrO_2(CaO)$ sample indicating FCC structure of Co with $\langle 110 \rangle$ zone axis. The streaks in the diffraction pattern indicate presence of stacking faults and the double spots indicate twinning formation within the metallic layer. The circle on the image indicates the area the diffraction pattern has been obtained. 78

Figure 3.14 Bright field image of Ni(Co) interphase (a) with its SAD pattern (b) in the reduced $Ni_{0.5}Co_{0.5}O/ZrO_2(CaO)$ sample indicating FCC structure of Co with $\langle 110 \rangle$ zone axis. The circle in the image indicates the area the diffraction pattern is taken from. 80

Figure 3.15 Bright field TEM image of the reduced $Ni_{0.5}Co_{0.5}O/ZrO_2$ phase showing deformation in the Ni(Co) phase through formation of twins in the Ni(Co). (Indicated with arrows on the figure)..... 83

- Figure 3.16 Stacking fault energy variations across the composition in the Ni-Co alloy. (a) Stacking fault energy change in the Co rich Ni-Co alloys¹²² and (b) Changes in the stacking fault energy ratio of Ni and the solute elements in the Ni rich alloys.¹²⁵84
- Figure 3.17 SAD pattern from the Ni(Co)-Ni_{0.5}Co_{0.5}O interface where the <111> planes of the metallic Ni(Co) are parallel with the <111> planes of the Ni_{0.5}Co_{0.5}O phase. The reflections from the Ni_{0.5}Co_{0.5}O phase are shown in solid lines and with italic font on the image.....86
- Figure 3.18 HREM image of the Ni(Co)-ZrO₂ interface indicating presence of clean interfaces without any inter-layer or compound in the reduced composite.....88
- Figure 3.19 Formation of dislocations in the Ni_xCo_{1-x}O phase after the reduction process90
- Figure 3.20 Dark field TEM images of the reduced Ni_{0.5}Co_{0.5}O/ZrO₂ phase showing deformation through dislocation formation in the Ni_{0.5}Co_{0.5}O originating from the Ni(Co)-Ni_{0.5}Co_{0.5}O interface (indicated with arrows on the figure).....91
- Figure 3.21 Bright field TEM image of the reduced CoO/ZrO₂ composite showing twinning formation in the Ni(Co) interphase adjacent to the porosity (Indicated with arrows on the figure).92
- Figure 4.1 Deformation and fracture behavior of the CoO/ZrO₂(CaO) composite in the (a) pristine and (b) reduced form upon the Vickers indentation test.103
- Figure 4.2 Deformation behavior of the reduced CoO/ZrO₂(CaO) adjacent to the Vickers indentation mark.105
- Figure 4.3 Deformation and fracture behavior in the Ni_{0.5}Co_{0.5}O/ZrO₂(CaO) system upon Vickers indentation showing (a) sharp cracks in the pristine/as-grown DSE system (cracks are shown with arrows) and (b & c) interfacial delamination, crack arrest and crack bridging across the metallic interphase in the partially reduced composites (shown with arrows on the (c)).107
- Figure 4.4 (a) Deformation and fracture behavior of the reduced Ni_{0.5}Co_{0.5}O/ZrO₂(CaO) system upon Vickers indentation test revealing (b) nucleation of secondary cracks within both Ni_{0.5}Co_{0.5}O and ZrO₂(CaO) and interfacial delamination from the metallic Ni(Co) interphase to ZrO₂(CaO) if moving away from the indent (shown with arrows on the image).109
- Figure 4.5 Crack arrest and crack bridging across the metallic interphase upon Vickers indentation of the reduced Ni_{0.5}Co_{0.5}O/ZrO₂(CaO).110
- Figure 4.6 Load-displacement curve in a nano-indentation experiment114
- Figure 4.7 (a) Topography image of the reduced Ni_{0.5}Co_{0.5}O/ZrO₂(CaO) along with the load displacement curves from (b) the metallic Ni(Co) interphase, (c) ZrO₂(CaO) and (d) Ni_{0.5}Co_{0.5}O after indentation of this region. (The thickness of the metallic interphase is about 180 nm here and the size of the image is 3×3 μm)116

Figure 4.8 (a) Topography image of the reduced $\text{Ni}_{0.5}\text{Co}_{0.5}\text{O}/\text{ZrO}_2(\text{CaO})$ after nano-indentation. (b) Hardness variation across the interfaces from $\text{Ni}_{0.5}\text{Co}_{0.5}\text{O}$ to $\text{ZrO}_2(\text{CaO})$. (c) Load-displacement curve for point c shown on the image. The indentation step size here is 150-200 nm and the metallic layer thickness is about 140 nm. 118

Figure 4.9 (a) Topography image of the fully reduced $\text{Ni}_{0.5}\text{Co}_{0.5}\text{O}/\text{ZrO}_2(\text{CaO})$ after nano-indentation in this region. (b) Hardness variation across the $\text{ZrO}_2(\text{CaO})$ - $\text{Ni}(\text{Co})$ - $\text{ZrO}_2(\text{CaO})$ phases. 119

Figure 4.10 (a) Topography image of the pristine $\text{Ni}_{0.5}\text{Co}_{0.5}\text{O}/\text{ZrO}_2(\text{CaO})$ after nano-indentation in this region. (b) Hardness variation across the interface from $\text{Ni}_{0.5}\text{Co}_{0.5}\text{O}$ to $\text{ZrO}_2(\text{CaO})$ 120

Figure 5.1 Step-by-step procedures for the conventional TEM sample preparation technique for the study of the deformation mechanism. These steps show (a) the reduced sample, (b) the sample after it is deformed by Vickers indentation and mounted on a TEM grid (the black spots on the surface of the sample indicate the indentation marks), (c) dimpling procedure at the bottom surface of the sample (d) the final ion milling stage (e) the final TEM sample after creating a hole at the center adjacent to the indentation mark. 125

Figure 5.2 A thin Pt layer is deposited adjacent to the indentation mark on the area of interest prior to TEM sample fabrication to protect the top surface of the sample from beam damage. .127

Figure 5.3 A thin membrane of the sample with 1-2 μm thickness is fabricated from the area of interest 128

Figure 5.4 Sample is welded to the micro-manipulator before it is detached from the substrate.129

Figure 5.5 Sample is removed from the bulk and transferred to the TEM grid using the micro-manipulator. 130

Figure 5.6 Sample is welded to the TEM grid using the Pt deposition source. 130

Figure 5.7 The sample is further thinned down on the TEM grid to obtain thickness of about or less than 100 nm. 131

Figure 5.8 Formation of twins within the metallic Co interphase in the area very near to the indentation mark ($\alpha=70^\circ$) in the deformed reduced $\text{CoO}/\text{ZrO}_2(\text{CaO})$ system. 134

Figure 5.9 Stacking fault formation indicating dislocation slip across the metallic Co interphase in the deformed reduced $\text{CoO}/\text{ZrO}_2(\text{CaO})$ system. The layer thickness in this region is about 250 nm. 134

Figure 5.10 Deformation twins along with an array of short dislocations distributed within the metallic Co interphase in the deformed reduced $\text{CoO}/\text{ZrO}_2(\text{CaO})$ system. The metallic layer thickness varies from 150-250 nm in this region. 135

- Figure 5.11 Dislocation formation within the Ni(Co) interphase in an area very near to the indentation mark in the reduced $\text{Ni}_{0.5}\text{Co}_{0.5}\text{O}/\text{ZrO}_2(\text{CaO})$ composite after deformation. 137
- Figure 5.12 Deformation twinning within the Ni(Co) interphase near the indentation mark after deformation of the reduced $\text{Ni}_{0.5}\text{Co}_{0.5}\text{O}/\text{ZrO}_2(\text{CaO})$ composite. The arrows on the image point to the twins within the metallic Ni(Co) interphase. 138
- Figure 5.13 Small scale deformation behavior of confined Co interphase with about 60 nm thickness. The Moiré fringes shown with arrows suggest presence of dislocations in this region. 141
- Figure 5.14 Dislocations extended into the confined Co interphase of about 60 nm thickness. . 142
- Figure 5.15 Twinning formation within Co with 70-80 nm thickness in the reduced deformed $\text{CoO}/\text{ZrO}_2(\text{CaO})$ composite. 144
- Figure 5.16 Stacking fault formation within the Co interphase after deformation. (shown with arrow on the image) The interphase thickness is about 60 nm in this region. 145
- Figure 5.17 Dislocation formation within the confined Ni(Co) interphase with about 75 nm thickness. 146
- Figure 5.18 Strain contrast within the Ni(Co) interphase pointing to the highly strained Ni(Co) film with little to no plastic deformation. The thickness of the confined Ni(Co) interphase shown here is 48 nm. (b) Traces of dislocation slip across the interphase in the Ni(Co) interphase with thickness of 60 nm (shown with arrows on the image). 147
- Figure 5.19 Crack tip interactions with the metal-ceramic lamellae in the reduced $\text{CoO}/\text{ZrO}_2(\text{CaO})$ sample. 150
- Figure 5.20 Crack arrest by the ductile interphase followed by extensive strain energy absorption within the CoO phase. The arrows indicate nucleation and extension of dislocation bands near the crack tip. 151
- Figure 5.21 (a) Dislocation nucleation within CoO indicates extensive plastic deformation of CoO near the crack tip in this area. The white arrows on the image point to the multiple cracks within the $\text{ZrO}_2(\text{CaO})$ phase, while the black arrow shows the crystal orientation of the CoO phase. (b) Limited plastic deformation of the metallic Co interphase (indicated by arrows on the image) leading to crack arrest and crack tip blunting. 153
- Figure 5.22 Crack tip interactions with the metallic interphase indicating crack arrest by the metallic Ni(Co) interphase. The thickness of the Ni(Co) interphase in this region is about 40-50 nm. 155
- Figure 5.23 Yield stress for an FCC thin film bound to a rigid substrate as a function of film thickness assuming the grain size to be constant.⁶⁴ 159

| | |
|---|-----|
| Figure 5.24 The equilibrium number of dislocations as a function of the applied stress intensity within a layer for different values of layer thickness in a model system. ⁵⁶ | 161 |
| Figure 5.25 Schematic illustration of the two plastic deformation modes; (a) slip versus (b) twinning in a FCC metal. ¹⁵⁴ | 164 |
| Figure 5.26 Twinning stress as a function of stacking fault formation energy for various Cu alloys. ^{152, 153} | 165 |
| Figure 5.27 Critical thickness of a twin as a function of its radius calculated for a gamma-based Ti-Al alloy. ¹⁶⁷ | 168 |
| Figure 5.28 Elastic strain energy per unit length of a twin as a function of twin thickness. The twin length is considered to be 700 nm here. ¹⁶⁷ | 169 |
| Figure 6.1 Finite element modeling of the stress distribution upon compressive loading of a Si miniature sample at the top surface. ¹⁷⁹ | 176 |
| Figure 6.2 The theta specimen under compression along with the geometrical parameters affecting the resulting stress and strain in the middle web. ¹⁷⁹ | 177 |
| Figure 6.3 (a) The FIB fabrication procedures followed to construct the theta specimens, (b and C) along with the resulting sample fabricated from the pristine $\text{Ni}_k\text{Co}_{1-x}\text{O}/\text{ZrO}_2(\text{CaO})$. The fabrication steps have been shown respectively. | 179 |
| Figure 6.4 (a) The fabricated theta specimen from the pristine $\text{Ni}_k\text{Co}_{1-x}\text{O}/\text{ZrO}_2(\text{CaO})$. (b & c) EBSD pattern from the middle web in the specimen from the area shown in the box on the image. Image (b) shows the EBSD pattern before ion sputtering and (c) shows the EBSD pattern after ion sputtering. | 181 |
| Figure 6.5 (a) The fabricated theta specimen from the pristine $\text{Ni}_k\text{Co}_{1-x}\text{O}/\text{ZrO}_2(\text{CaO})$. (b) Stress distribution within the sample considering the presence of the thermal mismatch strain in the sample. ¹⁷⁹ (c) Stress distribution within the sample after applying a compression load on the top surface. ¹⁷⁹ | 183 |
| Figure 6.6 (a) The fabricated theta specimen from the pristine $\text{CoO}/\text{ZrO}_2(\text{CaO})$ after loading. (b) Fracture on the top portion of the sample frame before the middle web. (c) Load-displacement curve for this specimen. | 184 |

TABLE OF TABLES

| | |
|--|----|
| Table 3.1 Coefficient of thermal expansion values of Ni, Co, $Ni_kCo_{1-x}O$ and $ZrO_2(CaO)$. ^{85, 132, 133} | 93 |
| Table 3.2 Thermal expansion mismatch values between the adjacent metal-ceramic interfaces in the reduced composite..... | 94 |

1 INTRODUCTION

As devices and components in modern materials shrink to small sizes, it becomes more crucial to understand the micron and nanoscale properties of such components. This understanding is critical since materials systems show significantly different physical and mechanical properties at submicron sizes. The final performance of submicron miniature devices is greatly influenced by many attributes of materials systems such as interfaces, bonding, adhesion, atomic structure, chemistry and plasticity. Therefore it is of particular importance to probe the length scale dependence properties of materials to further meet the current technological performance requirements.

Among the modern materials systems nano-composites are of great interest due to their wide applications in hard coatings¹⁻³, magnetic⁴ and semi-conducting applications⁵ as well as micro electromechanical systems^{6,7}. These applications generally require high wear protection and high composite durability. In order to meet the design requirements, both the materials properties and the final device performance should be optimized. Therefore, it is essential to establish a structure-property relationship between the microstructure and the deformation and fracture phenomena for this class of materials.

Although much effort has already been made to study the mechanical properties of composites, there is still a large gap connecting the deformation phenomena at different length scales. Developing a proper structure-property relationship for this class of materials would require a thorough as well as correlative understanding of the behavior of the system at various length scales. This multi-length scale approach allows one to tailor the microstructure at small length scales to further achieve the desired macro-scale properties in a system. This correlative study also leads to the realization that

the hierarchical order between the different length scales in a materials system is not necessarily a one way relation. In other words, modifications at the atomic level (addition of a solute element) and at the macro-scale (addition of a reinforcing phase) can lead to significant changes in the atomic structure as well as the bulk behavior.

This contribution particularly focuses on the microstructurally driven phenomenological aspect of deformation in ductile-brittle lamellar systems at various length scales. In this research, a directionally solidified eutectic composite is used as a model system to study the extent of local plasticity and strain energy absorption in a ductile-brittle model system. The model system selected for this study is $\text{Ni}_x\text{Co}_{1-x}\text{O}/\text{ZrO}_2(\text{CaO})$ directionally solidified eutectic (DSE). This system can form nanoscale ductile interphases of Ni(Co) protruding $\text{Ni}_x\text{Co}_{1-x}\text{O}$ and $\text{ZrO}_2(\text{CaO})$ ceramic phases upon chemical reduction. The resulting microstructure after the reduction of this system creates an excellent platform to study the correlative deformation and fracture phenomena at various length scales and the effect of size scale on the extent of plasticity in confined nanoscale metallic thin films. This thesis is a part of a larger scheme aiming to establish a correlative understating of deformation at different length scales in multi-layered systems. It is believed that a deeper understanding of deformation and fracture phenomena in this class of materials can be achieved through similar investigations on other lamellar systems.

This dissertation is organized as follows. First, the necessary background for the context of this research as well as the background information for $\text{Ni}_x\text{Co}_{1-x}\text{O}/\text{ZrO}_2(\text{CaO})$ model system is presented in Chapter 2. This chapter is further followed by the problem statement and the hypothesis for this research work. Chapter 3 presents the processing

and the characterization techniques utilized to create a proper ductile-brittle model system from the pristine $\text{Ni}_k\text{Co}_{1-x}\text{O}/\text{ZrO}_2(\text{CaO})$ composite model system. The chapter further follows by presenting the chemical and interfacial structure of the newly developed multi-layered system. Chapter 4 focuses on the toughening enhancement along with the deformation and crack propagation behavior of the reduced model system with respect to its pristine state. Using the nano-indentation technique local plasticity is further explored in this model system to verify the role of the metallic Ni(Co) interphases in this chapter. Chapter 5 contains the nanoscale deformation mechanisms operating within the metallic interphase upon deformation of this system, while Chapter 6 presents the attempts made to evaluate the mechanical properties of this model system through a novel miniature mechanical testing technique. Finally, Chapter 7 includes the summary and conclusions of this thesis work, and Chapter 8 presents the suggestions for the future work.

2 DEFORMATION AND FRACTURE PHENOMENA IN MULTI-LAYERED SYSTEMS

This section presents the literature review on the deformation and fracture mechanisms operating in ductile-brittle multi-layered composites. A whole volume of literature has been written on the engineering of composite systems and their deformation and fracture phenomena. In this chapter the deformation and fracture behavior in ceramic-ceramic and metal-ceramic composites as well as the major toughening mechanisms in such systems will be reviewed. This chapter is further continued by presenting the effect of size scale on the deformation and fracture mechanism in the multi-layered systems.

The second section of this chapter presents the scope of this thesis. This section starts with presenting the selected model system, $\text{Co}_{1-x}\text{Ni}_x\text{O}/\text{ZrO}_2(\text{CaO})$, for the research work in this thesis. The section further continues by presenting the hypotheses of this dissertation.

2.1 Literature Review

2.1.1 Toughening Mechanisms in Ceramic Composites

Mechanical properties of advanced composites are strongly influenced by various characteristics of the composite, such as interfacial structure, chemistry and bonding as well as the plasticity, residual stresses and size scale of the phase components.⁸⁻¹³ Enhancements of the physical and mechanical properties in composite systems can be obtained by improving the appropriate interfacial characteristics of the system. Among the class of interface controlled materials, oxide-oxide ceramic composites are known for

their high strength but the inability of the phases to exhibit deformation at room temperature.^{10, 14-17} This class of materials is generally known to exhibit room temperature brittle fracture as their dominant fracture mechanism where there is little to no interfacial crack deflection or interfacial delamination.^{18, 19} The lack of interfacial crack delamination in oxide-oxide eutectic composite systems has been attributed to relatively low interfacial energies compared to the cohesive energy of the phases.^{20, 21} As a result of this strong interfacial bonding, the interfaces effectively transmit the load across without energy dissipating mechanisms (e.g., interfacial delamination, crack deflection), and leave the impinging cracks unperturbed in the system.

Addition of porosity can change the mechanical properties of the composite extensively.^{140, 144} In general addition of porosity decreases the fracture energy and consequently the toughness of the materials. At high volume fractions of porosity, the highly porous phases contribute to crack arrest. Also an increase in the strength of the composite is observed with increasing the porosity level.

Several researchers have explored different strategies to increase the fracture toughness and enhance the mechanical behavior of ceramic composites.^{9, 17, 22-25} These studies have shown multiple toughening mechanisms simultaneously operating upon deformation in a system. Microcracking^{26, 27}, fiber pull-out²⁸, interfacial debonding leading to crack deflection^{29, 30}, and transformation toughening³¹ are a few of the energy dissipating mechanisms which contribute to toughening in ceramic composites.

To predict the competing mechanisms for crack propagation across the interface and crack deflection along the interface, He-Hutchinson and He-Evans-Hutchinson models for plain strain condition have been proposed; the latter model including the

residual stress in the system.^{32, 33} Both of these models describe the competing mechanisms for the crack penetration versus deflection by the ratio of the mechanical energy release rate for deflection and penetration ($\frac{G_d}{G_p}$). The criterion for this competition has been described in equation 2.1.³²

$$\frac{G_d}{G_p} > \frac{\Gamma_{ic}}{\Gamma_c} \quad 2.1$$

Where G_d is the energy release rate for crack deflection and G_p is the energy release rate for interfacial crack penetration. The toughness of the interface is Γ_{ic} and the mode I toughness for the material 1 is Γ_c . With the above condition to satisfy, the crack is likely to deflect along the interface. Figure 2.1 indicates the resulting crack penetration compared with the crack delamination along the interface in a multi-layered composite.

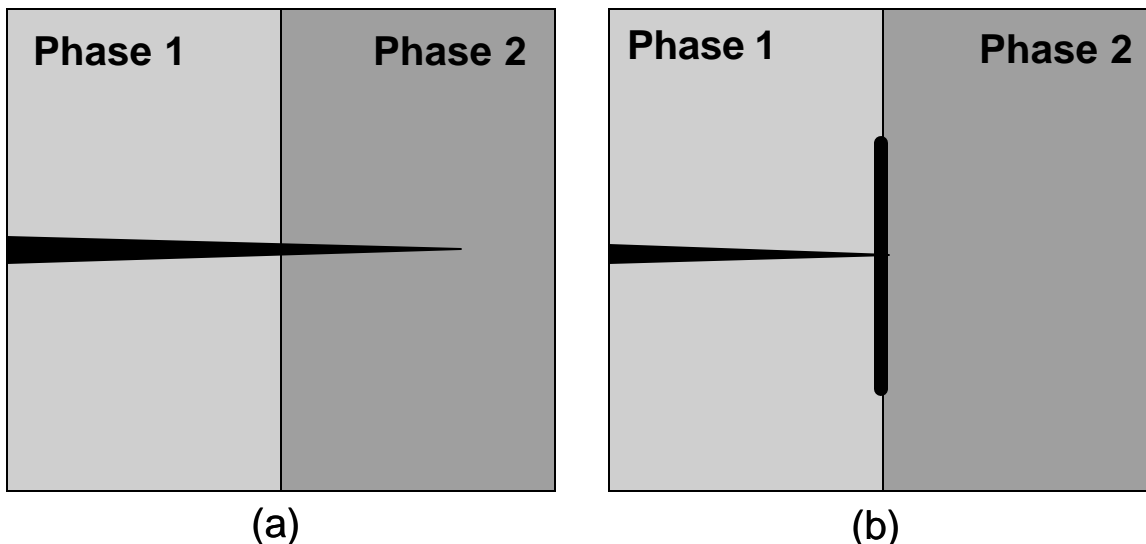


Figure 2.1 Competition between two fracture mechanisms: Crack penetration (a) versus crack delamination along the interface (b) in a multi-layered composite.

According to the He-Hutchinson model when the ratio of the mechanical energy release rate of the system exceeds the ratio of the interfacial fracture energy and the mode I fracture energy of the next component, interfacial debonding and crack deflection will occur in the system.³² Another interpretation of this model simply implies that when the interfacial fracture toughness of a composite is low relative to that of matrix, interfacial debonding and crack delamination becomes the leading fracture mechanism and contributes to the toughening enhancement of the composite.

Considering the role of materials properties in this criterion, the energy release rate depends on the elastic mismatch of the two components in the composite through the first Dundurs' parameter, α :³⁴

$$\alpha = \frac{\bar{E}_1 - \bar{E}_2}{\bar{E}_1 + \bar{E}_2} \quad \text{Where} \quad \bar{E} = \frac{E}{1 - \nu^2} \quad 2.2$$

where E is the elastic modulus and ν is the Poisson's ratio of the material. The above relation indicates the condition at which the interfacial debonding, and therefore, crack deflection can take place along the interface. The above criterion clearly shows the role of the Poisson's ratio and the Young's modulus of the phase components on the energy release rate upon fracture of a composite.

This model predicts crack deflection to become a more dominant fracture mechanism, with increasing the elastic mismatch in the system.³² Another factor that can significantly affect the tendency of the crack to penetrate or delaminate along the interface is the angle of incidence of the crack with respect to the interface (ω_2).³² The influential role of the angle of incidence on the crack propagation behavior (interfacial deflection versus penetration) results from the fact that the angle of incidence can

determine the angle of loading, which is a measure of the stress contribution at the crack tip for mode I (opening or tensile mode) versus mode II (sliding mode) fracture. As a result for shallower crack angles with respect to the interface, the shear component of the incident crack is higher and the crack is more likely to deflect along the interface.³⁵

Figure 2.2 shows the role of materials properties, such as the elastic modulus and the angle of incidence of the impinging crack, on the competing interfacial fracture mechanism (interfacial penetration versus interfacial delamination) in a composite.

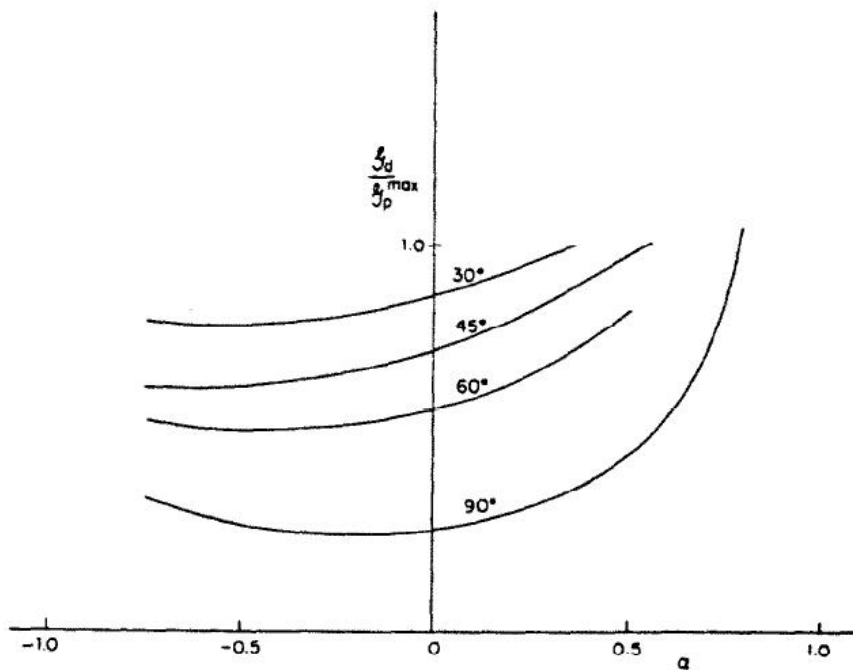


Figure 2.2 Ratio of the energy release rate of a deflected crack to the maximum energy release rate of a penetrating crack as a function of α for a wedge loaded crack.³²

Residual stresses in a composite also play a significant role on the crack propagation behavior of the system. Further analysis by He *et al.*³³ have revealed the important role of the residual stresses on the crack propagation behavior at the interface of a composite. This investigation showed that tensile stresses parallel with the interface can promote crack penetration, while compressive stresses parallel to the interface can significantly increase the critical value of $\frac{\Gamma_{ic}}{\Gamma_c}$ and therefore enhance interfacial deflection along the interface.

The models discussed here clearly indicate the significant role of interfaces on the competing interfacial fracture mechanisms in a multi-layered ceramic composite. This discussion also points to the important role of interfaces on the toughening enhancement of ceramic composite multi-layers.

2.1.2 Toughening Mechanisms in Metal-Ceramic Composites

Metal-ceramic composites are typically comprised of a brittle phase and a ductile phase to reinforce the toughness of the composite. Interfacial fracture behavior in metal-ceramic composites is influenced by several parameters such as the size and the geometric constraints of the phases, the nature of interface bonding, the load mixity and finally plasticity of the phases in the system.^{24, 25, 36-38}

The toughening mechanisms observed in metal-ceramic composites generally involve plastic deformation within the metallic phase through crack arrest, crack bridging across the metallic phase and interfacial delamination.^{24, 25, 29, 30, 36, 37, 39} Upon crack arrest by the metallic phase, the stress energy at the crack tip is transmitted into the metal

through elastic-plastic flow of the metallic phase leading to crack blunting at the interface. The plastic flow in the metal can further cause crack to open up at the other side of the interface and to result in “crack bridging” in the composite. The resulting toughness enhancement emerging from such bridging mechanism is significantly related to the strength, size and volume fraction of the metal reinforcement.²⁴ Chandrasekaran investigated the mechanical behavior of CoO/ZrO₂(CaO) DSE with a metallic Co interphase at the CoO-ZrO₂(CaO) interface and proposed crack re-nucleation and plastic deformation within the metal to be the possible toughening mechanisms operating in this system.⁴⁰

Interfacial fracture in metal-ceramic composites occurs through crack deflection along the interface. The crack deflection can occur in both ductile and brittle manner.^{25,36} Figure 2.3 shows a schematic view of the fracture mechanism in both ductile and brittle manner in metal-ceramic composites. As this Figure shows the ductile fracture generally occurs through void formation, growth and coalescence within the ductile phase adjacent to the interface. Al/Al₂O₃ composite is an example of such a mechanism, where void nucleation preferentially occurs at the junction of the Al₂O₃ grains.⁴¹ Void spacing along the interface has shown to have a strong influence on this type of fracture mechanism. The influence of void spacing is particularly stronger when this spacing is smaller than the size of the metallic layer thickness.^{42, 43} In this condition, void-crack coalescence is imminent since the voids are within the finite strain zone near the crack tip.

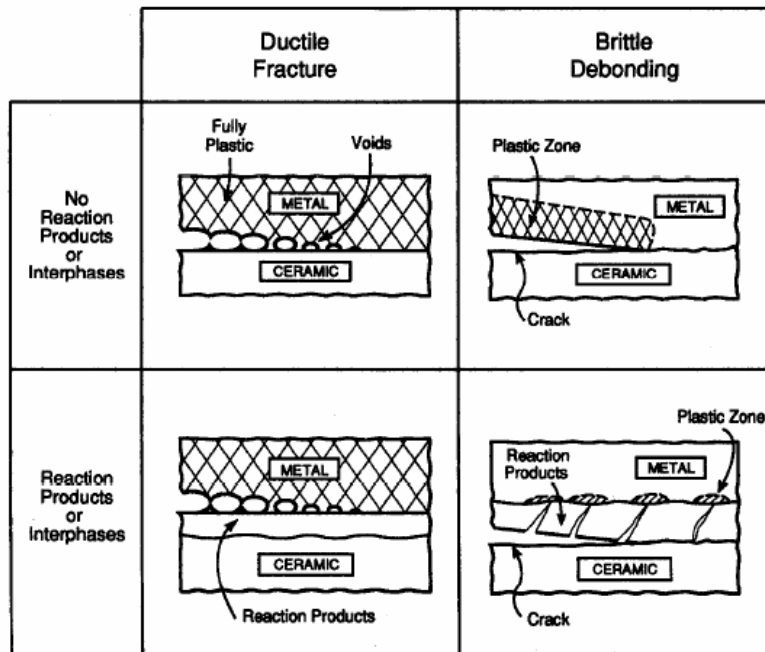


Fig. 1. A schematic indicating the various fracture mechanisms that occur in metal-ceramic interfaces.

Figure 2.3 Fracture mechanisms in both ductile and brittle manner in metal-ceramic composites.²⁵

Load mixity of the impinging crack is another important factor in ductile fracture as it can influence the crack path leading to the void formation and growth.^{32,35} The metal layer thickness also has an important geometric role for this type of fracture mechanism since it affects the stresses at the interface ahead of the crack tip.^{36,37} With decreasing the metal layer thickness, the mean stress ahead of the crack tip increases. This stress increase leads to a drop in the fracture resistance ahead of the crack tip. At such a size scale due to the elevated mean stress ahead of the crack tip failure can progress to locations further from the crack front. The effect of the metal layer thickness on the

fracture resistance in multi-layered systems points to the important role of plastic dissipation on the interfacial fracture mechanism of a composite.

The interfacial debonding and the extent of plastic dissipation in metal-ceramic composites are greatly inter-related to each other in the interfacial fracture of the metal-ceramic composites. In some metal-ceramic composites the sufficiently strong bonding at the interface leads to the failure of the composite through plastic dissipation in the metal with the interfacial debonding heavily suppressed. In other metal-ceramic composite systems however, interfacial debonding is the leading deformation mechanism which is further accompanied by the plastic dissipation within the metallic phase in the composite. W/ZrO₂ is an example of a metal-ceramic DSE composite where interfacial delamination, crack bridging and plastic dissipation within W simultaneously operate in the system upon indentation.⁴⁴ Interfacial delamination in this system has been related to the weak interfacial bonding between the W and ZrO₂ phases. Al₂O₃/Au, Al₂O₃/Pt and Al₂O₃/Nb are other examples of metal-ceramic composites which show both interfacial debonding and plastic dissipation upon deformation.⁴⁵⁻⁴⁷

Interfacial bonding between the metal and the ceramic has a significant influence on the interfacial fracture of a composite.^{25, 36, 48} Interfacial debonding in metal-ceramic composites is generally related to the interfacial fracture resistance at the metal-ceramic interface. Clean metal-ceramic interfaces without any interlayer or compound have been shown to exhibit higher fracture energies compared to the composites with interphase interfaces. Interphase interfaces in contrast show a profound effect on the interfacial fracture of metal-ceramic composites. Interphase interfaces could be crystalline reaction products, i.e. intermetallic, which form upon interdiffusion of different elements at the

interface. Previous studies have pointed to the intermetallic interfaces to have the highest fracture energy. After the intermetallic interphases, crystalline oxide interphase exhibit the highest level of fracture energy among the interphase interfaces.²⁵ Interphases can also be amorphous due to the flow of a phase or through a reaction. Amorphous interphases have shown to have lower fracture energies compared to the composites with intermetallic and crystalline interphases.²⁵

Among many influential parameters discussed here, interfacial fracture studies on metal-ceramic multi-layered composites point to the important role of metal layer thickness on the fracture energy of composites.^{25, 37, 49} $\text{Al}_2\text{O}_3/\text{Au}$ and $\text{Al}_2\text{O}_3/\text{Pt}$ systems present two examples of the systems where the role of the metal layer thickness on the fracture energy of the system is notable.²⁵ These studies have shown that with decreasing the metal layer thickness, strain energy absorption through plastic dissipation in metal is reduced to negligible levels. The role of the metal layer thickness on the deformation and fracture behavior of multi-layered systems is further discussed in the next section of this chapter.

2.1.3 Effect of Size Scale on the Mechanical Properties of Multi-Layered Composites

Deformation and fracture behavior of multi-layered composites has been the subject of study for a few decades.^{23, 24, 32, 35, 38, 39, 50} The main goal of these investigations has been to understand various competing fracture mechanisms operating in multi-layered systems and to investigate the resulting properties such as strength and toughness.^{8, 51-53} Such studies have considered the size scale to be in the range of several

microns to millimeters where the continuum dislocation models can occur. Among various dominating factors that can affect the mechanical properties of a system, this section focuses on the role of the component size scale, its effect on the plasticity and the resulting mechanical behavior of the system.

The operating fracture mechanisms observed in metal-ceramic and ceramic-ceramic systems with size scales in the order of several microns to millimeters have been previously discussed in sections 2.1.1 and 2.1.2 of this thesis. In the systems with relatively large size components, the ductile phase can contribute to plastic deformation and strain energy absorption through formation of dislocation cells, clusters and pile-ups.^{54, 55} Ductile metals in the absence of confinement hardly show brittle fracture since the tensile stress at the crack tip never reaches the cohesive strength necessary for fracture. This is due to easy dislocation emission and high dislocation mobility which causes crack tip blunting and consequently a decrease in the stress intensity at the tip of the crack in these systems.^{54, 55}

Upon decreasing the layer thickness or grain size to submicron sizes in multilayered or polycrystalline systems, the deformation mechanism can significantly change as there is a high ratio of internal interfacial area to the volume.⁵⁶⁻⁶² Mechanical properties of thin metallic films on hard substrates indicate enhanced strength of the film with decreasing the film thickness. Several models have been proposed to relate the critical stress for dislocation motion to the layer thickness in thin films or confined systems.⁶³⁻⁶⁶ These studies relate the enhanced strength of thin films to the high rates of strain hardening that occurs within the thin film during deformation.

Recent studies on the incoherent metal/metal multi-layered systems indicate enhancement of strength in such systems with decreasing the layer thickness.⁶⁷⁻⁷² These studies also suggest the conventional dislocation models, such as dislocation pile-ups, to be suppressed and emission of single dislocations from the interface to take place as the strengthening mechanism in the nanoscale multi-layered systems. This behavior is due to the fact that the high density of interfaces in confined multi-layered systems can act as barriers to dislocation motion, and as a result plastic deformation can be heavily suppressed in these systems.^{55, 67, 73, 74} These studies have shown the dislocations already present in the confined layer put a back stress on the crack tip to hinder further dislocation emission. This causes a dramatic drop in the number of dislocations in confined layer systems. As a result dislocations have to be treated individually in such systems.^{55, 56, 73} Many studies have pointed to the competition between cleavage and further dislocation emission at the crack tip in ductile phases upon reduction of the layer thickness to smaller values in confined systems. In ductile/brittle multi-layered systems, lack of plasticity in the alternative brittle layers can impose another degree of constraint to the strain energy absorption in the system, particularly when the ductile component is in the nanoscale sizes.^{42, 68, 75, 76} With decreasing the size scale to the nanoscale regime plasticity in the system is heavily suppressed since the plastic zone size is limited by the size of the ductile component. In such systems, further plastic strain energy absorption through load transfer to the adjacent layers is also hindered due to the brittle elastic nature of the neighboring components.

Several models have been proposed to explain the deformation mechanisms operating in multi-layered systems.^{77, 78} Among the present models, Koehler model⁷⁷

describes the effect of the large modulus mismatch between the adjacent layers in a laminated structure.^{55, 73, 77, 79} According to this model dislocations generated in the lower modulus layer (with lower dislocation line energy) have to overcome a large repulsive image stress from the high modulus phase (with higher dislocation line energy) before they can slip across the layer. In this model the source of resistance to dislocation motion is the modulus difference that exists across the interface. Koehler model is applied to the multi-layers in which, dislocation pile up is suppressed and Frank-Read sources do not exit. In this model it is assumed that the layer thickness is very small, although the effect of layer thickness has not been considered.

Hall-Petch model relates the stress concentration due to the dislocation pile up to the yield stress of the material.^{67, 78, 80} This model suggests that upon loading the multilayered/polycrystalline materials, dislocations pile up at the interfaces/boundaries till the applied stress plus the stress concentration due to pile up reaches the stress required for dislocation transmission across the interface. With reducing the layer thickness, the number of dislocations will decrease and therefore a lower stress concentration will be applied at the dislocation pile up. In this condition for further dislocation emission and slip across the interface, a higher applied stress is required in the system. According to this model a higher strength is reached in the system upon decreasing the layer thickness. Therefore the yield strength of the system, σ_y , is inversely proportional to the square root of layer thickness.^{55, 67, 74, 80, 81} Figure 2.4 (a) indicates a schematic representation of Hall-Petch model applied to multi-layered systems.

$$\sigma_y = \sigma_0 + k_y d^{-1/2} \quad 2.3$$

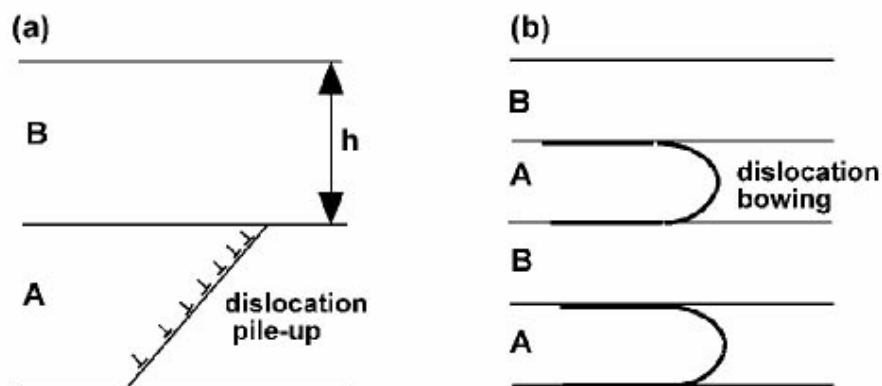


Figure 2.4 Schematic illustration of the strengthening mechanisms: (a) Hall-Petch model indicating the yield stress of the system to be inversely proportional to the layer thickness of the film and (b) Orowan model indicating dislocation bowing along the interfaces within the film in multi-layered systems.⁷³

Other studies have specifically shown a relationship between the yield stress for thin FCC films bonded to rigid substrates, the film grain size and its thickness.^{63, 64} The studies by Ronay⁶⁴ indicate the yield stress of the film to be inversely related to its thickness according to the relationship shown in equation 2.4:

$$\tau_y = \tau_s + \frac{1}{\pi} \left(\frac{b\gamma}{sl} \right)^{1/2} + mG \left(\frac{2b\gamma}{D} \right)^{1/2} \quad 2.4$$

where τ_s is the flow stress of the material without interfaces/boundaries. The second term in the equation indicates the stress required to overcome the long range stress field of the geometrically necessary dislocations. The third term indicates the stress required to overcome the short range interactions between the crossing dislocations. Also it should be noted that b is the Burgers vector, G is the shear modulus, s is a constant

depending on the orientation of the primary slip system of the film to the substrate, γ is the plastic strain, l is the film thickness and D is the grain size, and m is the Taylor orientation factor. Figure 2.5 shows the relation between the yield stress to the film thickness at a given grain size as indicated by equation 2.4. This figure clearly indicates the yield stress of the film to significantly increase with decreasing the film thickness.

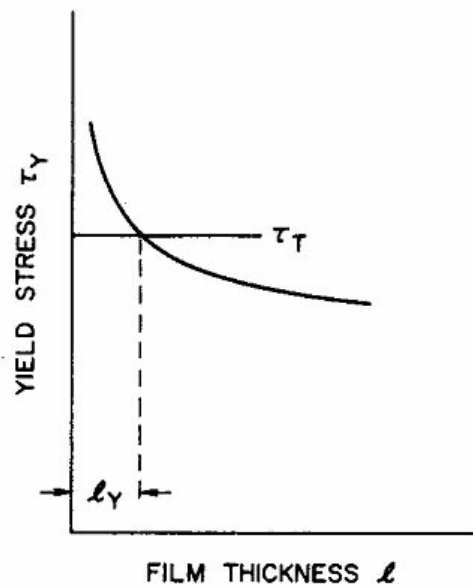


Figure 2.5 Yield stress of FCC thin film bound to rigid substrates as a function of film thickness with a constant grain size. In this figure τ_T is considered to be the applied stress and τ_Y to be the yield stress and l_Y to be the thickness of the film, below which the film does not yield.⁶⁴

The Orowan model^{55, 73} is another model that describes dislocation motion in thin confined interphases. According to this model in a multi-layered system, where dislocation pile up does not occur, further slip may take place via dislocation bowing along the confined ductile interphase. Figure 2.4 (b) shows a schematic representation of

this model in confined multi-layered systems. This model suggests dislocation bowing along the interface when the interfaces are impenetrable in a multi-layered system under loading. According to this model the yield strength of the material is proportional to $\frac{\ln(h)}{h}$; h being the layer thickness. The critical applied stress required for dislocations to bow in this model is proportional to the dislocation line curvature.

2.2 Scope of This Thesis

2.2.1 Importance of the Effect of Size Scale on the Deformation Behavior of Multi-Layered Composite Systems

The previous studies have provided a broad understanding of the deformation and fracture mechanisms operating at various length scales in multi-layered composite systems. Among many parameters, these studies have pointed to the important role of layer thickness on the deformation and fracture phenomena in the multi-layered systems and the resulting strength and toughness. A large number of the fundamental understandings about the deformation processes in sub-micron size scales have been derived from theoretical studies through simulations and modeling. Many of these fundamental concepts have been used to relate the resulting bulk properties in materials systems to their interfacial and atomic structure. However not many direct experimental observations have been performed to understand the microstructurally driven phenomenological aspect of deformation behavior at correlative length scales. Therefore there is a need to investigate the role of the microstructure and the size scale on the correlative deformation and fracture behavior of multi-layered systems at various length

scales via direct experimental observations. To understand the correlative deformation and fracture mechanisms operating in multi-layered systems, it is of great importance to first develop a proper multi-layered model system to study the deformation and fracture mechanism within the system at various length scales. Only obtaining a deep understanding of small scale deformation mechanisms in multi-layered composites can lead us to engineer composite systems with enhanced toughness and strength.

2.2.2 $\text{Ni}_x\text{Co}_{1-x}\text{O}/\text{ZrO}_2$: A Ductile-Brittle Multi-Layered Model System

Considering the importance of understanding the microstructurally driven phenomenological analysis of deformation behavior at different length scales in multi-layered systems, it is particularly necessary to study a model system where one can directly relate the microstructural and interfacial characteristics of the system to its deformation behavior at various length scales. For this purpose $\text{Ni}_k\text{Co}_{1-x}\text{O}/\text{ZrO}_2$ composite is a strong candidate as the model system in this thesis work. $\text{Ni}_k\text{Co}_{1-x}\text{O}/\text{ZrO}_2$ model system can form confined metallic interphases of Ni(Co) upon chemical reduction of this system at high temperatures.^{82, 83} Formation of nanoscale confined interphases in this model system creates a very unique platform to further investigate the role of size scale and chemistry on the correlative deformation mechanisms operating in the ductile-brittle multi-layered systems at small length scales.

In order to understand the microstructural evolution of $\text{Ni}_k\text{Co}_{1-x}\text{O}/\text{ZrO}_2$ and its deformation and fracture mechanism after reduction, it is necessary to first investigate the structure, crystallography and the deformation and fracture behavior of the system in its fully oxidized form. This section presents a summary of the previous studies on the

microstructure and crystallography of the $\text{Ni}_x\text{Co}_{1-x}\text{O}/\text{ZrO}_2$ composite as well as its deformation and fracture behavior. This section further continues by introducing the chemical reduction mechanism leading to the development of a ductile-brittle multi-layered system from $\text{Ni}_x\text{Co}_{1-x}\text{O}/\text{ZrO}_2$.

A. $\text{Ni}_x\text{Co}_{1-x}\text{O}/\text{ZrO}_2$ in the fully oxidized (or pristine/as-grown) form

$\text{Co}_{1-x}\text{Ni}_x\text{O}/\text{ZrO}_2(\text{CaO})$ Directionally Solidified Eutectic (DSE) composites are considered in-situ eutectic composites with alternate layers of $\text{Co}_{1-x}\text{Ni}_x\text{O}$ and $\text{ZrO}_2(\text{CaO})$. This composite has been originally grown using the optical floating zone method (OFZ) at the Université de Paris-Sud.^{17, 84, 85} To grow the DSE composite, the eutectic proportions of $\text{Co}_{1-x}\text{Ni}_x\text{O}$ and ZrO_2 powder (with different values of x) were mixed along with 15 mole percent CaO (as an additive) to stabilize ZrO_2 in its high temperature cubic form in the final crystal. The mixed powder was pressed in the form of rod and sintered at 1200 C prior to growth. The rods were then directionally solidified by the optical floating zone method (OFZ). A controlled Ar/ CO_2 atmosphere was used during the growth of the DSEs to prevent formation of cobalt spinel. The optimal growth rate for $\text{Co}_{1-x}\text{Ni}_x\text{O}/\text{ZrO}_2(\text{CaO})$ was determined to be about 10 mm/hr which gives the lamellar spacing in the order of 1 to 2 microns in the final microstructure.

All the compositions of $\text{Co}_{1-x}\text{Ni}_x\text{O}/\text{ZrO}_2(\text{CaO})$ maintain a lamellar microstructure but the domain size and lamellar quality could slightly vary from one composition to the other.^{17, 84, 85} Both $\text{Co}_{1-x}\text{Ni}_x\text{O}$ and $\text{ZrO}_2(\text{CaO})$ maintain cubic structure with Fm3m space group. $\text{Co}_{1-x}\text{Ni}_x\text{O}$ holds a rocksalt structure, while $\text{ZrO}_2(\text{CaO})$ maintains a fluorite structure in this composite.^{17, 86} The $\text{Co}_{1-x}\text{Ni}_x\text{O}/\text{ZrO}_2(\text{CaO})$ lamellar composite series have

a unique structure in which the composition of one layer, ZrO_2 , is kept constant while the composition of the other layer can be altered from pure CoO/NiO to a solid solution of these transition metal oxides. Previous studies have shown that the lattice parameter of $Co_{1-x}Ni_xO$ solid solution slightly increases with addition of CoO phase, while $ZrO_2(CaO)$ maintains the same lattice parameter across all the compositions of $Co_{1-x}Ni_xO/ZrO_2(CaO)$.^{17, 84, 85} Figure 2.6 shows the variation of the lattice parameter for $Co_{1-x}Ni_xO$ and $ZrO_2(CaO)$ as a function of its composition in this system.⁸⁴

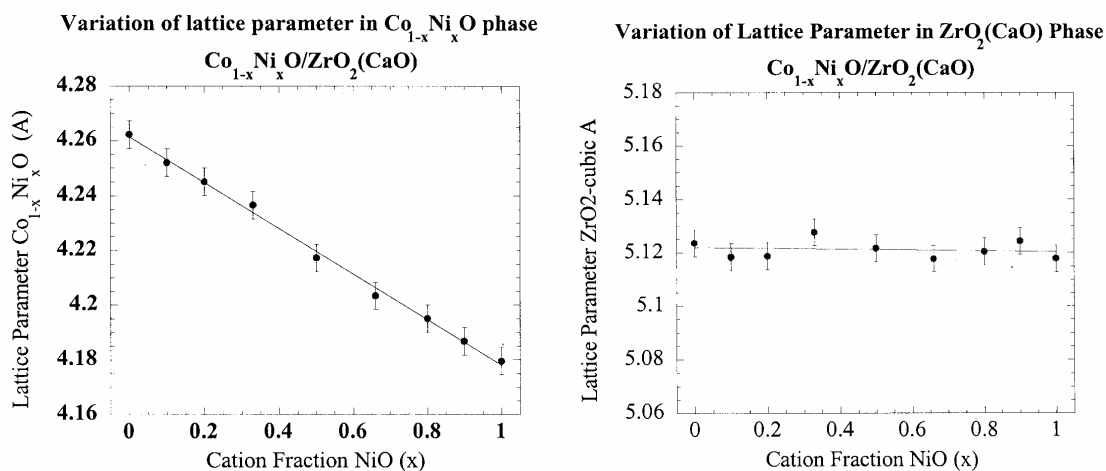


Figure 2.6 Variation of the lattice parameter in (a) $Co_{1-x}Ni_xO$ and (b) $ZrO_2(CaO)$ as a function of the composition in the $Co_{1-x}Ni_xO/ZrO_2(CaO)$ composite.^{10, 16, 17}

$Co_{1-x}Ni_xO/ZrO_2(CaO)$ DSE composites has been previously characterized to contain several identical interfaces with $\{111\} Co_{1-x}Ni_xO \parallel \{100\} ZrO_2$ interfacial orientation relationship throughout the $Co_{1-x}Ni_xO$ solid solution.^{84, 86-89} Multiple growth

orientation relationships have been observed between ZrO_2 and $\text{Co}_{1-x}\text{Ni}_x\text{O}$ depending on the composition.^{17, 84} However the same interfacial plane orientation relationship between the two ceramic phases was maintained over the whole composition range.

Residual stresses have been previously measured in the $\text{Co}_{1-x}\text{Ni}_x\text{O}/\text{ZrO}_2(\text{CaO})$ composite series. These measurements indicate large levels of thermal residual stresses (~ 1 GPa) to exist in the tensile form in $\text{Co}_{1-x}\text{Ni}_x\text{O}$ and in the compression form within $\text{ZrO}_2(\text{CaO})$.^{20, 90} The large levels of the residual stress in this system have been attributed to significant levels of interfacial constraint and strong interfacial bonding in this system.

Room temperature Vickers indentation studies in the $\text{Co}_{1-x}\text{Ni}_x\text{O}/\text{ZrO}_2$ system show a notable transition in the deformation and fracture behavior in this system upon moving from NiO to CoO rich compositions of this DSE series.^{10, 17, 85} The crack propagation behavior in the NiO rich composites ($x > 0.33$) of this DSE series show a brittle fracture of this system. With increasing the CoO content ($x < 0.33$) the interfacial fracture behavior in the $\text{Co}_{1-x}\text{Ni}_x\text{O}/\text{ZrO}_2$ system changes dramatically, indicating toughening enhancement to take place in the composite through microcracking, interfacial delamination and plastic deformation in $\text{Ni}_k\text{Co}_{1-x}\text{O}$ phase. Local hardness and plasticity measurements in the $\text{Co}_{1-x}\text{Ni}_x\text{O}/\text{ZrO}_2$ system show a decrease in plasticity and an increase in hardness upon addition of NiO in the $\text{Ni}_k\text{Co}_{1-x}\text{O}$ solid solution.^{10, 17} Figure 2.7 shows the variation for the nano-indentation hardness across the $\text{Ni}_k\text{Co}_{1-x}\text{O}$ solid solution in the single crystal as well as the DSE samples.

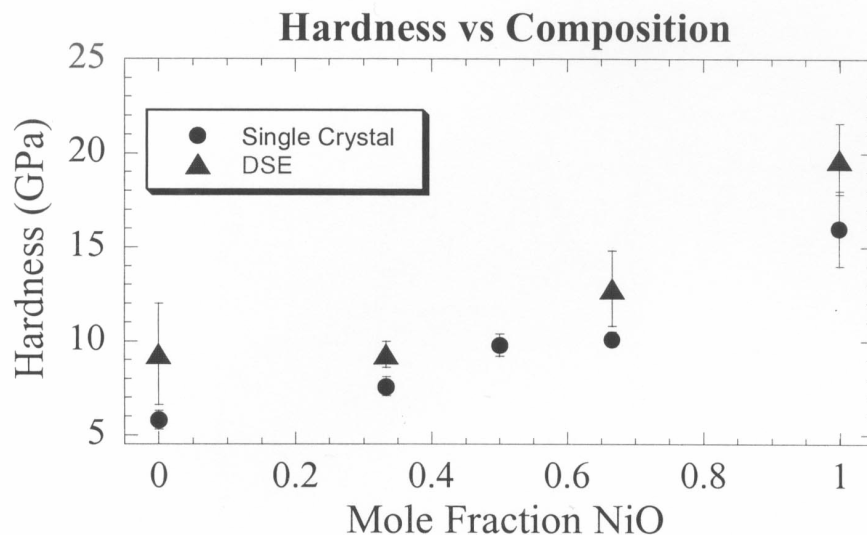


Figure 2.7 Variation of nano-hardness across the solid solution $\text{Ni}_x\text{Co}_{1-x}\text{O}$ in the single crystal and the DSE samples.^{10, 17}

The significant changes in the crack propagation behavior of $\text{Co}_{1-x}\text{Ni}_x\text{O}/\text{ZrO}_2$ system as a function of composition has been attributed to the presence of active slip systems operating in the CoO rich composites at room temperatures.^{10, 17} As a rocksalt structure, CoO has been previously shown to have $\{100\} \langle 110 \rangle$ slip system active at room temperature.⁹¹ In NiO however, $\{100\} \langle 110 \rangle$ slip system can only be activated at temperatures above 500 C.⁹²

$\text{ZrO}_2(\text{CaO})$ is considered as an elastic brittle materials till 800 °C above which it shows considerable dislocation activities on the $\{100\} \langle 110 \rangle$ slip system.⁹³⁻⁹⁵ This material has also shown significant slip on the $\{100\} \langle 110 \rangle$ in compression under indentation at 200 °C, since it has the lowest critical resolved shear stress.⁹⁶ The

previously measured hardness value of $\text{ZrO}_2(\text{CaO})$ has been reported to be about 20 GPa in the $\text{Co}_{1-x}\text{Ni}_x\text{O}/\text{ZrO}_2$ system which indicates far less plasticity of this phase compared to the hardness of $\text{Co}_{1-x}\text{Ni}_x\text{O}$ phase in this model system.¹⁷

B. Chemically Reduced $\text{Ni}_x\text{Co}_{1-x}\text{O}/\text{ZrO}_2$

Previous investigations have shown *in-situ* formation of metal-ceramic composites through reduction of ceramic oxide composites.^{82, 83, 97-100} Revcolevschi *et al.*^{53, 82, 83} first investigated the feasibility of the formation of a metal-ceramic multi-layered composite upon reduction of $\text{Ni}_x\text{Co}_{1-x}\text{O}/\text{ZrO}_2(\text{CaO})$ DSEs. Their investigations showed the formation of a unique metal-ceramic multi-layered structure as a result of the system performing as an electrochemical cell in a reducing environment at high temperatures. Figure 2.8 shows a schematic view of the reduction front leading to the formation of the metallic interphases in the $\text{Ni}_x\text{Co}_{1-x}\text{O}/\text{ZrO}_2(\text{CaO})$ system upon reduction.

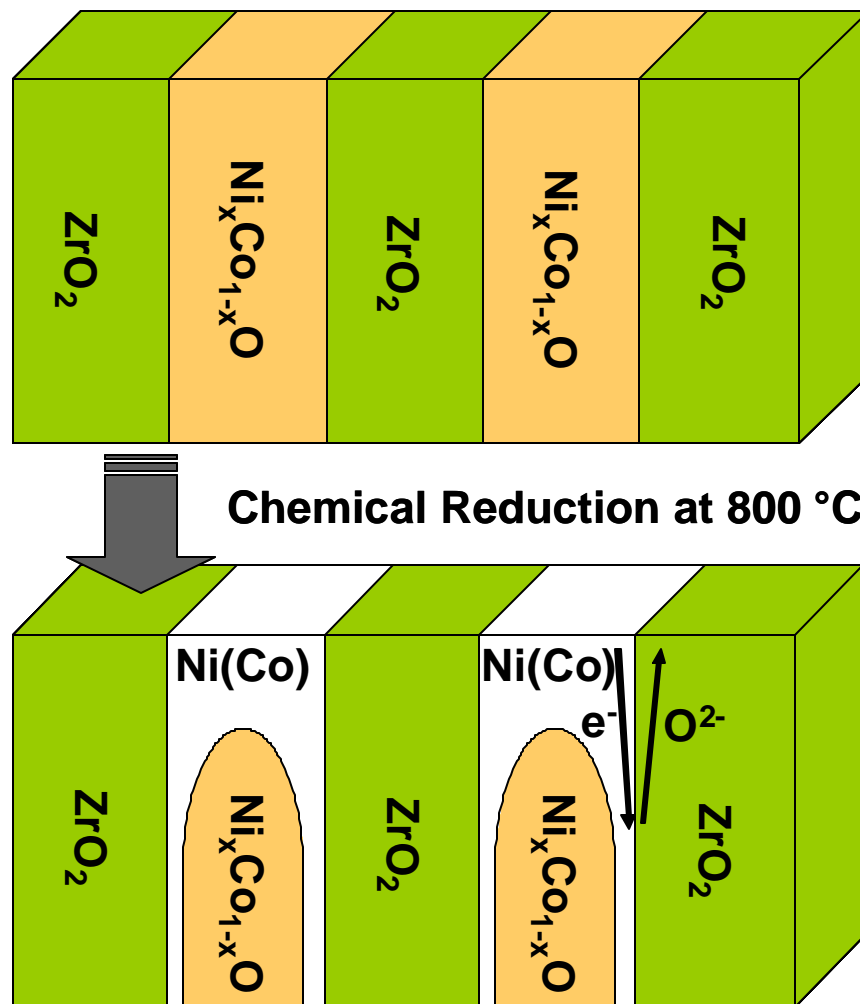
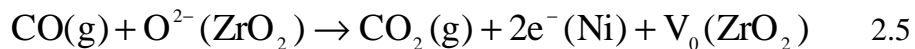


Figure 2.8 Schematic view of the composite showing the reduction front and formation of the metallic interphases in the $\text{Ni}_x\text{Co}_{1-x}\text{O}/\text{ZrO}_2(\text{CaO})$ system.

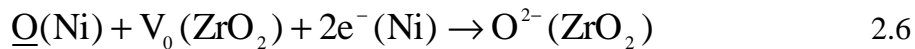
Studies by Revcolevschi *et al.*^{82, 83} on the reduction mechanism in $\text{Ni}_x\text{Co}_{1-x}\text{O}/\text{ZrO}_2(\text{CaO})$ system has shown that during the chemical reduction process, the composite behaves as an electrochemical cell due to high oxygen ion conductivity of ZrO_2 and high electronic conductivity of nickel and cobalt metals. Upon reduction, the transition metal oxide, $\text{Ni}_x\text{Co}_{1-x}\text{O}$, is quickly reduced and forms a dense metallic layer of

Ni(Co) at the top surface of the composite with some porosity mainly confined along the interface. The porosity formed during the chemical reduction of this sample is due to formation of oxygen vacant sites within the $\text{Ni}_k\text{Co}_{1-x}\text{O}$ phase. For further reduction to continue at the sub-surface, sub-surface oxygen atoms in the $\text{Ni}_k\text{Co}_{1-x}\text{O}$ phase have to reach the top surface of the system to react with the reducing agent. Since cubic ZrO_2 has high oxygen ion conductivity compared to that of the transition metal oxides, ZrO_2 provides a faster path for oxygen to reach the external surface, and therefore reduction at the sub-surface takes place via the ZrO_2 layer in this process.^{53, 83, 100-102} The reduction process has been previously investigated in this composite. Upon reduction of the composite for sufficient length of time, $\text{Ni}_k\text{Co}_{1-x}\text{O}$ phase is completely reduced to its metallic counterpart. $\text{ZrO}_2(\text{CaO})$, however, remains intact, maintaining its fully oxidized state during and after the reduction process. The following interfacial reactions indicate an example of the chemical reduction in NiO/ZrO_2 DSE systems:⁸³

At the external composite/gas interface:



At the internal interface of Ni/ZrO_2 :



At the interface of NiO/Ni :



where V_O indicates a vacancy in ZrO_2 phase and \underline{O} indicates a single oxygen atom. As shown in Figure 2.7, further reduction at the sub-surface leads to the formation of a “fork” morphology of Ni(Co) interphase separating $Ni_kCo_{1-x}O$ and $ZrO_2(CaO)$ ceramic oxide phases at their interface. Feasibility of the formation of the fork morphology has been employed in this thesis work to create confined metallic interphases between the oxide layers in the $Ni_kCo_{1-x}O/ZrO_2(CaO)$ composite.

2.2.3 Objectives

This thesis is a part of a bigger scheme intended to establish a predictive structure-property relationship in various interfacial materials systems. In this dissertation $Ni_kCo_{1-x}O/ZrO_2$ is chosen as model system to investigate the effect of confined metallic interphases on the interfacial fracture phenomena in multi-layered ceramic composites. $Ni_kCo_{1-x}O/ZrO_2$ is an ideal model system for this investigation since formation of metallic interphases of Ni(Co) are possible upon chemical reduction of this system at high temperatures. The study of such model systems along with similar ongoing research contribute to better understanding of deformation and fracture phenomena in multi-layered composites and help further develop a predictive model for structure-property relationships in such systems. Figure 2.9 shows the larger ongoing research scheme for the development of a predictive model system in deformation and fracture behavior of multi-layered systems.

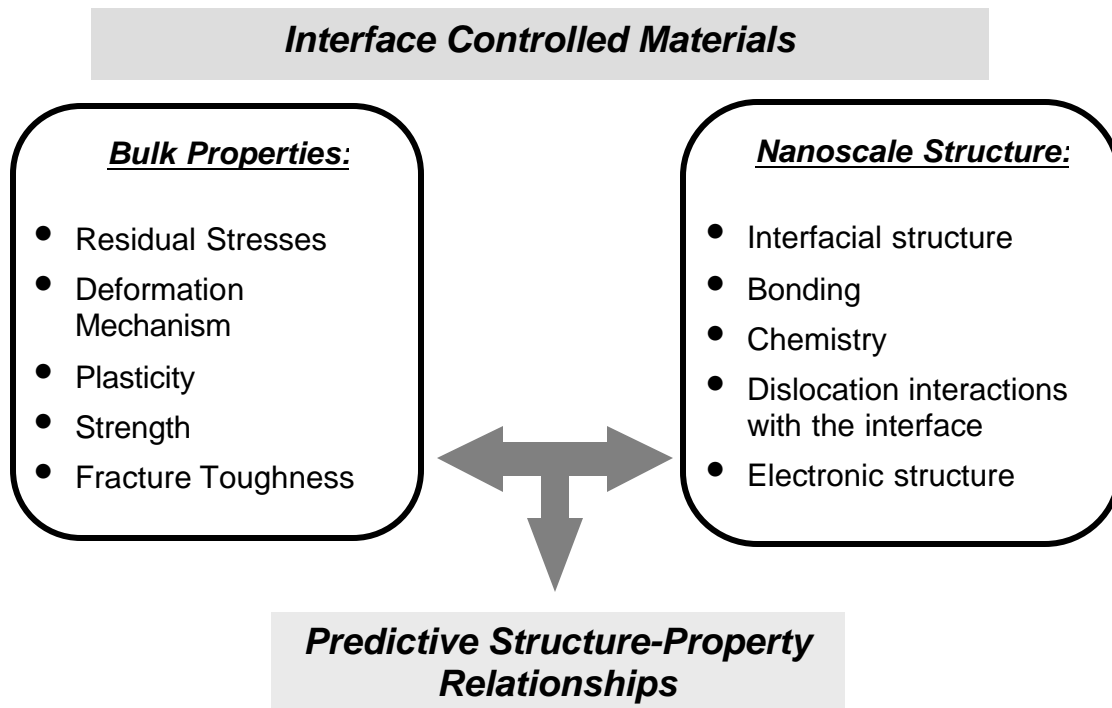


Figure 2.9 The ongoing research scheme for development of a predictive model system in deformation and fracture behavior of interface-controlled materials

The objective of this research is to understand the microstructurally driven phenomenological aspects of deformation behavior at different length scales in multi-layered systems. Previous investigations have shown cleavage and brittle fracture to occur in various materials systems as the thickness of the ductile laminate is reduced to submicron sizes. It is specifically the goal of this research to investigate the possibility of strain energy absorption and the extent of plasticity within the nanoscale confined Ni(Co) interphases upon deformation of the reduced $\text{Ni}_x\text{Co}_{1-x}\text{O}/\text{ZrO}_2$. Figure 2.10 shows the relation between the extent of plasticity and the size of the ductile interphase in ductile-brittle multi-layered systems.

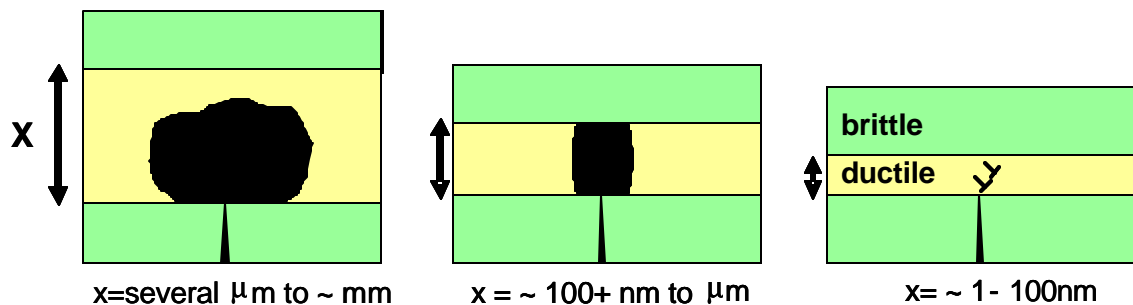


Figure 2.10 Correlation between the extent of plasticity and the size of the ductile interphase in ductile-brittle multi-layered systems.

In this study we have chosen two different chemistries in the $Ni_kCo_{1-x}O/ZrO_2$ DSE series which also maintain two different plasticity levels among the DSE series:

a) $x=0$ gives CoO/ZrO_2 system with limited plasticity of CoO at room temperature. In this system the effect of confined Co interphase (mediating CoO and ZrO_2) on the deformation and fracture behavior of the system is investigated at various length scales.

b) $x=0.5$ leads to $Ni_{0.5}Co_{0.5}O/ZrO_2$ system with brittle fracture at room temperature. In this system the effect of confined $Ni(Co)$ solid solution interphase on the deformation and fracture behavior of the composite is studied at different length scales.

This dissertation tries to address the following questions with respect to the deformation and fracture phenomena in the $Ni_kCo_{1-x}O/ZrO_2$ DSE model system with a confined metallic interphase. Figure 2.11 indicates a schematic illustration of the research scheme proposed here.

- a. Is there any enhancement of deformation and fracture behavior in the $\text{Ni}_x\text{Co}_{1-x}\text{O}/\text{ZrO}_2$ DSE series after formation of confined Co and Ni(Co) metallic interphases?
- b. Plasticity is significantly suppressed in the nanoscale regime. Is there any strain energy absorption within the nanoscale Co and Ni(Co) confined interphases upon deformation of $\text{Ni}_x\text{Co}_{1-x}\text{O}/\text{ZrO}_2$ system?
- c. Does the scale of the ductile interphase influence the competition between cleavage and plasticity in the system?
- d. Researchers have suggested emission and rearrangement of single dislocations to take place in the metallic multi-layers upon deformation. How do the dislocation activities and their configuration (i.e. dislocation pile-up, dislocation clusters and walls, twinning) in confined Co and Ni(Co) interphases in the $\text{Ni}_x\text{Co}_{1-x}\text{O}/\text{ZrO}_2$ model system change as a function of layer thickness (in the case of this study: 50 nm to 300 nm).
- e. Is there any dislocation nucleation/transmission into the adjacent ceramic phases to accommodate for stress relief within the confined metallic layer?
- f. How do the microstructural, chemical and interfacial characteristics of the system contribute to the strain energy absorption in this model system?
- g. Is there any difference in the nanoscale deformation mechanism in the reduced CoO/ZrO_2 and $\text{Ni}_{0.5}\text{Co}_{0.5}\text{O}/\text{ZrO}_2$ model systems?

The proposed research in this dissertation is meant towards a better understanding of the microstructurally driven phenomenological analysis of the deformation behavior of multi-layered composites. Such investigations are meant to help develop a predictive

scheme for structure-property relationships in the next generation of materials systems and devices.

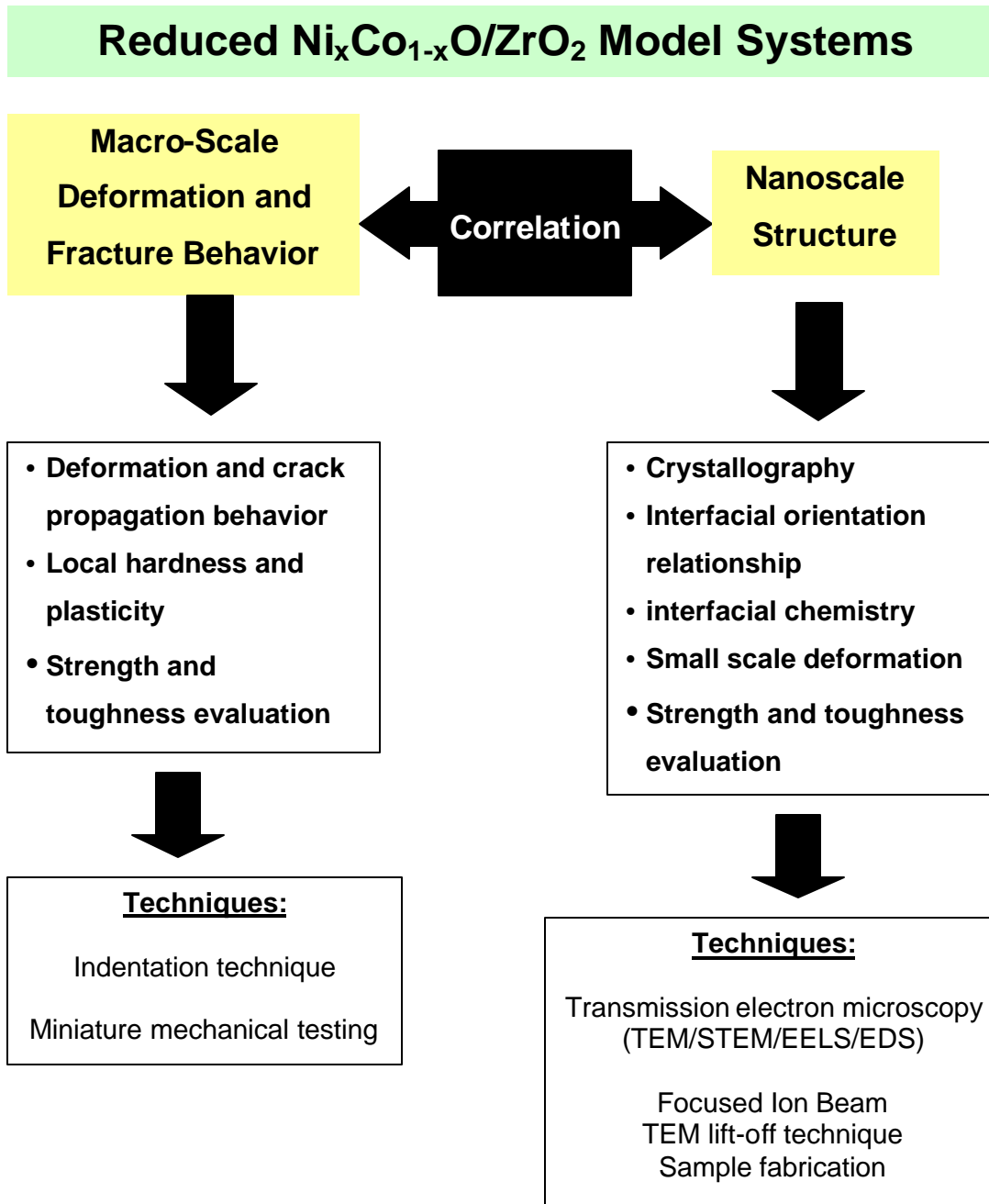


Figure 2.11 Schematic diagram of the research scheme in the present thesis work

3 DEVELOPMENT AND STRUCTURAL CHARACTERIZATION OF $\text{Ni}_x\text{Co}_{1-x}\text{O}/\text{ZrO}_2(\text{CaO})$ MODEL SYSTEM WITH A DUCTILE INTERPHASE

The first section of this chapter focuses on the formation of ductile interphases upon reduction of $\text{Ni}_x\text{Co}_{1-x}\text{O}/\text{ZrO}_2(\text{CaO})$ and introducing the experimental details of reduction process performed here. This section further presents the necessary background information about different conventional and analytical electron microscopy techniques used in this study.

Electron microscopy coupled with its analytical capabilities is a crucial tool to investigate the microstructural and chemical characteristics of $\text{Ni}_x\text{Co}_{1-x}\text{O}/\text{ZrO}_2(\text{CaO})$ model system. In the second section of this chapter, the microstructural evolution of the reduced $\text{Ni}_x\text{Co}_{1-x}\text{O}/\text{ZrO}_2(\text{CaO})$ model system is discussed. This section reveals the resulting crystallography and the chemical and the interfacial structure of the $\text{Ni}_x\text{Co}_{1-x}\text{O}/\text{ZrO}_2(\text{CaO})$ model system after its reduction.

3.1 Experimental Techniques

3.1.1 Reduction Technique

$\text{Ni}_x\text{Co}_{1-x}\text{O}/\text{ZrO}_2(\text{CaO})$ have been previously grown to single crystal rods using the optical floating zone method.^{17, 84} Disks with approximate thickness of 300 μm were cut from the single crystal rod and polished prior to reduction. The samples were then reduced in a 10%CO (by volume) balanced CO_2 gas mixture at 800 °C using a tube furnace for one hour. During the reduction process the samples were heated to 800 °C and cooled down to room temperature in N_2 atmosphere to prevent reduction/oxidation of

the sample during the heating/cooling period. Figure 3.1 indicates the heating/cooling diagram during the reduction process in this system.

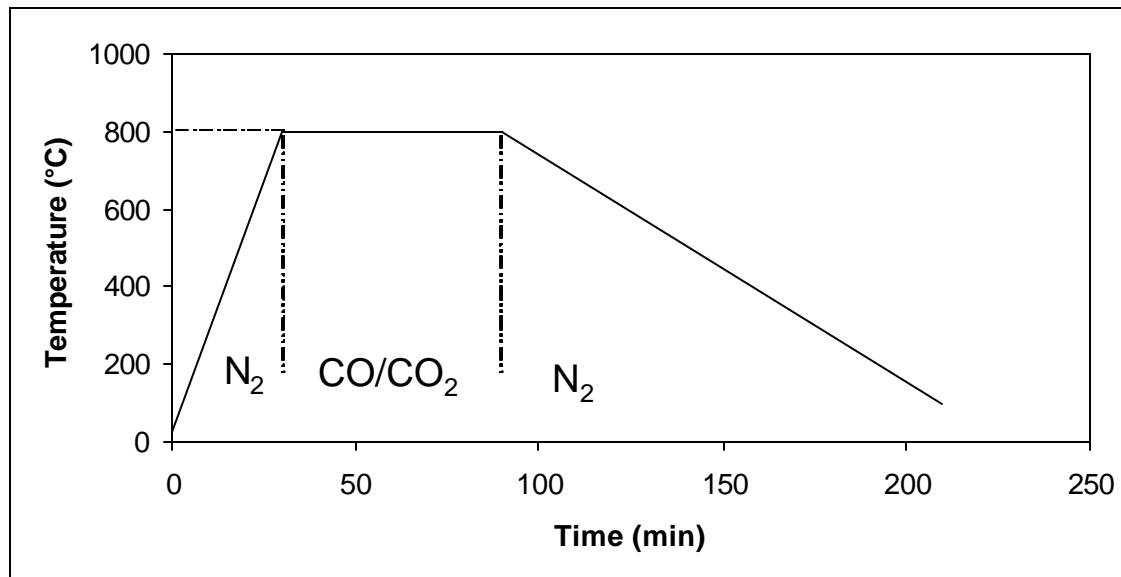


Figure 3.1 Heating/cooling diagram during the reduction process in this system.

After the reduction process the microstructure of the sample at the top surface (fully reduced area) and sub-surface (partially reduced area) was studied using Scanning Electron Microscopy. Hitachi S-4500 and Hitachi S-3500 scanning electron microscopes have been used to investigate the microstructural evolution of this composite after reduction.

To study the top surface of the sample after reduction, the microstructure of the reduced composite was directly studied in the SEM. To study the sub-surface

microstructure, the sample was first polished at the top surface to remove the fully reduced region and to reach the partially reduced area at the subsurface of the composite. Two different compositions of $\text{Ni}_x\text{Co}_{1-x}\text{O}/\text{ZrO}_2(\text{CaO})$ system, $\text{CoO}/\text{ZrO}_2(\text{CaO})$ ($x=0$) and $\text{Ni}_{0.5}\text{Co}_{0.5}\text{O}/\text{ZrO}_2(\text{CaO})$ ($x=0.5$), have been chosen to study the chemical and interfacial structure of this system upon their reduction and to further explore the small scale deformation mechanisms operating in the composite upon loading. The two compositions selected in this study maintain two different plasticity levels in this model system.

3.1.2 Transmission Electron Microscopy

Transmission Electron Microscopy (TEM) can be operated in two different modes; Conventional Transmission Electron Microscopy (CTEM) and Scanning Transmission Electron Microscopy (STEM). In the CTEM mode, a big part of the sample is illuminated by a parallel broad electron beam and the post-specimen optics are used to form the image. In the STEM mode, the electron beam is focused to form a small converged probe scanning across the area of interest in the sample and the pre-specimen lenses are used to generate an image.

In this study both CTEM and STEM modes have been used to characterize the chemical and microstructural changes in the composite. In this study, CTEM is performed to investigate the microstructure, crystallography and interfacial orientation relationship in the reduced model system. CTEM is also applied to investigate the small scale deformation mechanisms operating in the sample after its deformation. Various diffraction imaging techniques (i.e. bright field, dark field, central dark field) are utilized to for this investigation.

STEM is performed to investigate the chemical structure of the individual phases and the interfaces in the sample. The STEM mode operation is a prerequisite to perform Energy Dispersive X-ray Spectroscopy (EDXS) and Electron Energy Loss Spectroscopy (EELS) techniques to study the chemistry and interfacial structure of the model system studied here. In the STEM mode, the electron beam is in the form of a focused probe rastering across the area of interest in the sample.

Hitachi H8100 TEM, Hitachi HF2000 TEM, and JEOL JEM-2100F FAST TEM at Northwestern University, NUANCE CENTER are utilized for this investigation. All the instruments operate at an acceleration voltage of 200 kV. Hitachi H8100 TEM is equipped with a tungsten (W) hairpin filament, which is a thermionic emission source. This TEM is used to image and investigate the general microstructure of the sample.

The Hitachi HF2000 TEM has a cold field emission gun source and the JEOL JEM-2100F FAST TEM instrument is equipped with a Schottky field emitting gun source. Hitachi HF2000 TEM, and JEOL JEM-2100F FAST TEM are used to reveal the interfacial chemistry, structure and orientation relationship as well as the small scale deformation mechanisms operating in the composite after its deformation.

Hitachi HF2000 TEM and JEOL JEM-2100F FAST TEM are both equipped with single deflection scan coils, which enables STEM mode operation of these instruments. Oxford Pantafet[®] spectrometer with 135 eV resolution is used for the energy dispersive x-ray spectroscopy (EDXS) measurement. STEM mode operation is also used to perform electron energy loss spectroscopy (EELS) to investigate the interfacial chemistry of the samples across the phases in the composite. The EELS data collection was performed with a Gatan Image Filter[®] with the energy dispersion ranging from 2 to 0.05 eV over

1024 channels. Both EDXS and EELS spectrometers are interfaced with the PC running Inca and Digital Micrograph[®] software allowing the user to simultaneously collect the EDAX and EELS data for further analysis.

3.1.3 Principles of Scanning Transmission Electron Microscopy

The principles of image formation in the STEM mode are fundamentally different from that of CTEM mode. In the Conventional TEM mode, it is possible to form a bright/dark field image via selecting a portion of the electrons diffracted from the sample. The principles of the formation of a STEM image is similar to other scanning probe microscopy techniques, where a converged electron beam is scanned on the specimen through adjusting the scan coils within the microscope. In other words the STEM image is constructed by detecting the electron flux scattered from the sample surface in some direction with respect to the probe position. The spatial resolution in a STEM image directly depends on the probe size. Thus the smaller the probe size, the higher the spatial resolution is in the image. When the STEM detector is positioned to collect the scattered electrons in the direct beam (transmitted spot in the diffraction pattern), the STEM image formed will be a bright field image. In contrast when the STEM detector is positioned to collect the electrons scattered at high angles (diffracted spots in the diffraction pattern), one can form a dark field STEM image. Dark field STEM images are commonly formed via inserting an annular dark field (ADF) detector which is a doughnut shaped device. ADF detector collects all the diffracted beams (without the transmitted beam), resulting in the signal enhancement of the final image but reduction of diffraction contrast in the

image. Figure 3.2 shows a schematic of the formation of a bright/dark field image in the STEM mode.

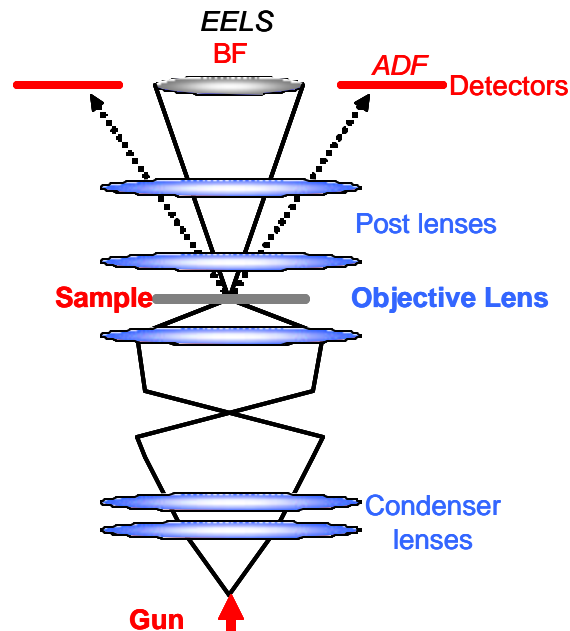


Figure 3.2 A schematic representation indicating formation of a bright/dark field STEM image in the STEM mode.

3.1.4 Electron Energy Loss Spectroscopy (EELS)

Electron Energy Loss Spectroscopy (EELS) is a powerful technique which enables the energy distribution of the inelastically scattered electrons after their interactions with the sample. An EELS spectrum maintains three different regions. The first region is called the zero loss peak (ZLP). This region corresponds to the electrons without any inelastic scattering upon passing through the sample. Since most electrons do not have inelastic interaction with thin samples, the zero loss peak usually appears to be a

strong peak at the origin of the energy scale with the intensity as high as about 10^9 counts. The second part of the spectrum is related to the low-loss region covering the electrons with inelastic scattering from 0 to 50 eV energy loss. This region of the spectrum covers electron energy loss through plasmon oscillations, and generation of inter- or intra-band transitions. The third region of the spectrum is the core loss region covering energy losses through inelastic scattering above 50 eV. This region of the spectrum includes absorption edges sharply rising from a smooth background, indicating the occurrence of the inner shell excitations in the sample. The rise of the absorption edges at a certain energy loss takes place at an ionization threshold, where the energy loss coordinate is approximately the binding energy of the corresponding atomic shell. Since the inner shell binding energy depends on the atomic number of the scattering atom, the absorption edge present in the spectrum is in fact a fingerprint for the present element in the sample.

Prior to spectrum analysis, it is essential to remove the background from the energy loss spectrum. The background intensity comes from the plural scattering of the outer-shell electrons in the sample. To remove the background several functions such as power-law fit, exponential, polynomial or log-polynomial should be used as long as they provide an appropriate fit to the background. Upon removing the background the absorption edges in the spectrum usually reveal their fine structure. This fine structure reflects the crystallographic or the band structure of the elements analyzed.

Plural scattering in the energy loss spectrum increases the intensity of the ionization edges through combining the inner and outer shell energy losses. To extract the single scattering intensity distribution from the specimen, the plural scattering should be

extracted from the energy loss spectrum. Fourier-Log and Fourier-Ratio are two main methods which are used to remove the plural scattering from the spectrum.

STEM mode operation combined with EELS allows one to simultaneously form an image from the area of interest and study its chemical nature. This technique is performed by forming a dark field STEM image of the area of interest (using the diffraction beam) and simultaneously directing the transmitted beam into the magnetic prism in the Gatan imaging filter for EELS data collection. The transmitted beam can provide information about the interfacial chemistry as well as elemental bonding and coordination from the area of interest in the sample, while the diffracted beam simultaneously provides an image from the area of interest. Figure 3.2 indicates a schematic diagram of dark field STEM imaging combined with EELS technique.

3.2 Characterization of the $\text{Ni}_x\text{Co}_{1-x}\text{O}/\text{ZrO}_2(\text{CaO})$ Model System Upon Reduction

3.2.1 Microstructural Evolution of the Reduced $\text{Ni}_x\text{Co}_{1-x}\text{O}/\text{ZrO}_2(\text{CaO})$ Model System

According to the discussion in section 2.2.2, chemical reduction of the $\text{Ni}_x\text{Co}_{1-x}\text{O}/\text{ZrO}_2(\text{CaO})$ DSE composites leads to the formation of metallic Ni, Co or Ni(Co) solid solution interphase at the DSE interfaces. In this section the microstructural changes in the $\text{Ni}_x\text{Co}_{1-x}\text{O}/\text{ZrO}_2(\text{CaO})$ DSEs are discussed upon reduction.

Figure 3.3 shows an SEM micrograph of the top surface of $\text{Ni}_x\text{Co}_{1-x}\text{O}/\text{ZrO}_2(\text{CaO})$ sample after reduction. This figure shows formation of a series of shrinkage cracks at the top surface of the reduced DSEs, indicating significant volume reduction from oxide to

its metal counterpart. Depth of shrinkage cracks was observed to be about the same order of the depth of complete reduction. Previous work has also reported the formation of arrays of cracks and bending of the lamellae as a result of oxygen vacancy formation after reduction.^{82, 83} A 41% volume reduction occurs during the reduction reaction as a result of oxygen vacancy formation assuming the $\text{Ni}_{0.5}\text{Co}_{0.5}\text{O}$ phase ($x=0.5$) to fully reduce to metallic Ni(Co) alloy. In the case of this study since the transition metal oxide in the area of interest is partially reduced to its metal counterpart, the volume reduction is much less than the above value. The volume shrinkage is in the form large cracks in the fully reduced region, while in the partially reduced area it is mainly distributed in the form of interfacial porosity.

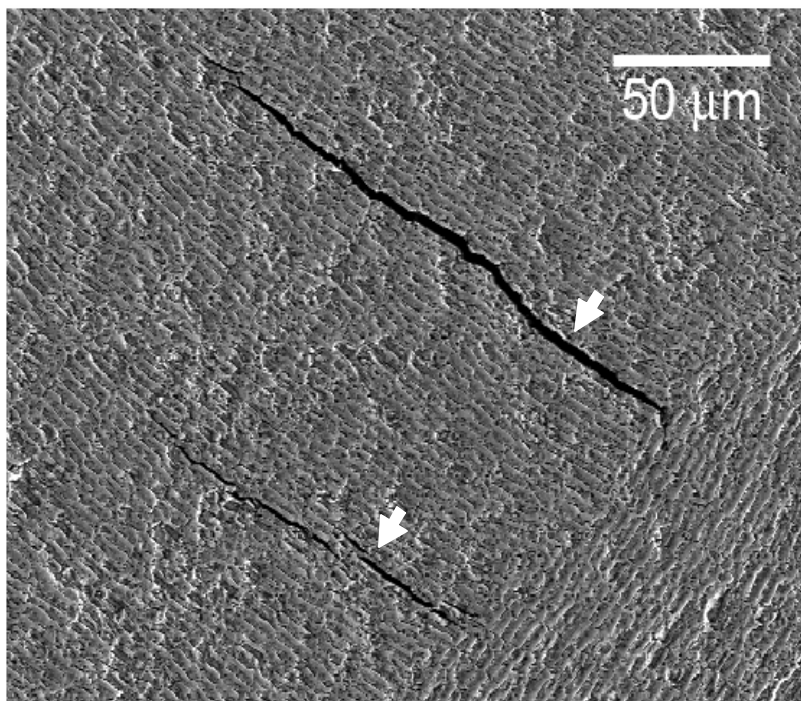


Figure 3.3 Formation of shrinkage cracks at the top surface of the composite after reduction (shown with arrows on the figure)

Figure 3.4 shows SEM micrographs of the top and the cross-section of $\text{Ni}_x\text{Co}_{1-x}\text{O}/\text{ZrO}_2(\text{CaO})$ sample after reduction. The transition metal oxide forms a porous $\text{Ni}(\text{Co})$ metallic phase surrounding the ZrO_2 fingers after $\text{Ni}_x\text{Co}_{1-x}\text{O}$ phase is fully reduced at the top surface (Figure 3.4 (a)). Looking at the cross-sectional view, the bright area at the top section of the sample (shown with arrows in Figure 3.4 (b)) indicates the depth of reduction for the reduced $\text{Ni}_x\text{Co}_{1-x}\text{O}$ phase. The partially reduced region in this sample can be seen as the bright strips of metal maintaining a “fork” morphology protruding into the interface of the oxide phases below the fully reduced area. Depth of reduction was observed to vary from one sample to the other depending on the lamellae

direction and the pristine microstructure considering the experimental condition to be consistent. This figure also shows $\text{Ni}_x\text{Co}_{1-x}\text{O}$ layer in some local areas at the sub-surface to completely reduce to its metallic form at the subsurface. The black arrows on the image point to the fully reduced areas surrounded by the partially reduced microstructure in this area. Figure 3.5 indicates the microstructure of the reduced $\text{CoO}/\text{ZrO}_2(\text{CaO})$ sample with a primary ZrO_2 phase at the top left corner of the image. Significant porosity formation around the primary ZrO_2 phase is an indication of the full CoO reduction in this area. Complete reduction of CoO phase is believed to take place due to the faster oxygen ion transfer through ZrO_2 in this region.

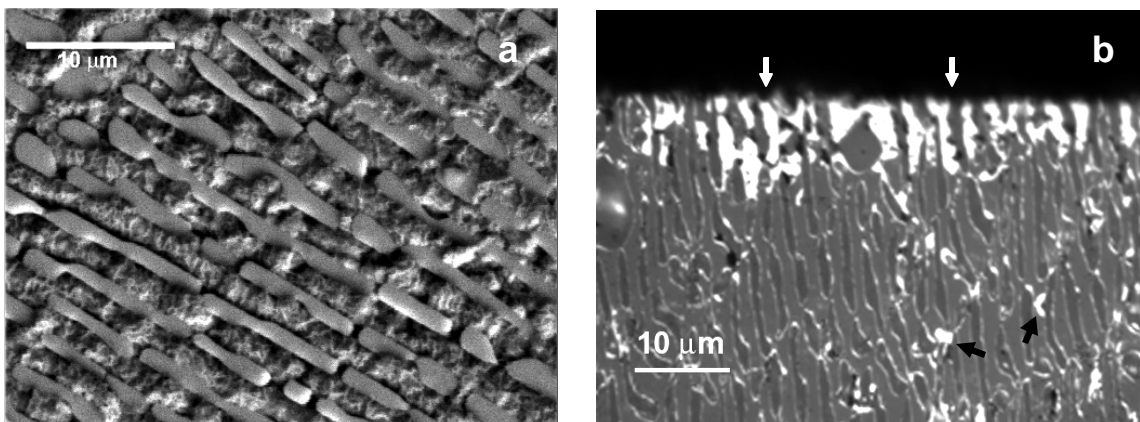


Figure 3.4 SEM micrographs of the top view (a) and cross-sectional view (b) of reduced $\text{Ni}_x\text{Co}_{1-x}\text{O}/\text{ZrO}_2(\text{CaO})$. (a) The porous matrix indicates the porous metallic $\text{Ni}(\text{Co})$ phase surrounding the ZrO_2 fingers. (b) The bright area shown with arrows at the top portion of the sample indicates the fully reduced region in the $\text{Ni}_x\text{Co}_{1-x}\text{O}$ phase.

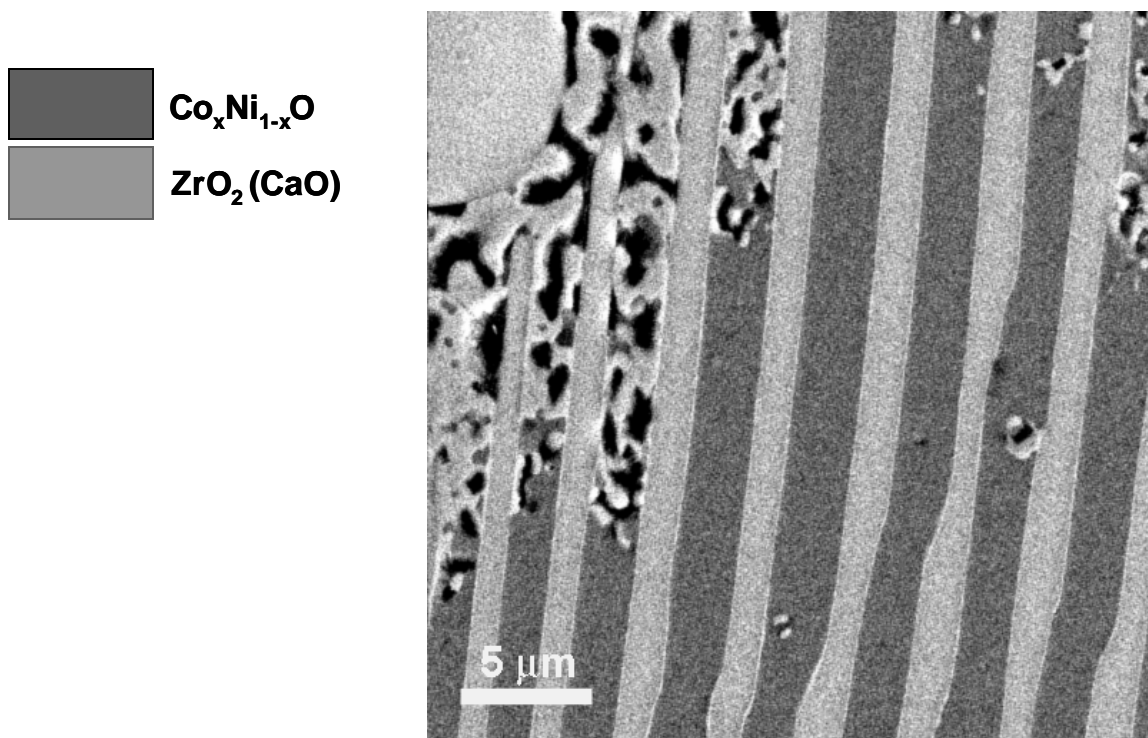


Figure 3.5 Cross-sectional microstructure of the reduced CoO/ZrO_2 sample indicating full reduction of CoO phase adjacent to the primary ZrO_2 phase.

Figure 3.6 shows a high magnification image of the microstructure of the fully oxidized and chemically reduced $\text{Ni}_k\text{Co}_{1-x}\text{O}/\text{ZrO}_2(\text{CaO})$ samples after polishing the top surface. Figure 3.6 (a) indicates the lamellae microstructure in the pristine sample. The bright strips between $\text{Ni}_k\text{Co}_{1-x}\text{O}$ and $\text{ZrO}_2(\text{CaO})$ in Figure 3.6 (b) indicate the metallic $\text{Ni}(\text{Co})$ phase formed in the composite with about 100 nm thickness after reduction. The black spots distributed along the metal-oxide interface in Figure 3.6 (b) are the pores formed due to volume reduction as the reduction front proceeds.

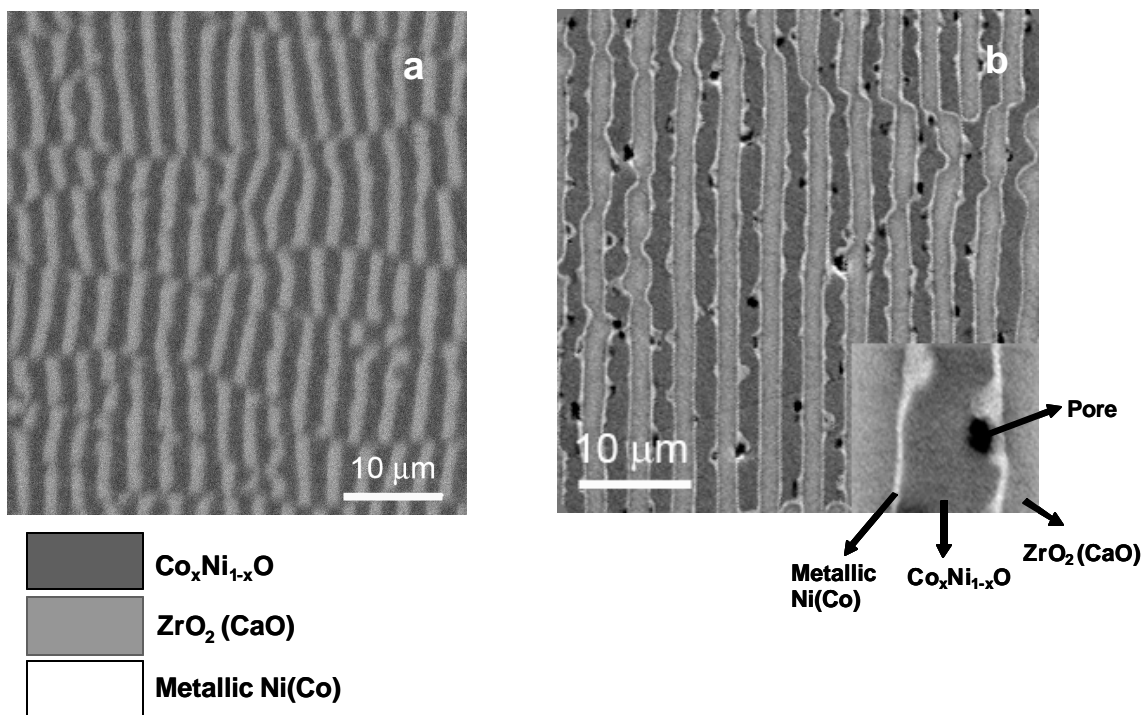


Figure 3.6 SEM micrograph showing the microstructure of $\text{Ni}_x\text{Co}_{1-x}\text{O}/\text{ZrO}_2(\text{CaO})$ system (a) before reduction and (b) after reduction (different region). Note the formation of bright metallic layers along the interfaces after reduction.

In this study we found a gradual decrease in the area density of the pores as a function of depth. The area density of the pores in this study is defined as the area of the pores measured on the surface divided by the total area. Figure 3.7 shows an example of this measurement, where the SEM image of the microstructure (Figure 3.7 (a)) is transformed into a binary image (Figure 3.7 (b)) with the pores shown as white areas on the black background. The area density of porosity was measured in several areas in the reduced $\text{Ni}_{0.5}\text{Co}_{0.5}\text{O}/\text{ZrO}_2(\text{CaO})$ sample and the porosity distribution in this sample is

shown in Figure 3.8. Figure 3.8 (a) indicates the area density of porosity at the partially reduced regions in the area of interest where the deformation mechanism is studied. This region maintains porosity distribution of about 2-4%, while at the subsurface, below the deformed region, this value is slightly decreased to 1-2% (Figure 3.8 (b)). The pores are oval-shaped mainly confined between the metal-ZrO₂ interface with the diameter size mainly varying from 100 nm to 800 nm in diameter. Figure 3.8 (c) shows the distribution profile for the area of the porosity after reduction of the sample. As this figure indicates majority of the pores maintain area of about 0.1-0.2 μm. Based on the measurement here the average area of each porosity is determined to be about 0.27 μm² in the reduced system.

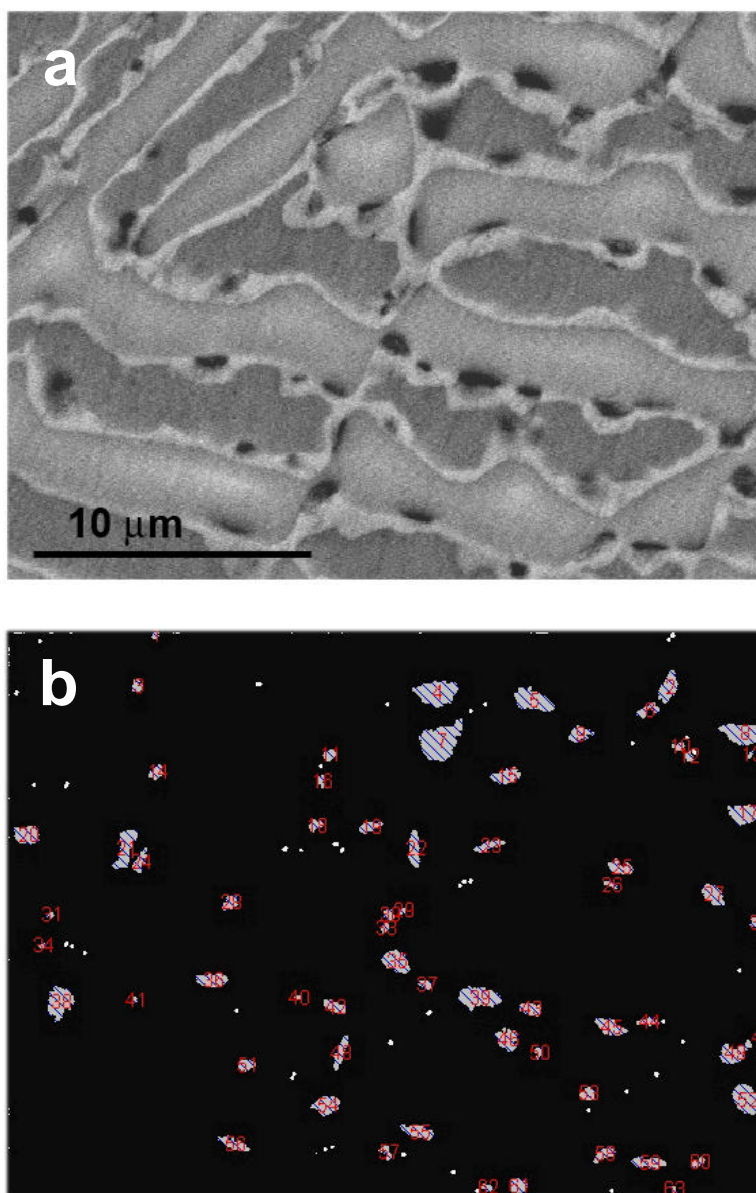


Figure 3.7 (a) SEM micrograph of the reduced DSEs indicating porosity formation along the metal-ZrO₂ interphase. (b) Binarized image of the SEM micrograph indicating the pores as white areas in the black matrix.

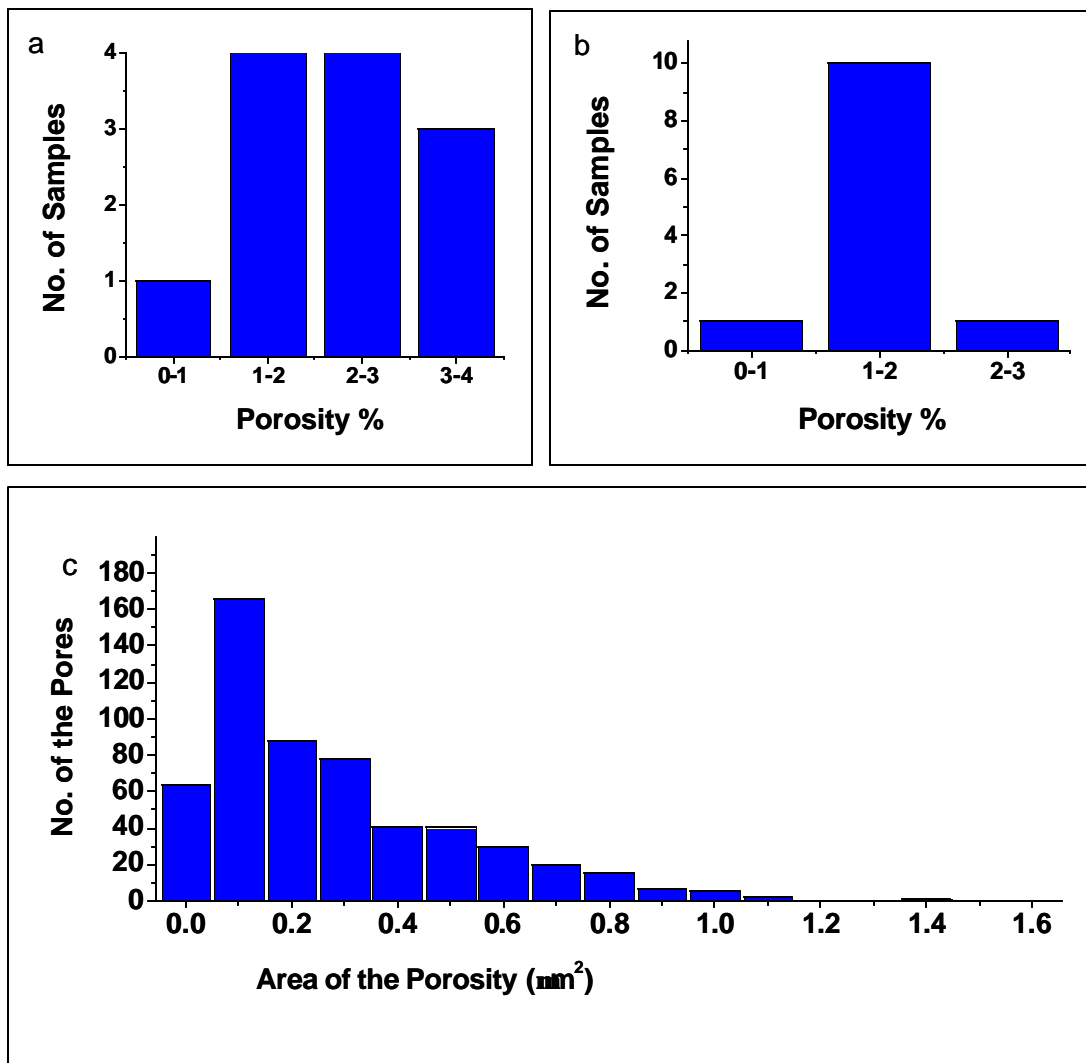


Figure 3.8 Porosity distribution at the (a) cross-section and (b) along the depth in the partially reduced regions of the $\text{Ni}_x\text{Co}_{1-x}\text{O}/\text{ZrO}_2(\text{CaO})$ sample with $x=0.5$. (c) The distribution profile for the area of the porosity after reduction of the sample.

Considering the pore morphology and its distribution in the sample, the 2-4% area density of the porosity in the microstructure appears to be in the form of a small number

of pores with relatively large sizes, on the same order of the size of the metallic interphase, fairly separated from each other. Figure 3.6 (b) presents an example of the pore morphology and its size compared to the other microstructural features in the composite.

3.2.2 Chemical Nature of the Reduced $\text{Ni}_x\text{Co}_{1-x}\text{O}/\text{ZrO}_2(\text{CaO})$ System

The chemical analysis of the reduced $\text{Ni}_x\text{Co}_{1-x}\text{O}/\text{ZrO}_2(\text{CaO})$ system aims to identify the chemistry of the present phases and to investigate the interfacial chemistry in the system after its reduction. Energy Dispersive X-ray Spectroscopy (EDXS) was performed on the ductile interphase in the reduced $\text{Ni}_{0.5}\text{Co}_{0.5}\text{O}/\text{ZrO}_2(\text{CaO})$ system to analyze the chemical composition of this phase and to investigate if NiO and CoO in the $\text{Ni}_{0.5}\text{Co}_{0.5}\text{O}$ phase are reduced with similar proportion. The Cliff-Lorimer approach was used to determine the standard K-factor, which was calculated from the $\text{Ni}_{0.5}\text{Co}_{0.5}\text{O}$ phase in the $\text{Ni}_{0.5}\text{Co}_{0.5}\text{O}/\text{ZrO}_2(\text{CaO})$ system. The Cliff-Lorimer approach can relate the signal intensity of the elements to their chemical composition in the quantitative x-ray analysis. This relationship has been shown in Equation 3.1.¹⁰³

$$\frac{C_A}{C_B} = K_{AB} \frac{I_A}{I_B} \quad 3.1$$

where, C_A and C_B are the composition of element A and B in the sample respectively, while I_A and I_B are the measured characteristic intensities coming from elements A and B respectively. K_{AB} is the Cliff-Lorimer factor, which related the measured intensities to the chemical composition in the sample.

The advantage of considering $\text{Ni}_{0.5}\text{Co}_{0.5}\text{O}$ layer (adjacent to the metallic Ni(Co) interphase) as a standard phase is that all the EDXS data (from both the metallic interphase and the standard phase) are obtained at the same time and under identical microscope conditions. Selection of $\text{Ni}_{0.5}\text{Co}_{0.5}\text{O}$ layer as the standard can further minimize possible errors involved during data collection and quantification. To calculate the composition of the metallic layer, the ratio of Ni to Co in the transition metal oxide for $x=0.5$ is considered to be one. Based on the previous studies by Brewer *et al.* on the chemical characterization of the pristine $\text{Ni}_x\text{Co}_{1-x}\text{O}/\text{ZrO}_2(\text{CaO})$ system, it is a fair estimate to consider Ni to Co ratio as one in the transition metal oxide with $x=0.5$ composition. Considering the above assumptions, EDXS quantification analysis of Ni(Co) interphase shows the metallic interphase to contain 52.3 ± 3.6 wt% Co and 47.7 ± 3.9 wt% Ni elements.

To probe any large scale inter-diffusion of Ni and Co elements into the $\text{ZrO}_2(\text{CaO})$ phase, Energy Dispersive X-ray Spectroscopy (EDXS) and Electron Energy Loss Spectroscopy (EELS) were performed on the reduced $\text{Ni}_x\text{Co}_{1-x}\text{O}/\text{ZrO}_2(\text{CaO})$ system. An abrupt drop in the Ni and Co content to small amounts is observed upon crossing the interface from the metallic interphase to $\text{ZrO}_2(\text{CaO})$, which rules out the large scale inter-diffusion of Ni and Co into $\text{ZrO}_2(\text{CaO})$ during reduction. This investigation also did not show any large scale inter-diffusion of Zr and Ca into the neighboring metallic interphase, which points to the stability of $\text{ZrO}_2(\text{CaO})$ during reduction.

Figure 3.9 shows an EDXS spectrum obtained from the middle of $\text{ZrO}_2(\text{CaO})$ phase in the reduced $\text{Ni}_{0.5}\text{Co}_{0.5}\text{O}/\text{ZrO}_2(\text{CaO})$ composite away from the interfaces. This spectrum indicates presence of small amounts of Ni and Co within the $\text{ZrO}_2(\text{CaO})$ phase.

Cubic $\text{ZrO}_2(\text{CaO})$ has been previously shown to have limited solubility of Co and Ni in itself during the growth of this system.^{84, 104, 105} Brewer *et al.*⁸⁴ specifically indicated presence of Ni and Co within $\text{ZrO}_2(\text{CaO})$ in the pristine $\text{Ni}_k\text{Co}_{1-x}\text{O}/\text{ZrO}_2(\text{CaO})$ composite. Laguna-Bercero *et al.*¹⁰⁵ have specifically studied the dissolution of Ni and Co elements and their ionic status in $\text{ZrO}_2(\text{Y}_2\text{O}_3)$ in the fully reduced $\text{NiO}/\text{ZrO}_2(\text{Y}_2\text{O}_3)$ and $\text{CoO}/\text{ZrO}_2(\text{Y}_2\text{O}_3)$ DSEs. Their studies on the fully reduced $\text{NiO}/\text{ZrO}_2(\text{Y}_2\text{O}_3)$ and $\text{CoO}/\text{ZrO}_2(\text{Y}_2\text{O}_3)$ DSE systems indicate presence of the transition elements in the form of NiO and CoO in the $\text{ZrO}_2(\text{Y}_2\text{O}_3)$ phase.¹⁰⁵ Moreover, the EDAX and EELS analysis show the Ni and Co content to have an abrupt drop upon passing across the interface from the metallic interphase into the $\text{ZrO}_2(\text{CaO})$ phase. Based on these observations, it is believed that the Ni and Co signal in the EDXS spectrum indicate small amounts of NiO and CoO previously diluted in the $\text{ZrO}_2(\text{CaO})$ phase during the growth of this system and no inter-diffusion of Ni and Co into $\text{ZrO}_2(\text{CaO})$ occurs during reduction.

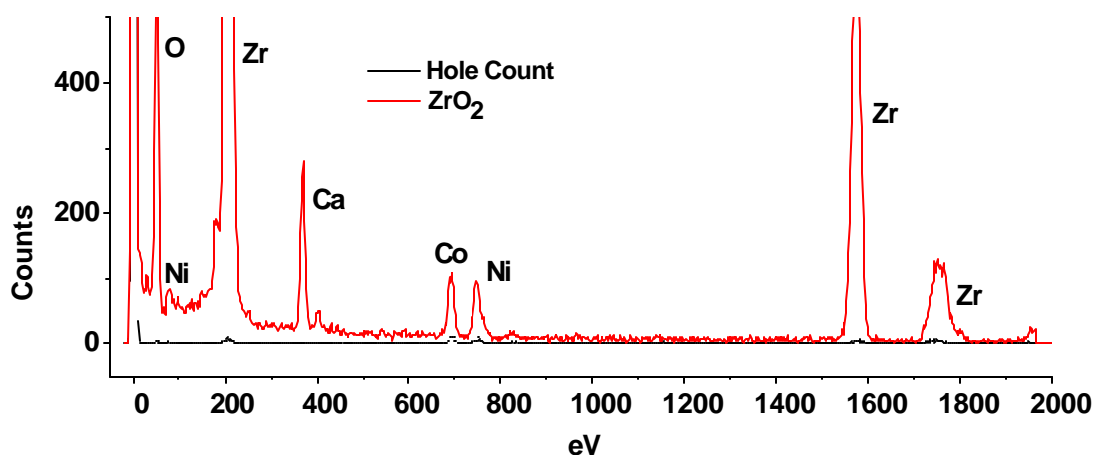


Figure 3.9 EDXS spectrum showing the chemistry of ZrO_2 in the $\text{Ni}_{0.5}\text{Co}_{0.5}\text{O}/\text{ZrO}_2$ and presence of small amount of Ni and Co in ZrO_2

To probe the chemical changes across the interface and to investigate the interfacial thickness of the composite electron energy loss spectroscopy (EELS) was performed in the STEM mode. A reduced $\text{CoO/ZrO}_2(\text{CaO})$ sample was chosen as an example of the reduced $\text{Ni}_x\text{Co}_{1-x}\text{O/ZrO}_2(\text{CaO})$ DSE series for this study. The STEM probe size used for this study was measured to be 0.67 nm in Full Width Half Maximum (FWHM). The energy resolution for EELS was determined to be 1 eV in full-width half-maximum of the zero-loss peak and a 0.3 eV/channel dispersion was used for data collection. The background was removed with a power law fit before the Co, O and Ca edges and the plural scattering was removed using the zero-loss spectrum from each point using the Fourier ratio function.

Figure 3.10 shows the EELS chemical profiles across the $\text{Co-ZrO}_2(\text{CaO})$ interface along with the dark field STEM image of the metal-ceramic multi-layered composite. The step size in the EELS line scan profile shown in this figure is 0.65 nm. The chemical changes across the interface is observed to take place within a thickness of approximately 2 nm indicating a sharp interface at the 2 nm length scale between the metal-oxide interfaces. The arrows on Figure 3.10 (c) indicate the region where all the chemical changes take place across the $\text{Co-ZrO}_2(\text{CaO})$ interface. This analysis indicates elimination of oxygen from the interphase and formation of a 2 nm sharp metal-ceramic interface upon reduction. The line scan EELS spectra also show the Co, Zr, Ca and O elements co-existing while passing across the interface. Ca has been previously reported to exist only in the $\text{ZrO}_2(\text{CaO})$ phase after the original growth of this composite.^{84, 106} Therefore, the rise of Ca edge in Figure 3.10 (b) (shown with an arrow) could be considered as an indication of the onset of the $\text{ZrO}_2(\text{CaO})$ phase in the spectra. It is hard

to specifically comment on the atomic scale inter-diffusion of Co, Zr, Ca and O at the Co-ZrO₂(CaO) interface, since after the reduction process the resulting metallic interphases do not maintain exact edge-on position with ZrO₂(CaO) and a few degrees misorientation exists between the two phases.

Figure 3.11 shows the interfacial chemistry across the Co-CoO interface upon moving from Co to CoO. The EELS spectra shown here is taken from the same area of the sample shown in Figure 3.11 (a) but on the Co-CoO interface. According to this figure all the chemical changes take place within a 1 nm thickness pointing to a formation of a sharp interface between Co and CoO.

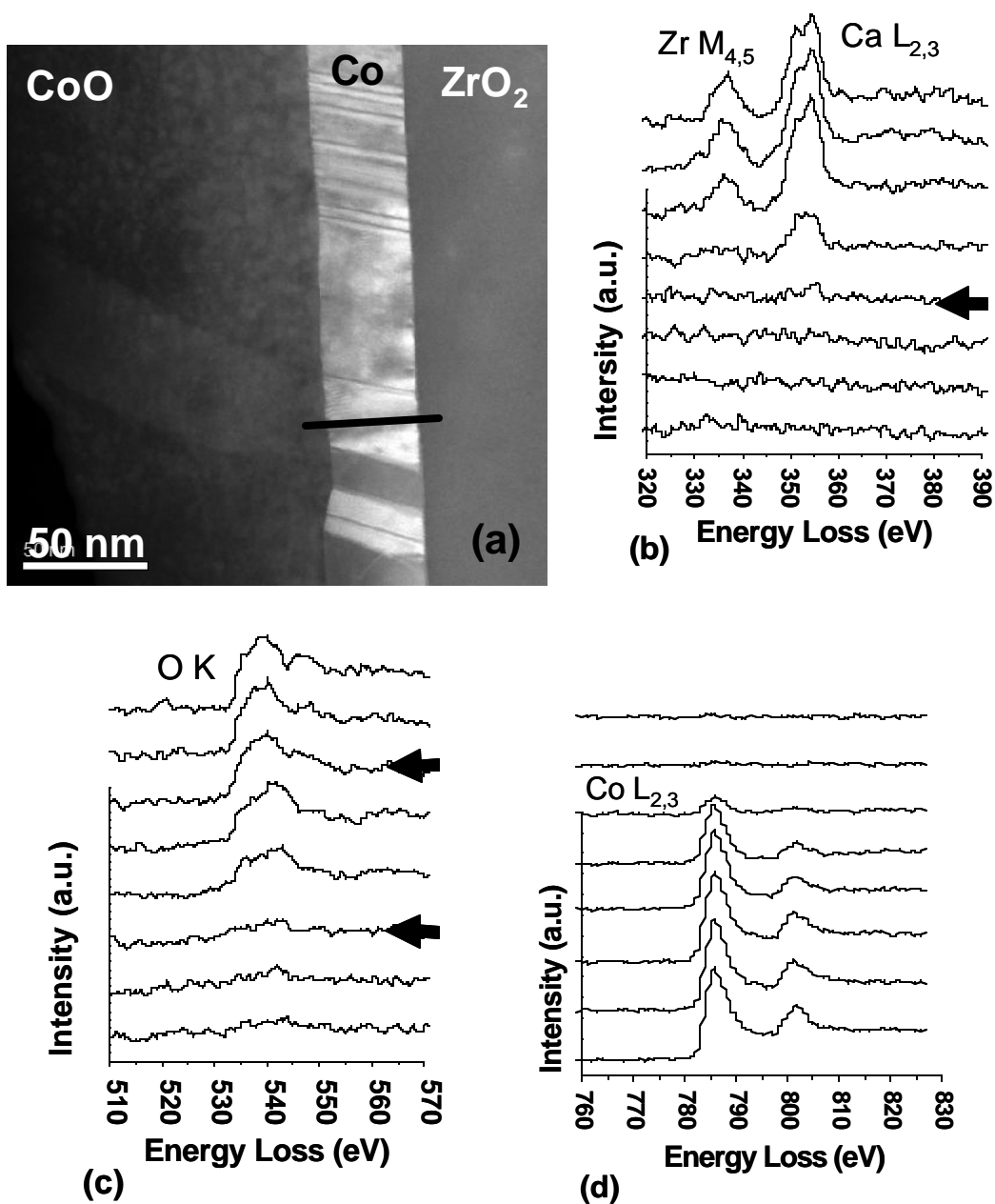


Figure 3.10 (a) DF STEM image of the reduced CoO/ZrO₂ composite along with electron energy loss spectra across the interface showing (b) Zr M_{4,5} and Ca L_{2,3} edge, (c) O K edge and (d) Co L_{2,3} edge moving from Co interphase to ZrO₂. (The black line on the STEM image shows the region of analysis) Step size=0.65nm

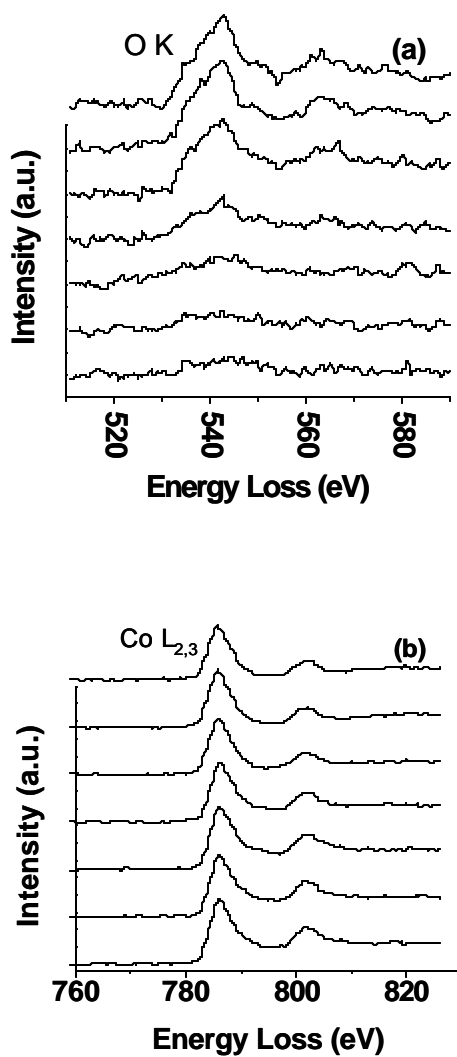
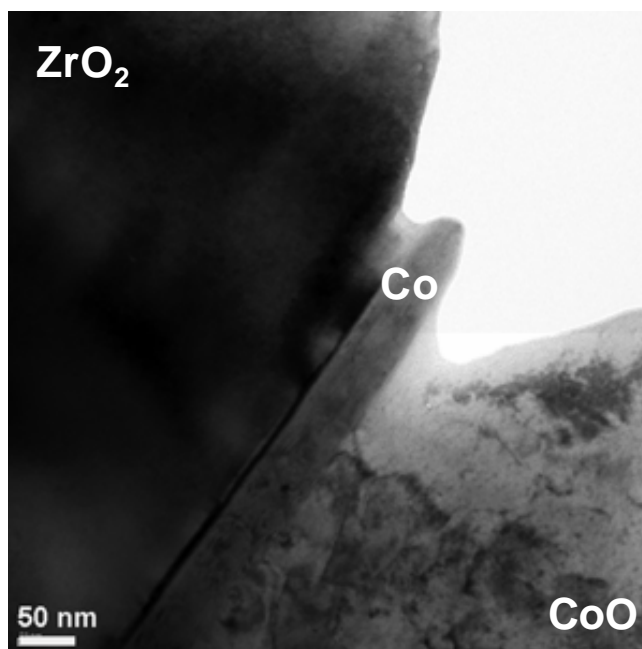


Figure 3.11 Electron energy loss spectra across the CoO-Co interface showing (a) the rise of O K edge and (b) Co L_{2,3} edge moving from Co interphase to CoO. (The area of analysis is shown in Figure 3.10 (a)) Step size=0.65nm

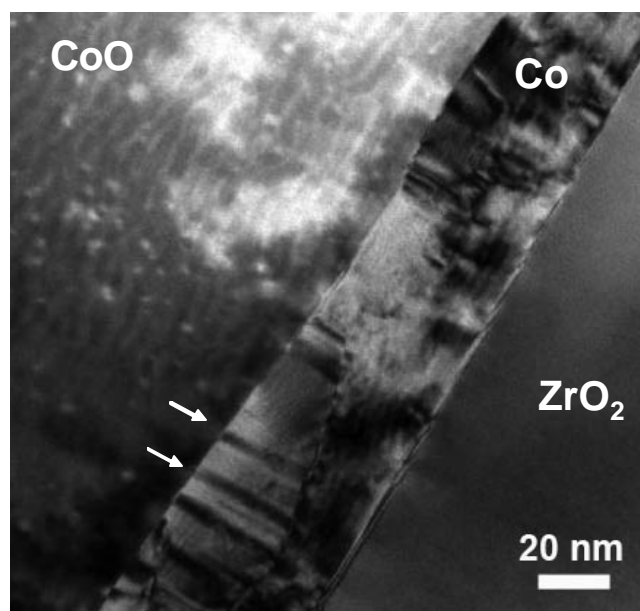
3.2.3 Crystallography of the Reduced $\text{Ni}_x\text{Co}_{1-x}\text{O}/\text{ZrO}_2(\text{CaO})$ System

TEM studies of the reduced DSEs show formation of the metallic interphase of Co and Ni(Co) upon reduction of $\text{Ni}_x\text{Co}_{1-x}\text{O}/\text{ZrO}_2(\text{CaO})$ system ($x=0$, $x=0.5$) at high temperatures with the metallic layer thickness varying from about 50 nm to 300 nm in size.

The metallic interphase maintains a single crystalline structure when the interphase thickness is mostly below 100 nm. Figure 3.12 (a) indicates an example of Co interphase maintaining a single crystalline structure with the layer thickness of about 60 nm. Small size twins are infrequently observed within the metallic interphase at such thickness. Figure 3.12 (b) indicates a region of the reduced $\text{CoO}/\text{ZrO}_2(\text{CaO})$ with a few small size twins within the metallic Co interphase. With increasing the layer thickness, the metallic interphase starts to transform into a polycrystalline structure. Figure 3.13 exhibits a bright field image of the reduced $\text{CoO}/\text{ZrO}_2(\text{CaO})$, indicating polycrystalline structure of the metallic Co interphase with the layer thickness of about 200 nm.



(a)



(b)

Figure 3.12 (a) Typical microstructure of the reduced composite with the metallic interphase maintaining single crystal structure (60 nm in this area) and (b) Small size twins are infrequently observed within the metallic interphase at such size scale (shown with arrows on the image).

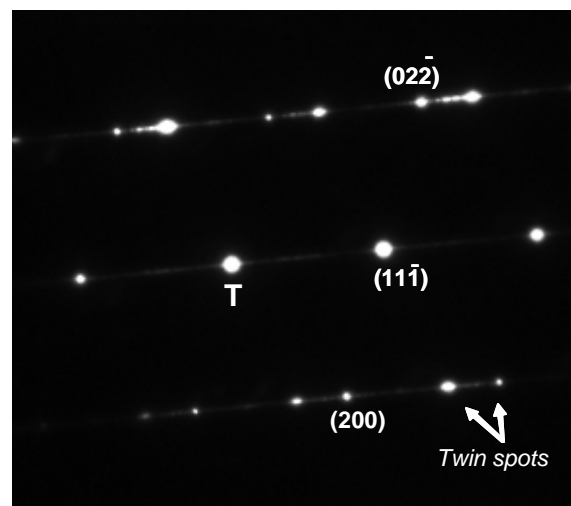
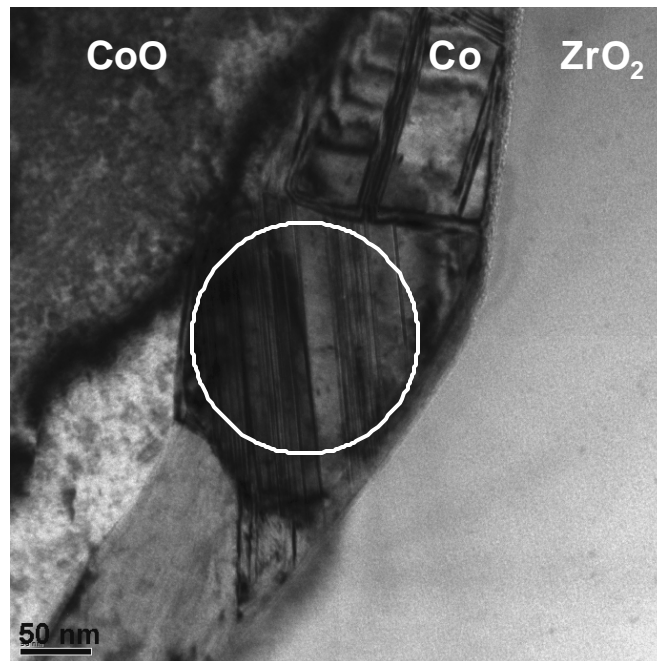


Figure 3.13 Bright field image of Co interphase with its SAD pattern in the reduced $\text{CoO}/\text{ZrO}_2(\text{CaO})$ sample indicating FCC structure of Co with $\langle 110 \rangle$ zone axis. The streaks in the diffraction pattern indicate presence of stacking faults and the double spots indicate twinning formation within the metallic layer. The circle on the image indicates the area the diffraction pattern has been obtained.

Selected area diffraction technique was performed on the reduced $\text{Ni}_x\text{Co}_{1-x}\text{O}/\text{ZrO}_2(\text{CaO})$ composite to determine the crystallographic structure of the metallic interphase. The metallic interphase maintains Face Centered Cube (FCC) structure across the chemically reduced DSEs studied in this work ($x=0$ and $x=0.5$). Figures 3.13 and 3.14 show Co ($x=0$) and Ni(Co) ($x=0.5$) interphases maintaining FCC crystallographic structure with $\langle 110 \rangle$ zone axis in the reduced $\text{Ni}_x\text{Co}_{1-x}\text{O}/\text{ZrO}_2(\text{CaO})$ system. Although the stable crystallographic structure of Co at room temperature is Hexagonal Closed Packed (HCP), the FCC crystal structure of Co observed in the reduced $\text{Ni}_x\text{Co}_{1-x}\text{O}/\text{ZrO}_2(\text{CaO})$ composite confirms the previously observed Co FCC structure in other composites.^{22, 107-110} Liu *et al.*¹⁰⁸ have observed a mixture of FCC-HCP structure of Co at room temperature in the WC-Co composites. Tai *et al.* have also observed Co phase to be a mixture of FCC-HCP structure in Al_2O_3 -Co composites.¹¹¹ The room temperature FCC structure of Co interphase has been previously attributed to various factors such as presence of solutes, existence of external stresses, and reduced film thickness.¹¹²⁻¹¹⁸ Cabral *et al.* have studied the FCC to HCP phase transformation of Co and have related this sluggish phase transformation to the small difference in the free energy of HCP to FCC Co (-2.2 cal/mol).¹¹⁴ This small difference in the free energy can be easily altered by various factors such as addition of solutes, and presence of stresses and can easily affect the HCP to FCC phase transformation in Co.¹¹⁴

Gallagher¹¹² has studied the effect of solute elements on the phase transformation of various elements and has specifically shown that addition of Ni to Co can drop the FCC to HCP transition temperature to values even below the room temperature. These studies suggest that presence of 50 wt% Ni in the Ni-Co solid solution alloy to be the

motive for the resulting FCC structure of the Ni(Co) interphase. The Ni-Co phase diagram also clearly indicates formation of FCC Ni(Co) alloy at room temperature with 50 wt% Ni.

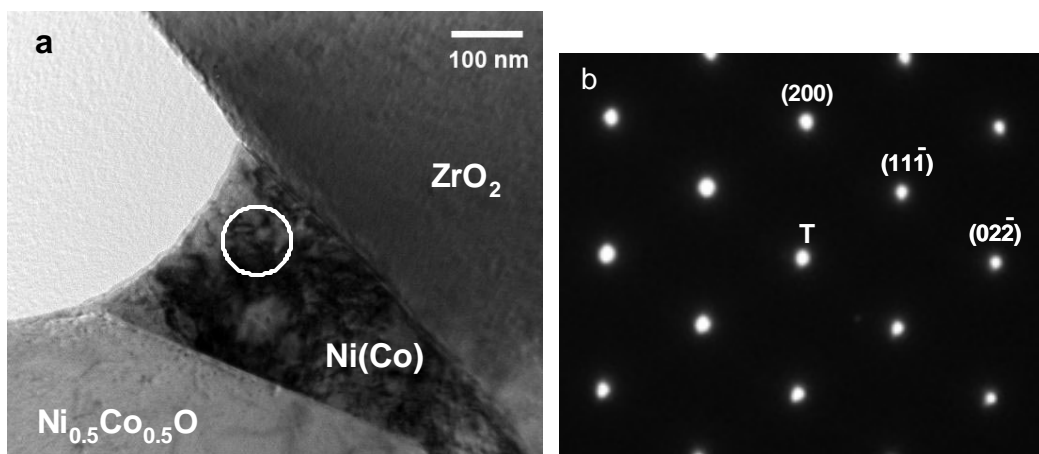


Figure 3.14 Bright field image of Ni(Co) interphase (a) with its SAD pattern (b) in the reduced $\text{Ni}_{0.5}\text{Co}_{0.5}\text{O}/\text{ZrO}_2(\text{CaO})$ sample indicating FCC structure of Co with $\langle 110 \rangle$ zone axis. The circle in the image indicates the area the diffraction pattern is taken from.

To understand the FCC to HCP phase transformation in the metallic Co interphase, it is important to have a close look at the microstructure after reduction of this phase. Figure 3.13 shows characteristics of deformation within the metallic Co interphase through formation of stacking faults and twins. The SAD pattern from the Co interphase in Figure 3.13 indicates double diffraction spots owing to the presence of twins and streaks passing through the diffraction spots indicative of the presence of stacking faults in this region of the sample. The diffraction pattern clearly shows twinning to take place

on the (111) mirror planes of the metallic Co interphase, which is the twinning plane for the FCC crystals. This observation confirms characteristics of local deformation to take place within the Co interphase.

Co thin films has been previously shown to form the FCC structure at room temperature.^{115, 116} Votava *et al.* have previously studied the phase transformation in thin Co films and have first reported the FCC structure of Co at room temperature upon cooling.¹¹⁶ Their studies show the FCC to HCP phase transformation in Co to be hindered due to the film size effects. Wright *et al.* reported similar observations where the Co structure is maintained as FCC up to a critical thickness.¹¹⁵ Both these investigations showed formation of stacking faults in the metallic cobalt thin films upon cooling.

The stacking faults in FCC Co at room temperature indicate the regions where the atomic stacking represents HCP structure. The unfaulted regions however, indicate the untransformed FCC areas upon cooling. for the Co phase transformation to take place, perfect dislocations contributing to this transformation should be able to move freely and with no obstacle.¹¹⁹⁻¹²¹ In a confined thin film of Co however, perfect dislocations contributing to this transformation are pinned at the grain boundaries or interfaces and cannot split up to accommodate the FCC to HCP phase transformation.¹¹⁶

It is believed that the FCC to HCP phase transformation in Co interphase in the reduced $\text{CoO/ZrO}_2(\text{CaO})$ composite is hindered due to the size scale and confinement of the interphase. For the phase transformation to take place in Co the normal propagation of stacking faults at the neighboring (111) planes should take place freely to accommodate the FCC to HCP phase transformation. In confined Co thin films in the reduced $\text{Ni}_k\text{Co}_{1-x}\text{O/ZrO}_2(\text{CaO})$, this propagation is very limited to very few number of

perfect dislocations and therefore the phase transformation is significantly hindered upon cooling this composite.

Further studies in the reduced $\text{Ni}_{0.5}\text{Co}_{0.5}\text{O}/\text{ZrO}_2(\text{CaO})$ composite show characteristics of local deformation in the Ni(Co) metallic interphase after reduction. Figure 3.15 presents examples of the deformation in the Ni(Co) solid solution interphase. This figure shows twinning formation in Ni(Co) interphase to have occurred upon reduction. A much lower twin density, however, is observed in the Ni(Co) interphase compared to that of the Co interphase. Dislocation formation is another microstructural feature that is observed in the Ni(Co) interphase after reduction. Ni(Co) interphases also show a significantly less number of stacking faults in Ni(Co) compared to the purely Co interphases.

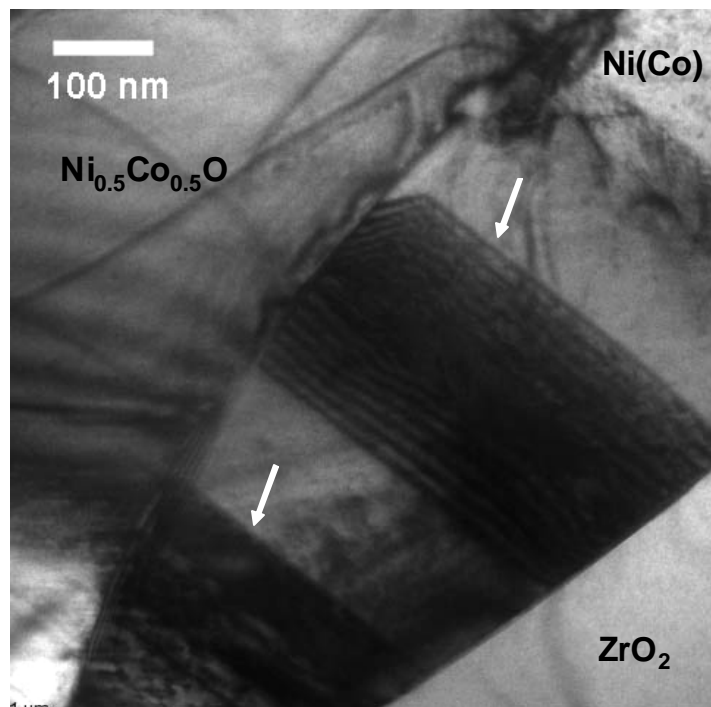


Figure 3.15 Bright field TEM image of the reduced $\text{Ni}_{0.5}\text{Co}_{0.5}\text{O}/\text{ZrO}_2$ phase showing deformation in the Ni(Co) phase through formation of twins in the Ni(Co). (Indicated with arrows on the figure)

It has been previously shown that addition of Ni to Co increases the stacking fault energy of Co.^{112, 122, 123} Figure 3.16 (a) and (b) both show the Ni-rich and the Co-rich sides of the Ni-Co composition alloy and indicate the rise in the stacking fault energy of Co upon addition of Ni. As a result of this rise in the energy, deformation through formation of dislocations becomes a more dominant mechanism in Ni(Co) solid solution alloys compared to pure Co.¹²⁴ The TEM observations of the microstructural characteristics in the Ni(Co) and Co interphases in this model system show that presence of Ni in the ductile interphase gives rise to dislocation formation as a more prominent deformation mechanism in this DSE series.

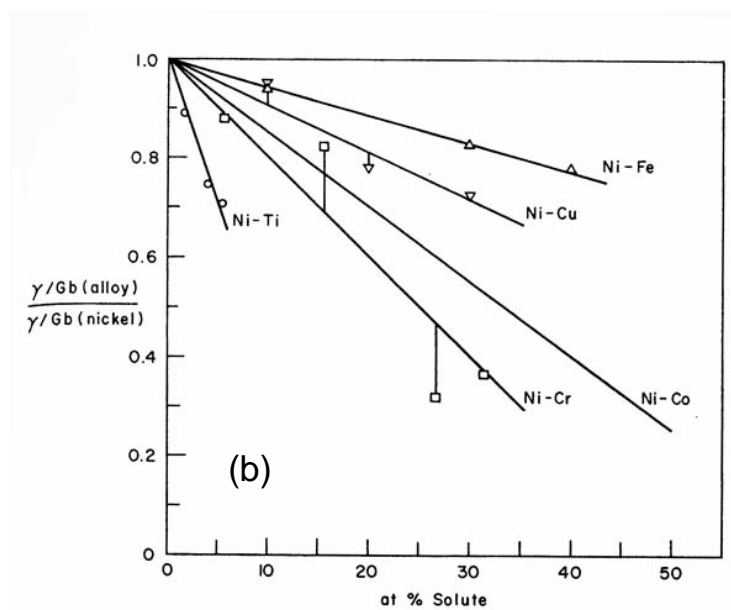
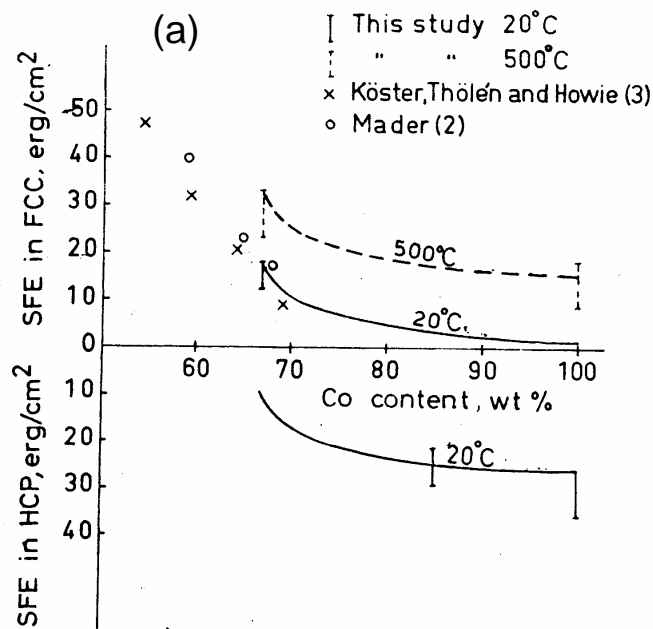


Figure 3.16 Stacking fault energy variations across the composition in the Ni-Co alloy. (a) Stacking fault energy change in the Co rich Ni-Co alloys¹²² and (b) Changes in the stacking fault energy ratio of Ni and the solute elements in the Ni rich alloys.¹²⁵

3.2.4 Interfacial Structure of the Reduced $\text{Ni}_x\text{Co}_{1-x}\text{O}/\text{ZrO}_2(\text{CaO})$ Model System

The experiments conducted on the reduced DSEs in this study confirm the early studies on the orientation relationship in the pristine $\text{Ni}_x\text{Co}_{1-x}\text{O}/\text{ZrO}_2(\text{CaO})$ where (111) planes of the transition metal oxide are parallel with (200) planes of $\text{ZrO}_2(\text{CaO})$ in the pristine DSE samples.⁸⁷⁻⁸⁹

Electron microscopy studies for the interfacial orientation relationship between the metal and the transition metal oxide show (hkl) planes of the metallic interphase to be parallel with (hkl) planes of the transition metal oxide in many areas of the composite. This means the same set of interfacial planes in the metallic interphase and the transition metal oxide exist across the $\text{Ni}_x\text{Co}_{1-x}\text{O}-\text{Ni}(\text{Co})$ interface. Figure 3.17 shows a SAD pattern from $\text{Ni}(\text{Co})-\text{Ni}_{0.5}\text{Co}_{0.5}\text{O}$ interface that indicates the interfacial orientation relationship between the metallic interphase and the transition metal oxide. This diffraction pattern shows the $[\bar{1}\bar{1}\bar{1}]$ planes of the metallic $\text{Ni}(\text{Co})$ to be parallel with the $[\bar{1}\bar{1}\bar{1}]$ planes of the $\text{Ni}_{0.5}\text{Co}_{0.5}\text{O}$ phase, indicating a twinned microstructure of the metallic interphase with respect to the transition metal oxide along the $\text{Ni}(\text{Co})-\text{Ni}_{0.5}\text{Co}_{0.5}\text{O}$ interface. This particular orientation relationship has also been shown by Dickey *et al.*¹²⁶, where they observed metallic Ni to form a twinned orientation with respect to the (111) interfacial plane of the NiO phase upon *in-situ* reduction of $\text{NiO}/\text{ZrO}_2(\text{CaO})$ composite inside the microscope.

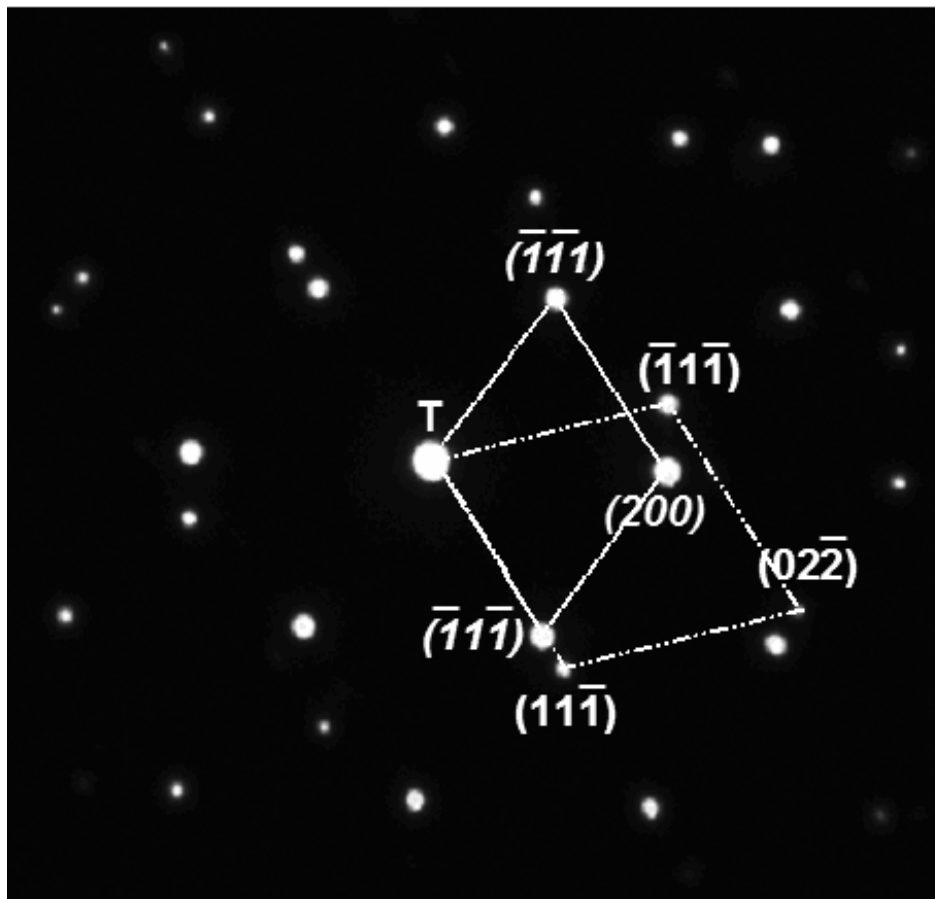


Figure 3.17 SAD pattern from the Ni(Co)-Ni_{0.5}Co_{0.5}O interface where the $\langle 111 \rangle$ planes of the metallic Ni(Co) are parallel with the $\langle 111 \rangle$ planes of the Ni_{0.5}Co_{0.5}O phase. The reflections from the Ni_{0.5}Co_{0.5}O phase are shown in solid lines and with italic font on the image.

Other low-indexed orientation relationships frequently observed between the metallic interphase and the transition metal oxide in this experiment are as:

$$\langle 100 \rangle \text{Ni}_x\text{Co}_{1-x}\text{O} \parallel \langle 112 \rangle \text{Ni(Co) or Co}$$

$$\langle 100 \rangle \text{Ni}_x\text{Co}_{1-x}\text{O} \parallel \langle 110 \rangle \text{Ni(Co) or Co}$$

It should be noted that many areas of the sample show a few degrees misorientation on the order of 2 to 10 degrees between the metallic interphase and the transition metal oxide from the exact edge-on position. This misorientation has also been reported by Laguna-Bercero *et al.* in the fully reduced samples of NiO/ZrO₂ and CoO/ZrO₂.¹⁰⁵ Further studies are required to investigate the origin of this small misorientation in the sample after its reduction. It is worth noting that besides the above orientation relationships in the metal-oxide interfaces, the interphase does not always maintain a low index crystallographic orientation relationship with the adjacent phase. This condition is particularly observed in the poly-crystalline areas of the metallic interphase where each grain maintains a random orientation relationship with the neighboring ceramic phases.

Figure 3.18 shows a high resolution TEM image of the interface between the ZrO₂(CaO) and Ni(Co) interphase, indicating the (200) planes of Ni(Co) to be parallel with (200) planes of ZrO₂(CaO). This image shows presence of clean interfaces without any interlayer or compound between the metallic interface and the ZrO₂(CaO) phase. This particular orientation relationship has been previously observed by Dickey *et al.*¹²⁷, where they deposited a thin film of Ni on YSZ. Their investigations indicate a cube-on-cube orientation relationship where the (200) interfacial planes of Ni are parallel with the (200) interfacial planes of YSZ. Observation of the same low-indexed interfacial planes between the metallic interphase and ZrO₂ in two different experimental conditions with different processing methods suggests this interfacial orientation relationship to be a low energy interfacial plane between the metal and the ZrO₂ phase.

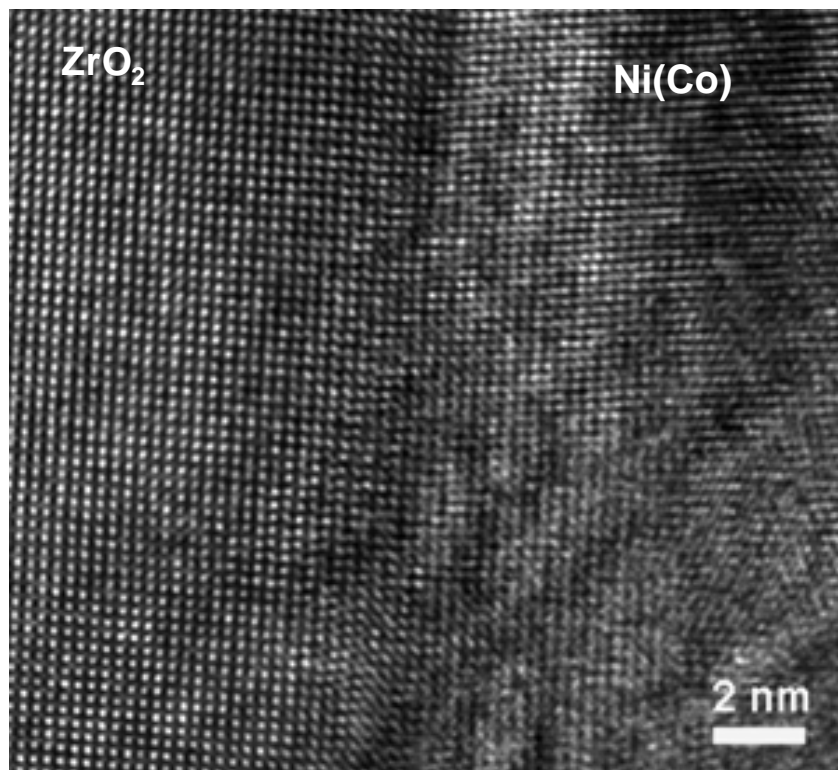


Figure 3.18 HREM image of the Ni(Co)-ZrO₂ interface indicating presence of clean interfaces without any inter-layer or compound in the reduced composite.

3.2.5 Evolution of Residual Stresses in the Reduced Ni_xCo_{1-x}O/ZrO₂(CaO)

Model System

Any phase transformation can lead to the stress generation in composite or alloy systems.¹²⁸⁻¹³⁰ Reduction of the Ni_xCo_{1-x}O/ZrO₂(CaO) model system is considered a phase transformation upon which Ni_xCo_{1-x}O is transformed into its metal counterpart. This transformation is accompanied by several aspects including cracking of the composite (mainly in the fully reduced region), formation of the interfacial porosity,

creep of the $\text{Ni}_k\text{Co}_{1-x}\text{O}$ phase (Figure 3.19), and the plastic deformation within the metallic interphase during the reduction process at high temperatures. Figure 3.19 shows local deformation in the reduced $\text{Ni}_k\text{Co}_{1-x}\text{O}/\text{ZrO}_2(\text{CaO})$ composite through formation of dislocations in the $\text{Ni}_{0.5}\text{Co}_{0.5}\text{O}$ phase. Figure 3.20 shows another region in the reduced $\text{Ni}_k\text{Co}_{1-x}\text{O}/\text{ZrO}_2(\text{CaO})$ sample, where dislocations in the transition metal oxide phase mostly originate from the metal-oxide interface into the $\text{Ni}_k\text{Co}_{1-x}\text{O}$ phase. Deformation of the $\text{Ni}_k\text{Co}_{1-x}\text{O}$ phase after reduction could be an indication of possible relaxation of thermal residual stresses within the system at high temperatures during the reduction process.

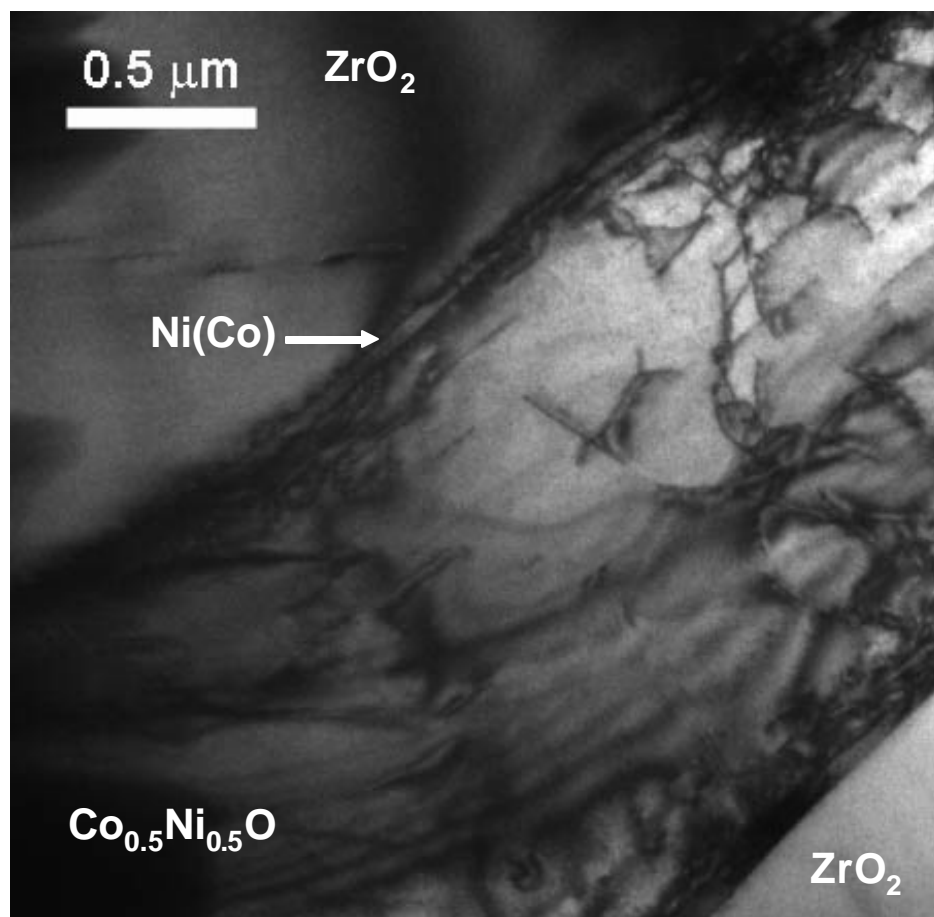


Figure 3.19 Formation of dislocations in the $\text{Ni}_x\text{Co}_{1-x}\text{O}$ phase after the reduction process

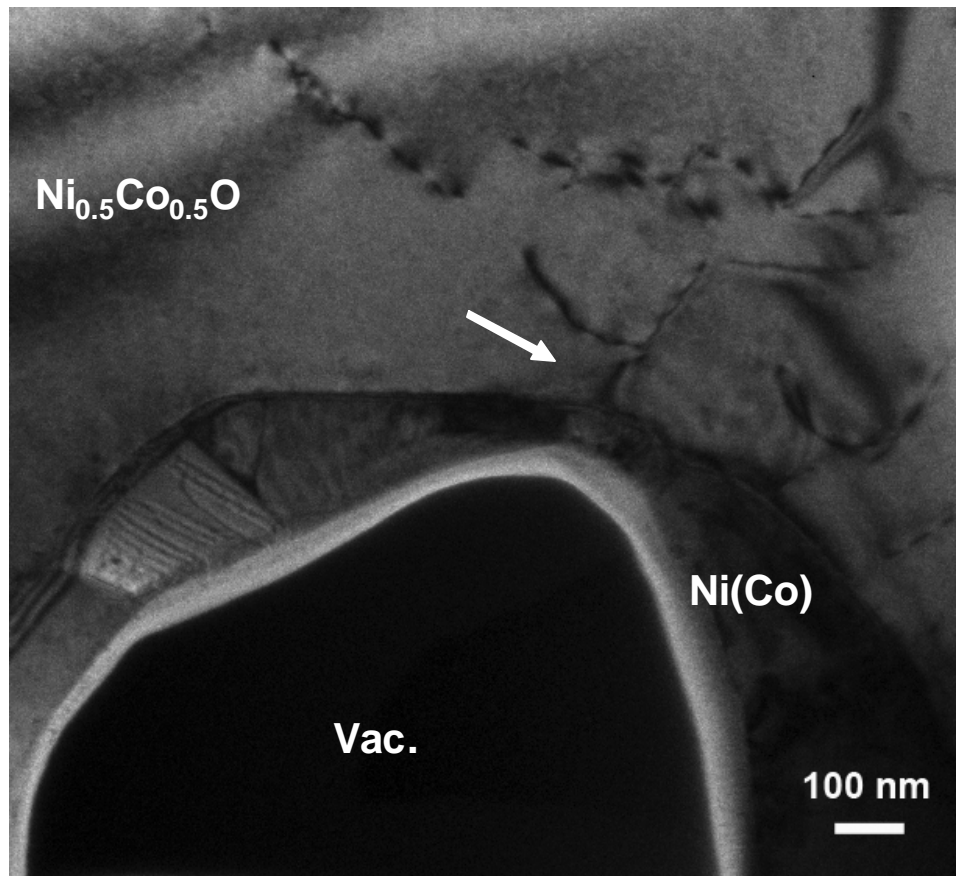


Figure 3.20 Dark field TEM images of the reduced $\text{Ni}_{0.5}\text{Co}_{0.5}\text{O}/\text{ZrO}_2$ phase showing deformation through dislocation formation in the $\text{Ni}_{0.5}\text{Co}_{0.5}\text{O}$ originating from the $\text{Ni}(\text{Co})$ - $\text{Ni}_{0.5}\text{Co}_{0.5}\text{O}$ interface (indicated with arrows on the figure).

To explain deformation after chemical reduction of the sample, it is important to understand the effect of reduction on the microstructure first. Reduction process in the pristine $\text{Ni}_k\text{Co}_{1-x}\text{O}/\text{ZrO}_2(\text{CaO})$ composite takes place at $800\text{ }^\circ\text{C}$ leading to the formation of FCC Co and Ni(Co) metallic interphase, oxygen depletion, phase shrinkage and porosity formation in the composite.¹³¹ $\text{Ni}_k\text{Co}_{1-x}\text{O}$ and the metallic interphase both have active slip systems at $800\text{ }^\circ\text{C}$ and are amenable to plastic deformation to accommodate

for the phase transformation and the phase shrinkage in the composite. Deformation observed in the $\text{Ni}_x\text{Co}_{1-x}\text{O}$ is likely to be the result of reduction process and the volume shrinkage at 800 °C, since dislocation and twinning formation during reduction are geometrically necessary to accommodate for the shrinkage and porosity formation in the composite. An example of this situation has been shown in Figure 3.21. This figure indicates twinning formation in Ni(Co) adjacent to the porosity which suggests the volume shrinkage to have been the motive for twinning in this region.

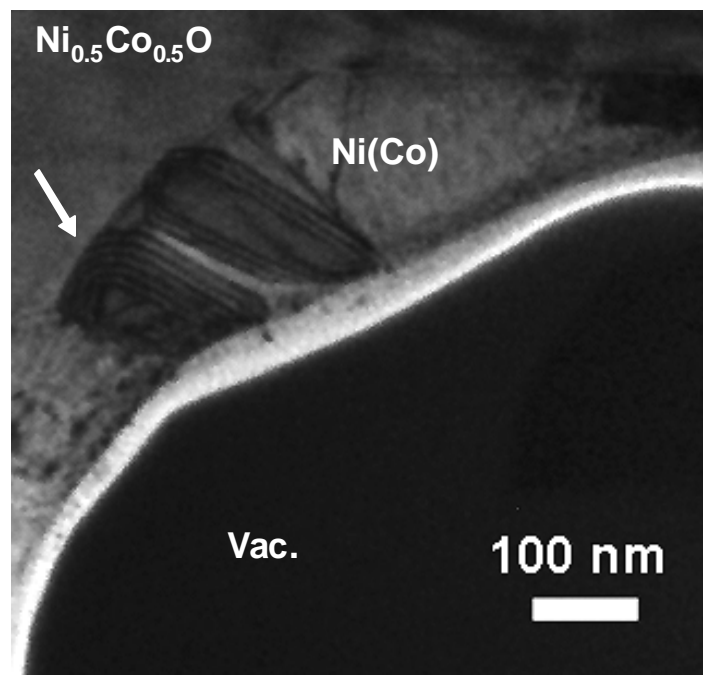


Figure 3.21 Bright field TEM image of the reduced CoO/ZrO_2 composite showing twinning formation in the Ni(Co) interphase adjacent to the porosity (Indicated with arrows on the figure).

After reduction and upon cooling the system to lower temperatures, thermal residual stresses may start to develop in the system due to the coefficient of thermal

expansion (CTE) mismatch between the phase components in the reduced $\text{Ni}_x\text{Co}_{1-x}\text{O}/\text{ZrO}_2(\text{CaO})$ composite. To understand the role of thermal stresses on the deformation of the system, it is important to consider the mismatch in the coefficient of thermal expansion (CTE) of the phase components in this composite. Table 3.1 indicates the CTE values previously measured for the Ni, Co, $\text{Ni}_x\text{Co}_{1-x}\text{O}$ and $\text{ZrO}_2(\text{CaO})$ phases.^{85, 132, 133} Considering the rule of mixtures to be applicable for the CTE value for the Ni(Co) solid solution interphase, the thermal expansion mismatch for the adjacent metal-ceramic phases in the reduced $\text{Ni}_x\text{Co}_{1-x}\text{O}/\text{ZrO}_2$ are calculated and given in Table 3.2. The mismatch values in Table 3.2 were calculated according to Equation 3.2. According to this Table large CTE mismatch values exist between the metal- $\text{Ni}_x\text{Co}_{1-x}\text{O}$ interface compared to that of the metal- ZrO_2 interface. This large mismatch in the CTE values could be the origin of deformation through dislocation formation at the $\text{Ni}_x\text{Co}_{1-x}\text{O}$ -metal interface upon cooling.

$$\text{CTE mismatch} = \frac{\text{CTE}(\text{Ni}_x\text{Co}_{1-x}\text{O}) - \text{CTE}(\text{Ni}(\text{Co}))}{\text{CTE}(\text{Ni}(\text{Co}))} \cdot 100 \quad 3.2$$

| Phase | Ni ¹³² | Co ¹³² | CoO ⁸⁵ | Ni _{0.5} Co _{0.5} O ⁸⁵ | ZrO ₂ (CaO) ¹³³ |
|-----------|-----------------------|-----------------------|-----------------------|---|---------------------------------------|
| CTE (1/K) | 10.8×10^{-6} | 10.7×10^{-6} | 14.4×10^{-6} | 15.8×10^{-6} | 10.3×10^{-6} |

Table 3.1 Coefficient of thermal expansion values of Ni, Co, $\text{Ni}_x\text{Co}_{1-x}\text{O}$ and $\text{ZrO}_2(\text{CaO})$.^{85, 132, 133}

| Interface | Ni(Co)- Ni _{0.5} Co _{0.5} O | Co-CoO | ZrO ₂ -Co | ZrO ₂ -Ni(Co) |
|-----------------|--|--------|----------------------|--------------------------|
| CTE Mismatch | 40% | 45% | 3.9% | 4.4% |

Table 3.2 Thermal expansion mismatch values between the adjacent metal-ceramic interfaces in the reduced composite.

Since Ni_kCo_{1-x}O phase still has active slip systems till about 500 °C^{91, 92} the thermal elastic strain developed upon cooling may continue to relax through plastic deformation in the oxide phase upon cooling down to this temperature. To have an estimate about the generated thermal strain in the Ni_kCo_{1-x}O phase upon cooling equation 3.3 is considered.

$$\epsilon = \alpha(\Delta T) \quad 3.3$$

Where ϵ is the thermal strain generated upon cooling, α is the coefficient of thermal expansion and ΔT is the temperature drop upon cooling in this equation. Since there are active slip systems operating within Ni_kCo_{1-x}O phase upon cooling until 500 °C, we calculate the thermal strain from 800 °C to 500 °C. According to equation 3.3, the thermal strain developed within the Ni_kCo_{1-x}O is estimated to be about 0.47% for CoO and 0.45% for Ni_{0.5}Co_{0.5}O upon cooling from 800 °C to 500 °C. This level of strain is quite high to cause yielding in ceramics. Also the nature of the interfaces in the pristine Ni_kCo_{1-x}O/ZrO₂ significantly changes upon reduction of the system. Pristine

$\text{Ni}_k\text{Co}_{1-x}\text{O}/\text{ZrO}_2(\text{CaO})$ DSEs have been previously characterized as an ionic system composed of a set of cation-anion planes alternatively sequenced with a common oxygen plane at their interface.⁸⁷ The strongly bonded interfaces in the pristine $\text{Ni}_k\text{Co}_{1-x}\text{O}/\text{ZrO}_2(\text{CaO})$ DSE system help the load transmit from one phase to the other, leading to significant levels of thermal residual stresses.^{20, 90} After reduction in contrast a ductile metallic interphase protrudes the ceramic oxide phases, leading to significant changes in the interfacial structure of the composite. As a result of this microstructural evolution, relaxation through plastic deformation can continue within the $\text{Ni}_k\text{Co}_{1-x}\text{O}$ phase upon cooling the system.

Upon further cooling to room temperature, the system may develop a new stress state in itself, since less active slip systems are available in the $\text{Ni}_k\text{Co}_{1-x}\text{O}$ phase. Further studies are needed to investigate the evolution of the residual stresses in the reduced $\text{Ni}_k\text{Co}_{1-x}\text{O}/\text{ZrO}_2(\text{CaO})$ composites upon reduction.

3.2.6 Summary and Conclusions

This chapter has experimentally investigated the possibility of the formation of ceramic composites with confined metallic interphases (thickness ~ 50-300 nm) mediating the oxide interfaces in $\text{Ni}_k\text{Co}_{1-x}\text{O}/\text{ZrO}_2(\text{CaO})$ DSEs upon chemical reduction. Distributed interfacial porosity and shrinkage cracks are other microstructural changes that take place in the system due to the formation of oxygen vacant sites after reduction of the oxide component.

Various electron microscopy techniques were utilized to investigate the crystallography, microstructure and chemistry of the system after its reduction. The

chemical and structural characterization of reduced $\text{Ni}_x\text{Co}_{1-x}\text{O}/\text{ZrO}_2(\text{CaO})$ composite model system shows formation of nanoscale metallic interphases of FCC Ni(Co) and Co with the interface thickness of about 2 nm with respect to the adjacent ceramic oxide layers. The electron microscopy studies on the metal-oxide interfaces indicate presence of clean interfaces without any inter-layer or compound. The interfacial orientation relationship in this composite indicates the system to maintain low energy interfaces between the adjacent metal-ceramic layers.

The phase transformation in this model system also leads to characteristics of deformation within the ductile interphase as well as the transition metal oxide layer. The deformation observed after reduction is believed to be the result of the volume shrinkage as well as the residual stress relaxation in the system during reduction at high temperatures.

4 CRACK PROPAGATION BEHAVIOR OF $\text{Ni}_x\text{Co}_{1-x}\text{O}/\text{ZrO}_2(\text{CaO})$ COMPOSITE WITH A NANOSCALE METALLIC INTERPHASE

Interfacial fracture phenomena in $\text{Ni}_x\text{Co}_{1-x}\text{O}/\text{ZrO}_2(\text{CaO})$ DSE composites have been extensively studied by various researchers.^{10, 17, 20, 86, 87} These investigations have pointed to the competition between the interfacial crack penetration and the interfacial delamination as a function of composition in this DSE series. The competition between the interfacial crack penetration and the interfacial delamination along the interface is one of the key points to the toughening enhancement in oxide-oxide DSE composites. Previous studies have shown various DSE systems to show brittle fracture through interfacial penetration as their dominant fracture mechanism. DSE composites such as NiO/ZrO_2 , YAG/alumina and alumina/zirconia are considered to be within this group.^{9, 19, 86, 134, 135} Little toughening has been observed to occur through crack bridging and crack deflection in some DSE systems such as $\text{LaB}_6/\text{ZrB}_2$, while other DSE systems like CoO/ZrO_2 have shown considerable toughening through significant crack deflection and secondary crack formation.^{10, 84, 136}

Brewer *et al.*¹⁷ have previously studied the interfacial fracture phenomena in a $\text{Ni}_x\text{Co}_{1-x}\text{O}/\text{ZrO}_2(\text{CaO})$ model system as a function of composition to explore the role of plasticity and strain energy absorption in this DSE model system. Their studies show a significant change in the deformation and fracture behavior across the DSE series from rich NiO to rich CoO composite series.^{9, 10, 84}

This chapter explores the deformation and fracture behavior of $\text{Ni}_x\text{Co}_{1-x}\text{O}/\text{ZrO}_2(\text{CaO})$ DSE composites upon formation of a nanoscale ductile interphase through chemical reduction of this system. A Vickers indentation technique is used to

investigate the crack propagation behavior of the composite and the role of the nanoscale ductile interphases on the toughening enhancement of the system. The chapter further evaluates the extent of strain energy absorption within the ductile interphases through assessment of the small scale plasticity and hardness across the reduced $\text{Ni}_x\text{Co}_{1-x}\text{O}/\text{ZrO}_2(\text{CaO})$ DSE interfaces.

4.1 Experimental Procedures

4.1.1 Vickers Indentation Test

$\text{Ni}_x\text{Co}_{1-x}\text{O}/\text{ZrO}_2(\text{CaO})$ DSE composites have been previously grown into a eutectic structure using the optical floating zone method.¹⁷ Two different compositions of $\text{Ni}_x\text{Co}_{1-x}\text{O}/\text{ZrO}_2(\text{CaO})$ DSEs, $\text{Ni}_{0.5}\text{Co}_{0.5}\text{O}/\text{ZrO}_2(\text{CaO})$ with ($x=0.5$) and $\text{CoO}/\text{ZrO}_2(\text{CaO})$ with ($x=0$), which show different plasticity levels and dissimilar fracture mechanisms^{10, 17, 84, 85}, have been chosen to study the deformation and fracture behavior of the system after its reduction. Vickers indentation tests were carried out to study the deformation and crack propagation behavior of the $\text{Ni}_x\text{Co}_{1-x}\text{O}/\text{ZrO}_2(\text{CaO})$ system in the pristine/as-grown and reduced form to understand the role of nanoscale ductile interphases on the interfacial fracture phenomena in this composite.

The formerly grown samples of $\text{Ni}_x\text{Co}_{1-x}\text{O}/\text{ZrO}_2(\text{CaO})$ were cut into disks of approximately 500 μm thickness using a wire saw from their single crystal rod. Pristine and reduced $\text{Ni}_x\text{Co}_{1-x}\text{O}/\text{ZrO}_2(\text{CaO})$ samples were prepared in two batches for the Vickers indentation test. The reduced $\text{Ni}_x\text{Co}_{1-x}\text{O}/\text{ZrO}_2(\text{CaO})$ samples were prepared through chemical reduction of this composite to form nanoscale metallic Ni(Co) and Co interphases in the microstructure. The details of the chemical reduction are described in

section 3.1.1 of this thesis. After the chemical reduction, the reduced $\text{Ni}_x\text{Co}_{1-x}\text{O}/\text{ZrO}_2(\text{CaO})$ samples were further polished at the top surface to remove the fully reduced region and to reach the partially reduced area of the composite. Polishing at the top surface was continued using 3 μm diamond film followed by 0.05 μm colloidal silica suspension to further remove the small scratches from the surface of the sample. To prepare the pristine batch, $\text{Ni}_x\text{Co}_{1-x}\text{O}/\text{ZrO}_2(\text{CaO})$ samples were polished at the top surface in the same manner as the reduced samples to create a fine surface finish in the composite prior to Vickers indentation test.

After sample preparation, the fully oxidized and partially reduced $\text{Ni}_x\text{Co}_{1-x}\text{O}/\text{ZrO}_2(\text{CaO})$ composites were indented at the top surface using a diamond-tip micro-indenter (Beuhler, Micromet®II Microhardness Tester). A load of 10 N was applied to the polished samples of fully oxidized and partially reduced composites for 20 seconds and under identical test conditions. Hitachi S-4500 scanning electron microscope was used to study the crack propagation and fracture behavior of the pristine and reduced composites upon Vickers indentation.

4.1.2 Nano-Indentation Test

To estimate the extent of plasticity and local hardness in the reduced model system, nano-indentation experiments were performed on the pristine and reduced $\text{Ni}_{0.5}\text{Co}_{0.5}\text{O}/\text{ZrO}_2(\text{CaO})$ composite DSEs. The samples were first prepared according to the sample preparation procedures described in section 4.1.1. The final polishing step using the 0.05 μm colloidal silica suspension helped with removal of the micro scratches and helped minimize the surface step at the interfaces between the metal-ceramic and the

ceramic-ceramic phases in the reduced and pristine composite. After polishing, the samples were attached to the magnetic puck using the instant adhesive (Mascot American item#12.214) and were then transferred to the Hysitron Tribo-Indenter instrument.

Since the purpose of this experiment is to mainly evaluate the mechanical response of the lamellae across the interfaces, it is important for the indentation marks not to overlap with each other. To meet this requirement, a cube corner diamond nano-indentation tip, with 90 degrees total angle was selected for this experiment. Since this tip has sharper angles and higher aspect ratio compared with the Berkovich tip, the resulting radius of the curvature for this tip (about 100-200 nm) is much smaller than that of the Berkovich tip. This geometry makes the cube corner tip a preferred choice for the assessment of local plasticity and deformation in small confined volumes. Using the cube corner tip indentations from 100 μN to 700 μN were first made to measure the size of the indents for the given load. For the measurements performed here a maximum load of 200 μN , which would give final displacement of about 20-30 nm in the metallic interphase was chosen. To achieve accurate hardness values tip area function calibrations were first performed using a standard Quartz sample before starting the actual experiment. After calibration, a set of indents with 200 μN load and about 150-200 nm minimum spacing were made across the metal-ceramic and ceramic-ceramic interfaces in the reduced and pristine $\text{Ni}_{0.5}\text{Co}_{0.5}\text{O}/\text{ZrO}_2(\text{CaO})$ sample.

4.2 Interfacial Fracture Phenomena in the Pristine and Reduced $\text{Ni}_x\text{Co}_{1-x}\text{O}/\text{ZrO}_2(\text{CaO})$ DSEs

Reduced $\text{Ni}_x\text{Co}_{1-x}\text{O}/\text{ZrO}_2(\text{CaO})$ shows enhanced energy dissipative mechanisms through plastic deformation, interfacial delamination, crack arrest and crack bridging across the metallic interphase compared to its fully oxidized state upon Vickers indentation. This enhancement is observed across all the chemically reduced $\text{Ni}_x\text{Co}_{1-x}\text{O}/\text{ZrO}_2(\text{CaO})$ DSE series. This enhancement is more significant in the pristine NiO-rich samples ($x > 0.3$), where the dominant fracture mechanism in the pristine composite indicates a brittle fracture through interfacial crack penetration.^{10, 84}

Figure 4.1 presents the mechanical response of the pristine and reduced $\text{CoO}/\text{ZrO}_2(\text{CaO})$ system ($x=0$) after Vickers indentation test. Figure 4.1a shows the fracture mechanism in the pristine $\text{CoO}/\text{ZrO}_2(\text{CaO})$ system with a mixed ductile-brittle fracture mode. This composite shows some toughening mechanisms, i.e. interfacial delamination and nucleation of secondary cracks, to operate in the composite, while unperturbed cracks emanating from the indent and propagating through the $\text{CoO}-\text{ZrO}_2(\text{CaO})$ interfaces still indicate brittle fracture of this system after indentation. The arrows on figure 4.1a indicate the sharp cracks propagating from the indentation mark in the sample. The indentation experiments recently performed on single crystal CoO and the $\text{CoO}/\text{ZrO}_2(\text{CaO})$ composite have shown limited plasticity of CoO at room temperature.^{10, 17} Earlier studies on CoO have also shown limited plasticity of this phase due to the activation of $\{100\} \langle 110 \rangle$ slip system at room temperatures.⁹¹ Brewer *et al.* have previously investigated the deformation mechanism of the pristine $\text{CoO}/\text{ZrO}_2(\text{CaO})$ composite and have suggested plastic dissipation within CoO to take place through

dislocation pile-up and interfacial crack delamination from CoO (elastoplastic) to $\text{ZrO}_2(\text{CaO})$ (elastic) phase upon indentation of this composite.¹⁷ These studies attributed the interfacial delamination at the CoO- $\text{ZrO}_2(\text{CaO})$ interface to the presence of active slip systems in CoO leading to the nucleation of ZSK (Zener-Stroh-Koehler) cracks at the CoO- $\text{ZrO}_2(\text{CaO})$ interface.^{17, 137}

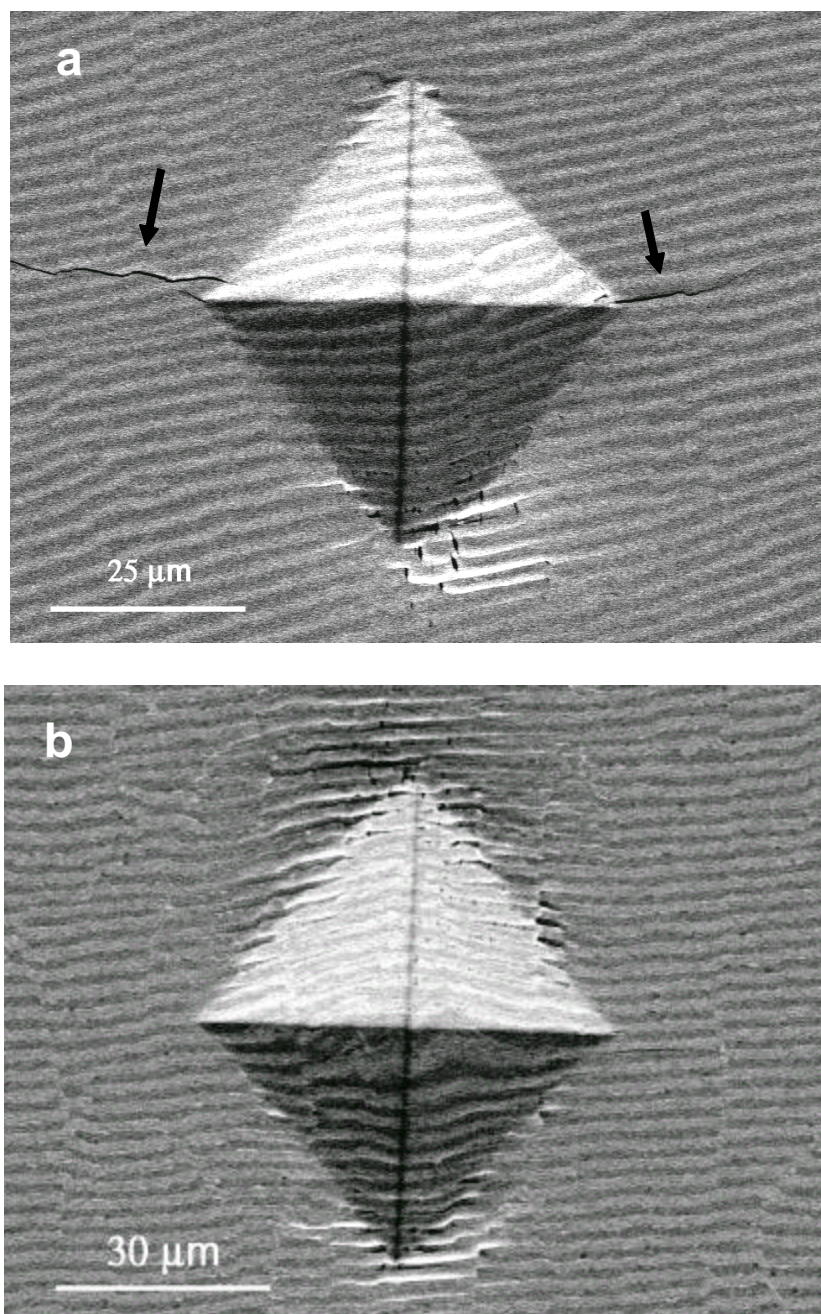


Figure 4.1 Deformation and fracture behavior of the CoO/ZrO₂(CaO) composite in the (a) pristine and (b) reduced form upon the Vickers indentation test.

Figure 4.1b indicates the deformation and fracture behavior of the reduced CoO/ZrO₂(CaO) system after formation of the nanoscale metallic Co interphases mediating CoO and ZrO₂(CaO). According to this figure the reduced CoO/ZrO₂(CaO) system does not show any signs of brittle fracture after formation of nanoscale metallic Co interphases, which indicates further contribution of nanoscale metallic Co interphases into the toughening enhancement of this system. Figure 4.2 clearly shows this contribution on the crack propagation behavior of the reduced CoO/ZrO₂(CaO) composite. According to Figures 4.1 and 4.2 nanoscale Co interphases can further enhance the deformation behavior of this system through plastic deformation, crack arrest, crack bridging across the Co interphase, and interfacial crack delamination.

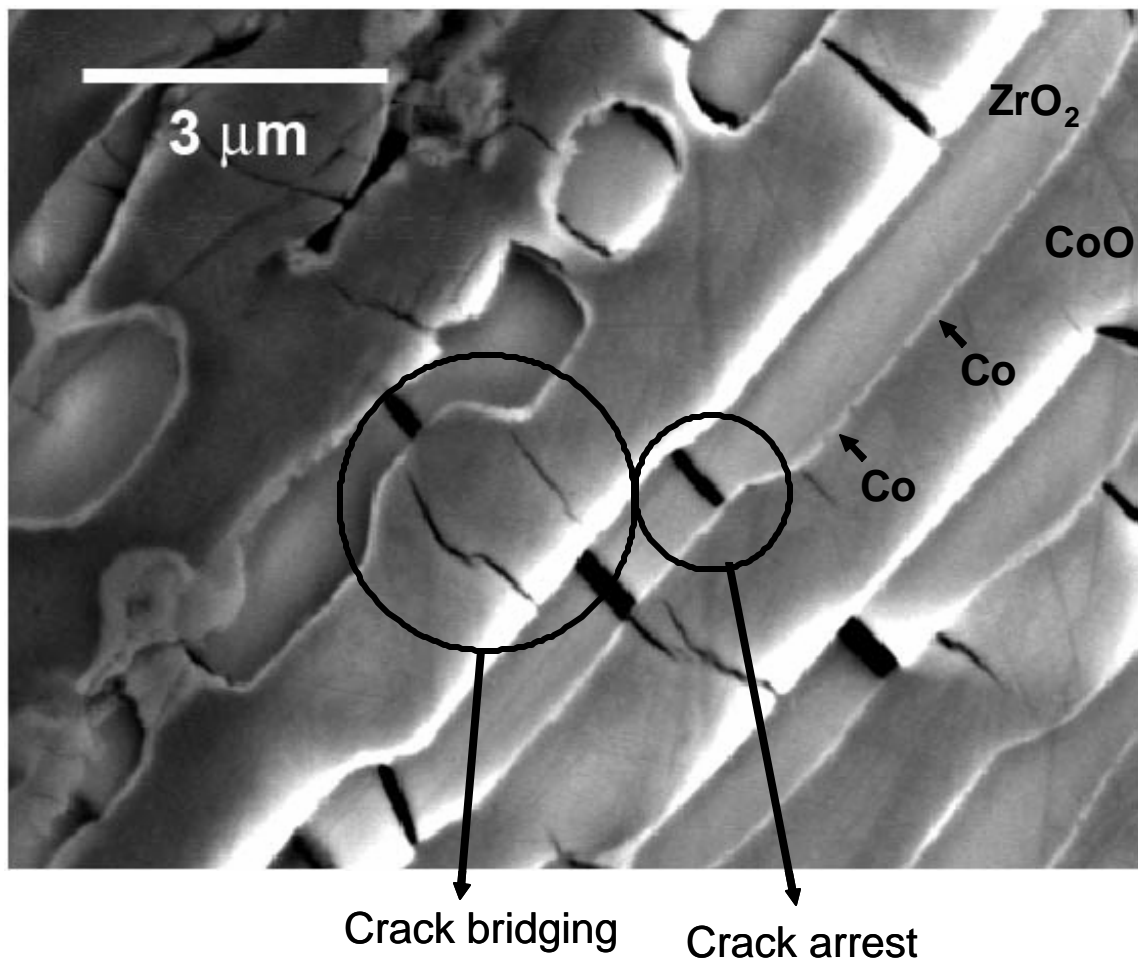


Figure 4.2 Deformation behavior of the reduced CoO/ZrO₂(CaO) adjacent to the Vickers indentation mark.

Figure 4.3 shows the deformation and fracture behavior in the fully oxidized and partially reduced Ni_{0.5}Co_{0.5}O/ZrO₂(CaO) system upon Vickers indentation testing of this composite. Figure 4.3a presents brittle fracture behavior in the pristine/as-grown Ni_{0.5}Co_{0.5}O/ZrO₂(CaO) system through the propagation of unperturbed cracks originating from the indent. Deformation and fracture behavior in pristine/as-grown

$\text{Ni}_x\text{Co}_{1-x}\text{O}/\text{ZrO}_2(\text{CaO})$ series have been previously studied by Brewer *et al.*¹⁷ This study indicates a brittle fracture behavior in the NiO rich samples ($x > 0.33$) in the $\text{Ni}_x\text{Co}_{1-x}\text{O}/\text{ZrO}_2(\text{CaO})$ composite series through interfacial penetration. The deformation and fracture mechanism in this system has been attributed to the nucleation of CK (Cottrell-Keh) crack in NiO rich phases which leads to the interfacial crack penetration in these DSE systems at room temperatures.^{17, 138} Figures 4.3b and 4.3c show deformation and fracture behavior of the reduced $\text{Ni}_{0.5}\text{Co}_{0.5}\text{O}/\text{ZrO}_2(\text{CaO})$ composite upon Vickers indentation of this sample under identical conditions. According to these figures, in the reduced $\text{Ni}_{0.5}\text{Co}_{0.5}\text{O}/\text{ZrO}_2(\text{CaO})$ composite, interfacial crack penetration is completely eliminated and other toughening mechanisms, i.e. interfacial delamination, crack arrest and crack bridging, start to operate in the system.

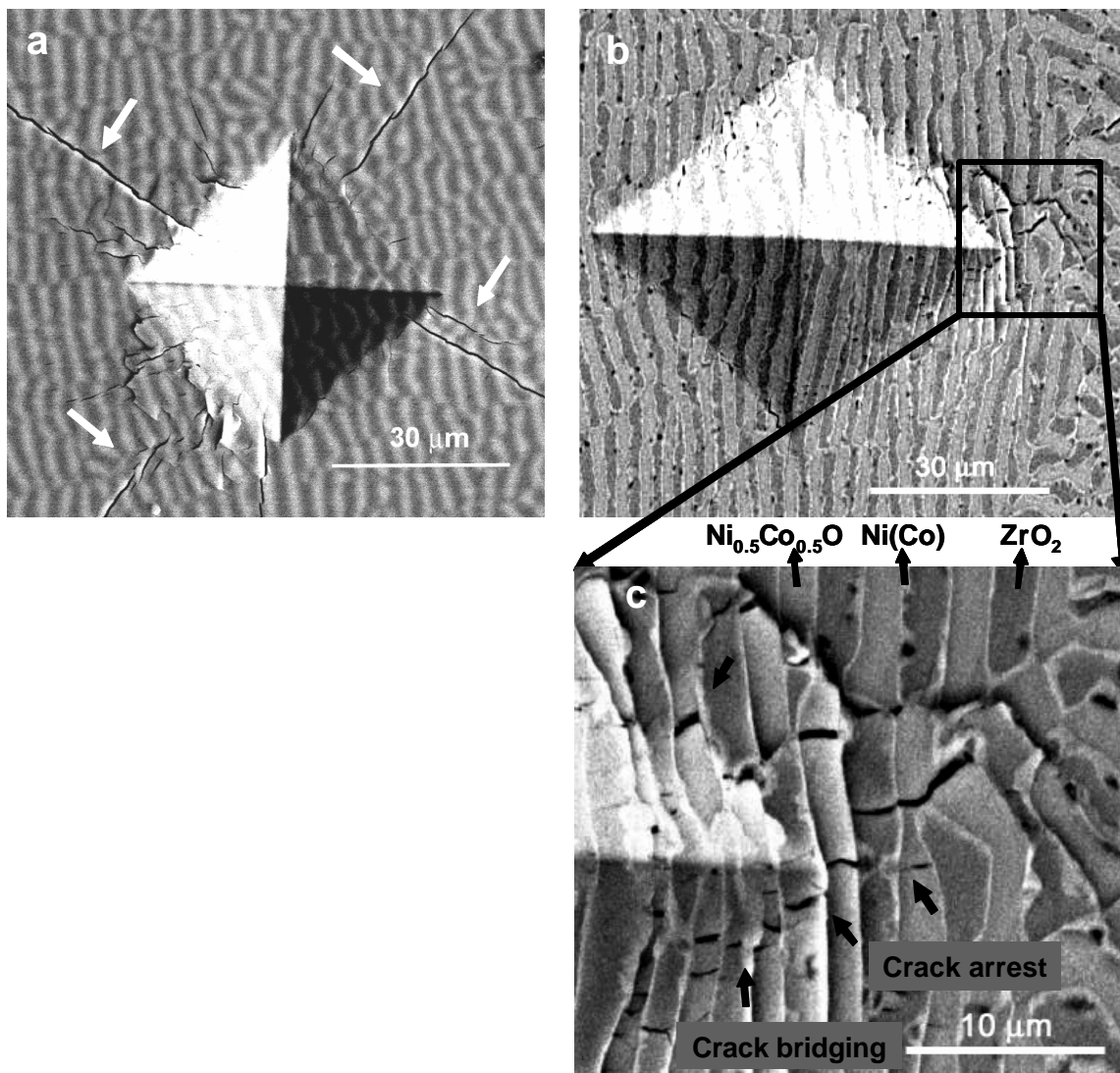


Figure 4.3 Deformation and fracture behavior in the $\text{Ni}_{0.5}\text{Co}_{0.5}\text{O}/\text{ZrO}_2(\text{CaO})$ system upon Vickers indentation showing (a) sharp cracks in the pristine/as-grown DSE system (cracks are shown with arrows) and (b & c) interfacial delamination, crack arrest and crack bridging across the metallic interphase in the partially reduced composites (shown with arrows on the (c)).

Figures 4.4 and 4.5 present the dominant deformation mechanisms operating adjacent to the indentation mark in the reduced $\text{Ni}_{0.5}\text{Co}_{0.5}\text{O}/\text{ZrO}_2(\text{CaO})$ composite.

According to these figures interfacial delamination from Ni(Co) interphase to $\text{ZrO}_2(\text{CaO})$, formation of secondary cracks, crack arrest and crack bridging across the metallic interphase are observed to significantly contribute to the toughening enhancement of the composite upon its deformation. These observations show nucleation of secondary cracks in both $\text{Ni}_{0.5}\text{Co}_{0.5}\text{O}$ and $\text{ZrO}_2(\text{CaO})$ phases, while interfacial delamination mainly takes place from metallic Ni(Co) phase to $\text{ZrO}_2(\text{CaO})$ if moving away from the indent in this composite. Crack arrest and crack bridging across the metallic Ni(Co) interphase are other toughening mechanisms that operate upon indentation in this system which point to the important role of the metallic interphases in the strain energy absorption in this composite.

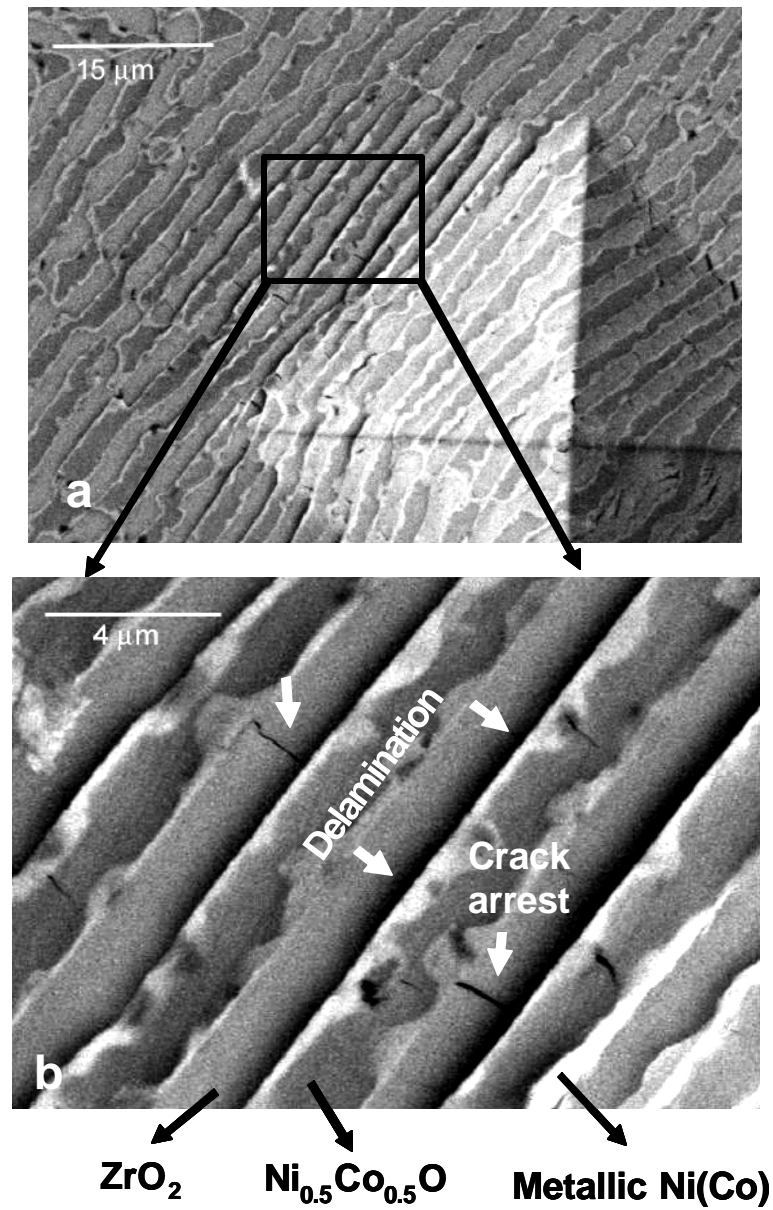


Figure 4.4 (a) Deformation and fracture behavior of the reduced $\text{Ni}_{0.5}\text{Co}_{0.5}\text{O}/\text{ZrO}_2(\text{CaO})$ system upon Vickers indentation test revealing (b) nucleation of secondary cracks within both $\text{Ni}_{0.5}\text{Co}_{0.5}\text{O}$ and $\text{ZrO}_2(\text{CaO})$ and interfacial delamination from the metallic $\text{Ni}(\text{Co})$ interphase to $\text{ZrO}_2(\text{CaO})$ if moving away from the indent (shown with arrows on the image).

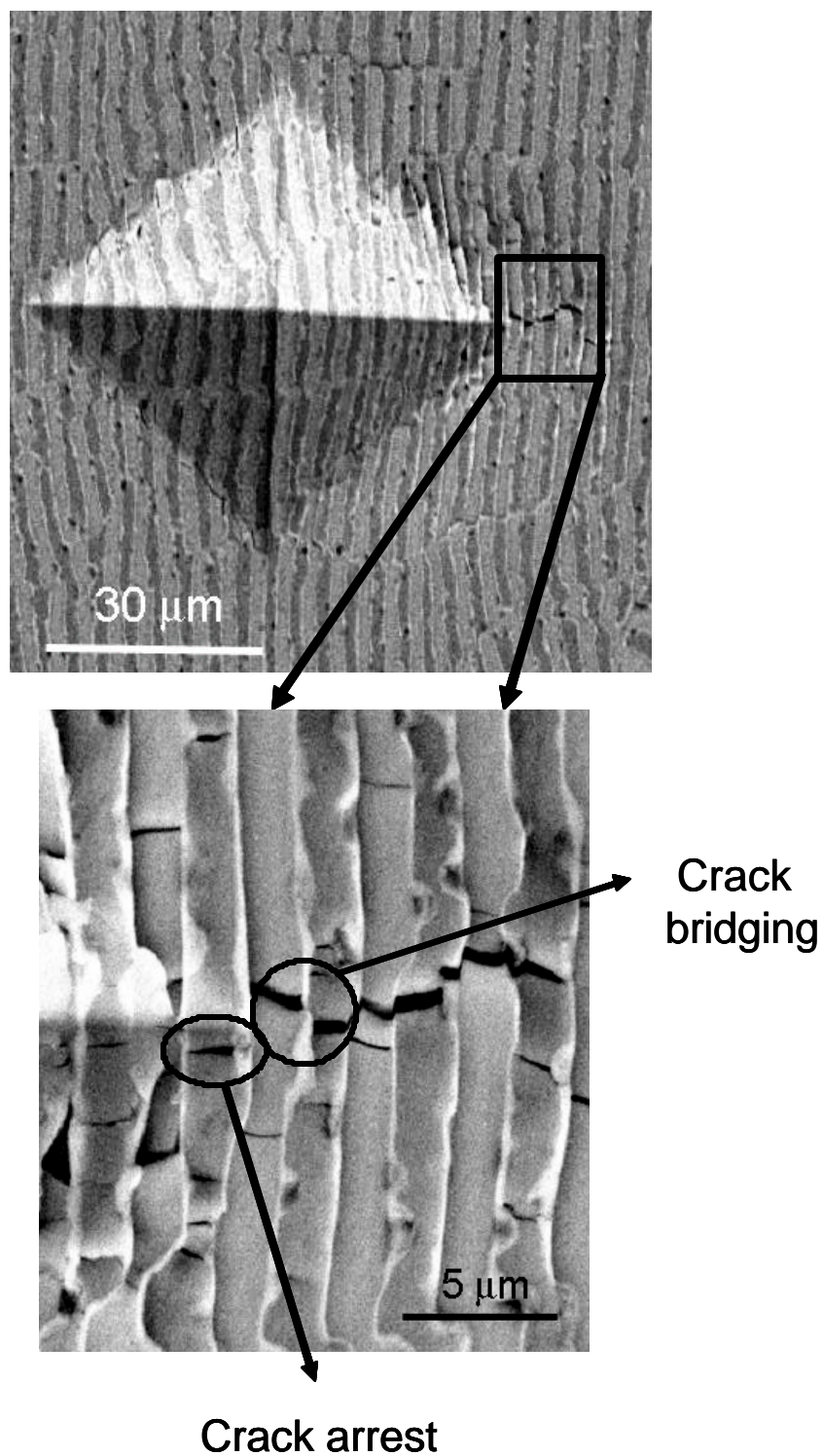


Figure 4.5 Crack arrest and crack bridging across the metallic interphase upon Vickers indentation of the reduced $\text{Ni}_{0.5}\text{CO}_{0.5}\text{O}/\text{ZrO}_2(\text{CaO})$.

The interfacial delamination from the metallic interphase to $\text{ZrO}_2(\text{CaO})$ can be explained by considering the elastic mismatch between $\text{Ni}(\text{Co})$ and $\text{ZrO}_2(\text{CaO})$ phases. As described in section 2.1.1 of this thesis, interfacial delamination becomes a more prominent fracture mechanism, with increasing the elastic mismatch between the two phases in a composite.³² In this system the interfacial delamination occurs upon moving from $\text{Ni}(\text{Co})$, which has a low elastic modulus, to $\text{ZrO}_2(\text{CaO})$ with a high elastic modulus. Although it should be noted that the reduced DSE series studied here do not show any interfacial debonding/delamination from the metallic interphase to the transition metal oxide. The absence of debonding at the metal- $\text{Ni}_x\text{Co}_{1-x}\text{O}$ interfaces is believed to be due to waviness of the $\text{Ni}_{0.5}\text{Co}_{0.5}\text{O}$ -metal interfaces after reduction of this system. Previous studies have clearly shown the level of smoothness, disorder and geometry of the interface to greatly affect the interfacial fracture mechanism in metal-ceramic composites.^{139, 140}

Interfacial porosity in the reduced DSEs is another important parameter that can significantly affect the toughness and fracture behavior of composites.^{23, 140-144} The influence of porosity on the mechanical behavior of a system is generally due to its contribution through crack tip blunting.¹⁴²⁻¹⁴⁴ When a crack is arrested by porosity, the crack tip radius is increased and therefore higher levels of applied stress are required for the crack tip stress to reach the critical value for further propagation. The presence of porosity can also locally change the modulus of the material and therefore influence the direction of the crack, particularly when the porosity spacing is on the same order or smaller than the porosity diameter.^{42, 43} With respect to the pore morphology and distribution in the $\text{Ni}_x\text{Co}_{1-x}\text{O}/\text{ZrO}_2(\text{CaO})$ sample, the 2-4% area density of the porosity in

the microstructure of the reduced $\text{Ni}_{0.5}\text{Co}_{0.5}\text{O}/\text{ZrO}_2(\text{CaO})$ appears to be in the form of large size pores with a relatively large separation distance from each other. Figure 3.8 (c) indicates the distribution profile for the area of the porosity in the reduced $\text{Ni}_{0.5}\text{Co}_{0.5}\text{O}/\text{ZrO}_2(\text{CaO})$ composite. This distribution profile gives the average area of the porosity to be about $0.27 \mu\text{m}^2$ for the individual pores in the sample. Considering Figure 3.6 (b), which shows the microstructural distribution of the porosity in the composite after reduction, the porosity spacing (at least $2\text{-}3 \mu\text{m}$) is about 10 times larger than the average porosity size in the microstructure of the reduced DSE composites. Due to this large separation distance the porosity is believed to have a minimal influence on the local deformation and crack propagation behavior of the reduced DSEs.

The present studies on the reduced and pristine $\text{CoO}/\text{ZrO}_2(\text{CaO})$ and $\text{Ni}_{0.5}\text{Co}_{0.5}\text{O}/\text{ZrO}_2(\text{CaO})$ composites clearly indicate the toughening enhancement to be more prominent in the NiO-rich compositions of this DSE series. In the pristine $\text{CoO}/\text{ZrO}_2(\text{CaO})$ composite, CoO already plays an important role in the toughening of the composite due to the limited plastic deformation of this phase at room temperature. Addition of nanoscale metallic Co interphases further contributes to this enhancement via crack arrest and crack bridging across the interphase. Contrary to the pristine $\text{CoO}/\text{ZrO}_2(\text{CaO})$ composite, Vickers indentation experiments in the pristine $\text{Ni}_{0.5}\text{Co}_{0.5}\text{O}/\text{ZrO}_2(\text{CaO})$ composite show brittle fracture of this system with no toughening mechanisms operating at room temperature. Upon reduction however various toughening mechanisms, i.e. interfacial delamination, plastic deformation, crack arrest and crack bridging, start to operate in the composite. The enhanced fracture and deformation behavior in the reduced $\text{Ni}_{0.5}\text{Co}_{0.5}\text{O}/\text{ZrO}_2(\text{CaO})$ system clearly points to the considerable

role of the nanoscale metallic interphases on the toughening enhancement of this composite.

4.3 Evaluation of the Small Scale Plasticity Across the Reduced $\text{Ni}_x\text{Co}_{1-x}\text{O}/\text{ZrO}_2(\text{CaO})$ DSEs Through Nano-Indentation Technique

Nano-indentation measurements have been previously performed on the pristine $\text{Ni}_x\text{Co}_{1-x}\text{O}/\text{ZrO}_2(\text{CaO})$ composite to assess quantities such as hardness and plasticity factor across different compositions of this solid solution composite.^{10, 17} The earlier indentation studies indicate an increase in the hardness of $\text{Ni}_x\text{Co}_{1-x}\text{O}$ with increasing the NiO fraction. These studies also show $\text{ZrO}_2(\text{CaO})$ to maintain far less plasticity compared with the $\text{Ni}_x\text{Co}_{1-x}\text{O}$ phase.

The purpose of the investigation here is to have a qualitative assessment of the local plasticity across the interfaces in the reduced DSE composite and to reveal the relative contribution of the metallic interphase to the local strain energy absorption in the system compared with that of the $\text{Ni}_{0.5}\text{Co}_{0.5}\text{O}$ and $\text{ZrO}_2(\text{CaO})$ ceramic phases.

Nano-indentation experiments are considered as complete mechanical tests, since it is possible to record the complete load-displacement curve upon indentation of the sample. The load-displacement curves in the nano-indentation test can tell a great deal about the mechanical behavior of a system and evaluate quantities such as hardness, modulus, and yield strength among many others properties.¹⁴⁵⁻¹⁴⁷ Figure 4.6 presents a typical load-displacement curve in a nano-indentation experiment. The loading portion of the indentation curve contains both elastic and plastic information about the sample, while the unloading curve gives information about the elastic behavior of the sample. The

quantity S here is defined as the slope of the upper portion of the unloading curve, which is also known as the contact stiffness. The hardness of a sample, H , can be determined according to equation 4.1.¹⁴⁵

$$H = \frac{P_{\max}}{A_c} \quad 4.1$$

Where P_{\max} is the maximum load and A_c is the projected contact area of the tip at the contact depth. To measure the proper value of A in the nano-indentation experiment, the area function (the indenter shape function) should first be calibrated through separate measurements on an isotropic standard material, i.e. fused quartz, which has a known modulus and hardness.

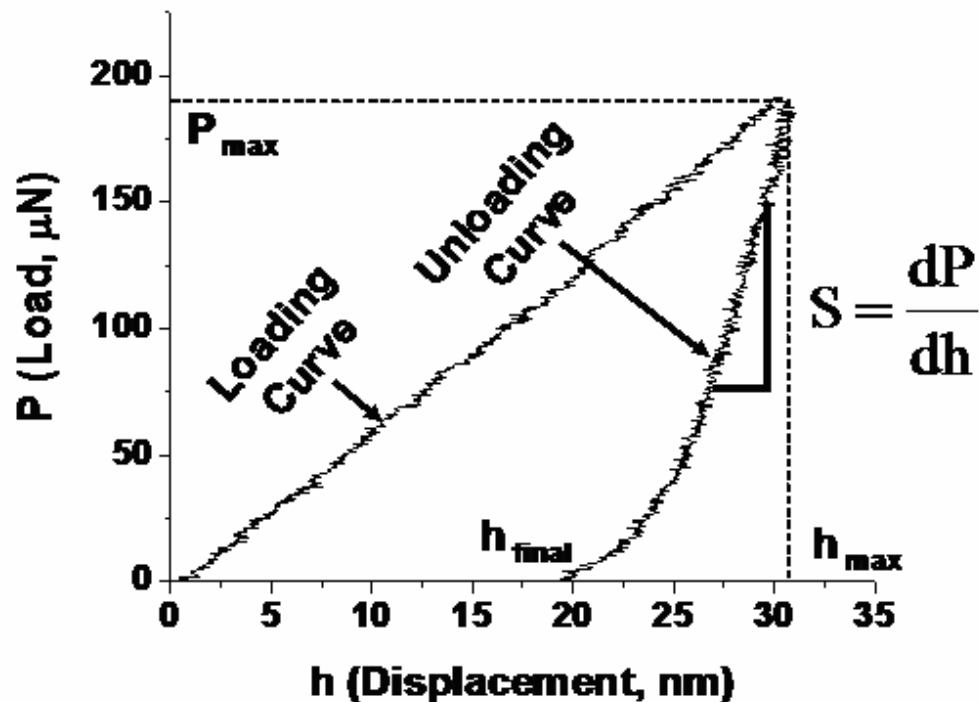


Figure 4.6 Load-displacement curve in a nano-indentation experiment

For the purpose of this study the pristine and the reduced $\text{Ni}_{0.5}\text{Co}_{0.5}\text{O}/\text{ZrO}_2(\text{CaO})$ composite were selected from the $\text{Ni}_x\text{Co}_{1-x}\text{O}/\text{ZrO}_2(\text{CaO})$ composite series for the nano-indentation experiments here. Figure 4.7 shows the shape of the indentation curves for $\text{Ni}_{0.5}\text{Co}_{0.5}\text{O}$, $\text{ZrO}_2(\text{CaO})$ and the $\text{Ni}(\text{Co})$ metallic interphase in the reduced $\text{Ni}_{0.5}\text{Co}_{0.5}\text{O}/\text{ZrO}_2(\text{CaO})$ composite. The indentation marks here have been made on the individual metal and oxide phases in the area shown in Figure 4.7a. As expected, considerable mechanical hysteresis is observed for the $\text{Ni}(\text{Co})$ metallic interphase (Figure 4.7b), indicating plastic deformation of this phase, compared with the adjacent $\text{Ni}_{0.5}\text{Co}_{0.5}\text{O}$ and $\text{ZrO}_2(\text{CaO})$ phases (Figures 4.7c & 4.7d). The minimal mechanical hysteresis from the $\text{ZrO}_2(\text{CaO})$ load-displacement curve (Figure 4.6c) particularly indicates deformation in this phase to be mainly elastic.

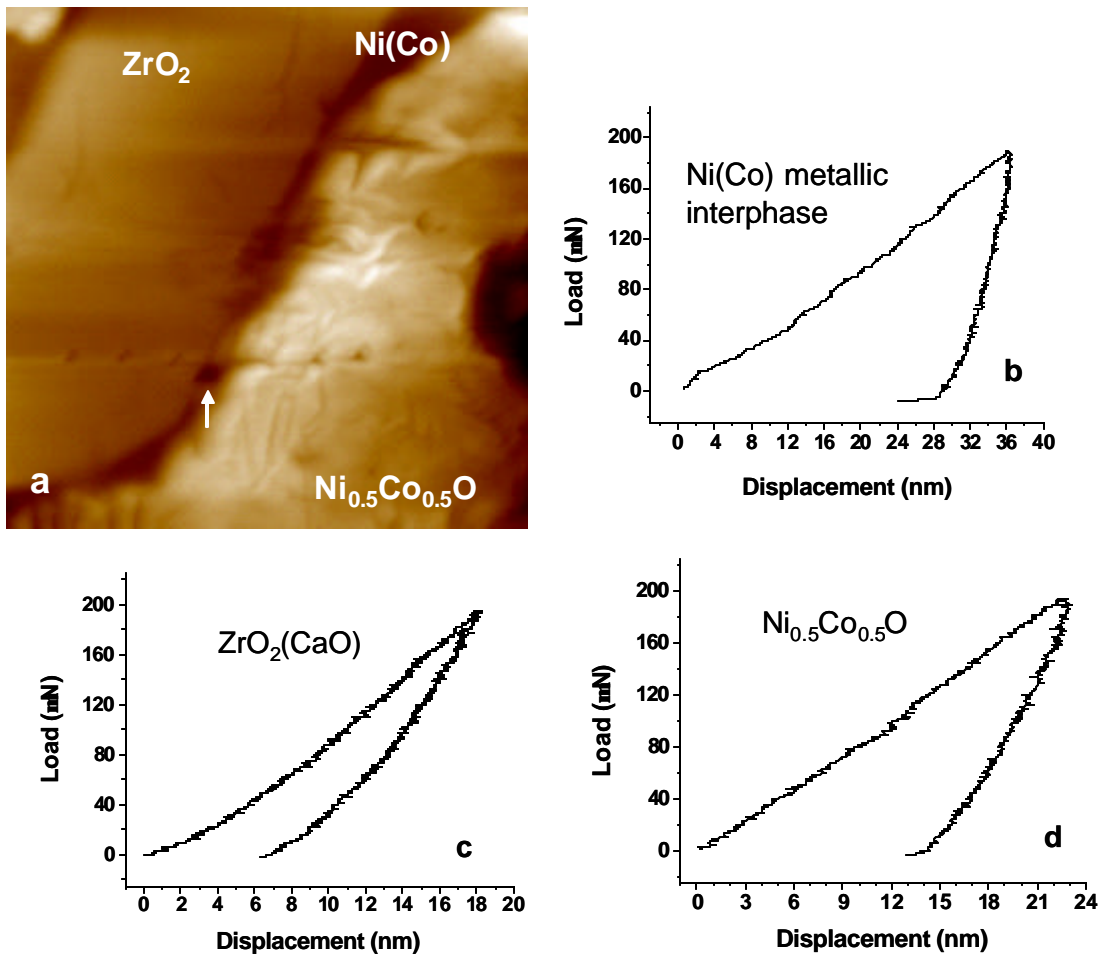


Figure 4.7 (a) Topography image of the reduced $\text{Ni}_{0.5}\text{Co}_{0.5}\text{O}/\text{ZrO}_2(\text{CaO})$ along with the load displacement curves from (b) the metallic $\text{Ni}(\text{Co})$ interphase, (c) $\text{ZrO}_2(\text{CaO})$ and (d) $\text{Ni}_{0.5}\text{Co}_{0.5}\text{O}$ after indentation of this region. (The thickness of the metallic interphase is about 180 nm here and the size of the image is $3 \times 3 \mu\text{m}$)

Figures 4.8 and 4.9 indicate the variation of nano-indentation hardness across the metal-ceramic interfaces in the reduced $\text{Ni}_{0.5}\text{Co}_{0.5}\text{O}/\text{ZrO}_2(\text{CaO})$ composites, while Figure 4.10 shows the hardness profile across the pristine $\text{Ni}_{0.5}\text{Co}_{0.5}\text{O}/\text{ZrO}_2(\text{CaO})$ composite upon indentation of this sample. According to Figures 4.8 to 4.10 there is an abrupt decrease in hardness as we pass across the metallic interphase in the reduced

$\text{Ni}_{0.5}\text{Co}_{0.5}\text{O}/\text{ZrO}_2(\text{CaO})$ composites. It should be noted that the metallic layer thickness shown in Figure 4.8 is only about 140 nm, which is smaller than the size of the projected contact area of the tip (~180 nm) at the contact depth. Therefore during indentation of the metallic interphase, the tip makes contact with the adjacent ceramic phases in addition to the metallic interphase. As a result the measured hardness value at this point represents the combined mechanical response of the interphase and the adjacent ceramic phases. Figure 4.9 indicates a hardness profile from a different region of the sample where the $\text{Ni}_{0.5}\text{Co}_{0.5}\text{O}$ phase is completely transformed into its metallic form; Ni(Co). Due to the full reduction of the transition metal oxide, the resulting metallic interphase is relatively thick (about 2 μm) in this region. The hardness profile across the $\text{ZrO}_2(\text{CaO})$ -Ni(Co)- $\text{ZrO}_2(\text{CaO})$ phases here indicates a considerable drop in hardness upon passing across the metallic interphase, which points to the major contribution of the metallic interphase towards strain energy absorption in the reduced $\text{Ni}_x\text{Co}_{1-x}\text{O}/\text{ZrO}_2(\text{CaO})$ system. In contrast, the high hardness values measured for the $\text{ZrO}_2(\text{CaO})$ phase indicate elastic brittle nature of this phase with a far less plasticity compared with the metallic interphase.

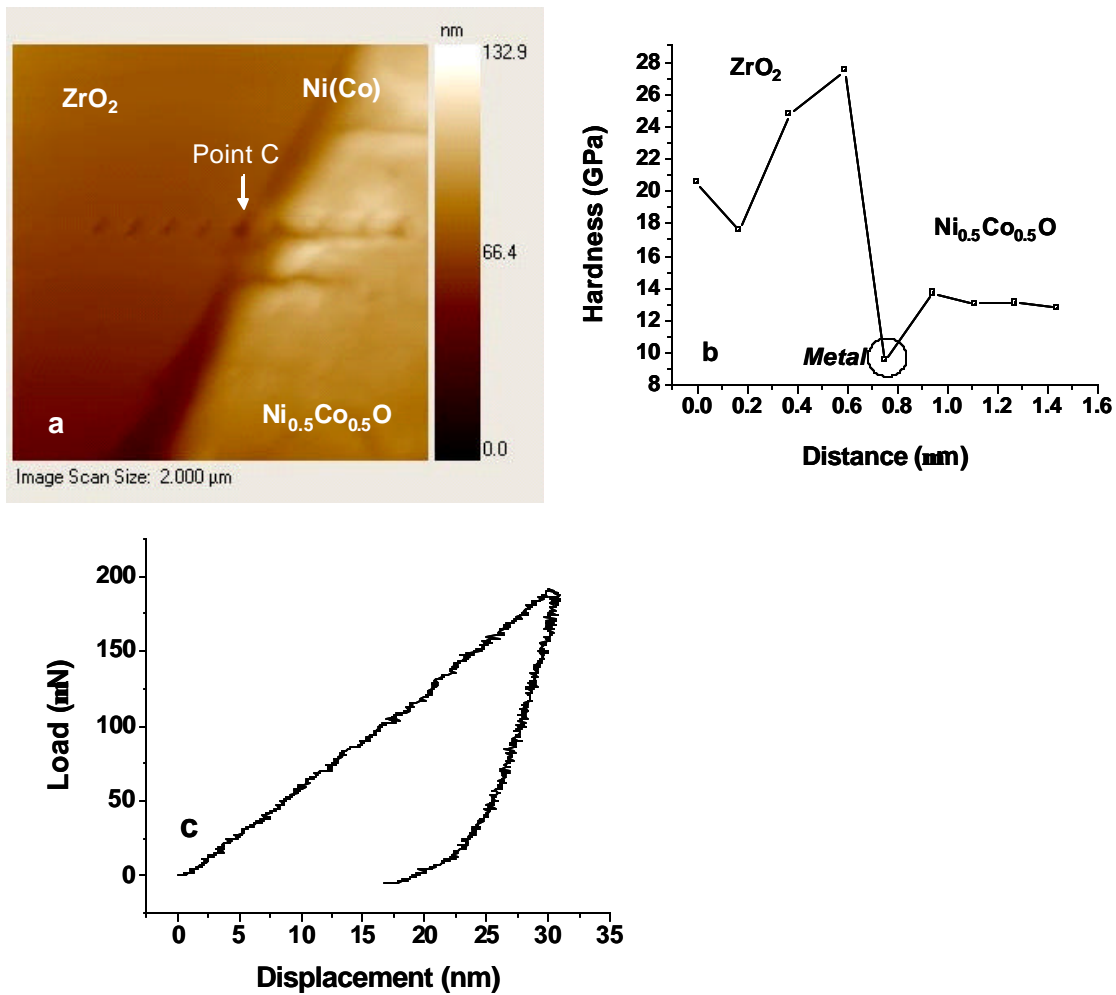


Figure 4.8 (a) Topography image of the reduced $Ni_{0.5}Co_{0.5}O/ZrO_2(CaO)$ after nano-indentation. (b) Hardness variation across the interfaces from $Ni_{0.5}Co_{0.5}O$ to $ZrO_2(CaO)$. (c) Load-displacement curve for point c shown on the image. The indentation step size here is 150-200 nm and the metallic layer thickness is about 140 nm.

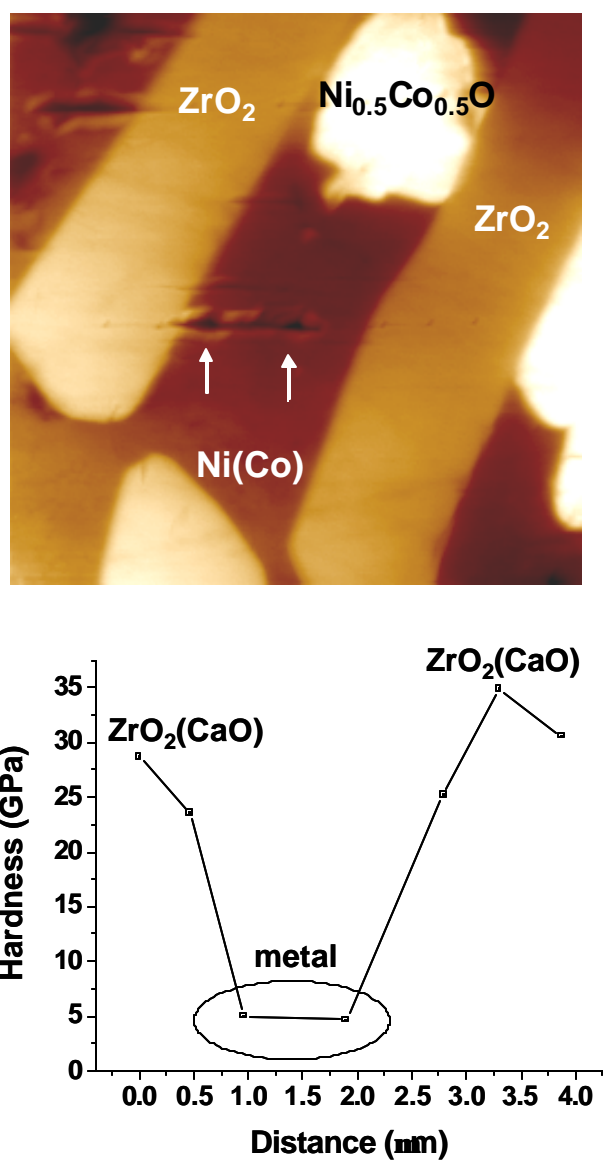


Figure 4.9 (a) Topography image of the fully reduced $\text{Ni}_{0.5}\text{Co}_{0.5}\text{O}/\text{ZrO}_2(\text{CaO})$ after nano-indentation in this region. (b) Hardness variation across the $\text{ZrO}_2(\text{CaO})$ - $\text{Ni}(\text{Co})$ - $\text{ZrO}_2(\text{CaO})$ phases.

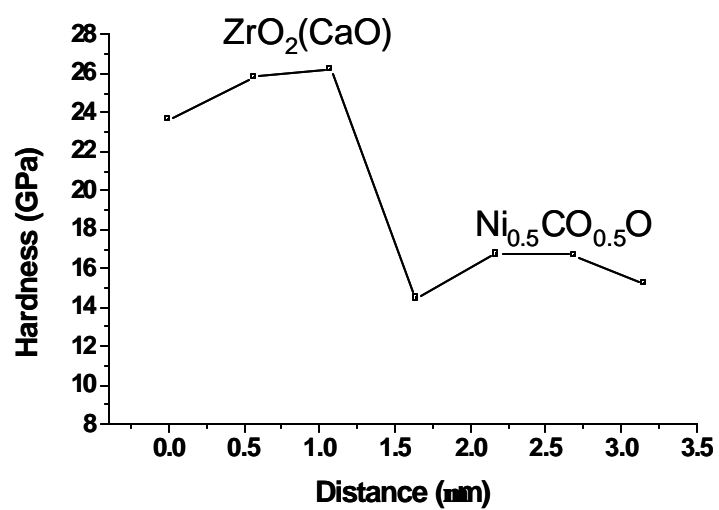
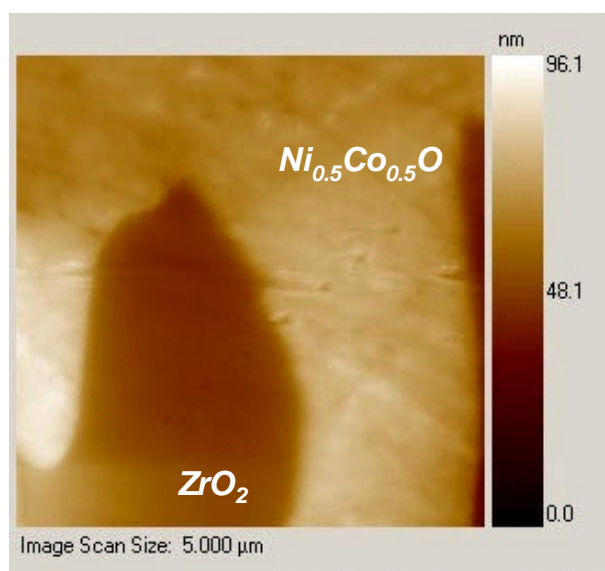


Figure 4.10 (a) Topography image of the pristine $\text{Ni}_{0.5}\text{Co}_{0.5}\text{O}/\text{ZrO}_2(\text{CaO})$ after nano-indentation in this region. (b) Hardness variation across the interface from $\text{Ni}_{0.5}\text{Co}_{0.5}\text{O}$ to $\text{ZrO}_2(\text{CaO})$.

To further investigate the extent of local plastic deformation in the reduced $\text{Ni}_x\text{Co}_{1-x}\text{O}/\text{ZrO}_2(\text{CaO})$ DSE composite, transmission electron microscopy is employed in the next chapter to reveal the small scale deformation mechanism in the metallic interphase and the role of $\text{Ni}_x\text{Co}_{1-x}\text{O}$ and $\text{ZrO}_2(\text{CaO})$ on the strain energy absorption mechanism upon deformation of this system.

4.4 Summary and Conclusions

This chapter presents the deformation and fracture mechanism in the reduced $\text{Ni}_x\text{Co}_{1-x}\text{O}/\text{ZrO}_2(\text{CaO})$ DSE model systems using the Vickers indentation technique. The presence of ductile interphases lead to several characteristic energy dissipative mechanisms, such as interfacial delamination, formation of secondary cracks, plastic deformation, crack arrest and crack bridging across the metallic interphase upon Vickers indentation of the DSE composites. The operating energy dissipative mechanisms here, i.e. interfacial crack delamination, crack arrest and crack bridging across the metallic interphase, further suggest toughness enhancement of this model system across the chemically reduced DSE series. This enhancement is more pronounced in the $\text{Ni}_{0.5}\text{Co}_{0.5}\text{O}/\text{ZrO}_2(\text{CaO})$ samples, where interfacial crack penetration is the dominant fracture mechanism operating in the fully oxidized form of this composite.

The nano-indentation technique was employed to verify the extent of plasticity and local deformation in the reduced $\text{Ni}_{0.5}\text{Co}_{0.5}\text{O}/\text{ZrO}_2(\text{CaO})$ DSE composites. The hardness measurements across the metallic interphase point to the considerable strain energy absorption and plastic deformation in the metallic interphase compared with the ceramic oxide phases in the system.

5 5 SMALL SCALE DEFORMATION AND FRACTURE BEHAVIOR: $\text{Ni}_x\text{Co}_{1-x}\text{O}/\text{ZrO}_2(\text{CaO})$ MODEL SYSTEM WITH A DUCTILE INTERPHASE

This chapter focuses on the deformation and fracture mechanism in the reduced $\text{Ni}_x\text{Co}_{1-x}\text{O}/\text{ZrO}_2(\text{CaO})$ model system at small length scales. The objective of this study is to specifically understand the role of the nanoscale metallic interphase and its layer thickness and chemistry on the strain energy absorption in ductile-brittle multi-layered systems. The chapter starts with describing the sample preparation techniques used for this investigation. Conventional transmission electron microscopy sample preparation method along with FIB lift-out sample preparation technique is performed to study the nanoscale deformation mechanisms and the crack tip interactions with the ductile-brittle lamellar structure in the model system here upon Vickers indentation test.

This work reveals the small scale deformation mechanisms at the vicinity of Vickers indentation mark in two different compositions of the reduced $\text{Ni}_x\text{Co}_{1-x}\text{O}/\text{ZrO}_2(\text{CaO})$ model system; $\text{CoO}/\text{ZrO}_2(\text{CaO})$ (with $x=0$) and $\text{Ni}_{0.5}\text{Co}_{0.5}\text{O}/\text{ZrO}_2(\text{CaO})$ (with $x=0.5$), with the layer thickness ranging from about 50 to 300 nm. The chapter further investigates the crack tip interactions with the nanoscale Ni(Co) ductile interphases and the role $\text{Ni}_x\text{Co}_{1-x}\text{O}$ and $\text{ZrO}_2(\text{CaO})$ on the strain energy absorption in the model system studied here.

5.1 Sample Preparation Methods

$\text{Ni}_x\text{Co}_{1-x}\text{O}/\text{ZrO}_2(\text{CaO})$ DSEs have been previously grown into interpenetrating single crystal $\text{Ni}_x\text{Co}_{1-x}\text{O}$ and $\text{ZrO}_2(\text{CaO})$ phases.⁸⁴ The samples were first cut into dicks

from the original single crystal rod and were reduced at high temperature to create ductile Ni(Co) interphases, mediating the oxide layers in the system. The details of the reduction experiment and the resulting microstructure have been presented in chapter 3 of this thesis. Two different compositions of $\text{Ni}_x\text{Co}_{1-x}\text{O}/\text{ZrO}_2(\text{CaO})$ system, $\text{CoO}/\text{ZrO}_2(\text{CaO})$ with $x=0$ and $\text{Ni}_{0.5}\text{Co}_{0.5}\text{O}/\text{ZrO}_2(\text{CaO})$ with $x=0.5$, which maintain two different plasticity levels in the $\text{Ni}_x\text{Co}_{1-x}\text{O}$ solid solution¹⁰ are chosen for this study.

Conventional transmission electron microscopy imaging techniques were utilized to study the small scale deformation mechanisms adjacent to the deformed region within the sample. Two different sample preparation methods were chosen to study the deformation and fracture mechanism at small length scales in the reduced $\text{Ni}_x\text{Co}_{1-x}\text{O}/\text{ZrO}_2(\text{CaO})$ model system. Conventional sample preparation method, described in section 5.1.1, was chosen to study the strain energy absorption within the metallic interphase in the area around the Vickers indentation mark. FIB-lift-off TEM sample preparation method was employed to specifically study the crack tip interactions with the metallic interphase as well as the ceramic phases. Using these two different sample preparation methods here, it was possible to compare the resulting deformation behavior at small length scales within the composite for each method and to verify the operating deformation mechanisms in the sample upon deformation.

To study the small scale deformation mechanism, the reduced specimens were first polished using the diamond film followed by the colloidal silica (Interment) to reach the partially reduced region of the microstructure at the subsurface in the reduced DSEs. Reduced samples of the oxide DSEs were then indented at the top surface using the Vickers Indenter (Beuhler, Micromet®II Microhardness Tester). A 10 N load was

applied to the polished samples of the partially reduced composites using a diamond-tip micro-indenter and was held for 20 seconds for this test. Sections 5.1.1 and 5.1.2 of this chapter describe the sample preparation methods employed to study the deformation mechanisms in the reduced DSEs adjacent to the deformation zone.

5.1.1 Conventional TEM Sample Preparation Technique

Figure 5.1 shows the step by step procedures for the conventional TEM sample preparation method used in this study. As this figure shows after polishing and indenting the surface of the reduced sample, the indented samples were thinned down from the bottom side to approximate thickness of about 80 μm . The samples were first mounted onto a slotted molybdenum grid and then gently dimpled from the bottom surface to approximately 30 μm thickness. The samples were ion milled to electron transparency using the Fischione ion miller model 1010 at liquid nitrogen temperature to minimize the ion beam damage to the sample.

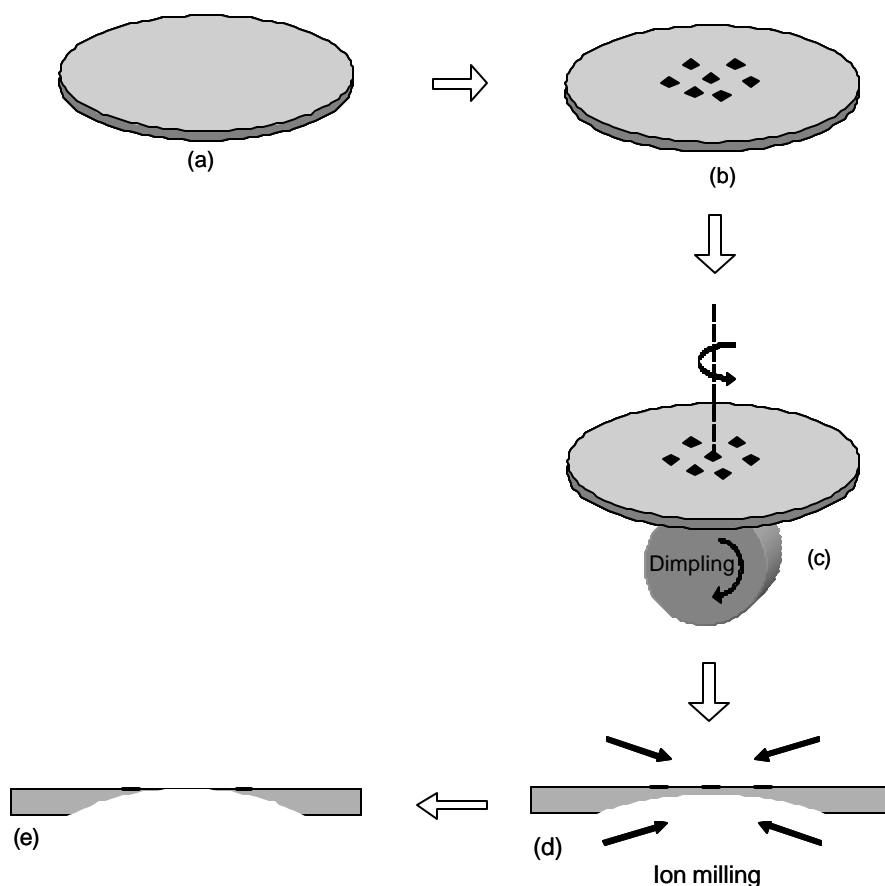


Figure 5.1 Step-by-step procedures for the conventional TEM sample preparation technique for the study of the deformation mechanism. These steps show (a) the reduced sample, (b) the sample after it is deformed by Vickers indentation and mounted on a TEM grid (the black spots on the surface of the sample indicate the indentation marks), (c) dimpling procedure at the bottom surface of the sample (d) the final ion milling stage (e) the final TEM sample after creating a hole at the center adjacent to the indentation mark.

5.1.2 FIB Lift-off TEM Sample Preparation Technique

FEI Dual-Beam DB-235 Focused Ion Beam (FIB) in the Frederick Seitz Materials Research Laboratory (MRL), Center for Microanalysis of Materials (CMM) at the

University of Illinois at Urbana Champaign (UIUC) was used to prepare TEM lift-off samples from the vicinity of the Vickers indentations made on the reduced DSE samples. This instrument operates at 30 kV and is equipped with a micromanipulator which allows one to prepare site-specific lift-off TEM samples at the area of interest in the sample.

After the reduced $\text{Ni}_k\text{Co}_{1-x}\text{O}/\text{ZrO}_2(\text{CaO})$ sample was polished and indented, the sample was coated with a thin layer of gold to prevent charging during fabrication. After Au deposition, the sample was transferred into the FIB instrument. A Pt layer of $4 \times 29 \mu\text{m}$ with $1 \mu\text{m}$ thickness was deposited on the area of interest adjacent to the indentation mark to protect the region from beam damage (Figure 5.2). The material on each side of the Pt layer was then sputtered away to fabricate a thin membrane of the sample. Beam sizes from 20000 pA down to 1000 pA were applied respectively to make step-like trenches on both sides of the Pt layer during fabrication. To provide a uniform film thickness and avoid formation of a wedge-shaped membrane, the sample was tilted from its original position (± 1.2 degrees from zero degrees position) prior to sputtering in the last thinning stage. The thinning process was continued till a final membrane thickness of 1-2 μm was obtained. After the thinning process, a “U-shaped” cut was made at the bottom of the membrane to detach the membrane from the bulk substrate (Figure 5.3).

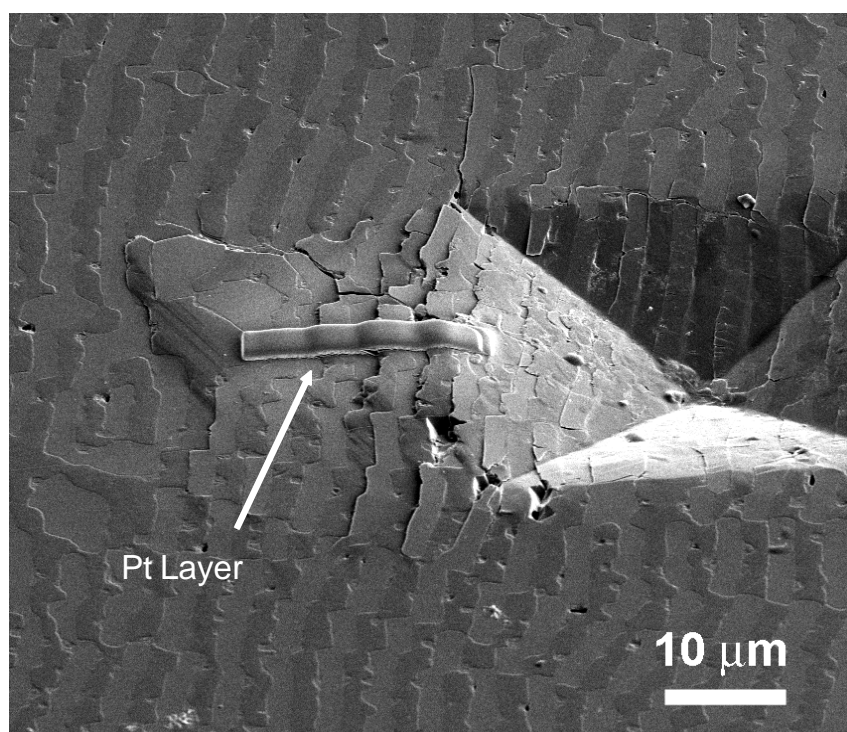


Figure 5.2 A thin Pt layer is deposited adjacent to the indentation mark on the area of interest prior to TEM sample fabrication to protect the top surface of the sample from beam damage.

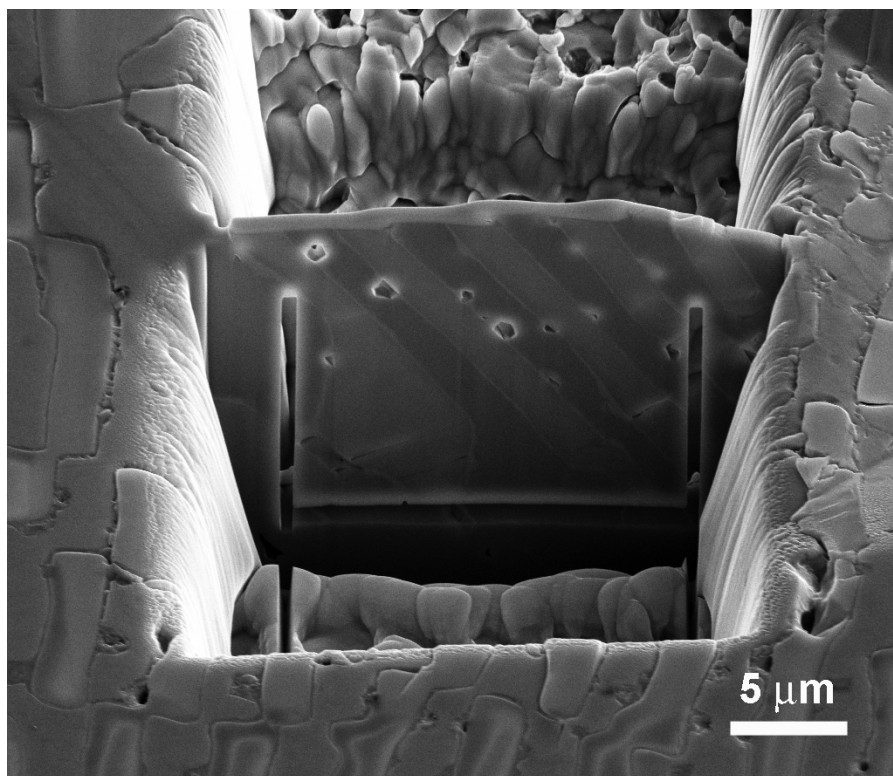


Figure 5.3 A thin membrane of the sample with 1-2 μm thickness is fabricated from the area of interest

A micromanipulator was applied to pick up the final membrane from the bulk sample and to transfer it to the TEM grid. The micromanipulator was first welded to the top edge of the membrane using the Pt deposition source and the sample was completely detached from the substrate on the top portion (Figure 5.4). The sample was then removed from the bulk (Figure 5.5) and welded to the TEM grid using the Pt deposition source (Figure 5.6). A final thinning process was performed on the membrane using a 100 pA beam size to further thin down the specimen to electron transparency while

attached to the TEM grid. Figure 5.7 shows the final FIB lift-off TEM sample after the last thinning stage.

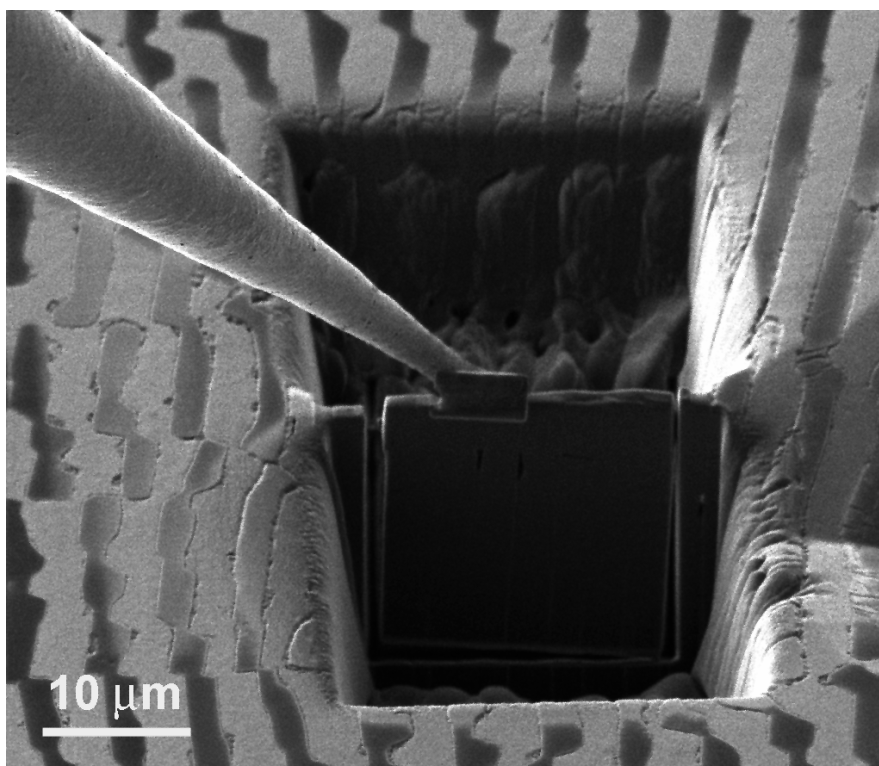


Figure 5.4 Sample is welded to the micro-manipulator before it is detached from the substrate.

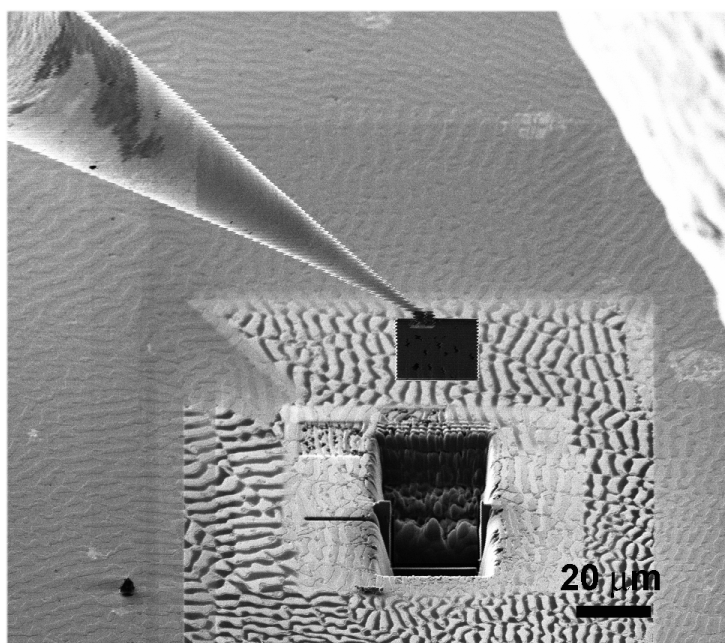


Figure 5.5 Sample is removed from the bulk and transferred to the TEM grid using the micro-manipulator.

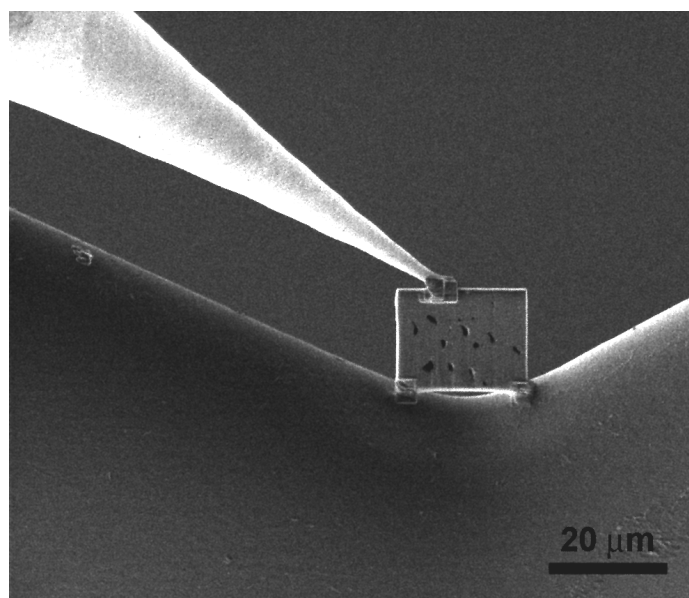


Figure 5.6 Sample is welded to the TEM grid using the Pt deposition source.

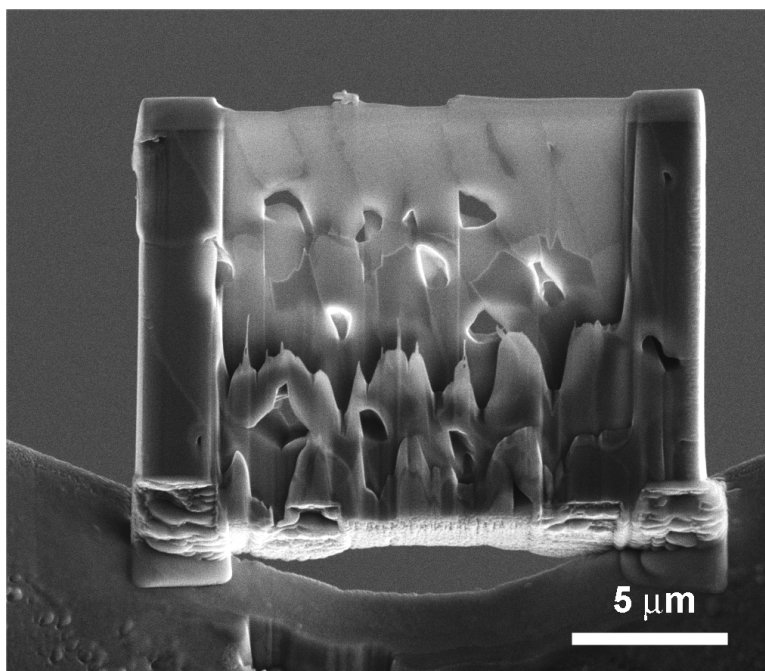


Figure 5.7 The sample is further thinned down on the TEM grid to obtain thickness of about or less than 100 nm.

After the proper thickness in the membrane was achieved during the FIB fabrication process, the sample was ion milled using Fischione ion miller (IBT) to remove the re-deposited amorphous layer from the TEM sample. The operating condition for IBT was chosen to be 5 kV and 2 mA for the top and bottom guns. Ion milling process was continued till the damaged layer was removed from the thin membrane.

5.2 Observations of the Small Scale Deformation Behavior in the Reduced $\text{Ni}_x\text{Co}_{1-x}\text{O}/\text{ZrO}_2(\text{CaO})$ Model System

TEM investigations on the reduced $\text{Ni}_x\text{Co}_{1-x}\text{O}/\text{ZrO}_2(\text{CaO})$ model system reveal the significant role of the metallic interphases to strain energy absorption upon

deformation of this system. These investigations show the small scale deformation mechanism to be slightly different in the pure Co interphase compared with the Ni(Co) solid solution interphase. Also the extent of plasticity and strain energy absorption was observed to decrease upon reducing the size scale. The following sections in this chapter discuss the role of chemistry and thickness, ranging from 50 to 300 nm, on the small scale deformation mechanism operating in the reduced $\text{Ni}_x\text{Co}_{1-x}\text{O}/\text{ZrO}_2(\text{CaO})$ DSEs in detail.

5.2.1 Observation of the Small Scale Deformation Behavior in the Metallic Interphases with the Thickness of 100 nm or Higher

Figures 5.8 to 5.12 show the various deformation mechanisms operating within the metallic interphases of above 100 nm thickness in the reduced indented $\text{Ni}_x\text{Co}_{1-x}\text{O}/\text{ZrO}_2(\text{CaO})$ systems. These images indicate the region very near to the indentation mark in the reduced indented $\text{CoO}/\text{ZrO}_2(\text{CaO})$ and $\text{Ni}_{0.5}\text{Co}_{0.5}\text{O}/\text{ZrO}_2(\text{CaO})$ composites.

Figures 5.8 to 5.10 show bright field TEM micrographs of the deformation mechanism in the reduced $\text{CoO}/\text{ZrO}_2(\text{CaO})$ after indentation of this composite. Figure 5.8 indicates the metallic Co interphase to heavily deform and transform into a twinned structure upon deformation. The metallic Co layer thickness in this image is just above 100 nm. The angle “ α ” specified on this figure indicates the angle between the adjacent twinned grains in Co interphase. The angle α in this region is measured to be 70° degrees, while the angle between two different $\{111\}$ planes in cubic structures has been previously measured to be $70^\circ 23'$.¹⁴⁸ Since the twinning angle in this region is equal to the angle between two different $\{111\}$ planes in FCC crystals, it is believed that

deformation twinning takes place on the (111) planes of metallic Co interphase upon deformation in the reduced $\text{CoO/ZrO}_2(\text{CaO})$ composite. A higher twinning density is observed within the metallic Co interphase at this size scale after deformation of the samples (compared to the samples before deformation). Therefore it is believed that deformation twinning is one of the major deformation mechanisms operating at this size scale within the metallic Co interphase.

Figure 5.9 shows another deformed area very close to the indentation mark in the reduced $\text{CoO/ZrO}_2(\text{CaO})$ composite with the thickness of about 250 nm. This figure shows formation of stacking faults across the metallic interphase indicating dislocation slip to occur across the Co interphase upon deformation. Figure 5.10 presents another area in the deformed reduced $\text{CoO/ZrO}_2(\text{CaO})$ composite with the thickness varying in the range of 150-250 nm. This image indicates formation of short arrays of dislocations along with twinning within the Co interphase in this composite.

TEM observations in this composite show deformation twins, stacking fault formation and dislocation formation to be contributing to strain energy absorption in the reduced $\text{CoO/ZrO}_2(\text{CaO})$ system at length scales of above 100 nm. Deformation twinning is considered to be the dominant deformation mechanism for Co interphase, since a higher density of twins is observed compared to that of dislocations in the deformed reduced $\text{CoO/ZrO}_2(\text{CaO})$ system.

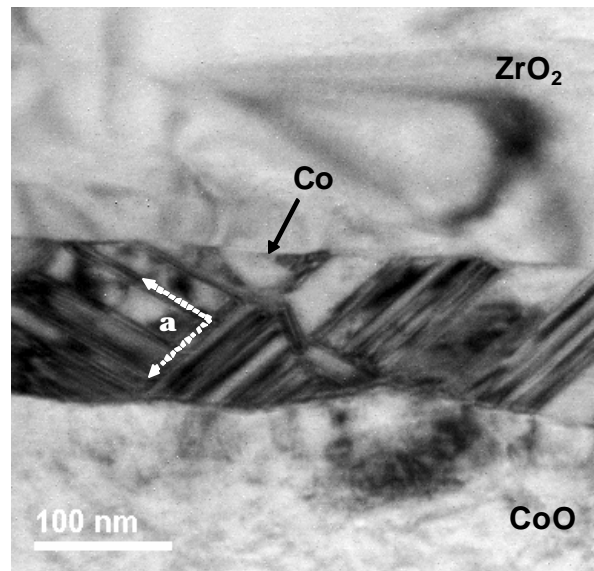


Figure 5.8 Formation of twins within the metallic Co interphase in the area very near to the indentation mark ($\alpha=70^\circ$) in the deformed reduced $\text{CoO}/\text{ZrO}_2(\text{CaO})$ system.

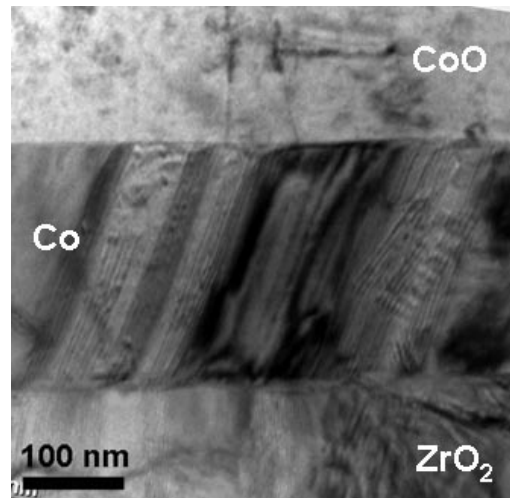


Figure 5.9 Stacking fault formation indicating dislocation slip across the metallic Co interphase in the deformed reduced $\text{CoO}/\text{ZrO}_2(\text{CaO})$ system. The layer thickness in this region is about 250 nm.

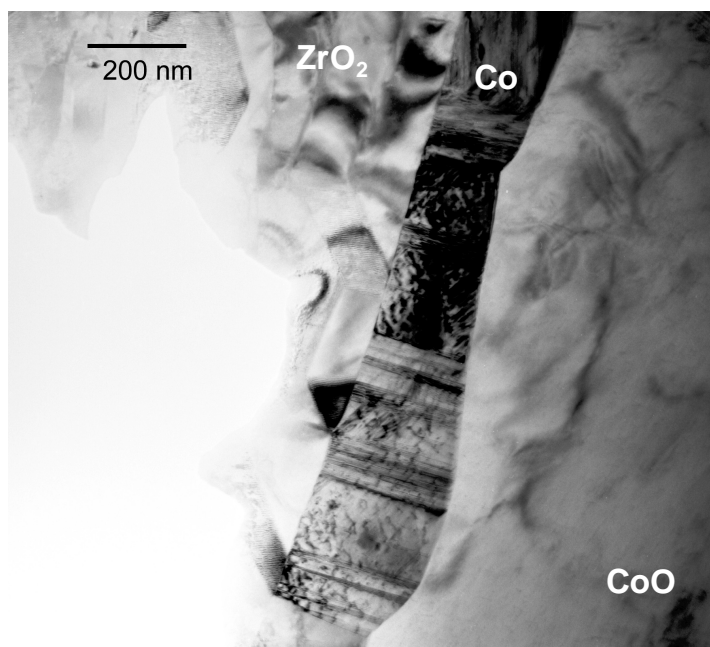


Figure 5.10 Deformation twins along with an array of short dislocations distributed within the metallic Co interphase in the deformed reduced CoO/ZrO₂(CaO) system. The metallic layer thickness varies from 150-250 nm in this region.

Reduced samples of Ni_{0.5}Co_{0.5}O/ZrO₂(CaO) show a similar deformation mechanism at small length scales compared with the reduced CoO/ZrO₂(CaO) composite. However the small differences observed in the strain energy absorption mechanisms between the two composites point to the important role of chemistry and the solute elements on the fracture and deformation mechanism of the composite.

Figure 5.11 presents an area of Ni(Co) metallic interphase in the reduced Ni_{0.5}Co_{0.5}O/ZrO₂(CaO) composite near the indentation mark. This figure shows the strain energy absorption to prominently take place through dislocation formation in the Ni(Co) interphase. This figure also indicates formation of an array of short dislocation lines with

a certain spacing from each other within the Ni(Co) metallic layer with above 100 nm thickness. Beside dislocation formation, mechanical twins are other deformation features that are observed within the Ni(Co) interphase. Figure 5.12 shows an example of twinning in the Ni(Co) interphase in the reduced $\text{Ni}_{0.5}\text{Co}_{0.5}\text{O}/\text{ZrO}_2(\text{CaO})$ composite after deformation. The arrows on this figure indicate the twins formed within the metallic interphase. This figure also shows re-deposition of an amorphous layer from the sputtered away material at the edge of the sample. Re-deposition of an amorphous layer at the edge of the TEM membrane is a sample preparation artifact that occurs during the FIB TEM lift-off sample preparation technique.

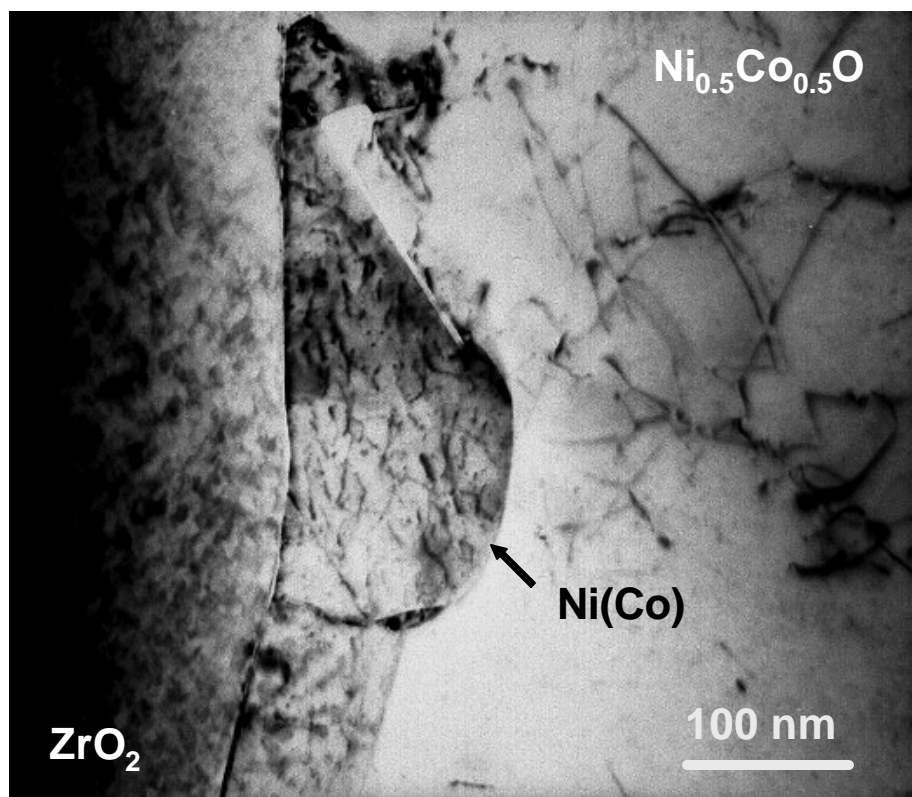


Figure 5.11 Dislocation formation within the Ni(Co) interphase in an area very near to the indentation mark in the reduced $\text{Ni}_{0.5}\text{Co}_{0.5}\text{O}/\text{ZrO}_2(\text{CaO})$ composite after deformation.

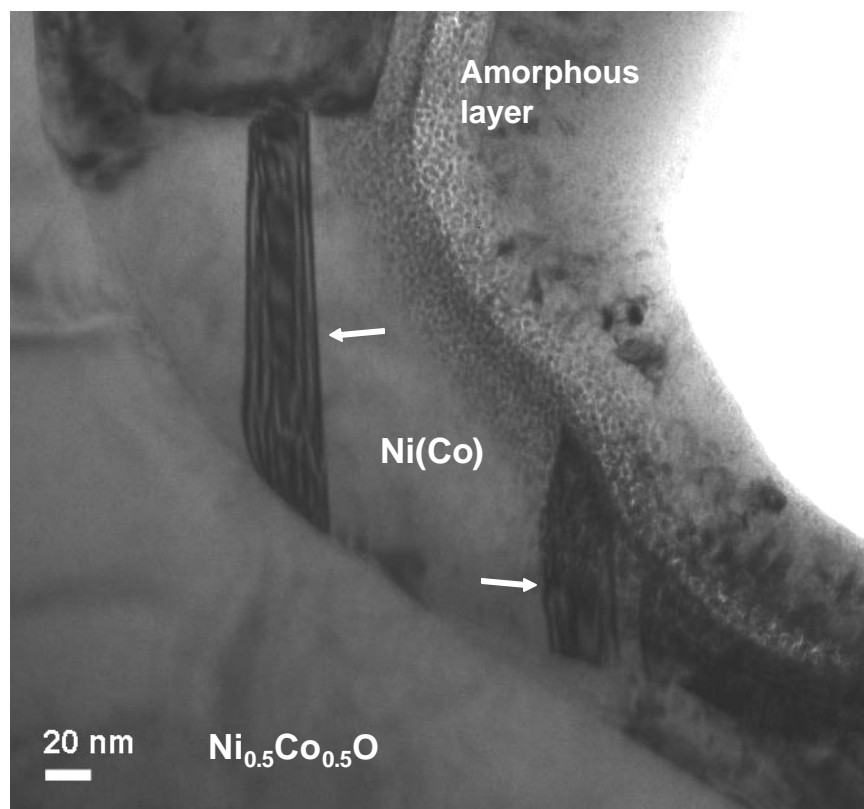


Figure 5.12 Deformation twinning within the Ni(Co) interphase near the indentation mark after deformation of the reduced $\text{Ni}_{0.5}\text{Co}_{0.5}\text{O}/\text{ZrO}_2(\text{CaO})$ composite. The arrows on the image point to the twins within the metallic Ni(Co) interphase.

According to the electron microscopy studies in the reduced deformed $\text{Ni}_x\text{Co}_{1-x}\text{O}/\text{ZrO}_2(\text{CaO})$ with $x=0$ and 0.5 , the nanoscale metallic interphases contribute to strain energy absorption through plastic deformation. However addition of Ni into the metallic interphase causes a transition in the deformation mechanism of the metallic interphase. This transition clearly indicates the role of alloying on the twinning and the stacking fault formation energy of alloys. The dominant deformation mechanism in the metallic Co interphase is deformation twinning and stacking fault formation, upon

indentation of the reduced $\text{CoO/ZrO}_2(\text{CaO})$ system. In contrast, in the $\text{Ni}(\text{Co})$ solid solution interphase the strain energy absorption mechanism is mainly via dislocation formation and a lower twinning incidence in $\text{Ni}(\text{Co})$ is observed compared to pure Co interphase. Previous studies have pointed to the role of alloying elements on the stacking fault formation energy of various alloys including Co-Ni.^{112, 122, 124} As previously discussed in Section 3.2.3 of this thesis, earlier studies have pointed to the effect of alloying on the twinning and the stacking fault formation energy of Co. According to these investigations, upon addition of Ni to Co, the stacking fault formation energy of the alloy is increased and therefore a lower stacking fault and twinning incidence is observed with increasing the Ni content.^{112, 122, 124} Figure 3.16 points to the stacking fault formation energy change for a series of FCC Ni-Co alloys at room temperature.¹²² This plot clearly shows an increase in the stacking fault formation energy of Ni-Co alloy upon addition of Ni.

Ray has specifically studied the rolling textures in different compositions of Ni-Co alloy and has shown the deformation texture to vary as a function of the solute element.¹²⁴ His investigations show twinning to be the major deformation texture in the Co rich alloys. With increasing the Ni content, however, twinning propensity drops and dislocation slip becomes a more dominant deformation mechanism. These studies have shown twinning along with dislocation slip to occur in Ni-Co solid solution alloys with Ni composition between 40-60%.

The EDXS chemical analysis of $\text{Ni}(\text{Co})$ interphase after reduction of $\text{Ni}_{0.5}\text{Co}_{0.5}\text{O/ZrO}_2(\text{CaO})$ composite shows the $\text{Ni}(\text{Co})$ interphase to contain about 52.3 ± 3.6 wt% Co and 47.7 ± 3.9 wt% Ni. Moreover the TEM investigations in the reduced

$\text{Ni}_x\text{Co}_{1-x}\text{O}/\text{ZrO}_2(\text{CaO})$ with $x=0$ and 0.5 clearly indicate a shift in the deformation mechanism of the system from mainly twinning (in Co) to dislocation slip (in Ni(Co)) with the interphase thickness of about or greater than 100 nm. As a result the observations in this thickness range suggest the small scale deformation mechanisms operating in the metallic Ni(Co) and Co interphases in the reduced $\text{Ni}_x\text{Co}_{1-x}\text{O}/\text{ZrO}_2(\text{CaO})$ model system to be similar to the conventional deformation mechanisms operating in large grain sized Co and Ni-Co alloys.

5.2.2 Observations of the Small Scale Deformation Behavior in the Metallic Interphases with the Thickness of Less Than 100 nm

With decreasing the size of the interphase thickness to values smaller than 100 nm, particular changes are observed in the small scale deformation mechanism of the metallic interphase upon deformation of the reduced $\text{Ni}_x\text{Co}_{1-x}\text{O}/\text{ZrO}_2(\text{CaO})$ composite. Figures 5.13 to 5.18 show the various deformation mechanisms operating within the metallic interphase with less than 100 nm thickness in this model system. Figure 5.13 indicates the deformation behavior of metallic Co interphase with the interphase thickness of about 60 nm. The figure shows an area of Co interphase very near to the indentation mark in the reduced CoO/ZrO_2 sample. At this size scale the interphase remains single crystalline and the twinning incidence is significantly reduced within the metallic interphase. Also as the figure presents, the Moiré fringes within the metallic Co interphase (indicated with arrows on the image) suggest presence of dislocations within the confined Co layer in this region. Figure 5.14 presents a similar situation, where the

dislocations originating from the metal-ceramic interfaces extend into the metallic Co layer of about the same thickness.

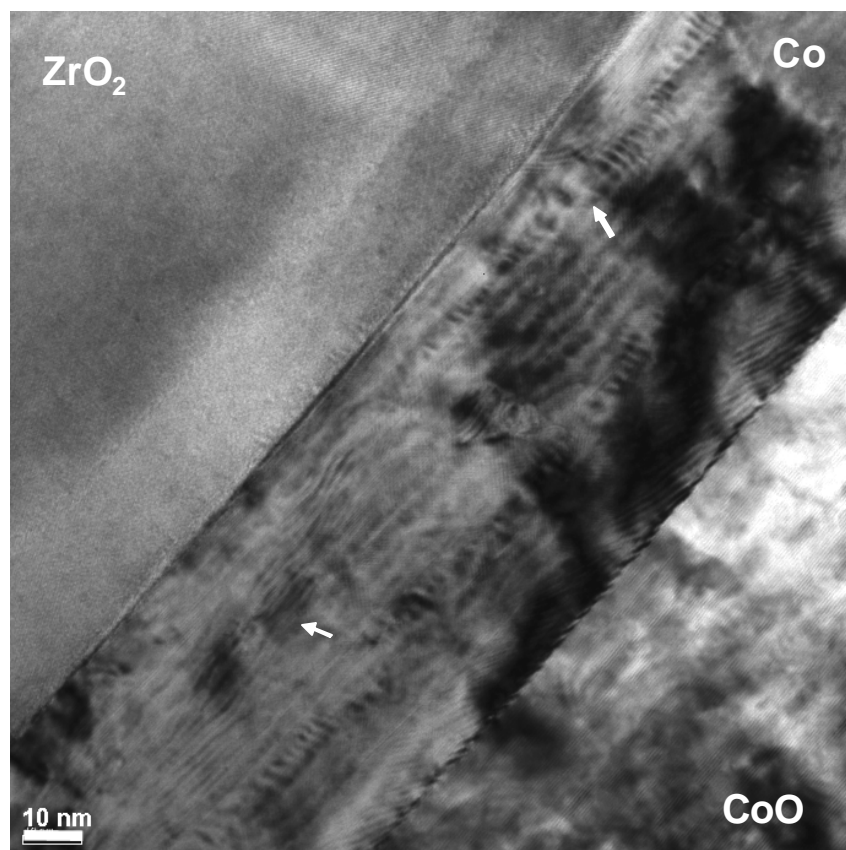


Figure 5.13 Small scale deformation behavior of confined Co interphase with about 60 nm thickness. The Moiré fringes shown with arrows suggest presence of dislocations in this region.

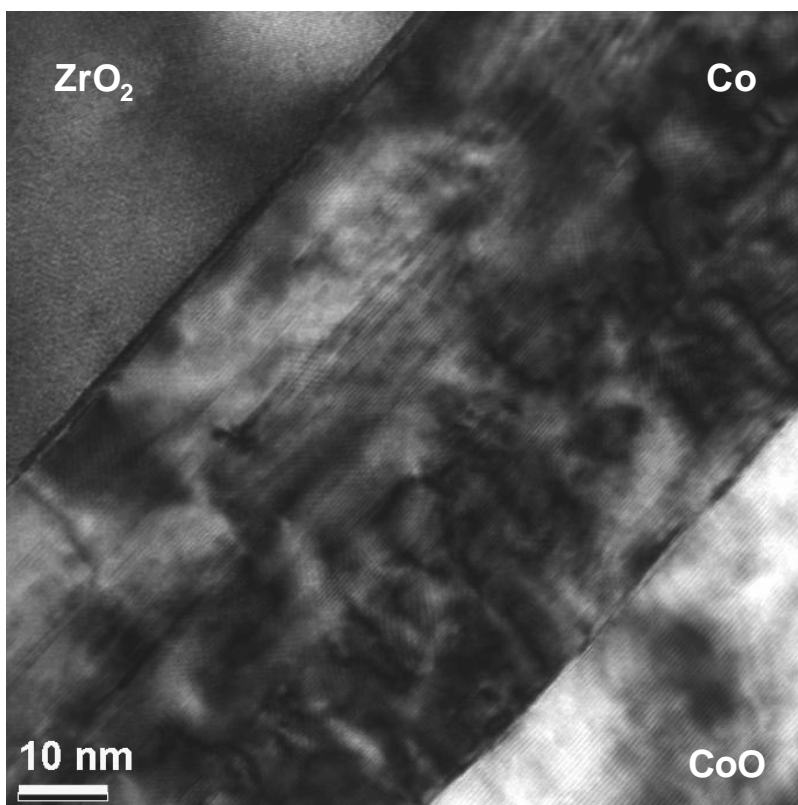


Figure 5.14 Dislocations extended into the confined Co interphase of about 60 nm thickness.

Figure 5.15 indicates another region of Co interphase with 70 to 80 nm thickness. This region shows presence of small and narrow twins within the Co interphase. Figure 5.16 presents another area of Co interphase indicating sharp streaks along the metallic interphase with thickness of about 60 nm after deformation. The streaks here suggest presence of stacking faults within the metallic Co interphase in the deformed reduced CoO/ZrO₂(CaO) composite.

The TEM observations at this size scale in the deformed reduced CoO/ZrO₂(CaO) composite show the twinning propensity to significantly drop in the Co interphase upon decreasing the interphase thickness to values of about 80 nm or less. Also, at this size scale the twins in the metallic Co interphase maintain a much smaller thickness compared with that of the Co interphase at larger thickness (above 100 nm). The origin of the twins occasionally observed in the Co interphase at this size scale could not be determined at this stage since similar twinning propensity is observed in the reduced CoO/ZrO₂ sample before and after deformation. In-Situ TEM mechanical testing is required to further reveal the twinning formation process during deformation of the sample.

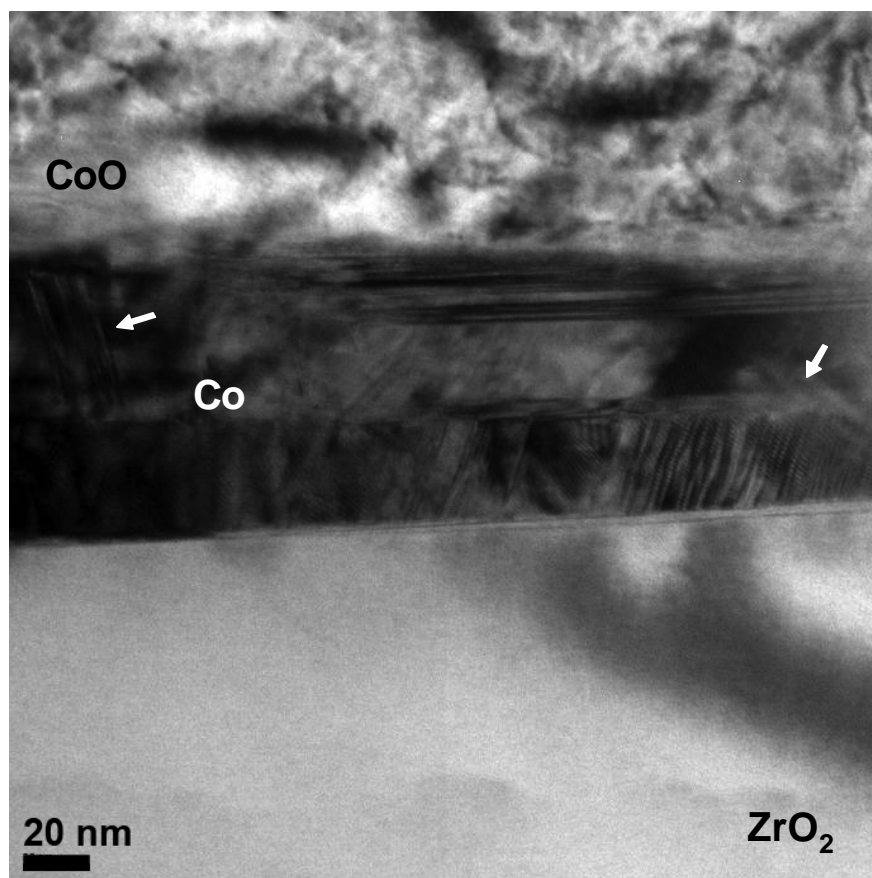


Figure 5.15 Twinning formation within Co with 70-80 nm thickness in the reduced deformed CoO/ZrO₂(CaO) composite.

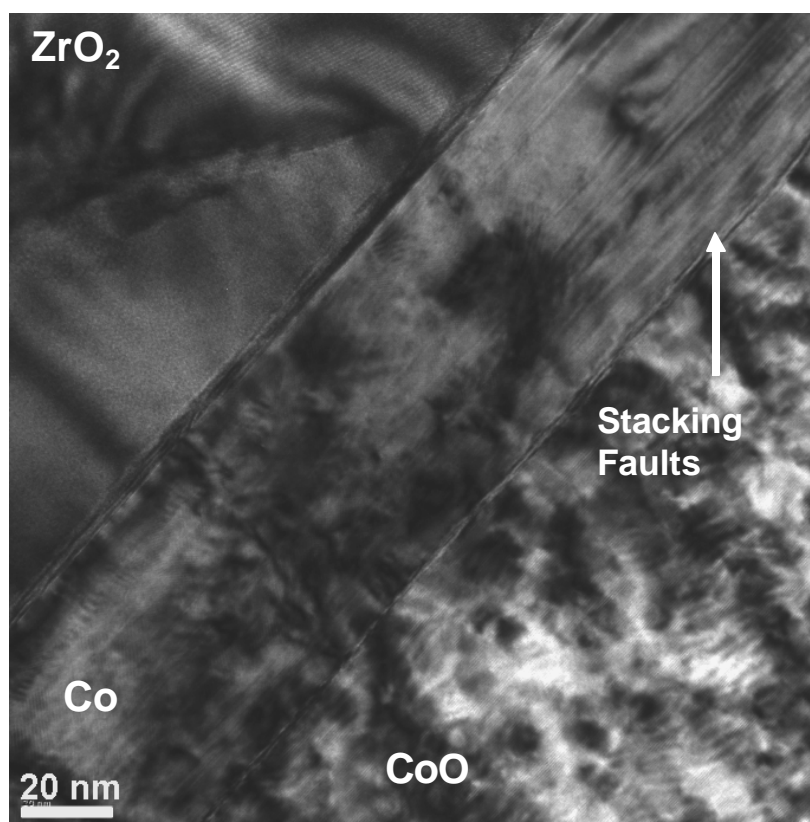


Figure 5.16 Stacking fault formation within the Co interphase after deformation. (shown with arrow on the image) The interphase thickness is about 60 nm in this region.

Figure 5.17 presents the small scale deformation behavior in the reduced $\text{Ni}_{0.5}\text{Co}_{0.5}\text{O}/\text{ZrO}_2(\text{CaO})$ composite very close to the indentation mark with the metallic Ni(Co) layer thickness of about 75 nm. This region shows limited plastic deformation to occur in the form of dislocations extended into the Ni(Co) interphase. Figure 5.18 (a) presents another area of Ni(Co) interphase with thickness of about 48 nm. A considerable elastic strain contrast in the metallic interphase can be seen in Figure 5.18 (a). This contrast indicates highly strained Ni(Co) film with little to no plastic deformation,

confined between $\text{Ni}_{0.5}\text{Co}_{0.5}\text{O}$ and $\text{ZrO}_2(\text{CaO})$. Figure 5.18 (b) reveals traces of dislocation slip passing across the Ni(Co) interphase (thickness of 60 nm) close to the indentation mark.

According to the Figures here, dislocation formation is found to be the main deformation mechanism within Ni(Co) interphase at such size scales. Moreover, a drop is observed in the dislocation density within the Ni(Co) interphase with decreasing the metallic layer thickness. This investigation also did not show twinning formation within the Ni(Co) interphase at this size scale.

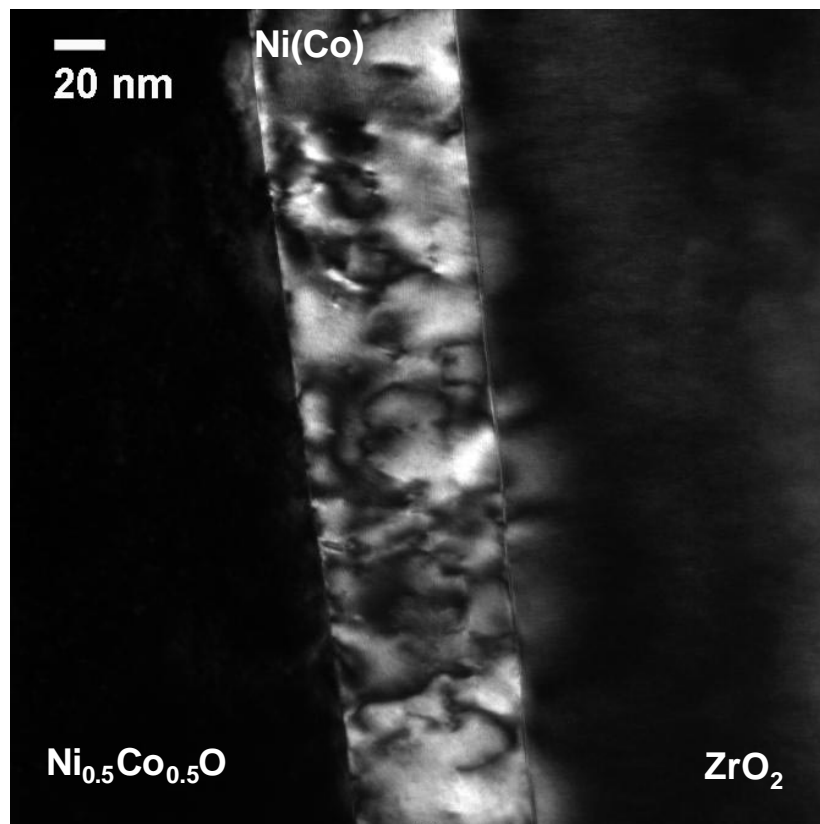
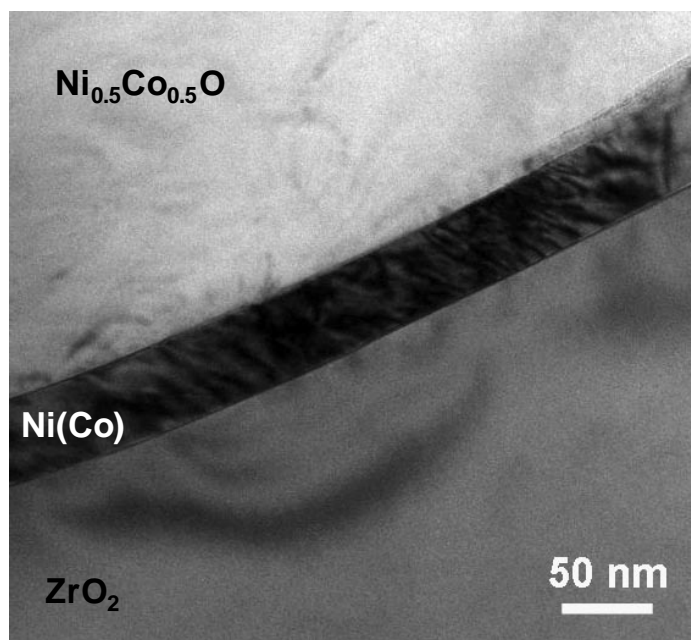
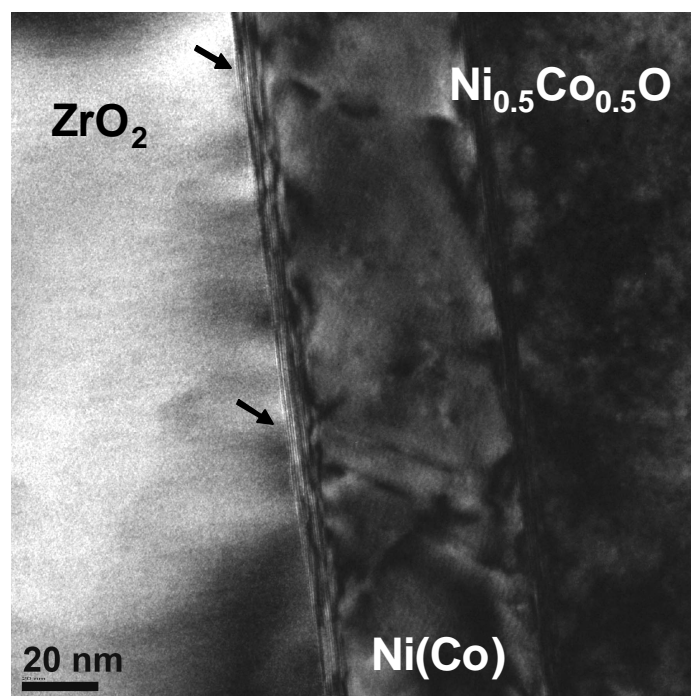


Figure 5.17 Dislocation formation within the confined Ni(Co) interphase with about 75 nm thickness.



(a)



(b)

Figure 5.18 Strain contrast within the $\text{Ni}(\text{Co})$ interphase pointing to the highly strained $\text{Ni}(\text{Co})$ film with little to no plastic deformation. The thickness of the confined $\text{Ni}(\text{Co})$ interphase shown here is 48 nm. (b) Traces of dislocation slip across the interphase in the $\text{Ni}(\text{Co})$ interphase with thickness of 60 nm (shown with arrows on the image).

The TEM investigations on the small scale deformation mechanism of the reduced $\text{Ni}_x\text{Co}_{1-x}\text{O}/\text{ZrO}_2(\text{CaO})$ model system show the extent of strain energy absorption and plasticity to significantly decrease within the metallic interphase for thickness values below 100 nm. The TEM observations at small interphase size scales indicate the confined metallic interphases to be highly strained with little to no plastic deformation with less dislocation activities. Another important observation shows the twinning propensity to significantly drop with decreasing the interphase thickness.

5.2.3 Mechanics of Crack Tip Interactions with the Metallic Interphase at Small Scales

To investigate the small scale mechanics of deformation and fracture behavior in the reduced $\text{Ni}_x\text{Co}_{1-x}\text{O}/\text{ZrO}_2(\text{CaO})$ composite, the deformation zone of the model system was studied using the transmission electron microscopy. For this investigation FIB lift-off technique described in Section 5.1.2 of this thesis was employed to prepare TEM samples from the deformed zone adjacent to the Vickers indentation mark.

Figures 5.19 to 5.22 indicate the small scale mechanics of crack tip interactions with the lamellae after Vickers indentation of the reduced $\text{CoO}/\text{ZrO}_2(\text{CaO})$ and $\text{Ni}_{0.5}\text{Co}_{0.5}\text{O}/\text{ZrO}_2(\text{CaO})$ composites. Figure 5.19 indicates a low magnification image of the deformation zone in the reduced $\text{CoO}/\text{ZrO}_2(\text{CaO})$ close to the indentation mark. The two cracks (labeled on the image) captured within the $\text{ZrO}_2(\text{CaO})$ layer in this area of the sample show the brittle fracture of $\text{ZrO}_2(\text{CaO})$ upon deformation of this composite. The strain field contrast within the $\text{ZrO}_2(\text{CaO})$ layer near crack 1 reveals the elastic deformation of this phase after indentation of this system. The strained area adjacent to

the crack is shown by an arrow in the upper right corner of the image. This figure also reveals the contribution of the metallic layer to crack arrest and crack tip blunting for both cracks 1 and 2 in this area of the sample.

Significant strain energy absorption through plastic deformation occurs within CoO after the crack arrest by the ductile interphase. Figure 5.19 clearly shows this strain energy absorption for “crack 2”. Figure 5.20 shows a higher magnification image for crack 2, where large dislocation bands are nucleated from the Co-CoO interface near the crack tip and are extended into the CoO phase. CoO has been previously shown to contribute to strain energy absorption in the pristine CoO/ZrO₂(CaO) system as a result of its limited plasticity at room temperature.^{17, 91} Figure 5.20 also points to the significant contribution of CoO to the strain energy absorption in the system compared with that of the metallic Co interphase (layer thickness of about 40-50 nm here). Although the metallic Co interphase in this region is fairly small (40-50 nm) it can arrest the crack probably through crack tip blunting and limited plastic deformation of this phase. In this region it was not possible to further study the extent of strain energy absorption within the Co interphase adjacent to the crack tip due to the relatively thick Co film at the vicinity of the crack tip.

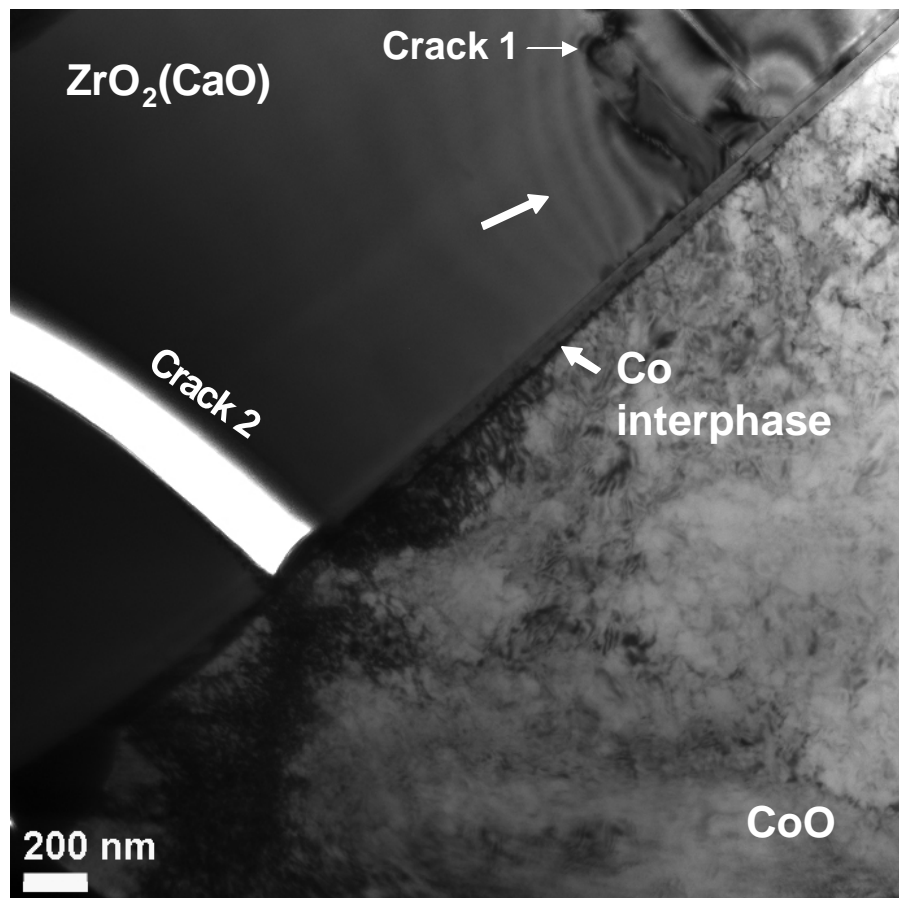


Figure 5.19 Crack tip interactions with the metal-ceramic lamellae in the reduced CoO/ZrO₂(CaO) sample.

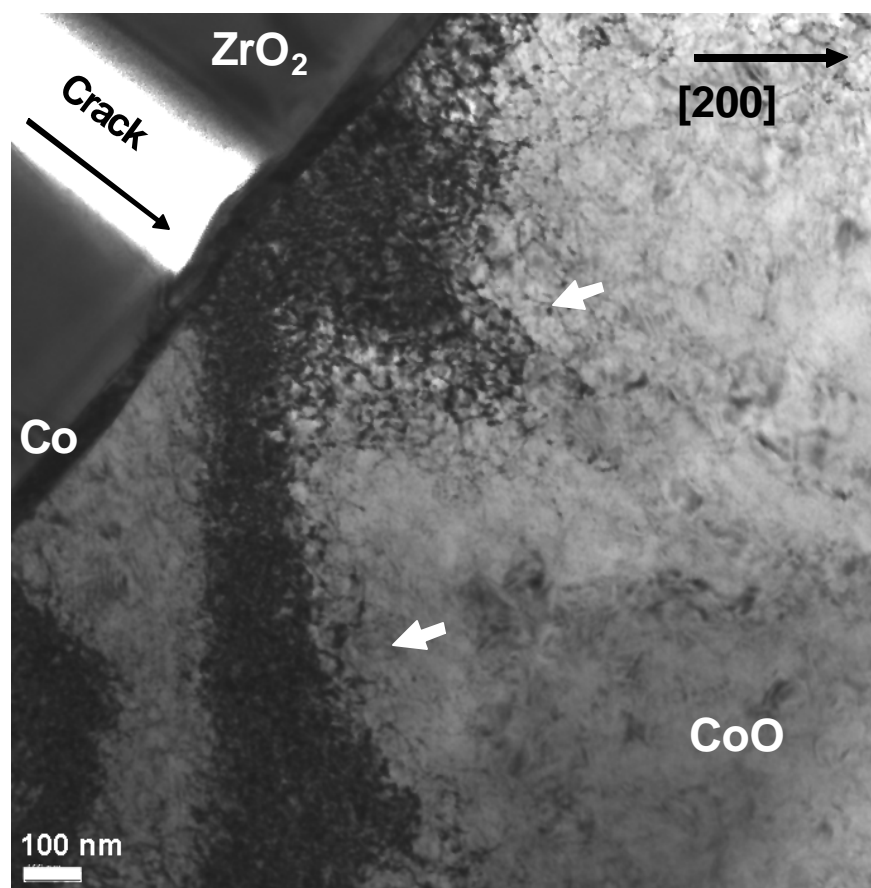


Figure 5.20 Crack arrest by the ductile interphase followed by extensive strain energy absorption within the CoO phase. The arrows indicate nucleation and extension of dislocation bands near the crack tip.

Figure 5.21 shows the crack arrest and crack tip blunting by the metallic Co interphase after deformation of the reduced $\text{CoO}/\text{ZrO}_2(\text{CaO})$ sample. The higher magnification image of the deformation behavior is shown in (b) where the crack tip blunting and crack arrest lead to limited deformation of Co through formation of dislocations adjacent to the crack tip (shown with arrows on the image). Although Co interphase in this area is very narrow in width (thickness $\sim 50\text{-}60\text{ nm}$), it is well-extended

along CoO and $\text{ZrO}_2(\text{CaO})$ phases and can favorably contribute to strain energy absorption in the system. No indication of strain energy absorption through plastic deformation of Co is, however, observed at extended length scales further away from the crack tip. Also further TEM investigations in this area do not show any indication of twinning within Co upon deformation in this sample. This figure also reveals strain energy absorption extended into CoO through dislocation emission from the Co-CoO interface at the crack tip vicinity.

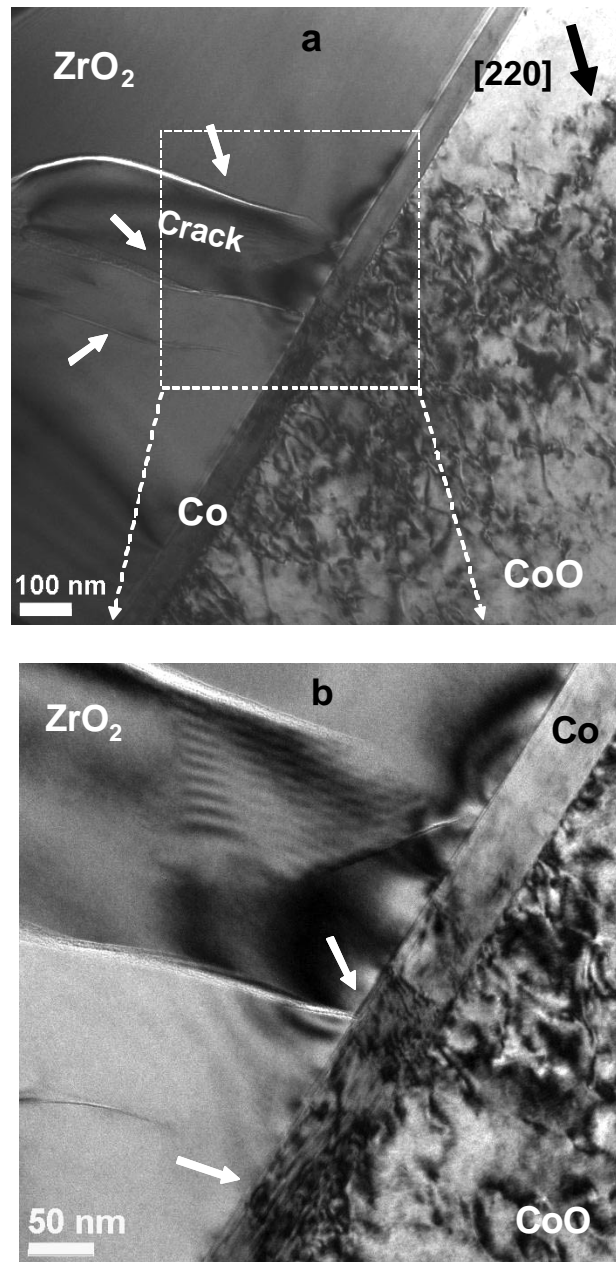


Figure 5.21 (a) Dislocation nucleation within CoO indicates extensive plastic deformation of CoO near the crack tip in this area. The white arrows on the image point to the multiple cracks within the ZrO₂(CaO) phase, while the black arrow shows the crystal orientation of the CoO phase. (b) Limited plastic deformation of the metallic Co interphase (indicated by arrows on the image) leading to crack arrest and crack tip blunting.

The crack tip interactions with the lamellae in the reduced $\text{CoO/ZrO}_2(\text{CaO})$ clearly suggest a dual behavior of Co interphase at small size scales (less than 100 nm) where the strain energy absorption within Co seems to equally compete with the strain energy transfer through this phase from ZrO_2 into the CoO phase. Therefore it is believed that the metallic Co interphase at such size scales is more likely to transfer the strain energy into the next layer rather than considerably absorbing it within itself.

Figure 5.22 indicates an area of the reduced $\text{Ni}_{0.5}\text{Co}_{0.5}\text{O/ZrO}_2(\text{CaO})$ sample with crack arrest by the metallic Ni(Co) interphase. The observations in the deformed reduced $\text{Ni}_{0.5}\text{Co}_{0.5}\text{O/ZrO}_2(\text{CaO})$ system indicate a similar deformation mechanism where the Ni(Co) interphase contributes to crack tip blunting and crack arrest. These investigations however did not show any contribution of the $\text{Ni}_{0.5}\text{Co}_{0.5}\text{O}$ phase to strain energy absorption through plastic deformation in this region. Due to the relatively large thickness of the sample here it was not possible to further study the deformed region within the Ni(Co) interphase at the vicinity of the crack tip.

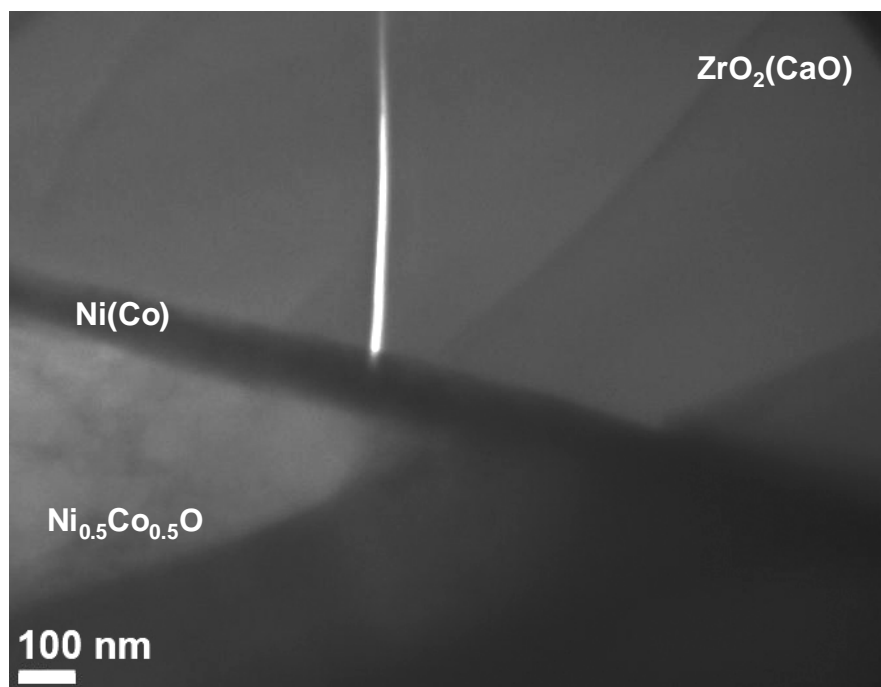


Figure 5.22 Crack tip interactions with the metallic interphase indicating crack arrest by the metallic Ni(Co) interphase. The thickness of the Ni(Co) interphase in this region is about 40-50 nm.

5.2.4 Differences in the Deformation Mechanisms Observed in the Metallic Interphase across the Size Scale Studied Here

The deformation mechanism in the reduced $\text{Ni}_x\text{Co}_{1-x}\text{O}/\text{ZrO}_2(\text{CaO})$ composite at various length scales for both Co and Ni(Co) interphase shows strain energy absorption mechanisms operating in the reduced model system through plastic deformation within the metallic interphase. Some differences in the small scale deformation mechanism are however noticed across the size scale in this model system. For the interphases of above 100 nm thickness, we observe the deformation mechanism in the metallic Co interphase

to be mainly through formation of twins and stacking faults. Upon addition of Ni, twinning propensity starts to decrease in the solid solution interphase and dislocation slip becomes a more prominent deformation mechanism upon deformation. Previous work suggests this change in the deformation mechanism to be related to the increase in the stacking fault formation energy with addition of Ni to the system.¹¹²

With decreasing the grain size to less than 100 nm, the extent of plasticity within the metallic interphase is significantly reduced. The metallic interphase in this size scale is observed to be highly strained with little to no plastic deformation. Moreover, twinning incidence is significantly suppressed with decreasing the layer thickness and dislocation slip remains to be the prominent deformation mechanism in the system. Small scale TEM observations show the plastic deformation within the metallic interphase at such size scales (below 100 nm) to be mainly in the form of single dislocations confined within the metallic interphase.

5.3 Operative Deformation Mechanisms in the Reduced $\text{Ni}_x\text{Co}_{1-x}\text{O}/\text{ZrO}_2(\text{CaO})$ Composite

TEM investigations in the reduced $\text{Ni}_x\text{Co}_{1-x}\text{O}/\text{ZrO}_2(\text{CaO})$ composite clearly indicate the ductile interphases to significantly contribute to the strain energy absorption upon deformation of the system. These studies show a drop in the dislocation activities within the metallic interphase with decreasing the interphase size scale to values below 100 nm. Also no large scale plasticity is observed in the metallic interphase with thickness values below 100 nm. Although, at this thickness range (<100 nm), the metallic interphase still contributes to strain energy absorption through localized plastic

deformation and crack tip blunting at the neighboring regions to the indentation mark and the crack tip.

With decreasing the size scale, a contrast associated with the bend contours is observed within the microstructure, which indicates the metallic interphase undergoing elastic strain without yielding (i.e. Figure 5.18). This elastic strain within the metallic interphase suggests the failure mechanism in the film to shift from the ductile manner to the semi-brittle manner. It also indicates the metallic interphase to transfer the load to the adjacent layer rather than absorbing the strain energy within itself.

In the following sections the two deformation mechanisms, twinning and dislocation formation, in this model system are discussed.

5.3.1 Dislocation Nucleation in the Metallic Interphase

To understand the role of size scale on the deformation mechanism of the ductile-brittle $Ni_xCo_{1-x}O/ZrO_2(CaO)$ composite, previous studies should be considered. *in situ* TEM deformation of nanocrystalline metallic Ni shows array of dislocations within the Ni grains with a particular distance from each other.¹⁴⁹ TEM observations during deformation of nanocrystalline metals, such as Cu and Ni have shown a high dislocation density in the grains of about 100 nm in size to values as small as 20 nm.¹⁵⁰ With decreasing the grain size to values such as 20 nm, a drop is observed in the dislocation density and other mechanisms such as grain boundary sliding have been suggested to be responsible during deformation.¹⁵¹ These studies suggest a critical thickness below which the dislocation sources may not be able to operate, since the stress for dislocation

nucleation and motion at such a critical thickness reaches the theoretical shear stress of the crystal.

In the model system studied here, the nanoscale metallic interphases are in the form of single crystalline films confined between two rigid ceramic phases. Previous studies by Ronay⁶⁴ show the relation between the yield stress for thin FCC films bonded to rigid substrates and their grain size and film thickness. As previously discussed in Chapter 2, these studies clearly show that the yield stress of the film is inversely related to its thickness according to the relationship shown in equation 5.1.⁶⁴ This increase in the yield stress is due to the high levels of strain hardening that occurs in the thin film with decreasing the film thickness, as shown by

$$\tau_y = \tau_s + \frac{1}{\pi} \left(\frac{b\gamma}{sl} \right)^{1/2} + mG \left(\frac{2b\gamma}{D} \right)^{1/2} \quad 5.1$$

where τ_s is the flow stress of the material without interfaces or grain boundaries in equation 5.1. l in this equation is the film thickness and D is the grain size. Other parameters are described as G to be the shear modulus, s to be a constant depending on the orientation of the primary slip system of the film to the substrate, γ to be the plastic strain, and m to be the Taylor orientation factor. The second term in the equation indicates the stress required to overcome the long range stress field of the geometrically necessary dislocations, while the third term indicates the stress required to overcome the short range interactions between the crossing dislocations. Figure 5.23 shows the dependence of the yield stress to film thickness at a constant grain size based on equation 5.1. As this figure shows, the yield stress in a thin film increases with decreasing the film

thickness. In other words, with decreasing the layer thickness to smaller values, a higher applied load is required for further dislocation emission in the film.

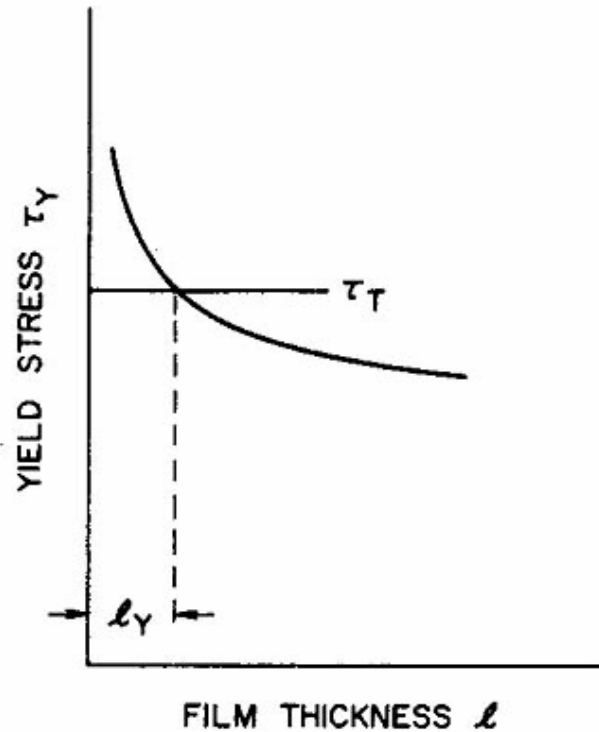


Figure 5.23 Yield stress for an FCC thin film bound to a rigid substrate as a function of film thickness assuming the grain size to be constant.⁶⁴

Previous studies have clearly shown that for a given applied load and a film thickness, there is an equilibrium number of dislocations that can form a pileup in the film.⁵⁶ These studies have defined an energy criterion to calculate the equilibrium number of dislocations in a thin film. According to this criterion, a dislocation would nucleate in

a film only if the total energy of the system is reduced upon this nucleation. Equation 5.2 gives the equilibrium number of dislocations in a confined thin film based on these calculations.⁵⁶

$$n = \frac{4\pi(1 - \nu)}{\ln\left(\frac{\tilde{h}}{\tilde{r}}\right)} \left(\frac{\tilde{K}_{app} \sqrt{\tilde{h}}}{A\sqrt{2\pi}} \sin\phi \cos\frac{\phi}{2} - \tilde{\gamma} \right) \quad 5.2$$

In this equation n is the equilibrium number of dislocations in the film, ν is the Poisson's ratio, \tilde{K}_{app} is the applied stress intensity, \tilde{h} is the normalized ductile layer thickness, ϕ is the angle between the slip plane and the interface, A is a constant, and \tilde{r} is the normalized core radius of the dislocation cluster in the film. Figure 5.24 shows the relationship between the equilibrium number of dislocations within a thin film and the applied stress intensity for different values of layer thickness, assuming the other parameters to be given. This figure clearly indicates a decrease in the number of the dislocations (n) upon reducing the layer thickness (\tilde{h}), for a constant applied stress intensity (\tilde{K}_{app}).

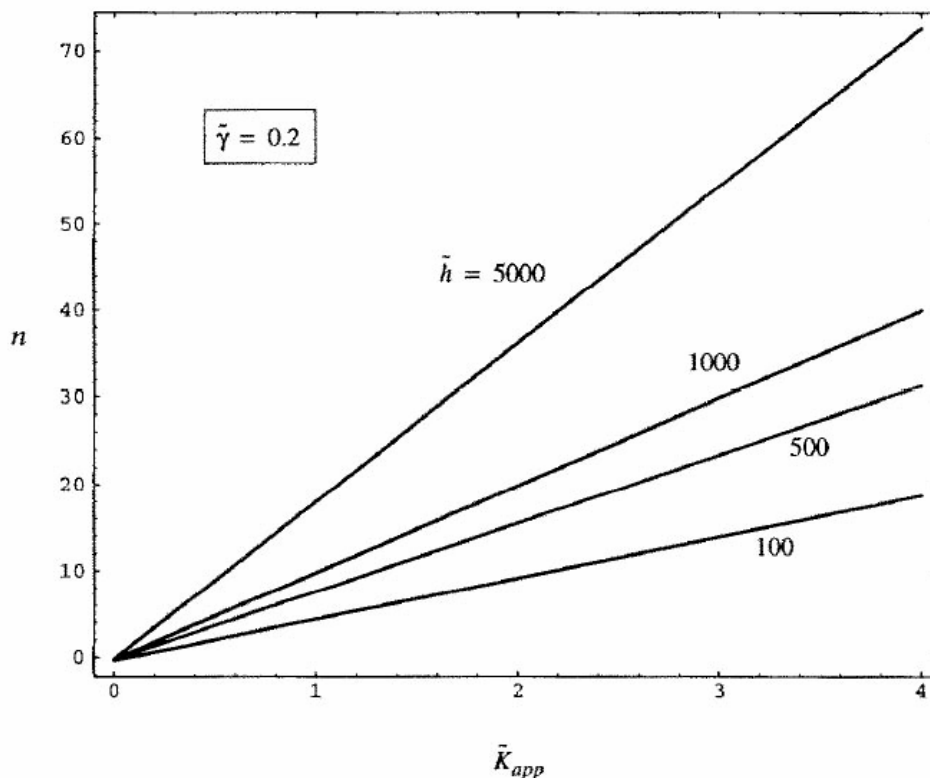


Figure 5.24 The equilibrium number of dislocations as a function of the applied stress intensity within a layer for different values of layer thickness in a model system.⁵⁶

The models above point to the fact that in a multi-layered system, the already existing dislocations within the thin confined film apply a back stress on the crack tip, which hinders further dislocation emission in the film.⁵⁶ Therefore, for further deformation to occur in the thin film, higher levels of applied load are required for the dislocation motion. With increasing the applied load, the tensile stress at the crack tip gradually increases till it reaches the cohesive strength of crystal in the thin film leading to cleavage in the multi-layered systems.

In this investigation, the experimental observations indicate a drop in the dislocation activities with decreasing the size scale. These observations are consistent with the theoretical models discussed above. In the reduced $\text{Ni}_k\text{Co}_{1-x}\text{O}/\text{ZrO}_2(\text{CaO})$, with reduction of the layer thickness, the dislocations in the metallic film impose a back stress on the interface, which hinders further dislocation emission from the interfaces, resulting in the hardening and the increase in yield stress of the metallic interphase. The drop in the dislocation activities within the metallic interphase in the reduced $\text{Ni}_k\text{Co}_{1-x}\text{O}/\text{ZrO}_2(\text{CaO})$ is believed to be due to the reduced size scale of the metallic interphase in this model system.

5.3.2 Deformation Twinning in the Metallic Interphase

Twinning is another deformation mechanism that has been observed in the metallic interphases in the reduced $\text{Ni}_k\text{Co}_{1-x}\text{O}/\text{ZrO}_2(\text{CaO})$. The twins have been mostly observed to develop across the confined metallic interphases of the thickness of above 100 nm. Upon decreasing the interphase thickness, the twinning propensity is dropped and the twins maintain a narrower thickness. TEM investigations have also shown significant elastic strain with little to no plastic deformation in the metallic interphases with thickness of less than 100 nm (Figure 5.18).

To understand the differences in the small scale deformation mechanisms in the metallic interphase in the reduced $\text{Ni}_k\text{Co}_{1-x}\text{O}/\text{ZrO}_2(\text{CaO})$ composite, it is important to first describe various deformation mechanisms operating in FCC materials. Slip and twinning are the two major deformation mechanisms operating in FCC systems upon deformation at room temperature.^{152, 153} For any type of dislocation activity to occur in FCC materials

as a result of deformation, a Shockley partial dislocation should be nucleated first. Shockley partial dislocations can be nucleated/adsorbed from/into the grain boundaries in a material. Nucleation and emission of partial dislocations on the (111) planes of FCC crystals can result in the formation of stacking faults within the crystal. Upon formation of a stacking fault, the normal FCC sequence of the crystal (ABCABC) changes into a HCP structure with a faulted sequence (ABAB) with respect to the (111) mirror plane in FCC crystals. For an FCC crystal to form a twin, several partial dislocations on the adjacent (111) planes need to be generated to create a partial dislocation network across the adjacent (111) planes. As a result, twinning is known to require a significant level of shearing leading to a considerable reorientation of the crystal lattice compared with dislocation slip. Figure 5.25 presents a schematic representation for twinning compared to slip in FCC metallic systems.¹⁵⁴

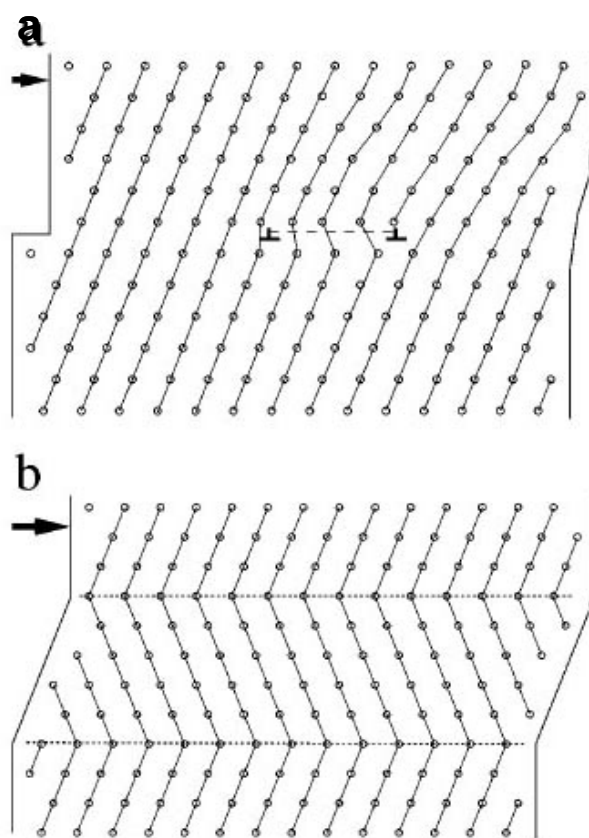


Figure 5.25 Schematic illustration of the two plastic deformation modes; (a) slip versus (b) twinning in a FCC metal.¹⁵⁴

Several parameters can affect twinning formation within a crystal upon deformation. Chemistry and stacking fault formation energy of the system are among the parameters affecting twinning formation.^{112, 122, 124, 153, 155} The effect of chemistry on the stacking fault formation energy and consequently twinning propensity have been already discussed in Section 5.2.1 of this thesis and is clearly shown in Figures 3.16 and 5.26. Figure 3.16 clearly shows the effect of the presence of solute elements on the stacking

fault formation energy in Ni-Co alloy systems. Similar investigations point to a relationship between the stacking fault formation energy and the required stress for the nucleation of twins in a system. Figure 5.26 shows this relationship between the stacking fault formation energy and the twinning stress for various Cu alloys as an example for FCC alloy systems.^{156, 157} In the reduced $\text{Ni}_x\text{Co}_{1-x}\text{O}/\text{ZrO}_2(\text{CaO})$ composite model system, a transition is observed between the deformation mode from twinning (in Co) to slip (in Ni(Co)), which clearly points to the role of chemistry on the stacking fault formation energy and consequently the twinning incidence within the metallic interphase.

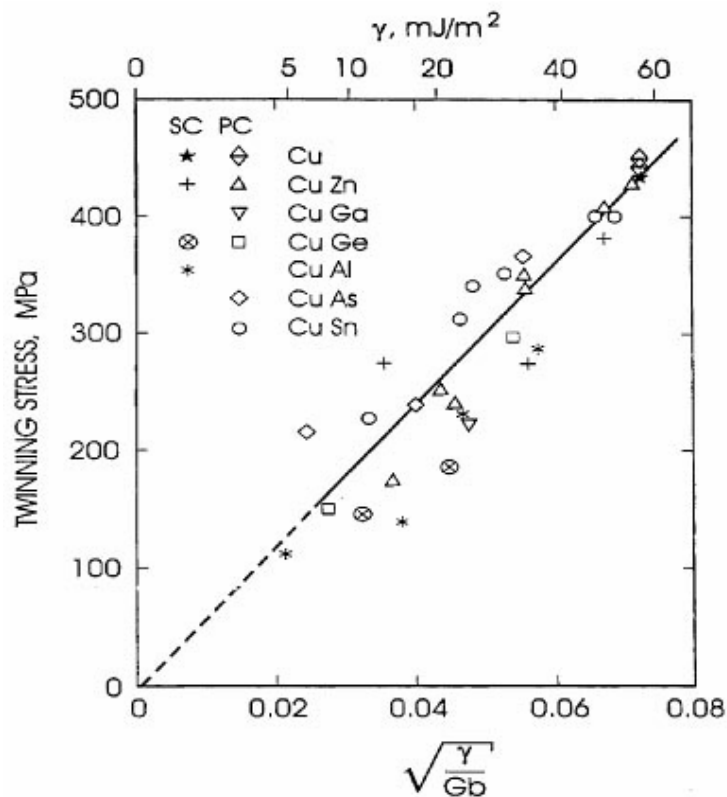


Figure 5.26 Twinning stress as a function of stacking fault formation energy for various Cu alloys.^{152, 153}

Another important parameter in the generation of twins is the stress at the crack tip during deformation.^{158, 159} Investigations by Hai *et al.* show that an appropriate combination of crystallographic orientation, loading mode and the crack tip morphology can lead to the generation of twins in materials that have no inclination to the formation of twins.¹⁵⁹ As an example, pure aluminum is generally known for not exhibiting deformation twins as this material has a high stacking fault formation energy.^{155, 160} However, Pond *et al.*¹⁶¹ were the first who found evidence of twinning at the crack tip in aluminum using transmission electron microscopy. Studies by Hai *et al.*¹⁵⁹ further demonstrated possibility of the nucleation of twins from the crack tip on the (111) planes of aluminum in certain combinations of loading mode and crystallographic orientation.

In the case of the reduced $\text{Ni}_x\text{Co}_{1-x}\text{O}/\text{ZrO}_2(\text{CaO})$ composite, a significant drop is observed in the twinning propensity of this system with decreasing the size scale. This drop seems to be independent of the crack tip morphology, crystallography and the loading mode, since the drop in the twinning incidence is generally observed in all the interphases with the small thickness. Therefore, other mechanisms are believed to be involved in the changes observed in the small scale deformation behavior of the system.

Grain size is another factor that should be discussed in the context of twinning formation.^{152, 153, 162} Armstrong *et al.* first conducted a comprehensive study for the deformation twinning in BCC metals.¹⁶² According to their studies, similar to dislocation slip in metals, a Hall-Petch relationship exists between the grain size and the twinning stress. Therefore a higher twinning stress is required for the onset of twinning with decreasing the grain size. Grain size dependency of twinning has been observed in many systems with various crystal structures.¹⁶³⁻¹⁶⁵ El-Danaf *et al.*^{163, 166} confirmed the effect

of the grain size on twinning propensity in a 70/30 brass alloy, where at the 250 μm grain size, the twinning density is much greater compared to the alloy with grain sizes of 30 and 9 μm . Another study by Lahaie *et al.*¹⁶⁴ showed twinning formation to occur upon deformation of fine grained Mg alloys with the grain size of 15 μm . No evidence of twinning was, however, observed in Mg alloy with 1 μm grain size.

Previous studies have investigated the development and growth of a twin within a polycrystalline system based on an energy criterion.^{167, 168} This energy criterion considers an energy balance between the initial and final equilibrium state upon development of a twin in a FCC system. It also takes into account the elastic strain energy within the volume of the material, the interfacial energy of the twin boundary and the intrinsic dissipation associated upon twinning. According to this energy balance a twin can grow to a maximum critical thickness, proportional to its radius.^{167, 168} Equation 5.3 indicates this relationship for FCC materials,

$$h_c = \beta h_{\text{min}} \quad 5.3$$

$$h_{\text{min}} = \frac{1}{\gamma_T} \sqrt{\frac{\sigma R_T}{\beta K}} \quad \text{and} \quad \beta = 1 + \frac{\mu R_T^3}{K 4v}$$

where h_c is the critical thickness of the twin, h_{min} is the energetically most favorable thickness of the twin band, R_T is the average in-plane radius of the twin, γ_T is the magnitude of a simple shear of a twin, v is the volume, μ is the elastic shear modulus, K is the energy factor, and σ is the interfacial energy density.

This criterion gives a direct relationship between the thickness of the twin (h) and its radius (R_T). Figure 5.27 indicates this relationship for different twin shapes/sizes in a

gamma-based Ti-Al alloy. Different values of the fR_T^3/V term in this figure represents different twin shapes in the system. Based on this energy criterion, a twin can grow to a maximum critical thickness, related to its relative radius.¹⁶⁷ Upon further growth of the twin beyond its critical thickness, the energy equilibrium becomes unstable and a new twin band is created in the system instead of the growth of the original twin.

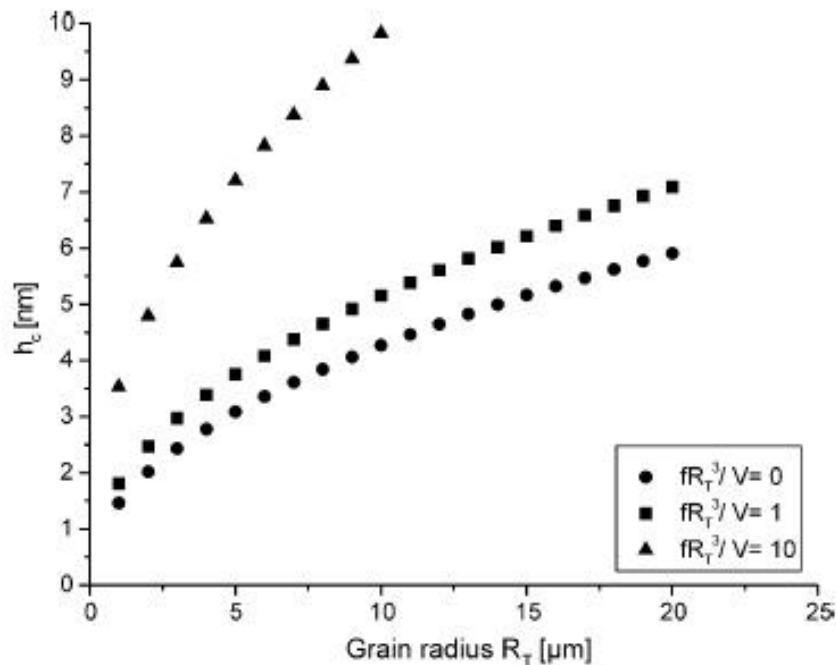


Figure 5.27 Critical thickness of a twin as a function of its radius calculated for a gamma-based Ti-Al alloy.¹⁶⁷

Further analysis of this energy criterion also gives a relation between the twin thickness and the elastic strain energy associated with the growth of a twin.^{167, 168} Figure 5.28 clearly shows this relationship between the elastic strain energy per unit length of a

twin to its thickness. As this figure indicates, the elastic strain energy per unit length of the twin is lower for a smaller twin thickness. An interpretation of this relation leads to the point that the twins would acquire a smaller thickness in nano-crystalline materials compared to the large-grained systems to minimize the elastic strain energy associated with them. It should be noticed that this energy balance does not consider the initial presence of a twin nucleus and the inelastic accommodation of the stress at the vicinity of the twin edges. It also considers a homogeneous, linearly elastic and isotropic material for their investigation. Although this criterion represents a simple model for the twin growth in FCC structures, a more qualitative interpretation of this model indicates higher stability of narrower twins in small-grained structures.

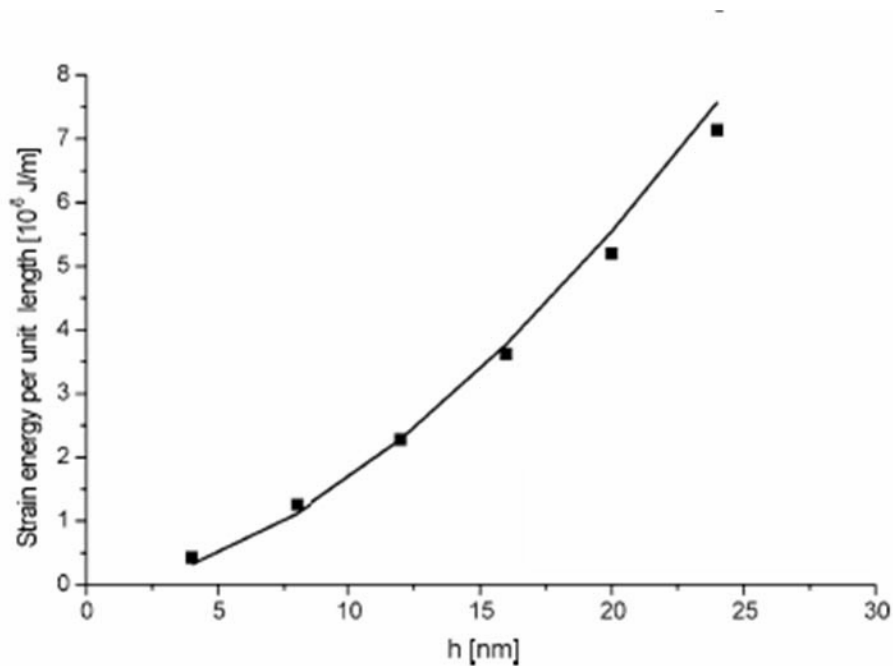


Figure 5.28 Elastic strain energy per unit length of a twin as a function of twin thickness. The twin length is considered to be 700 nm here.¹⁶⁷

In the studies conducted on the reduced $\text{Ni}_x\text{Co}_{1-x}\text{O}/\text{ZrO}_2(\text{CaO})$ composite, the twinning propensity is dropped with decreasing the size scale. Moreover the twin thickness in this composite is reduced with decreasing the layer thickness. The observations in the reduced $\text{Ni}_x\text{Co}_{1-x}\text{O}/\text{ZrO}_2(\text{CaO})$ composite are in agreement with the calculations done by Fischer¹⁶⁷ and Petryk¹⁶⁸ in terms of the development of the twins in FCC materials. The simulations discussed above clearly show that the elastic strain energy associated with the development of a twin is smaller for a smaller twin thickness. Therefore it is very likely for the twins to maintain a narrower thickness to further help minimize the elastic strain associated with them. In the reduced $\text{Ni}_x\text{Co}_{1-x}\text{O}/\text{ZrO}_2(\text{CaO})$ composite with thickness of less than 100 nm, the drop in the twinning propensity could be a direct result of the size scale leading to the minimization of the elastic strain energy within the interphase.

Although the role of size scale on the resulting deformation behavior of the metallic interphases is evident, it is believed that apart from the role of size scale, the boundary conditions also play a significant role in the resulting deformation behavior of the metallic interphases in this model system. To identify the role of the boundary conditions in our system, the small scale deformation mechanism in other nano-crystalline FCC metallic systems should first be considered. Deformation twinning has been shown to occur upon deformation in several nano-crystalline metallic systems such as Ni, Cu and Al.^{155, 169-171} As an example, electrodeposited nano-crystalline Ni film with an average grain size of 30 nm shows twinning formation after deformation of this

sample.¹⁷¹ Also the molecular dynamic simulations clearly show twinning to be an operating deformation mechanism in nano-crystalline FCC metals such as Cu and Ni¹⁵⁵

Due to these observations, it is believed that with decreasing the size scale the boundary conditions in the system start to influence the deformation mechanisms operating in the metallic interphase in the reduced $\text{Ni}_k\text{Co}_{1-x}\text{O}/\text{ZrO}_2(\text{CaO})$. To create a twin in a FCC crystal, several partial dislocations are required to be generated from the grain boundaries/interphases on the adjacent (111) planes in a thin crystal (Figure 5.25). A combination of easy atomic shuffling and a minimum magnitude for the associated twinning shear results in the formation of twins within a crystal.¹⁵³

In the reduced $\text{Ni}_k\text{Co}_{1-x}\text{O}/\text{ZrO}_2(\text{CaO})$ composite, the metal-ceramic laminates are very well bonded together. $\text{Ni}_k\text{Co}_{1-x}\text{O}$ and $\text{ZrO}_2(\text{CaO})$ are considered as stiff materials with no ductility at room temperature. Alternatively, twinning is known as a shearing process which leads to a significant reorientation of the lattice in the system.

In the reduced $\text{Ni}_k\text{Co}_{1-x}\text{O}/\text{ZrO}_2(\text{CaO})$ model system, the drop in the twinning propensity with decreasing the size scale, is believed to be the result of a combination of size scale and the presence of the rigid lattice planes at the interfaces in the composite. For the twins to initiate and grow within the ductile interphase, the rigid ceramic phases bound to the metallic interphase should be able to accommodate the significant volume reorientation of the metallic interphase. Dislocation slip on the other hand is a deformation process which does not require massive reorientation of the lattice. Therefore, it is believed that the combination of size scale and the boundary conditions in this model system lead to the significant drop in the twinning propensity. A more

thorough investigation is required to further understand the role of the interfaces on the initiation and growth of the twins in the metallic interphases studied here.

Another important parameter that can affect the deformation mechanism is the confining pressure. Molecular dynamics simulations by Xu *et al.*^{172, 173} on BCC molybdenum clearly indicate a shift from deformation twinning to dislocation slip with increasing the confining pressure on the system. These studies indicate an increase in the homogeneous nucleation stress of the deformation twins with increasing the pressure in the system. In order to examine the role of confining pressure on the operating deformation mode in the model system here, the stress state in the reduced $\text{Ni}_x\text{Co}_{1-x}\text{O}/\text{ZrO}_2(\text{CaO})$ model system should be measured. In addition, the molecular dynamics simulations should be carried out to further reveal the role of the confining pressure on the operating deformation mechanisms for FCC materials.

5.4 Summary and Conclusions

TEM studies of the reduced $\text{Ni}_x\text{Co}_{1-x}\text{O}/\text{ZrO}_2(\text{CaO})$ show a size dependent strain energy absorption mechanism operating within the confined metallic interphases of Co and Ni(Co) after deformation of this composite. In this study, the thickness of the metallic interphase changes from about 50 nm to 300 nm. At large interphase size scales (> 100 nm), the interphases show a significant contribution to strain energy absorption within the system through plastic deformation. This deformation is observed to be mainly in the form of twins and stacking faults in Co metallic interphase and dislocation slip in Ni(Co) interphase.

At smaller size scales (<100 nm), plasticity within the metallic interphase is hindered and the dislocation activity is reduced. The microstructural observations in the metallic interphases at small length scales (<100nm) point to the presence of elastic strain within the metallic interphase with little plasticity and minimal number of twins. The decrease in the dislocation activities and the thickness of the twins has been related to the decrease in the interphase thickness. Also with decreasing the interphase thickness, a lower twinning propensity is observed within the interphase.

With decreasing the interphase thickness to values below 100 nm, although the metallic interphase does not show significant plastic deformation upon deformation of the system, it still contributes to crack arrest and crack tip blunting. Crack tip interactions with the metallic interphase of (thickness of less than 100 nm) clearly show that at such size scales Co mainly transfer the load from ZrO_2 to CoO phase with little plastic deformation. These studies point to the significant role of CoO in the strain energy absorption of the system through its plastic deformation.

6 EVALUATION OF THE MECHANICAL PROPERTIES IN THE $\text{Ni}_x\text{Co}_{1-x}\text{O}/\text{ZrO}_2(\text{CaO})$ MODEL SYSTEM VIA A MINIATURE MECHANICAL TESTING METHOD

The previous chapters in this thesis suggest toughening enhancement of the reduced $\text{Ni}_x\text{Co}_{1-x}\text{O}/\text{ZrO}_2(\text{CaO})$ system through observation of several toughening mechanisms, operating within the reduced composite. The next immediate step in this research would be to assess the strength and toughness of the system before and after reduction through mechanical testing to further evaluate this toughness enhancement. Since the depth of reduction in the reduced $\text{Ni}_x\text{Co}_{1-x}\text{O}/\text{ZrO}_2(\text{CaO})$ system varies only from about 50 to 100 nm, miniature mechanical testing would be an ideal route for this evaluation.

This chapter starts with presenting the basics of the miniature mechanical testing technique termed “The Theta Specimen”. This technique was developed and utilized for testing the $\text{Ni}_x\text{Co}_{1-x}\text{O}/\text{ZrO}_2(\text{CaO})$ model system. The chapter further continues by presenting the experimental techniques employed for fabrication and characterization of the Theta specimens from $\text{Ni}_x\text{Co}_{1-x}\text{O}/\text{ZrO}_2(\text{CaO})$ followed by their testing.

6.1 Design of the Theta Specimen

Since materials show significantly different physical and mechanical properties at small sizes compared with that of their bulk properties, development of a miniature mechanical testing stage is very crucial for the design of the nanostructures. For this project, a miniature testing stage termed “The Theta Specimen” was utilized for testing the material properties of the $\text{Ni}_x\text{Co}_{1-x}\text{O}/\text{ZrO}_2(\text{CaO})$ system.

The novel design of the “Theta Specimen” originally grew out of the work by Durelli *et al.*¹⁷⁴⁻¹⁷⁶ in the 1960s. This design was further employed to create a platform for the measurement of the mechanical properties of various materials at micron size scales under pure tension.^{177, 178} This testing stage is a standing hexagonal-framed micron-scale structure with a horizontal thin sliver in the middle. Applying compressive forces on the top axis of the hexagon (using Nano-Indentation technique) results in uniaxial stresses within the horizontal sliver located at the middle of the structure. Figure 6.1 shows a schematic front view of the testing stage as well as the simulated stress distribution within the stage upon compressive loading at the top surface for silicon.¹⁷⁹ The unique stress distribution within this geometry allows one to examine the mechanical properties of the material under pure tension at micron and nanoscales.

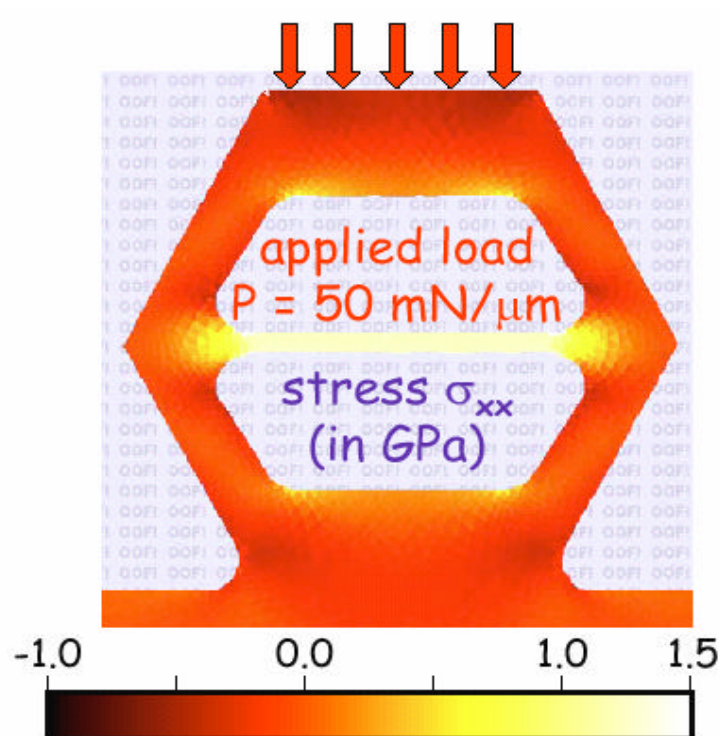


Figure 6.1 Finite element modeling of the stress distribution upon compressive loading of a Si miniature sample at the top surface.¹⁷⁹

Upon compression loading at the top surface, one can calculate the tensile stress along the middle beam to the applied load and consequently to the strain according to the relation in equations 6.1 and 6.2.¹⁷⁷

$$\sigma_{xx} = k\left[\frac{P}{Dt}\right] = E'\epsilon \quad 6.1$$

$$\epsilon_{xx} = M\left(\frac{\delta}{D}\right) \quad 6.2$$

where σ_{xx} is the tensile stress along the middle beam, p is the applied load, D is the diameter of the sample and K is a dimensionless constant that depends on the thickness of

the middle beam to the diameter of the sample. The strain in the x direction, ϵ_{xx} , is proportional to the displacement at the top surface (δ), the diameter of the sample (D), and M which is a constant depending on k. Figure 6.2 indicates these parameters on the specimen.

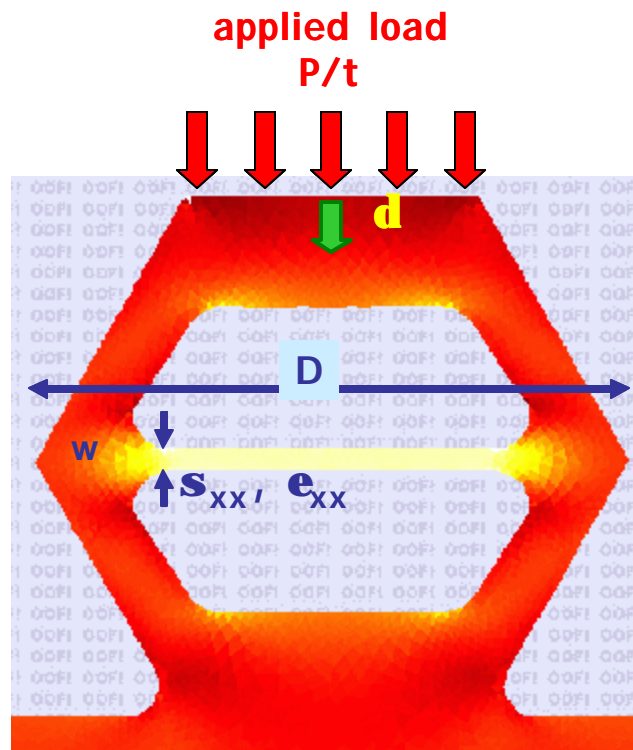


Figure 6.2 The theta specimen under compression along with the geometrical parameters affecting the resulting stress and strain in the middle web.¹⁷⁹

Quinn *et al.*¹⁷⁷ successfully tested single crystal silicon fabricated in the form of theta structures using the Theta specimen method. They used the indentation technique to apply load on the top surface of the sample. The resulting investigations in their work

indicate this method to be a suitable and simple design for materials testing at small scales under pure tension. The Theta specimen testing stage is employed in this thesis to examine the mechanical properties of the $\text{Ni}_x\text{Co}_{1-x}\text{O}/\text{ZrO}_2(\text{CaO})$ model system.

6.2 Experimental Procedures

To fabricate theta specimens from the $\text{Ni}_x\text{Co}_{1-x}\text{O}/\text{ZrO}_2(\text{CaO})$ model system, FEI Dual-Beam DB-235 Focused Ion Beam (FIB) in the Frederick Seitz Materials Research Laboratory (MRL), Center for Microanalysis of Materials (CMM) at the University of Illinois at Urbana Champaign (UIUC) was used. Beam sizes starting from 7000 pA to 500 pA were used to fabricate the small theta structures from $\text{Ni}_x\text{Co}_{1-x}\text{O}/\text{ZrO}_2(\text{CaO})$. The theta specimens were fabricated at the edge of the substrate, since it was possible to access the top and front sides of the samples by simply tilting the stage. Figure 6.3 (a) illustrates this geometry with respect to the ion beam directions. Figures 6.3 (b) and (c) show the fabrication steps respectively applied to make $\text{Ni}_x\text{Co}_{1-x}\text{O}/\text{ZrO}_2(\text{CaO})$ theta specimens.

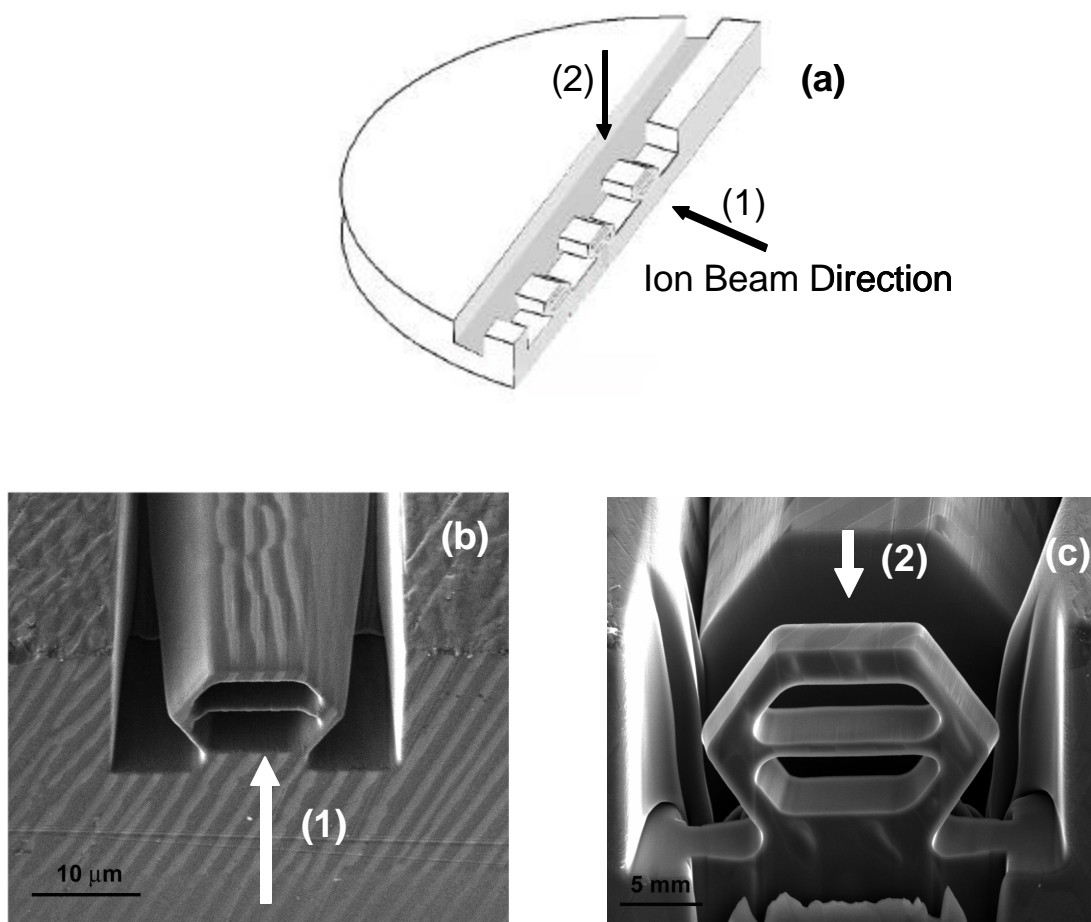


Figure 6.3 (a) The FIB fabrication procedures followed to construct the theta specimens, (b and c) along with the resulting sample fabricated from the pristine $\text{Ni}_x\text{Co}_{1-x}\text{O}/\text{ZrO}_2(\text{CaO})$. The fabrication steps have been shown respectively. (Image drawing: Courtesy of Ajit Jillavenkatesa, NIST, Gaithersburg, MD)

JSM-7000F SEM located at the Center for Microanalysis of Materials (CMM) at the University of Illinois at Urbana Champaign (UIUC) was used for the surface characterization of the specimens. The EBSD technique was used to reveal the crystallography of the middle beam and to further relate the crystallographic orientation to the mechanical properties of the sample.

Figures 6.4 (a) to (c) show the sample with the EBSD pattern from the middle beam in the $\text{Ni}_x\text{Co}_{1-x}\text{O}/\text{ZrO}_2(\text{CaO})$ sample. Figure 6.4 (b) shows the EBSD pattern taken from the center of the middle beam directly after fabrication of the sample. As this pattern shows, during the FIB fabrication the surface of the sample is significantly damaged by the ion beam. To remove the top damaged layer, the samples were ion milled for 10 minutes using the Fischione ion miller model 1010 located at CMM. Figure 6.4 (c) shows the resulting EBSD pattern after ion milling the sample.

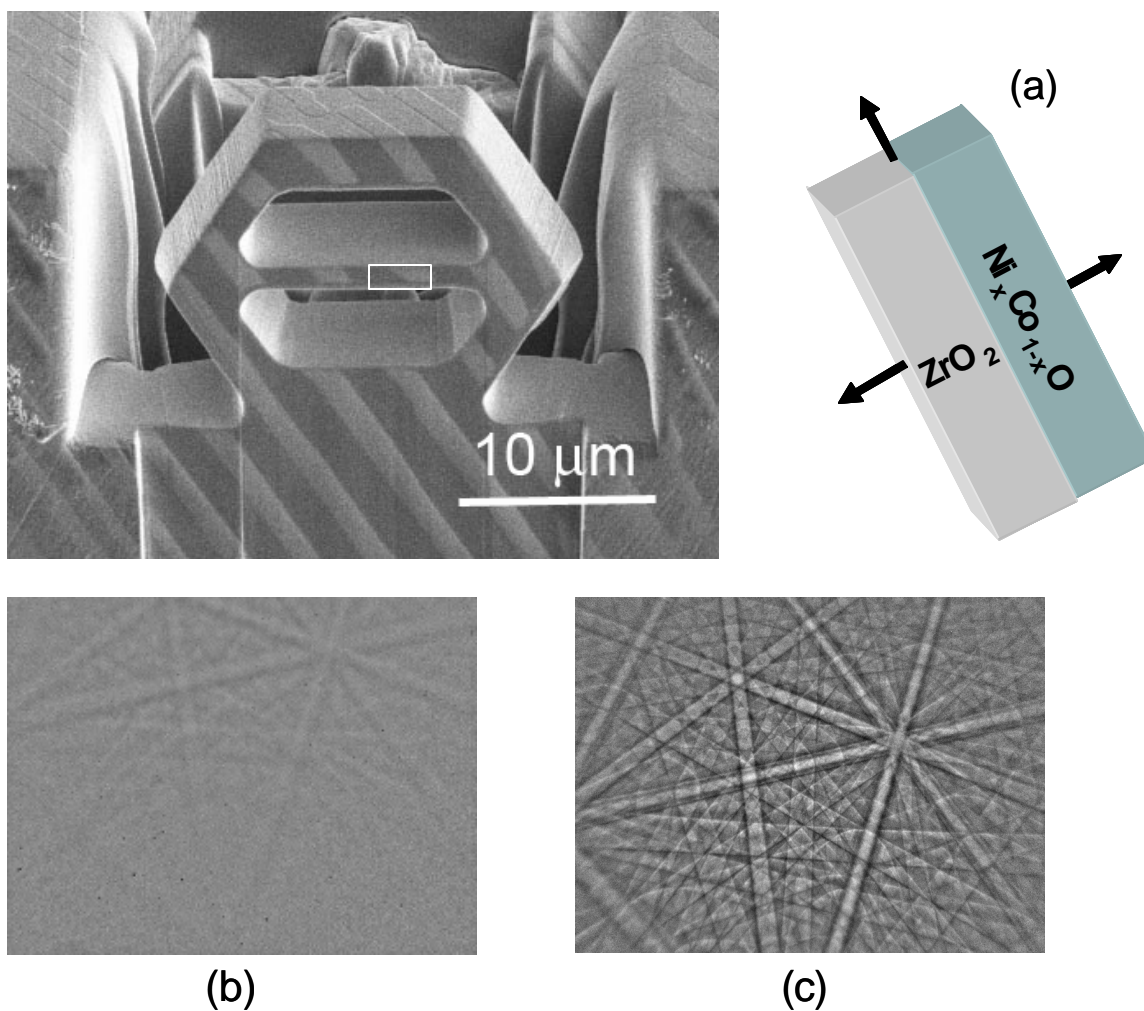


Figure 6.4 (a) The fabricated theta specimen from the pristine $Ni_xCo_{1-x}O/ZrO_2(CaO)$. (b & c) EBSD pattern from the middle web in the specimen from the area shown in the box on the image. Image (b) shows the EBSD pattern before ion sputtering and (c) shows the EBSD pattern after ion sputtering.

The samples were then tested using a MTS nano-indenter with a spherical diamond tip of 10 μm radius. The samples were loaded starting from 1mN force. The testing was continued each time by increasing the load increment till the samples failed. In addition, the stress distribution in the DSE samples with and without loading was

simulated using OOF software. The simulated stress distribution allowed for relating the mechanical properties of the sample to its microstructure, the testing design, and the stress distribution.

6.3 Mechanical Testing of $\text{Ni}_x\text{Co}_{1-x}\text{O}/\text{ZrO}_2(\text{CaO})$ Theta Structures

Figures 6.5 and 6.6 show the OOF simulation of a pristine DSE sample before and after loading, along with the load-displacement curve after testing a theta specimen from $\text{CoO}/\text{ZrO}_2(\text{CaO})$ DSE. According to Figure 6.5 due to the thermal mismatch strain in the sample, a large thermal residual stress already exists in the sample before loading. As this simulation shows, a higher tensile stress concentration exists on the top frame of the specimen, highlighted with arrows on figures 6.5 (b) and (c). Figure 6.6 shows the load-displacement curve as well as the fractured specimen frame in a fully oxidized $\text{CoO}/\text{ZrO}_2(\text{CaO})$ sample after loading. This sample is different from the one shown in Figure 6.5. Therefore the stress distribution may have local differences compared to the stress distribution in Figure 6.6. However the general tension stresses observed at the top portion of the sample are still present in this sample, as they arise from the thermal mismatch between the adjacent phases in the composite. As Figure 6.6 shows, the top frame in this sample fractured prior to failure in the middle web. This clearly verifies the results of the OOF simulation that points to the presence of a large thermal stress within the frame before loading. Therefore, there is no guarantee that the middle web will reach fracture since the top frame may prematurely fail due to the presence of large thermal stresses.

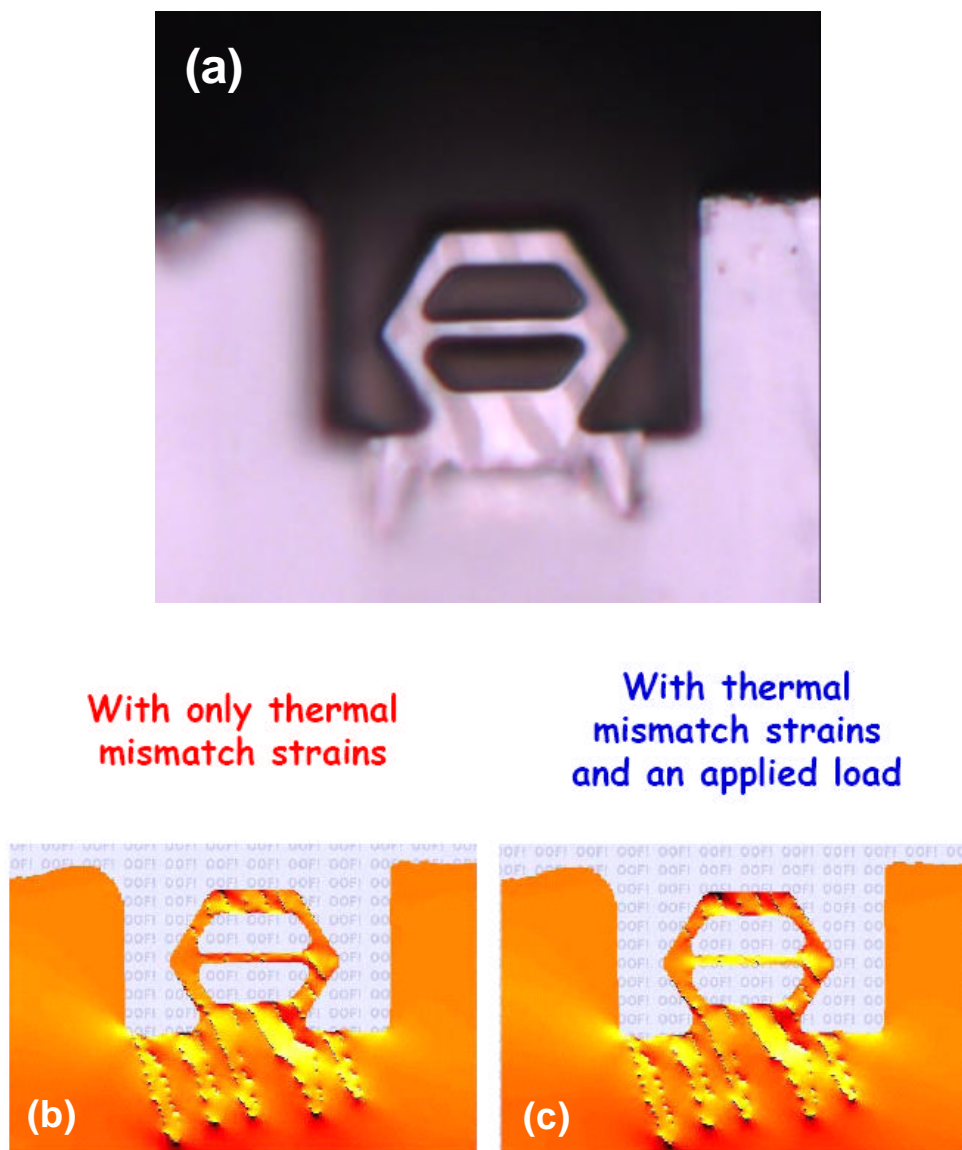


Figure 6.5 (a) The fabricated theta specimen from the pristine $\text{Ni}_x\text{Co}_{1-x}\text{O}/\text{ZrO}_2(\text{CaO})$. (b) Stress distribution within the sample considering the presence of the thermal mismatch strain in the sample.¹⁷⁹ (c) Stress distribution within the sample after applying a compression load on the top surface.¹⁷⁹

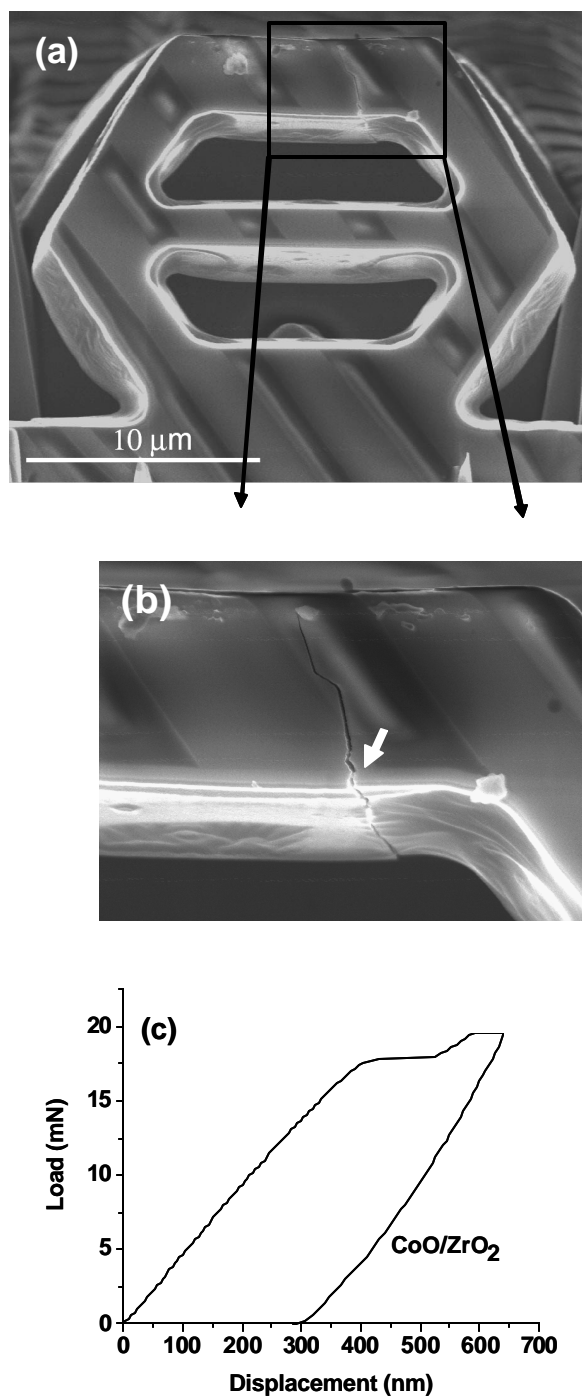


Figure 6.6 (a) The fabricated theta specimen from the pristine $\text{CoO}/\text{ZrO}_2(\text{CaO})$ after loading. (b) Fracture on the top portion of the sample frame before the middle web. (c) Load-displacement curve for this specimen.

6.4 Summary and Conclusions

This chapter presents the attempts made to evaluate the mechanical properties of $\text{Ni}_x\text{Co}_{1-x}\text{O}/\text{ZrO}_2(\text{CaO})$ model system via a novel miniature mechanical testing technique. The experiments performed here did not lead to the understanding of the mechanical properties of this system due to the complex stress state in the composite. The experimental observations in this study showed the frame in the testing stage to fracture prior to the failure of the middle web in the sample. Also the stress simulations in the sample show high levels of tensile stress to exist in the frame causing failure of the frame prior to the middle web during the experiment.

7 SUMMARY AND CONCLUSIONS

The proposed study in this thesis is intended to create a research scheme for a deeper understanding of the materials systems and to develop a predictive model for structure-property relationships for the next generation of materials systems, i.e. composites. The scheme of this thesis is designed to study the microstructurally driven phenomenological analysis of deformation behavior in ductile-brittle multi-layered systems at various length scales. This investigation aims to understand the underlying implications of the microstructure, size scale and the interfacial structure on the extent of plastic deformation in nanoscale ductile-brittle composite systems.

The objective of this thesis covers two aspects of the global research scheme in composite systems.

- To explore the feasibility of the formation of new multi-layered composite systems via novel techniques.
- To investigate the correlative structure-property relationships for the deformation and fracture behavior of the resulting composite model system at various length scales.

In this dissertation, $\text{Ni}_x\text{Co}_{1-x}\text{O}/\text{ZrO}_2(\text{CaO})$ directionally solidified eutectic has been chosen as the model system to explore the formation of confined nanoscale metallic Ni(Co) interphases upon chemical reduction of this system. This composite proved to be a desired model system for the novel formation of confined nanoscale metallic Ni(Co) interphases due to the following aspects:

- Formation of confined metallic Ni(Co) interphases is feasible in the $\text{Ni}_x\text{Co}_{1-x}\text{O}/\text{ZrO}_2(\text{CaO})$ system due to the formation of an electrochemical cell

in the system at high temperatures. The electrochemical behavior of this system at the interface owes itself to the high electrical conductivity of Ni(Co) and high ionic conductivity of $\text{ZrO}_2(\text{CaO})$.

- The $\text{Ni}_x\text{Co}_{1-x}\text{O}/\text{ZrO}_2(\text{CaO})$ composite series in fully oxidized form maintain a well-defined interfacial orientation relationship over the whole $\text{Ni}_x\text{Co}_{1-x}\text{O}-\text{ZrO}_2(\text{CaO})$ interfaces present in the composite. This uniformity in the atomic and interfacial structure over the whole composite makes this system an ideal candidate for the study of the correlative fracture and deformation mechanisms operating at various length scales.
- The interfaces in $\text{Ni}_x\text{Co}_{1-x}\text{O}/\text{ZrO}_2(\text{CaO})$ composite maintain a clean interfacial structure with no precipitate or segregate.

The following remarks regarding the present work on the $\text{Ni}_x\text{Co}_{1-x}\text{O}/\text{ZrO}_2(\text{CaO})$ composite model system summarizes the key aspects of the development of this novel metal-ceramic structure:

- This study showed that formation of a confined metallic Ni(Co) interphase is amenable in the $\text{Ni}_x\text{Co}_{1-x}\text{O}/\text{ZrO}_2(\text{CaO})$ composite upon chemical reduction of this system at high temperatures. Microstructural studies in this system show formation of Ni(Co) interphases mediating the $\text{Ni}_x\text{Co}_{1-x}\text{O}-\text{ZrO}_2(\text{CaO})$ interface after chemical reduction at high temperatures. Development of this novel metal-ceramic multi-layered structure is due to the formation of an electrochemical cell at the $\text{Ni}_x\text{Co}_{1-x}\text{O}-\text{ZrO}_2(\text{CaO})$ interface at high temperatures. This exploration offers novel processing methods for the

formation of nanoscale multi-layered metal-ceramic composites upon the chemical reaction route.

- Various electron microscopy techniques (including EDXS, EELS and diffraction imaging) were utilized to investigate the chemical, interfacial and microstructural evolution in the developed metal-ceramic multi-layered system. This investigation confirmed that the metallic Ni(Co) interphase maintains a clean and sharp interface with the adjacent ceramic phases, $\text{Ni}_x\text{Co}_{1-x}\text{O}$ and $\text{ZrO}_2(\text{CaO})$, without any interlayer or interfacial segregate.
- Formation of interfacial porosity due to volume shrinkage is another reaction product upon reduction of the system. The 2-4% measured volume shrinkage is mainly distributed in the form of interfacial porosity in the partially reduced area of the sample in the developed structure. This porosity formation is due to the formation of oxygen vacant sites upon reduction of the system.

Scanning and transmission electron microscopy techniques were utilized to investigate the correlative deformation and fracture mechanisms operating in the reduced $\text{Ni}_x\text{Co}_{1-x}\text{O}/\text{ZrO}_2(\text{CaO})$ system at micron and nano size scales. Using transmission electron microscopy, the role of size scale on the extent of strain energy absorption within the nanoscale confined interphase was investigated at small length scales. The metallic layer thickness in this investigation varied from 50 nm to 300 nm. Moreover FIB lift-off technique was utilized to study the crack tip interactions with the lamellae and to further investigate the role of the microstructure on the deformation mechanism operating in this system at small length scales. The following points summarize the important features of

the deformation and fracture behavior of the $\text{Ni}_x\text{Co}_{1-x}\text{O}/\text{ZrO}_2(\text{CaO})$ model system with nanoscale confined metallic interphases:

- Vickers indentation behavior of the composite before and after reduction indicates that the confined interphase plays a significant role in the crack propagation behavior of the system. The reduced $\text{Ni}_x\text{Co}_{1-x}\text{O}/\text{ZrO}_2(\text{CaO})$ system exhibits enhanced energy dissipative mechanisms through plastic deformation, interfacial delamination, crack arrest and crack bridging across the nanoscale metallic interphase compared to its fully oxidized state upon Vickers indentation. The deformation mechanisms observed upon Vickers indentation of this system clearly indicate that the confined metallic interphase contributes to the toughening enhancement of the system. This enhancement is observed across the reduced $\text{Ni}_x\text{Co}_{1-x}\text{O}/\text{ZrO}_2(\text{CaO})$ DSE series studied here ($x=0$ and 0.5).
- This study revealed that the role of metallic interphase in strain energy absorption is more prominent at larger interphase size scales (above 100 nm). Upon decreasing the interphase thickness (below 100 nm), no large scale plasticity is observed within the interphase and a drop in the dislocation activity within the metallic interphase is observed.
- The investigations on the crack tip interactions with the metal-ceramic lamellae in the reduced $\text{Ni}_x\text{Co}_{1-x}\text{O}/\text{ZrO}_2(\text{CaO})$ DSE indicate that at small interphase size scales (below 100 nm) the extent of plasticity within the metallic interphase is very limited. At this size scale the metallic interphase still contributes to crack tip blunting and local plasticity in the system. For

further strain energy absorption, the metallic interphase transfers the load to the adjacent CoO ceramic phase rather than absorbing the strain energy within itself through plastic deformation.

- This research also highlights the role of chemistry on the small scale deformation mechanism in this model system. The TEM investigations on the reduced $\text{Ni}_x\text{Co}_{1-x}\text{O}/\text{ZrO}_2(\text{CaO})$ DSE model system clearly show twinning and stacking fault formation to be the prominent deformation mechanism in the Co interphase. Addition of Ni element to the interphase, however, increases the stacking fault formation energy in the Ni(Co) solid solution. Due to this energy rise, deformation through formation of dislocations becomes a more dominant mechanism in the Ni(Co) solid solution interphases.
- This study also showed the role of size scale on the nanoscale deformation mechanisms operating in the metallic interphase. Upon reduction of the interphase layer thickness (below 100 nm), twinning propensity is significantly suppressed in the metallic interphase. This observation also revealed that with decreasing the interphase thickness, the thickness of the twin layers is significantly reduced in size. The changes observed in the deformation mechanism of the confined interphase are believed to be due to the decrease in size scale. Moreover, the presence of rigid lattice planes in the metal-ceramic interfaces is believed to have an important role in suppressing the twinning formation nucleating from the interface.

The remarks derived from this study point to the importance of understanding the structure-property relationships in the multi-layered composites and the role of size scale,

confinement, and chemistry along with the interfacial characteristics of the system to its toughening enhancement. The aim of this dissertation is to shed light onto the phenomenological contribution of the interfacial and microstructural attributes within a composite system to its macro-scale toughness enhancement. Finally, this dissertation further points to the importance of developing a predictive structure-property relationship of deformation and fracture phenomena in multi-layered ductile-brittle composites.

8 SUGGESTIONS FOR FUTURE WORK

This thesis should be considered as the springboard to more extensive and elaborate studies to understand the deformation mechanism of the confined nanoscale multi-layered systems in general and the $\text{Ni}_x\text{Co}_{1-x}\text{O}/\text{ZrO}_2(\text{CaO})$ model system in specific.

According to the conclusions of this thesis, addition of a metallic interphase to the $\text{Ni}_x\text{Co}_{1-x}\text{O}/\text{ZrO}_2(\text{CaO})$ model system leads to the toughening enhancement of this system. The next immediate step in this research would be to evaluate the mechanical properties of the $\text{Ni}_x\text{Co}_{1-x}\text{O}/\text{ZrO}_2(\text{CaO})$ model system before and after reduction through miniature mechanical testing techniques.

A miniature nano-indentation stage has been recently developed where one can observe the failure and deformation of the sample during the mechanical testing in the SEM.^{180, 181} This direct observation can reveal several key points about the failure mechanism of a system during deformation. Similarly, a miniature compression testing technique has been recently designed by Uchic *et al.*^{182, 183}, where they successfully fabricated and tested cylindrical-shaped samples of various materials in different sizes to examine the effect of size scale on the strength of the material. Using such testing techniques it is possible to evaluate the mechanical properties of the $\text{Ni}_x\text{Co}_{1-x}\text{O}/\text{ZrO}_2(\text{CaO})$ model system before and after reduction and to further study the role of metallic interphases in this model system.

The Theta-specimen design is another novel method for the evaluation of the mechanical properties of materials. As previously described in chapter 6, this method was employed to measure the mechanical properties of the model system here. However due to the presence of a complex stress state within the frame, the testing did not lead to the

evaluation of the mechanical properties of the composite. Recent developments in this technique have shown less sensitivity of the stress distribution in the stage to the non-ideal loading configurations in the system. Also subtle changes in the geometry of the testing stage are believed to better accommodate for the pre-existing stresses in the sample. Fabrication of a thinner middle web in this structure would help create the same level of stress with less applied load on the top portion of the specimen. This can lead to the failure of the middle web before the frame in the sample. It would be of particular interest to investigate the feasibility of employing this testing stage for the evaluation of the mechanical properties of composite materials both through simulation and mechanical testing.

In situ TEM miniature mechanical testing is another technique that leads to further understanding of the deformation process and the toughening enhancement in the reduced $\text{Ni}_x\text{Co}_{1-x}\text{O}/\text{ZrO}_2(\text{CaO})$ model system. *In situ* TEM miniature mechanical testing allows one to further investigate several aspects of small scale deformation such as observation of the crack tip interactions with the lamellae, nucleation and propagation of defects and the development of the deformation zone in each layer upon the impinging crack.^{75, 184-189} *In situ* TEM mechanical testing also helps with a more thorough understanding of the deformation process through differentiating between the nucleating defects during deformation and the previously existing defects in the lamellae. In addition it reveals the interaction between the moving defects with the interfaces/boundaries in the reduced $\text{Ni}_x\text{Co}_{1-x}\text{O}/\text{ZrO}_2(\text{CaO})$ model system.¹⁹⁰

REFERENCES

1. A. Leyland, and A. Matthews: Design Criteria for Wear-Resistant Nanostructured and Glassy-Metal. *Surface & Coatings Technology* 177, 317 (2004).
2. A. A. Voevodin, S. D. Walck, and J. S. Zabinski: Architecture of Multilayer Nanocomposite Coatings with Super-Hard Diamond-Like Carbon Layers for Wear Protection at High Contact Loads. *Wear* 203, 516 (1997).
3. A. Leyland, and A. Matthews: On the Significance of the H/E Ratio in Wear Control: A Nanocomposite Coating Approach to Optimized Tribological Behavior. *Wear* 246, 1 (2000).
4. J. T. Culp, J. H. Park, I. O. Benitez, M. W. Meisel, and D. R. Talham: Two Applications of Metal Cyanide Square Grid Monolayers: Studies of Evolving Magnetic Properties in Layered Films and Templating Prussian Blue Family Thin Films. *Polyhedron* 22, 2125 (2003).
5. B. Panda, C. B. Samantaray, A. Dhar, S. K. Ray, and D. Bhattacharya: Electrical Properties of R.F. Magnetron Sputtered Baxsr1-Xtio3 Films on Multi-Layered Bottom Electrodes for High-Density Memory Application. *Journal of Materials Science-Materials in Electronics* 13, 263 (2002).
6. L. L. Zhang, J. Tsaur, and R. Maeda: Residual Stress Study of $\text{SiO}_2/\text{Pt}/\text{Pb}(\text{Zr},\text{Ti})\text{O}_3/\text{Pt}$ Multilayer Structure for Micro Electro Mechanical System Applications. *Japanese Journal of Applied Physics Part 1-Regular Papers Short Notes & Review Papers* 42, 1386 (2003).
7. L. N. Tsai, G. R. Shen, Y. T. Cheng, and W. Hsu: Performance Improvement of an Electrothermal Microactuator Fabricated Using Ni-Diamond Nanocomposite. *Journal of Microelectromechanical Systems* 15, 149 (2006).
8. R. M. Cannon, D. Korn, G. Ellsner, and M. Ruhle: Fracture Properties of Interfacially Doped Nb- Al_2O_3 Bicrystals: II, Relation of Interfacial Bonding, Chemistry and Local Plasticity. *Acta Materialia* 50, 3903 (2002).
9. L. N. Brewer, D. P. Endler, S. Austin, V. P. Dravid, and J. M. Collins: Interface Modification for Increased Fracture Toughness in Reaction-Formed Yttrium Aluminum Garnet/Alumina Eutectic Composites. *Journal of Materials Research* 14, 3907 (1999).
10. L. N. Brewer, M. U. Guruz, and V. P. Dravid: Interfacial Fracture Mechanisms in Solid Solution Directionally Solidified Eutectic Oxide Composites. *Acta Materialia* 52, 3781 (2004).

11. D. A. Muller, S. Subramanian, P. E. Batson, J. Silcox, and S. L. Sass: Structure, Chemistry and Bonding at Grain Boundaries in Ni₃Al .1. The Role of Boron in Ductilizing Grain Boundaries. *Acta Materialia* 44, 1637 (1996).
12. S. Subramanian, D. A. Muller, J. Silcox, and S. L. Sass: Structure, Chemistry and Bonding at Grain Boundaries in Ni₃Al .2. The Structure of Small Angle Boundaries, Ni-Enrichment and Its Influence on Bonding, Structure, Energy and Properties. *Acta Materialia* 44, 1647 (1996).
13. B. W. Kempshall, Y. H. Sohn, S. K. Jha, S. Laxman, R. R. Vanfleet, and J. Kimmel: A Microstructural Observation of near-Failure Thermal Barrier Coating: A Study by Photostimulated Luminescence Spectroscopy and Transmission Electron Microscopy. *Thin Solid Films* 466, 128 (2004).
14. D. Y. Park, and J. M. Yang: Fracture Behavior of Directionally Solidified CeO₂- and Pr₂O₃-Doped Y₃Al₅O₁₂/Al₂O₃ Eutectic Composites. *Materials Science and Engineering A-Structural Materials Properties Microstructure and Processing* 332, 276 (2002).
15. J. Llorca, and V. M. Orera: Directionally Solidified Eutectic Ceramic Oxides. *Progress in Materials Science* 51, 711 (2006).
16. S. R. Choi, and N. P. Bansal: Mechanical Behavior of Zirconia/Alumina Composites. *Ceramics International* 31, 39 (2005).
17. L. N. Brewer: Solid Solution Directionally Solidified Eutectics: Model Systems for Structure-Based Property Relationships in Interfacial Fracture. Ph.D. Thesis, Northwestern University 2001.
18. J. Y. Pastor, P. Poza, J. Llorca, J. I. Pena, R. I. Merino, and V. M. Orera: Mechanical Properties of Directionally Solidified Al₂O₃-ZrO₂(Y₂O₃) Eutectics. *Materials Science and Engineering A-Structural Materials Properties Microstructure and Processing* 308, 241 (2001).
19. J. M. Yang, S. M. Jeng, and S. Y. Chang: Fracture Behavior of Directionally Solidified Y₃Al₅O₁₂/Al₂O₃ Eutectic Fiber. *Journal of the American Ceramic Society* 79, 1218 (1996).
20. E. C. Dickey, V. P. Dravid, and C. R. Hubbard: Interlamellar Residual Stresses in Single Grains of NiO-ZrO₂(Cubic) Directionally Solidified Eutectics. *Journal of the American Ceramic Society* 80, 2773 (1997).
21. M. D. Brumels, and B. J. Pletka: Fracture Initiation in the Directionally Solidified NiO-CaO Eutectic. *Journal of the American Ceramic Society* 70, 305 (1987).
22. C. Choi, D. C. Seo, J. J. Lee, and J. K. Kim: Effect of Embedded Optical Fibers on the Interlaminar Fracture Toughness of Composite Laminates. *Composite Interfaces* 5, 225 (1998).

23. F. W. Zok: Developments in Oxide Fiber Composites. *Journal of the American Ceramic Society* 89, 3309 (2006).
24. A. G. Evans, and R. M. Mcmeeking: On the Toughening of Ceramics by Strong Reinforcements. *Acta Metallurgica* 34, 2435 (1986).
25. A. G. Evans, and B. J. Dalgleish: The Fracture-Resistance of Metal Ceramic Interfaces. *Acta Metallurgica et Materialia* 40, S295 (1992).
26. K. T. Faber, and A. G. Evans: 2 Toughening Mechanisms - Crack Deflection and Microcracking. *American Ceramic Society Bulletin* 60, 382 (1981).
27. A. G. Evans, and K. T. Faber: Toughening of Ceramics by Circumferential Microcracking. *Journal of the American Ceramic Society* 64, 394 (1981).
28. P. F. Becher: Microstructural Design of Toughened Ceramics. *Journal of the American Ceramic Society* 74, 255 (1991).
29. K. T. Faber, and A. G. Evans: Crack Deflection Processes .2. Experiment. *Acta Metallurgica* 31, 577 (1983).
30. K. T. Faber, and A. G. Evans: Crack Deflection Processes .1. Theory. *Acta Metallurgica* 31, 565 (1983).
31. R. M. Mcmeeking, and A. G. Evans: Mechanics of Transformation-Toughening in Brittle Materials. *Journal of the American Ceramic Society* 65, 242 (1982).
32. M. Y. He, and J. W. Hutchinson: Crack Deflection at an Interface between Dissimilar Elastic-Materials. *International Journal of Solids and Structures* 25, 1053 (1989).
33. M. Y. He, A. G. Evans, and J. W. Hutchinson: Crack Deflection at an Interface between Dissimilar Elastic-Materials - Role of Residual-Stresses. *International Journal of Solids and Structures* 31, 3443 (1994).
34. J. Dundurs, and D B. Bogy: Edge-Bonded Dissimilar Orthogonal Elastic Wedges under Normal and Shear Loading. *Journal of Applied Mechanics* 36, 650 (1969).
35. A. G. Evans, B. J. Dalgleish, M. He, and J. W. Hutchinson: On Crack Path Selection and the Interface Fracture Energy in Bimaterial Systems. *Acta Metallurgica* 37, 3249 (1989).
36. A. G. Evans, A. Bartlett, J. B. Davis, B. D. Flinn, M. Turner, and I. E. Reimanis: The Fracture-Resistance of Metal Ceramic Intermetallic Interfaces. *Scripta Metallurgica et Materialia* 25, 1003 (1991).

37. M. Hasegawa, S. J. Zhu, Y. Kagawa, and A. G. Evans: Effect of Metal Layer Thickness on the Decohesion of High Purity Copper-Sapphire Interfaces. *Acta Materialia* 51, 5113 (2003).
38. S. X. Mao, and A. G. Evans: The Influence of Blunting on Crack Growth at Oxide/Metal Interfaces. *Acta Materialia* 45, 4263 (1997).
39. M. Y. He, F. E. Heredia, D. J. Wissuchek, M. C. Shaw, and A. G. Evans: The Mechanics of Crack-Growth in Layered Materials. *Acta Metallurgica et Materialia* 41, 1223 (1993).
40. B. Chandrasekaran: Tailoring of Cobalt Oxide-Zirconium Oxide (Cubic) Co-ZrO₂(C) Directionally Solidified Eutectic with a Metal Interphase. ed. 1999), pp. 615.
41. B. D. Flinn, F. W. Zok, F. F. Lange, and A. G. Evans: Processing and Properties of Al₂O₃-Al Composites. *Materials Science and Engineering A-Structural Materials Properties Microstructure and Processing* 144, 153 (1991).
42. A. G. Varias, Z. Suo, and C. F. Shih: Ductile Failure of a Constrained Metal Foil. *Journal of the Mechanics and Physics of Solids* 39, 963 (1991).
43. A. G. Varias, Z. Suo, and C. F. Shih: Mode Mixity Effect on the Damage of a Constrained Ductile Layer. *Journal of the Mechanics and Physics of Solids* 40, 485 (1992).
44. T. C. Isabell, V. P. Dravid, and D. N. Hill: Crack Interface Interactions in a Tungsten-Yttria-Stabilized-Zirconia Directionally Solidified Eutectic. *Journal of the American Ceramic Society* 79, 412 (1996).
45. I. E. Reimanis, B. J. Dalgleish, M. Brahy, M. Ruhle, and A. G. Evans: Effects of Plasticity on the Crack-Propagation Resistance of a Metal/Ceramic Interface. *Acta Metallurgica et Materialia* 38, 2645 (1990).
46. M. Degraef, B. J. Dalgleish, M. R. Turner, and A. G. Evans: Interfaces between Alumina and Platinum - Structure, Bonding and Fracture-Resistance. *Acta Metallurgica et Materialia* 40, S333 (1992).
47. I. E. Reimanis: Fracture at Nb/Al₂O₃ Interfaces. *Scripta Metallurgica et Materialia* 27, 1729 (1992).
48. A. G. Evans, J. W. Hutchinson, and Y. Wei: Interface Adhesion: Effects of Plasticity and Segregation. *Acta Materialia* 47, 4093 (1999).
49. J. W. Hutchinson, and A. G. Evans: Mechanics of Materials: Top-Down Approaches to Fracture. *Acta Materialia* 48, 125 (2000).

50. H. C. Cao, and A. G. Evans: On Crack Extension in Ductile/Brittle Laminates. *Acta Metallurgica* 39, 2997 (1991).
51. M. F. Ashby, F. J. Blunt, and M. Bannister: Flow Characteristics of Highly Constrained Metal Wires. *Acta Metallurgica* 37, 1847 (1989).
52. K. S. Chan, M. Y. He, and J. W. Hutchinson: Cracking and Stress Redistribution in Ceramic Layered Composites. *Materials Science and Engineering A-Structural Materials Properties Microstructure and Processing* 167, 57 (1993).
53. B. Bonvalotdubois, G. Dhalenne, and A. Revcolevschi: Crystallographically Aligned Metal-Oxide Composite Made by Reduction of a Directionally Solidified Oxide Eutectic. *Materials Research Society Symposium, Pittsburgh, Pa., 1989*, pp. xv, 615.
54. V. A. Lubarda, J. A. Blume, and A. Needleman: An Analysis of Equilibrium Dislocation Distributions. *Acta Metallurgica et Materialia* 41, 625 (1993).
55. G. S. Was, and T. Foecke: Deformation and Fracture in Microlaminates. *Thin Solid Films* 286, 1 (1996).
56. K. H. Hsia, Z. Suo, and W. Yang: Cleavage Due to Dislocation Confinement in Layered Materials. *Journal of the Mechanics and Physics of Solids* 42, 877 (1994).
57. D. R. Bloyer, K. T. V. Rao, and R. O. Ritchie: Laminated Nb/Nb₃Al Composites: Effect of Layer Thickness on Fatigue and Fracture Behavior. *Materials Science and Engineering A-Structural Materials Properties Microstructure and Processing* 240, 393 (1997).
58. Y. Choi, and S. Suresh: Size Effects on the Mechanical Properties of Thin Polycrystalline Metal Films on Substrates. *Acta Materialia* 50, 1881 (2002).
59. P. M. Anderson, T. Foecke, and P. M. Hazzledine: Dislocation-Based Deformation Mechanisms in Metallic Nanolaminates. *MRS Bulletin* 24, 27 (1999).
60. L. B. Freund: Dislocation Mechanisms of Relaxation in Strained Epitaxial-Films. *MRS Bulletin* 17, 52 (1992).
61. B. M. Clemens, H. Kung, and S. A. Barnett: Structure and Strength of Multilayers. *MRS Bulletin* 24, 20 (1999).
62. Z. P. Bazant, Z. Y. Guo, H. D. Espinosa, Y. Zhu, and B. Peng: Epitaxially Influenced Boundary Layer Model for Size Effect in Thin Metallic Films. *Journal of Applied Physics* 97, (2005).
63. W. D. Nix: Yielding and Strain Hardening of Thin Metal Films on Substrates. *Scripta Materialia* 39, 545 (1998).

64. M. Ronay: Yield Stress of Thin FCC Polycrystalline Metal-Films Bonded to Rigid Substrates. *Philosophical Magazine A-Physics of Condensed Matter Structure Defects and Mechanical Properties* 40, 145 (1979).
65. L. B. Freund: The Mechanics of Dislocations in Strained-Layer Semiconductor-Materials. *Advances in Applied Mechanics* 30, 1 (1994).
66. H. D. Espinosa, S. Berbenni, M. Panico, and K. W. Schwarz: An Interpretation of Size-Scale Plasticity in Geometrically Confined Systems. *Proceedings of the National Academy of Sciences of the United States of America* 102, 16933 (2005).
67. A. Misra, M. Verdier, Y. C. Lu, H. Kung, T. E. Mitchell, N. Nastasi, and J. D. Embury: Structure and Mechanical Properties of Cu-X (X = Nb,Cr,Ni) Nanolayered Composites. *Scripta Materialia* 39, 555 (1998).
68. A. Misra, J. P. Hirth, and R. G. Hoagland: Length-Scale-Dependent Deformation Mechanisms in Incoherent Metallic Multilayered Composites. *Acta Materialia* 53, 4817 (2005).
69. M. A. Phillips, B. M. Clemens, and W. D. Nix: Mechanical Properties of Al/Al₃Sc Metallic Multilayers - Deformation Mechanisms at the Nanoscale. *Thermec'2003, Pts 1-5 Materials Science Forum* 426-4, 3373 (2003).
70. M. A. Phillips, B. M. Clemens, and W. D. Nix: A Model for Dislocation Behavior During Deformation of Al/Al₃Sc (FCC/L1(2))Metallic Multilayers. *Acta Materialia* 51, 3157 (2003).
71. M. A. Phillips, B. M. Clemens, and W. D. Nix: Microstructure and Nanoindentation Hardness of Al/Al₃Sc Multilayers. *Acta Materialia* 51, 3171 (2003).
72. J. R. Weertman, D. Farkas, K. Hemker, H. Kung, M. Mayo, R. Mitra, and H. Van Swygenhoven: Structure and Mechanical Behavior of Bulk Nanocrystalline Materials. *MRS Bulletin* 24, 44 (1999).
73. A. Misra, and H. Kung: Deformation Behavior of Nanostructured Metallic Multilayers. *Advanced Engineering Materials* 3, 217 (2001).
74. J. D. Embury, and J. P. Hirth: On Dislocation Storage and the Mechanical Response of Fine-Scale Microstructures. *Acta Metallurgica et Materialia* 42, 2051 (1994).
75. K. Hattar, J. Han, M. T. A. Saif, and I. M. Robertson: *In situ* Transmission Electron Microscopy Observations of Toughening Mechanisms in Ultra-Fine Grained Columnar Aluminum Thin Films. *Journal of Materials Research* 20, 1869 (2005).
76. J. J. Kruzic, J. M. McNaney, R. M. Cannon, and R. O. Ritchie: Effects of Plastic Constraint on the Cyclic and Static Fatigue Behavior of Metal/Ceramic Layered Structures. *Mechanics of Materials* 36, 57 (2004).

77. J. S. Koehler: Attempt to Design a Strong Solid. *Physical Review B* 2, 547 (1970).
78. D. A. Hardwick: The Mechanical-Properties of Thin-Films - a Review. *Thin Solid Films* 154, 109 (1987).
79. S. L. Lehoczky: Retardation of Dislocation Generation and Motion in Thin-Layered Metal Laminates. *Physical Review Letters* 41, 1814 (1978).
80. T. H. Courtney: *Mechanical Behavior of Materials*. McGraw Hill, Boston, 2nd ed. (2000).
81. J. D. Embury, and C. W. Sinclair: The Mechanical Properties of Fine-Scale Two-Phase Materials. *Materials Science and Engineering A-Structural Materials Properties Microstructure and Processing* 319, 37 (2001).
82. A. Revcolevschi, and G. Dhalenne: Engineering Oxide Oxide and Metal-Oxide Microstructures in Directionally Solidified Eutectics. *Advanced Materials* 5, 657 (1993).
83. B. Bonvalotdubois, G. Dhalenne, J. Berthon, A. Revcolevschi, and R. A. Rapp: Reduction of NiO Platelets in a NiO/ZrO₂(CaO) Directional Composite. *Journal of the American Ceramic Society* 71, 296 (1988).
84. L. N. Brewer, V. P. Dravid, G. Dhalenne, and M. Velazquez: Solid-Solution Directionally Solidified Eutectic Oxide Composites: Part I. Eutectic Growth and Characterization. *Journal of Materials Research* 17, 760 (2002).
85. L. N. Brewer, V. P. Dravid, M. Velazquez, and A. Revcolevschi: Solid Solution Directionally Solidified Eutectic Oxide Composites: Part II. Co_{1-x}Ni_xO Single-Crystal Growth and Characterization. *Journal of Materials Research* 17, 768 (2002).
86. E. C. Dickey: *Interface Structure and Interfacial Phenomena in Nickel Oxide - Cubic Zirconia Directionally Solidified Eutectics*. Ph.D. thesis, Northwestern University 1997.
87. E. C. Dickey, V. P. Dravid, P. D. Nellist, D. J. Wallis, and S. J. Pennycook: Three-Dimensional Atomic Structure of NiO-ZrO₂(Cubic) Interfaces. *Acta Materialia* 46, 1801 (1998).
88. V. P. Dravid, C. E. Lyman, M. R. Notis, and A. Revcolevschi: High-Resolution Transmission Electron-Microscopy of Interphase Interfaces in NiO-ZrO₂(CaO). *Ultramicroscopy* 29, 60 (1989).
89. V. P. Dravid, C. E. Lyman, M. R. Notis, and A. Revcolevschi: Low-Energy Interfaces in NiO-ZrO₂(CaO) Eutectic. *Metallurgical Transactions a-Physical Metallurgy and Materials Science* 21, 2309 (1990).

90. L. N. Brewer, R. A. Peascoe, C. R. Hubbard, and V. P. Dravid: Residual Stress Distributions in the Solid Solution Eutectic, $\text{Co}_{1-x}\text{Ni}_x\text{O}/\text{ZrO}_2(\text{CaO})$. *Journal of the American Ceramic Society* 86, 2188 (2003).
91. F. Guiberteau, C. Clauss, A. Dominguezrodriguez, and J. Castaing: Plastic-Deformation of CoO Single-Crystals by Compression Along (111). *Journal of Materials Science Letters* 8, 216 (1989).
92. F. Guiberteau, A. Dominguezrodriguez, M. Spendel, and J. Castaing: Plastic-Deformation of Bunsenite (NiO) at Temperatures Below 1050-Degrees-C. *Revue De Physique Appliquee* 21, 87 (1986).
93. T. J. Marrow, S. G. Roberts, and A. K. Pearcehiggins: The Brittle/Ductile Transition in Cubic Stabilized Zirconia. *Journal of the European Ceramic Society* 14, 447 (1994).
94. D. S. Cheong, A. Dominguezrodriguez, and A. H. Heuer: High-Temperature Plastic-Deformation of Y_2O_3 -Stabilized ZrO_2 Single-Crystals .3. Variation in Work-Hardening between 1200-Degrees-C and 1500-Degrees-C. *Philosophical Magazine a-Physics of Condensed Matter Structure Defects and Mechanical Properties* 63, 377 (1991).
95. A. Dominguezrodriguez, V. Lanteri, and A. H. Heuer: High-Temperature Precipitation Hardening of 2-Phase Y_2O_3 -Partially-Stabilized ZrO_2 Single-Crystals - a 1st Report. *Journal of the American Ceramic Society* 69, 285 (1986).
96. B. Y. Farber, A. S. Chiarelli, and A. H. Heuer: A Dislocation Mechanism of Crack Nucleation in Cubic Zirconia Single-Crystals. *Philosophical Magazine a-Physics of Condensed Matter Structure Defects and Mechanical Properties* 70, 201 (1994).
97. A. Revcolevschi, and G. Dhalenne: Crystallographically Aligned Metal-Oxide Composite Made by Reduction of a Directionally Solidified Oxide Oxide Eutectic. *Nature* 316, 335 (1985).
98. E. Ustundag, R. Subramanian, R. Vaia, R. Dieckmann, and S. L. Sass: *In situ* Formation of Metal-Ceramic Microstructures, Including Metal-Ceramic Composites, Using Reduction Reactions. *Acta Metallurgica et Materialia* 41, 2153 (1993).
99. H. Kondo, T. Sekino, N. Tanaka, T. Nakayama, T. Kusunose, and K. Niihara: Mechanical and Magnetic Properties of Novel Ytria-Stabilized Tetragonal Zirconia/Ni Nanocomposite Prepared by the Modified Internal Reduction Method. *Journal of the American Ceramic Society* 88, 1468 (2005).
100. B. Bonvalotdubois, G. Dhalenne, and A. Revcolevschi: Electrochemical Behavior of Lamellar Interfaces in $\text{CoO-ZrO}_2(\text{CaO})$ Aligned Eutectic Structures Submitted to Chemical Reduction. *Materials Research Society Symposium Proceedings* 138, 587 (1989).

101. J. W. Patterson, E. C. Bogren, and R. A. Rapp: Mixed Conduction in $Zr_{0.85}Ca_{0.15}O_{1.85}$ and $Th_{0.85}Y_{0.15}O_{1.925}$ Solid Electrolytes. *Journal of the Electrochemical Society* 114, 752 (1967).
102. J. M. Dixon, L. D. Lagrange, U. Merten, C. F. Miller, and J. T. Porter: Electrical Resistivity of Stabilized Zirconia at Elevated Temperatures. *Journal of the Electrochemical Society* 110, 276 (1963).
103. D. B. Williams, and C. B. Carter: *Transmission Electron Microscopy: A Textbook for Materials Science*. Plenum Press, New York, 1st ed. (1996).
104. K. E. Smith, R. Kershaw, K. Dwight, and A. Wold: Preparation and Properties of Cubic ZrO_2 Stabilized with Ni(II). *Materials Research Bulletin* 22, 1125 (1987).
105. M. A. Laguna-Bercero, A. Larrea, R. I. Merino, J. I. Pena, and V. M. Orera: Stability of Channeled Ni-YSZ Cermets Produced from Self-Assembled NiO-YSZ Directionally Solidified Eutectics. *Journal of the American Ceramic Society* 88, 3215 (2005).
106. G. Dhalenne, and A. Revcolevschi: Directional Solidification in the NiO- ZrO_2 System. *Journal of Crystal Growth* 69, 616 (1984).
107. W. Betteridge: Properties of Metallic Cobalt. *Progress in Materials Science* 24, 51 (1979).
108. S. R. Liu, and Y. Liu: Beta→Alpha Transformation of Gamma-Phase in Sintered WC-Co Cemented Carbides. *Journal of Materials Science & Technology* 12, 398 (1996).
109. S. Ram: Self-Confined Dimension of Thermodynamic Stability in Co-Nanoparticles in FCC and BCC Allotropes with a Thin Amorphous Al_2O_3 Surface Layer. *Acta Materialia* 49, 2297 (2001).
110. S. Rana, and S. Ram: X-Ray Diffraction and X-Ray Photoelectron Spectroscopy Studies of Stabilized Cobalt Nanoparticles with a Thin Al_2O_3 Surface Layer. *Materials Science and Technology* 21, 243 (2005).
111. W. P. Tai, and T. Watanabe: Preparation and Mechanical Properties of Al_2O_3 Reinforced by Submicrometer Co Particles. *Journal of Materials Science* 33, 5795 (1998).
112. P. C. J. Gallagher: Influence of Alloying, Temperature, and Related Effects on Stacking Fault Energy. *Metallurgical Transactions* 1, 2429 (1970).
113. J. P. Gao, X. Y. Song, J. X. Zhang, K. Y. Yang, and X. M. Liu: Thermodynamic Functions and Phase Transformation of Metal Nanocrystals. *Journal of Materials Science & Technology* 21, 705 (2005).

114. C. Cabral, K. Barmak, J. Gupta, L. A. Clevenger, B. Arcot, D. A. Smith, and J. M. E. Harper: Role of Stress Relief in the Hexagonal-Close-Packed to Face-Centered-Cubic Phase-Transformation in Cobalt Thin-Films. *Journal of Vacuum Science & Technology a-Vacuum Surfaces and Films* 11, 1435 (1993).
115. J. G. Wright: FCC-HCP Phase-Transition in Electrolytically Deposited Epitaxial Cobalt Films. *Thin Solid Films* 22, 197 (1974).
116. E. Votava: The Phase Transformation in Thin Cobalt Films. *Journal of the Institute of Metals* 90, 129 (1961).
117. H. T. Hesemann, P. Mullner, O. Kraft, and E Arzt: Nucleation Model for HCP Martensite: Application to Co Thin Films. *Journal De Physique IV* 112, 107 (2003).
118. E. Delamott, and C. Altstett: Transformation Strain in Stressed Cobalt-Nickel Single Crystals. *Transactions of the Metallurgical Society of AIME* 245, 651 (1969).
119. P. Gaunt, and J. W. Christian: The Cubic-Hexagonal Transformation in Single Crystals of Cobalt and Cobalt-Nickel Alloys. *Acta Metallurgica* 7, 529 (1959).
120. A. Seeger: Versetzungen Und Allotrope Umwandlungen .2. *Zeitschrift Fur Metallkunde* 47, 653 (1956).
121. C. R. Houska, B. L. Averbach, and M. Cohen: The Cobalt Transformation. *Acta Metallurgica* 8, 81 (1960).
122. T. Ericsson: Temperature and Concentration Dependence of Stacking Fault Energy in Co-Ni System. *Acta Metal.* 14, 853 (1966).
123. D. I. L. Beeston B. E. P., Smallman R. E.: The Stacking Fault Energy of Some Nickel-Cobalt Alloys. *Metal Science Journal* 2, 12 (1968).
124. R. K. Ray: Rolling Textures of Pure Nickel, Nickel-Iron and Nickel-Cobalt Alloys. *Acta Metallurgica et Materialia* 43, 3861 (1995).
125. B. E. P. Beeston, and L. K. France: Stacking-Fault Energies of Some Binary Nickel Alloys Fundamental to Nimonic Series. *Journal of the Institute of Metals* 96, 105 (1968).
126. E. C. Dickey, V. P. Dravid, P. D. Nellist, D. J. Wallis, S. J. Pennycook, and A. Revcolevschi: Structure and Bonding at Ni-ZrO₂ (Cubic) Interfaces Formed by the Reduction of a NiO-ZrO₂ (Cubic) Composite. *Microscopy and Microanalysis* 3, 443 (1997).
127. E. C. Dickey, Y. M. Bagiyono, G. D. Lian, S. B. Sinnott, and T. Wagner: Preferred Crystallographic Orientation Relationships of Nickel Films Deposited on (100) Cubic-Zirconia Substrates. *Thin Solid Films* 372, 37 (2000).

128. R. G. Stringfellow, D. M. Parks, and G. B. Olson: A Constitutive Model for Transformation Plasticity Accompanying Strain-Induced Martensitic Transformations in Metastable Austenitic Steels. *Acta Metallurgica et Materialia* 40, 1703 (1992).
129. H. H. Pan, and G. J. Weng: Thermal-Stress and Volume Change During a Cooling Process Involving Phase-Transformation. *Journal of Thermal Stresses* 15, 1 (1992).
130. Z. Suo, D. V. Kubair, A. G. Evans, D. R. Clarke, and V. K. Tolpygo: Stresses Induced in Alloys by Selective Oxidation. *Acta Materialia* 51, 959 (2003).
131. N. Alem, and V. P. Dravid: Interfacial Fracture Phenomena in Ceramic Composite Directionally Solidified Eutectics with a Ductile Interphase. *Journal of the American Ceramic Society* 89, 767 (2006).
132. M. A. Laguna-Bercero, A. Larrea, J. I. Pena, R. I. Merino, and V. M. Orera: Structured Porous Ni and Co-YSZ Cermets Fabricated from Directionally Solidified Eutectic Composites. *Journal of the European Ceramic Society* 25, 1455 (2005).
133. S. K. Filatov, and Frankkam.Va: Structural Characteristics of Cubic ZrO₂ Stabilized by Calcium. *Soviet Physics Crystallography, Ussr* 14, 414 (1969).
134. J. Echigoya, Y. Takabayashi, H. Suto, and M. Ishigame: Structure and Crystallography of Directionally Solidified Al₂O₃-ZrO₂-Y₂O₃ Eutectic by the Floating Zone-Melting Method. *Journal of Materials Science Letters* 5, 150 (1986).
135. V. M. Orera, R. I. Merino, J. A. Pardo, A. Larrea, J. I. Pena, C. Gonzalez, P. Poza, J. Y. Pastor, and J. Llorca: Microstructure and Physical Properties of Some Oxide Eutectic Composites Processed by Directional Solidification. *Acta Materialia* 48, 4683 (2000).
136. H. Deng, E. C. Dickey, Y. Paderno, V. Paderno, V. Filippov, and A. Sayir: Crystallographic Characterization and Indentation Mechanical Properties of LaB₆-ZrB₂ Directionally Solidified Eutectics. *Journal of Materials Science* 39, 5987 (2004).
137. A. N. Stroh: A Theory of the Fracture of Metals. *Advances in Physics* 6, 418 (1957).
138. A. S. Keh, J. C. M. Li, and Y. T. Chou: Cracks Due to the Piling-up of Dislocations on 2 Intersecting Slip Planes in MgO Crystals. *Acta Metallurgica* 7, 694 (1959).
139. D. A. Bonnell, and J. Kiely: Plasticity at Multiple Length Scales in Metal-Ceramic Interface Fracture. *Physica Status Solidi a-Applied Research* 166, 7 (1998).
140. K. T. Faber: Ceramic Composite Interfaces: Properties and Design. *Annual Review of Materials Science* 27, 499 (1997).
141. F. Tancret, and F. Osterstock: Influence of Porosity on the Hydrostatic Constraint Factor for Evaluating Toughness from Vickers Indentation Cracks in Brittle Materials. *Philosophical Magazine Letters* 84, 1 (2004).

142. Z. Y. Deng, J. H. She, Y. Inagaki, J. F. Yang, T. Ohji, and Y. Tanaka: Reinforcement by Crack-Tip Blunting in Porous Ceramics. *Journal of the European Ceramic Society* 24, 2055 (2004).
143. M. G. Holmquist, and F. F. Lange: Processing and Properties of a Porous Oxide Matrix Composite Reinforced with Continuous Oxide Fibers. *Journal of the American Ceramic Society* 86, 1733 (2003).
144. M. G. Pontin, and F. F. Lange: Effects of Porosity on the Threshold Strength of Laminar Ceramics. *Journal of the American Ceramic Society* 88, 376 (2005).
145. W. C. Oliver, and G. M. Pharr: Measurement of Hardness and Elastic Modulus by Instrumented Indentation: Advances in Understanding and Refinements to Methodology. *Journal of Materials Research* 19, 3 (2004).
146. G. M. Pharr, and W. C. Oliver: Measurement of Thin-Film Mechanical Properties Using Nanoindentation. *MRS Bulletin* 17, 28 (1992).
147. G. M. Pharr, W. C. Oliver, and F. R. Brotzen: On the Generality of the Relationship among Contact Stiffness, Contact Area, and Elastic-Modulus During Indentation. *Journal of Materials Research* 7, 613 (1992).
148. J. W. Edington: *Practical Electron Microscopy in Materials Science*. Appendix 6 (1976).
149. R. Mitra, W. A. Chiou, and J. R. Weertman: *In situ* Study of Deformation Mechanisms in Sputtered Free-Standing Nanocrystalline Nickel Films. *Journal of Materials Research* 19, 1029 (2004).
150. C. J. Youngdahl, J. R. Weertman, R. C. Hugo, and H. H. Kung: Deformation Behavior in Nanocrystalline Copper. *Scripta Materialia* 44, 1475 (2001).
151. H. Van Swygenhoven, and J. R. Weertman: Deformation in Nanocrystalline Metals. *Materials Today* 9, 24 (2006).
152. M. A. Meyers, O. Vohringer, and V. A. Lubarda: The Onset of Twinning in Metals: A Constitutive Description. *Acta Materialia* 49, 4025 (2001).
153. J. W. Christian, and S. Mahajan: Deformation Twinning. *Progress in Materials Science* 39, 1 (1995).
154. N. Bernstein, and E. B. Tadmor: Tight-Binding Calculations of Stacking Energies and Twinnability in FCC Metals. *Physical Review B* 69, (2004).
155. A. G. Froseth, P. M. Derlet, and H. Van Swygenhoven: Twinning in Nanocrystalline FCC Metals. *Advanced Engineering Materials* 7, 16 (2005).

156. J. A. Venables: Deformation Twinning in Face-Centred Cubic Metals. *Philosophical Magazine* 6, 379 (1961).
157. Vohringer, O.: Influence of Alloy-Type and Concentration on Yield-Point of Alpha-Copper Alloys. *Zeitschrift Fur Metallkunde* 65, 352 (1974).
158. E. B. Tadmor, and S. Hai: A Peierls Criterion for the Onset of Deformation Twinning at a Crack Tip. *Journal of the Mechanics and Physics of Solids* 51, 765 (2003).
159. S. Hai, and E. B. Tadmor: Deformation Twinning at Aluminum Crack Tips. *Acta Materialia* 51, 117 (2003).
160. E. B. Tadmor, and N. Bernstein: A First-Principles Measure for the Twinnability of FCC Metals. *Journal of the Mechanics and Physics of Solids* 52, 2507 (2004).
161. R. C. Pond, and L. M. F. Garciagarcia: Deformation Twinning in Aluminum. *Institute of Physics Conference Series* 495 (1982).
162. W. P. J. Armstrong R. W.: A Constitutive Relation for Deformation Twinning in Body Centered Cubic Metals. *The Metallurgical Society of AIME proceedings, Metallurgical effects at high strain rates* 401, (1973).
163. E. El-Danaf, S. R. Kalidindi, R. D. Doherty, and C. Necker: Deformation Texture Transition in Brass: Critical Role of Micro-Scale Shear Bands. *Acta Materialia* 48, 2665 (2000).
164. D. Lahaie, J. D. Embury, M. M. Chadwick, and G. T. Gray: A Note on the Deformation of Fine-Grained Magnesium Alloys. *Scripta Metallurgica et Materialia* 27, 139 (1992).
165. M. A. Meyers, U. R. Andrade, and A. H. Chokshi: The Effect of Grain-Size on the High-Strain, High-Strain-Rate Behavior of Copper. *Metallurgical and Materials Transactions a-Physical Metallurgy and Materials Science* 26, 2881 (1995).
166. E. El-Danaf, S. R. Kalidindi, and R. D. Doherty: Influence of Grain Size and Stacking-Fault Energy on Deformation Twinning in FCC Metals. *Metallurgical and Materials Transactions A-Physical Metallurgy and Materials Science* 30, 1223 (1999).
167. F. D. Fischer, T. Schaden, F. Appel, and H. Clemens: Mechanical Twins, Their Development and Growth. *European Journal of Mechanics A-Solids* 22, 709 (2003).
168. H. Petryk, F. D. Fischer, W. Marketz, H. Clemens, and F. Appel: An Energy Approach to the Formation of Twins in TiAl. *Metallurgical and Materials Transactions A-Physical Metallurgy and Materials Science* 34A, 2827 (2003).
169. M. W. Chen, E. Ma, K. J. Hemker, H. W. Sheng, Y. M. Wang, and X. M. Cheng: Deformation Twinning in Nanocrystalline Aluminum. *Science* 300, 1275 (2003).

170. Y. T. T. Zhu, and T. G. Langdon: Influence of Grain Size on Deformation Mechanisms: An Extension to Nanocrystalline Materials. *Materials Science and Engineering A-Structural Materials Properties Microstructure and Processing* 409, 234 (2005).
171. K. S. Kumar, S. Suresh, M. F. Chisholm, J. A. Horton, and P. Wang: Deformation of Electrodeposited Nanocrystalline Nickel. *Acta Materialia* 51, 387 (2003).
172. D. S. Xu, J. P. Chang, J. Li, R. Yang, D. Li, and S. Yip: Dislocation Slip or Deformation Twinning: Confining Pressure Makes a Difference. *Materials Science and Engineering A-Structural Materials Properties Microstructure and Processing* 387-89, 840 (2004).
173. D. S. Xu, R. Yang, J. Li, J. P. Chang, H. Wang, D. Li, and S. Yip: Atomistic Simulation of the Influence of Pressure on Dislocation Nucleation in BCC Mo. *Computational Materials Science* 36, 60 (2006).
174. A. J. Durelli, and V. J. Parks: Influence of Size and Shape on Tensile Strength of Brittle Materials. *British Journal of Applied Physics* 18, 387 (1967).
175. A. J. a. P. V. J. Durelli: The Theta Specimen for Determining Tensile Strength of Brittle Materials. *American Society for Testing and Materials, Philadelphia*, pp. 114 (1962).
176. A. J. Durelli: *Applied Stress Analysis*. Prentice-Hall, Englewood Cliffs, New Jersey, pp. 173 (1967).
177. F. E. Quinn G.D., Xiang D., Jillavenkatesa A., Ma L., Smith D., Beall J.: A Novel Test Method for Measuring Mechanical Properties at the Small-Scale: The Theta Specimen. *American Ceramic Society, Ohio*, pp. 117 (2005).
178. J. A. Xiang D., Quinn G.D., Smith D.B., Beall J.A., Fuller D.R. Jr.: Theta-Like Specimens for Measuring Mechanical Properties at the Small-Scale: Experimental. Submitted to the *Journal of the American Ceramic Society* (2006).
179. D. R. Fuller: Private Communications.
180. R. Rabe, J. M. Breguet, P. Schwaller, S. Stauss, F. J. Haug, J. Patscheider, and J. Michler: Observation of Fracture and Plastic Deformation During Indentation and Scratching inside the Scanning Electron Microscope. *Thin Solid Films* 469-70, 206 (2004).
181. J. Michler, R. Rabe, J. L. Bucaille, B. Moser, P. Schwaller, and J. M. Breguet: Investigation of Wear Mechanisms through *in situ* Observation During Microscratching inside the Scanning Electron Microscope. *Wear* 259, 18 (2005).

182. M. D. Uchic, D. M. Dimiduk, J. N. Florando, and W. D. Nix: Sample Dimensions Influence Strength and Crystal Plasticity. *Science* 305, 986 (2004).

183. M. D. Uchic, and D. A. Dimiduk: A Methodology to Investigate Size Scale Effects in Crystalline Plasticity Using Uniaxial Compression Testing. *Materials Science and Engineering A-Structural Materials Properties Microstructure and Processing* 400, 268 (2005).

184. I. M. Robertson, A. Beaudoin, K. Al-Fadhalah, L. Chun-Ming, J. Robach, B. D. Wirth, A. Arsenlis, D. Ahn, and P. Sofronis: Dislocation-Obstacle Interactions: Dynamic Experiments to Continuum Modeling. *Materials Science and Engineering A-Structural Materials Properties Microstructure and Processing* 400, 245 (2005).

185. Y. Zhu, and H. D. Espinosa: An Electromechanical Material Testing System for *in situ* Electron Microscopy and Applications. *Proceedings of the National Academy of Sciences of the United States of America* 102, 14503 (2005).

186. D. E. Newbury, and D. B. Williams: The Electron Microscope: The Materials Characterization Tool of the Millennium. *Acta Materialia* 48, 323 (2000).

187. Y. Ikuhara: Towards New Transmission Electron Microscopy in Advanced Ceramics. *Journal of the Ceramic Society of Japan* 110, 139 (2002).

188. K. Jagannadham, H. G. F. Wilsdorf, and J. Weertman: Dislocations at Ductile/Plastic Crack Tips: *In-Situ* TEM Observations. *Materials Research Innovations* 1, 254 (1998).

189. S. Li, T. H. Yip, R. V. Ramanujan, and M. H. Liang: *In situ* TEM Studies of the Mechanisms of Crack Nucleation and Propagation in Fully Lamellar Microstructures. *Materials Science and Technology* 19, 902 (2003).

190. T. C. Lee, I. M. Robertson, and H. K. Birnbaum: TEM *In situ* Deformation Study of the Interaction of Lattice Dislocations with Grain-Boundaries in Metals. *Philosophical Magazine A-Physics of Condensed Matter Structure Defects and Mechanical Properties* 62, 131 (1990).